

Microstructural/petrological characteristics of peridotite xenoliths in the back-arc spreading/rifting zones and implication for the evolution and seismic anisotropy in the uppermost mantle

メタデータ	言語: en 出版者: Shizuoka University 公開日: 2014-01-14 キーワード (Ja): キーワード (En): 作成者: Satsukawa, Takako メールアドレス: 所属:
URL	https://doi.org/10.14945/00007479

THE S I S

Microstructural/petrological characteristics of
peridotite xenoliths in the back-arc spreading/rifting
zones and implication for the evolution and seismic
anisotropy in the uppermost mantle

Takako SATSUKAWA

Graduate School of
Science and Technology, Educational Division
Department of Environment and Energy Systems
Shizuoka University

January 2012

THE S I S

Microstructural/petrological characteristics of peridotite
xenoliths in the back-arc spreading/rifting zones
and implication for the evolution and seismic anisotropy in
the uppermost mantle

(かんらん捕獲岩の微細構造と岩石学的特徴:背弧拡大域及びリフト帯における最上部マントル構造発達過程と地震波特性への応用)

佐 津 川 貴 子

静岡大学

大学院自然科学系教育部

環境・エネルギーシステム専攻

2012年1月

Abstract

This thesis deals with the microstructural development in the uppermost mantle associated with melt/fluid rock interactions in peridotites induced by the back-arc spreading, as well as the implication for the seismic properties of the uppermost mantle. Ichinomegata peridotites xenoliths preserved the normal seafloor spreading, whereas Oki-Dogo peridotites preserved the extension and the thinning of continental crust. For comparison, we have studied spinel peridotite xenoliths from another tectonic setting: Kilbourne Hole (New Mexico, USA) and Knippa peridotites (Texas, USA). Peridotite xenoliths from Kilbourne Hole represented the early stages of spreading in an active rift zone, whereas Knippa peridotites xenoliths were derived from the mantle lithosphere that could have recorded deformations in relation to the thinning of continental crust.

The mineral chemistry of Ichinomegata peridotites shows a typical residual peridotite trend, depleted in LREE (light rare earth element). However, their strong Th-U positive anomaly indicates a possible metasomatic origin associated to the subduction of the Pacific plate. The chemical composition of Oki-Dogo peridotites shows that they were affected by various degree of metasomatism by melt, which might be related to back-arc spreading.

Olivine CPO of Ichinomegata peridotites are consistent with slip on (010)[100] and {0kl}[100]. The angle between the [100] maximum concentration and the foliation decreases with increasing fabric strength. By using those angles, shear strain was estimated to vary from 0.31 to 4.26, and temperature variation possibly suggested that *J*-index increased with decreasing of depth. These observations indicated that a strain gradient revealed by the peridotite xenoliths studied could be

related to back-arc spreading. Three directions have been identified within thin sections of Ichinomegata peridotites: foliation defined by pyroxene rich layers, the [100] maximum concentration of olivine, and shape preferred orientation of olivine. From the relationships between these three axes, shear plane was considered to be parallel to the [100] maximum concentration of olivine, not foliation. Those structural features were compatible with those found in the Oman ophiolite.

Olivine CPO of Oki-Dogo peridotites are consistent with the (010)[100] slip system. Samples have low Mg# and show relatively high concentration in [010], however there were no strong relationships among them. Although Oki-Dogo peridotites could be deformed in the presence of melt, there was no strong interaction between deformation and melts percolation.

Olivine CPO of Kilbourne Hole peridotite xenoliths indicated the preservation of b-axis fiber fabrics with a strong concentration of [010] with girdles of [100] and [001]. After calculating seismic properties, we concluded that these xenoliths were derived from a lateral shear zone (vertical foliation (XY plane) and horizontal lineation within the plane of the foliation (X-axis)). The shear-wave splitting observed in the Rio Grande rift was a reflection of the lithospheric fabric and the presence of melts as thin cracks or dikes; the orientation of such melt pockets parallel to the XY plane.

Knippa is located in Laurentian continental margin and records the deformation related to alternate extension and compression. Olivine CPO of Knippa peridotites preserved olivine a-axis fiber fabrics with a strong concentration of [100] and girdles of [010] and [001]. Assuming a lithospheric mantle having a horizontal flow direction parallel to fast directions, the change of delay time could be explained by fabric variation, that was, peridotites beneath the transitional crust could preserve

greater deformation from the Paleozoic Ouachita orogeny (young) rather than the lithosphere beneath the Mesoproterozoic craton (old).

In the summary, the uppermost mantle evolution in Ichinomegata peridotite xenoliths shows possible evidence that preserved strain gradient field during the latest geological event, back-arc spreading. Oki-Dogo peridotites show no clear change in microstructure and CPO with metasomatism, and there is no strong interaction between percolation of melts and deformation. In contrast, there is strong concentration of [010] from Kilbourne Hole samples, which documents the deformation under the existence of fundamental melts due to the present continental rifting.

The microstructure and geochemical characteristics observation in Oki-Dogo peridotite xenoliths were affected by the supply of upwelling-derived melts, in the end of the back-arc spreading, which may supply the trigger the termination of back-arc spreading and basins. There are no samples in back-arc region that show strong fabrics like Knippa, indicating that this strong CPO could be developed during these continuous deformations.

Overall, in the initial stage of the back-arc spreading, the active spreading starts where the uppermost mantle deformed similar system to the mid ocean ridge spreading. After that, passive extension, which depending on the surrounding environments, was induced. There are no strong reactions between melt percolation and deformation in comparison with the continental rift zone, probably due to its small size and short period. In conclusion, this study showed the uppermost mantle evolution during the back-arc spreading, which is one of the keys for the understanding of its process, and provided several aspects of the contrasts between the back-arc spreading and the mid ocean ridge/continental rifting.

Key words: seismic properties, uppermost mantle flow, oceanic crust, peridotite xenoliths, olivine, orthopyroxene, clinopyroxene, crystallographic preferred orientation, melt/liquid-rock interaction, back-arc spreading, rifting.

Acknowledgements

I first wish to express my gratitude to **Dr. Katsuyoshi Michibayashi** of Shizuoka University for his kind guidance, and critical discussions and suggestions for this thesis. I am grateful to **Dr. Benoit Ildefonse**, **Dr. David Mainprice**, **Dr. Marguerite Godard** and **Dr. Sylvie Denouchy** of Université Montpellier II, France, for their helpful recommendations and advice on my work, during my stays in Montpellier.

I would like to thank **Prof. Elizabeth Y. Anthony**, **Prof. Robert J. Stern**, **Prof. Jay Pulliam**, **Prof. Stephen S. Gao**, **Prof. Kelly H. Liu** and **Dr. Raye Urmidola** for their support and cooperation. **Prof. Toshiaki Masuda**, **Dr. Satish M. Kumar**, **Prof. Mitsuhiro Toriumi**, **Prof. Aimin Lin**, **Prof. Hideki Wada**, **Prof. Adolphe Nicolas**, **Prof. Françoise Boudier**, **Dr. Andréa Tommasi**, **Prof. Alain Vauchez**, **Dr. Jean-Louis Bodinier** and **Dr. Olivier Alard** are thanked for the encouragements, valuable suggestions, and discussions that helped to improve an early draft of the manuscript. I thank **Prof. Shoji Arai** of Kanazawa University, **Dr. Natsue Abe** of JAMSTEC and **Junji Yamamoto** of Kyoto University for their helpful recommendations regarding the sampling of Oki-Dogo peridotite xenoliths. I am specially thankful to **Dr. Ikuo Katayama**, **Dr. Yoshio Kono**, **Dr. Keshav Shantanu**, **Dr. Vincent Soustelle**, **Dr. Luiz F. G. Morales**, **Dr. Claudio Marchesi** and **Dr. Ken-ichi Hirauchi** for their technical and helpful advice and support. I wish to thank to **Dr. Tatsu Kuwatani**, **Mr. Wataru Nishikanbara**, **Dr. Yumiko Harigane**, **Ms. Miki Tasaka**, **Mr. Masashi Muramoto**, **Mr. Yuya Kusafuka**, Michibayashi laboratory's members (**Ms. Yuri Shinkai**, **Mr. Naoaki Komori**, **Mr. Masashi Kino**, **Mr. Tatsunori Ikeya**, **Mr. Toshiya Umegaki**, **Mr. Yosuke Kondo**, **Ms. Ayaka**

Onoue, Mr. Tomoki Shibata and **Mr. Keisuke Furuhata**), graduated students and post doctoral researchers of Université Montpellier II (**Dr. Mickaël Bonnin**, **Dr. Amélie Vergne**, **Ms. Kate Higgie**, **Mr. Roberto Agrusta**, **Mr. Steve Peuble**, **Mr. Théo Berthet**, **Mr. Camille Clerc**, **Mr. Grégory Fanjat**, **Ms. Fatna Kourim**, **Ms. Kamar Chetouani**, **Ms. Amel Barich**, **Mr. Zoltan Konc** and **Mr. Erwin Frets**) and my friends for their helpful advice.

CPO figures were made using the interactive programs developed by **Dr. David Mainprice** of Université Montpellier II, France. **Prof. Mitsuhiro Toriumi** and **Dr. Tatsu Kuwatani** are thanked for their assistance in operating the JEOL JXA-8200 electron microprobe at the University of Tokyo. **Dr. Satish M. Kumar** is thanked for his assistance in operating the JEOL JXA- 733 electron microprobe at of analytical instruments housed at the Center for Instrumental Analysis, Shizuoka University. I am grateful to **Prof. Hiroyuki Kagi** of University of Tokyo, Japan, for his assistance during Raman spectra analyses. **Dr. Fabrice Barou** is thanked for his assistance in operating SEM-EBSD facility (JEOL JSM- 5600 and CamScan X500FE Crystal Probe) at Géosciences Montpellier of Université Montpellier II. **Dr. Olivier Bruguier** is thanked for his assistance in operating the LA-ICPMS of Université Montpellier II. I thank **Dr. Aaron Stallard**, University of Canterbury, New Zealand, for improving the English of the manuscript and **Mr. Hideki Mori** for technical assistance with the preparation of thin sections. I thank the **IRIS DMS** for providing the seismic waveform data used in the study.

This work was supported by Grant-in-Aid for Scientific Research (223708) as part of a JSPS Research Fellowship for Young Scientists (to TS), research grant (16340151, 19340148, 22244062) from the Japan Society for the Promotion of Science (to KM), a scholarship from the Mitsui Scholarship Foundation for Career

Development awarded to TS, Texas Advanced Research Program (to EYA and RJS), and EAR-0750711 by the U.S. National Science Foundation (to JP, EYA, and RJS), the Norman Hackerman Advanced Research Program 003661-0003-2006 (to EYA and RJS) and the US National Science Foundation awards EAR-0739015 and EAR-0952064 (to KHL and SSG).

Finally, I deeply thank my family, **Mr. Hiroaki Satsukawa**, **Mrs. Teruyo Satsukawa** and **Ms. Hanako Satsukawa** for their attentive support.

Thesis Summary

This thesis investigates high-temperature deformation processes associated with melt/fluid rock interactions in peridotites, as well as the seismic properties of the uppermost mantle. This thesis composed of six chapters containing three individual papers published to earth science journals.

Chapter 1: “**Introduction**”. This chapter introduces the geodynamics in the back-arc spreading, an overview of the uppermost mantle structure, and geological and seismological background of analyzed samples in this thesis.

Chapter 2: “**Microstructures and melt/fluid rock interactions of the uppermost mantle beneath the back-arc region of Japan Sea: Peridotite xenoliths from Ichinomegata and Oki-Dogo**”. It contains a paper entitled “Determination of slip system in olivine based on crystallographic preferred orientation and subgrain rotation axis: examples from Ichinomegata peridotite xenoliths, Oga peninsula, Akita prefecture” published in *The Journal of the Geological Society of Japan (2009)*. This chapter describes geochemical characteristics and microstructure evolution of peridotite xenoliths from the uppermost mantle lithosphere entrained by Ichinomegata volcano and Oki-Dogo Island.

Chapter 3: “**Seismic anisotropy of the uppermost mantle beneath the back-arc region of Japan Sea: Evidence from Ichinomegata and Oki-Dogo peridotite xenoliths**”. This chapter shows that those anisotropy of Ichinomegata and Oki-Dogo shown in Chapter 2 could be one of the dominant sources in explaining the observed delay times of shear-wave velocity in this region.

Chapter 4: “**Seismic anisotropy of the uppermost mantle beneath the Rio Grande rift: Evidence from Kilbourne Hole peridotite xenoliths**”. It contains a

paper published in *Earth and Planetary Science Letters* (2011). This chapter describes shear-wave splitting observed in the Rio Grande rift is a reflection of the lithospheric fabric and the presence of melts as thin cracks or dikes.

Chapter 5: “**Uppermost mantle anisotropy beneath the southern Laurentian margin: Evidence from Knippa peridotite xenoliths**”. This Chapter contains a paper published in *Geophysical Research Letters* (2010). It describes the mantle lithospheric fabric revealed by the xenoliths mostly explains the magnitude of shear-wave splitting observed along the southern margin of the Laurentian craton that could be related to ‘frozen’ deformation associated with the alternate processes of extension and compression beneath the southern Laurentian margin.

Chapter 6: “**Microstructure and seismic properties at the spreading/rifting zone**”. This chapter provides brief summaries, which shows microstructural and petrological characteristics in the four peridotite xenoliths (Ichinomegata, Oki-Dogo, Kilbourne Hole and Knippa) and the uppermost evolution during the back-arc spreading.

Contents

Abstract	i
Acknowledgements	v
Thesis Summary	viii
Chapter 1. Introduction	1
1-1. Geodynamics in the spreading/rifting zone on the Earth	2
1-2. Back-arc spreading	2
1-3. The uppermost mantle structure	4
1-3-1. Seismic anisotropy in the uppermost mantle	5
1-3-2. Peridotite in the upper mantle	7
1-4. Geological and seismological background of analyzed samples ·	9
1-4-1. Ichinomegata, NE Japan	9
1-4-2. Oki-Dogo, SW Japan	10
1-4-3. Kilbourne Hole (New Mexico, USA)	12
1-4-4. Knippa (Texas, USA)	13
Figures	15
Chapter 2. Microstructures and melt/fluid rock interactions of the uppermost mantle beneath the back-arc region of Japan Sea: Peridotite xenoliths from Ichinomegata and Oki-Dogo	20
Abstract	22
2-1. Introduction	23
2-2. Geological setting and petrography of peridotite xenoliths	26
2-2-1. Ichinomegata peridotite xenoliths	26
2-2-2. Oki-Dogo peridotite xenoliths	27

2-2-3. Shingu peridotite xenoliths	29
2-3. Mineral composition	30
2-3-1. Major elements	30
2-3-2. Trace elements	32
2-4. FTIR analyses of water contents in olivine and pyroxenes.....	33
2-4-1. Analytical procedures	33
2-4-2. Results	34
2-5. Microstructures of peridotite xenoliths	35
2-5-1. Methods of fabric analysis	35
2-5-2. Crystallographic preferred orientations (CPOs) of peridotite xenoliths	36
2-5-3. Analysis of subgrain rotation axes	38
2-5-4. Fabric strength of olivine	41
2-5-5. Microstructural analyses	42
2-6. Discussion	43
2-6-1. Evidence of fluid/melts rock interaction of peridotite xenoliths from Japan arc	43
2-6-2. Dominant slip systems of minerals in peridotite xenoliths	45
2-6-3. Implication for the dynamics of the back-arc region and development of oceanic lithosphere.....	47
2-6-4. Relationships between deformation and melt-rock interaction in the metasomatized peridotites	51
2-6-5. Structural history of the uppermost mantle in the back-arc of SW Japan	54
2-7. Conclusion.....	56

Figures and Tables	58
Chapter 3. Seismic anisotropy of the uppermost mantle beneath the back-arc region of Japan Sea: Evidence from Ichinomegata and Oki-Dogo peridotite xenoliths	105
Abstract	106
3-1. Introduction	107
3-2. Geological setting and samples	108
3-3. Rock seismic properties	109
3-4. Interpretation and discussion	112
Figures and Tables	115
Chapter 4. Seismic anisotropy of the uppermost mantle beneath the Rio Grande rift: Evidence from Kilbourne Hole peridotite xenoliths, New Mexico	127
Abstract	128
4-1. Introduction	129
4-2. Geological setting	130
4-3. Seismic data	131
4-4. Mineral compositions, microstructures, and fabric analyses	132
4-5. Rock seismic properties	135
4-6. Variation in seismic properties as a function of modal composition	136
4-7. Discussion: Seismic anisotropies beneath the Rio Grande rift	137
4-8. Conclusions	143
Figures and Tables	145
Chapter 5. Uppermost mantle anisotropy beneath the southern	

Laurentian margin: Evidence from Knippa peridotite xenoliths, Texas	156
Abstract	157
5-1. Introduction	157
5-2. Geological setting	158
5-3. Microstructural and Fabric Analyses.....	159
5-4. Rock Seismic Properties	162
5-5. Seismic data	162
5-6. Discussion and Conclusions.....	163
Figures and Tables	167
Chapter 6. Microstructure and seismic properties at the spreading/rifting zone	172
6-1. Microstructural and petrological characteristics in the four peridotite xenoliths localities: a summary	173
6-2. The uppermost mantle evolution during the back-arc spreading	176
Figures and Tables	179
References	182

Chapter 1

Introduction

1-1. Geodynamics in the spreading/rifting zone on the Earth	2
1-2. Back-arc spreading	2
1-3. The uppermost mantle structure	4
1-3-1. Seismic anisotropy in the uppermost mantle.....	5
1-3-2. Peridotite in the upper mantle	7
1-4. Geological and seismological background of analyzed samples	9
1-4-1. Ichinomegata, NE Japan.....	9
1-4-2. Oki-Dogo, SW Japan	10
1-4-3. Kilbourne Hole (New Mexico, USA)	12
1-4-4. Knippa (Texas, USA).....	13
Figures	15

1-1. Geodynamics in the spreading/rifting zone on the Earth

Rheological properties control the dynamics and evolution of the whole mantle of Earth. After the formation of Earth, it has been reduced energy, such as potential energy and thermal energy that preserved inside of the Earth, to the universe. These reduction processes result in geodynamics; volcanisms and earthquakes, for instance. In 1970's, the establishment of plate tectonics theory made it possible to explain the fundamental geological phenomena. There are three types of plate boundaries: divergent boundaries (mid ocean ridges or rifting zone), convergent boundaries (subduction zone or continental collision) and transform boundaries. Back-arc basins form at convergent plate boundaries and represent extensional processes that seem to be opposite sense of convergence, rather divergence. Divergent boundaries are recognized as spreading and rifting zone, and they are particularly important for producing crust, deformation for lithosphere, asthenospheric flow, partial melting, and melt/fluid rock interaction. Evolution of ocean basins and the rifting of continents are fundamental components of plate tectonics, and the process of continental break-up remains controversial (Kendall et al., 2005). Moreover, each of these processes can result in anisotropic structure and thus, essentially control the evolution of the Earth.

1-2. Back-arc spreading

Back-arc spreading is one of the spreading type, resulting in the formation of back-arc basin. The Western Pacific region has many arc-trench systems and producing more than 70 % of all back-arc basins on the Earth (Fig. 1). There are two types of back-arc basins: oceanic type and continental type (Tamaki, 1995). Oceanic type is formed at the back-arc side of oceanic island arcs (e.g., Mariana trough, Lau

basin), whereas continental type occurs at the back-arc side of continental arc (e.g., Japan sea, Kuril basin).

Two models are proposed to explain the back-arc spreading (Fig. 2). Extensional stresses generated from trench rollback (and retrograde migration of their associated slabs) were identified as the likely origin of back-arc basins (Dvorkin et al., 1993; Faccenna et al., 1996; Jolivet et al., 1994); however, the exact mechanism as to how subduction dynamics controlled the process was not apparent. There are other processes besides trench motion that are important in producing back-arc basins. Extensional forces may arise from gravitational collapse of regions with thickened crust (Martinod et al., 2000) or from far-field stresses due to changes in plate direction and continent–continent collisions (Silver et al., 1998). These effects have been shown to be important for back-arc basin development in the Aegean and Japan Seas as their contribution likely modulated the more dominant extensional forces from roll-back subduction (Jolivet et al., 1994).

Based on the observations of back-arc basin ages, histories of spreading, quiescence and compression in the overriding plate, Clark et al. (2008) did the modeling for understanding the time-development of these subduction zones and back-arc basins. They found that quasi-episodicity is the dominant form of episodic back-arc development in the present, in which the back-arc shifts between phases of rifting, spreading and quiescence (Clark et al., 2008). Those subduction zones for which the subducting plates are moving slowly, such as in the Mediterranean or the Scotia Sea, experience only pseudo-episodicity, where the spreading moves linearly towards the trench but often does so in discrete ridge-jump events.

The Japan Sea is the one of the back-arc basins which has a complicated geological structure (Tamaki et al., 1992), affected by its genesis of splitting the

eastern margin of the Eurasian continent (e.g., Otofujii and Matsuda, 1984; Otofujii et al., 1985). Its floor is composed by oceanic crust, rifted continental crust and stretched continental crust (Tamaki et al., 1992). Tamaki (1995) proposed a tectonic model based on several studies of topography, paleomagnetism, and ocean drilling (Fig. 3a). Proto Japanese island arc situated on the continental margin of the Eurasian plate (30 Ma), then back-arc spreading was developed from the northeast Japan to the southwest Japan (Fig. 3b). In the initial stage, crustal thinning and extension was induced and seafloor spreading was triggered by the breakup of the lithosphere along the strike-slip margin at the northeast Japan Sea. The spreading center propagated southwestward to increase the area of the oceanic crust. In the meantime, the crust of the southwest Japan has been extended and thinned of the arc crust and formed basins and rises (Fig. 3c), indicating that normal seafloor spreading occurred in the northeast Japan arc. On the other hand, the extension and the thinning of continental crust were induced in the southwest Japan arc during the Japan Sea opening. However, the evolution of back-arc spreading has not been fully understood; for example, the cause of formation, processes of evolution, similarity and differences to the mid ocean ridge (Tamaki, 1995). Mantle peridotites are expected to be complicated in petrography, geochemistry and microstructure, which reflecting such an active tectonic environment. Most of the basic geological structure of the present Japanese Islands was formed during this time. The surface dynamics is related to the deeper part, thus we can estimate the mantle flow evolution from the recorded in the peridotite xenoliths. There are a few localities ever known that produce mantle-derived xenoliths, which will provide us with information on deep processes and materials beneath the Japan Sea.

1-3. The uppermost mantle structure

1-3-1. Seismic anisotropy in the uppermost mantle

Seismic tomography, which obtained by linearization with respect to a reference Earth model proposed by Aki and Lee (1976), is the powerful tool to reveal the whole mantle structure and deformation of the mantle. The topographic images resulted from such linearized inversion are dependent on the initial reference models and hypocentral locations (e.g., Michael, 1988). In these decades, a dense network of seismic stations has been deployed across in the worldwide to investigate mantle wedge structures. Recent investigations of shear-wave splitting and petrophysical studies have shown the relationships between petrofabric and seismic anisotropies (e.g., Ben Ismaïl and Mainprice, 1998). Seismic anisotropy presents near the surface due to aligned cracks (e.g., Crampin, 1984), in the lower crust, upper and lower mantle due to the mineral preferred orientation (e.g., Karato, 1998; Mainprice et al., 2000). The seismic anisotropy resulting from olivine CPO tends to produce a maximum seismic wave velocity parallel to the direction of plastic flow within the upper mantle (Nicolas and Christensen, 1987). In some cases, another physical factors could contribute to the measured anisotropy, for example mineral preferred orientation and alignment of melt inclusions (e.g., Mainprice, 1997). Also, the variation of seismic properties of the uppermost mantle is controlled by not only the crystallographic preferred orientations (CPOs), but also the modal composition and the orientation of the structural frame (e.g., Nicolas and Christensen, 1987). The role of seismic anisotropy estimated from mantle rocks has become increasingly important to understand the evolution of the uppermost mantle, which is due to the elastic anisotropy of the volumetrically dominant phases of olivine, orthopyroxene and clinopyroxene, and the strong statistical alignment of their CPOs. Leading by Nicolas and Christensen (1987), various peridotites have been examined around the world.

There are several methods for the calculation of seismic properties as reviewed in Mainprice (2007), we use the simplest and best known averaging techniques for obtaining estimates of the effective elastic constants of polycrystals, the Voigt (1928) and Reuss (1929) averages. In this calculation, one only uses the volume fraction of each phase, the orientation and the elastic constants of the single crystals or grains. In terms of statistical probability functions, these are first order bounds as only the first order correlation function is used, which is the volume fraction. Note no information about the shape or position of neighboring grains is used. The Voigt average is found by simply assuming that the strain field is everywhere constant. The strain at every position is set equal to the macroscopic strain of the sample. M_{voigt} is then estimated by a volume average of local stiffnesses M_i with orientation x_i , and volume fraction x_i ,

$$M_{\text{voigt}} = \sum x_i M_i$$

Reuss average is found by assuming that the stress field is everywhere constant. The stress at every position is set equal to the macroscopic stress of the sample. M_{Reuss} is then estimated by the volume average of local compliances M_i ,

$$1/M_{\text{Reuss}} = \sum x_i / M_i$$

These two estimates are not equal for anisotropic solids with the Voigt being an upper bound and the Reuss a lower bound. A physical estimate of the moduli should lie between the Voigt and Reuss average bounds as the stress and strain distributions are expected to be somewhere between uniform strain (Voigt bound) and uniform stress (Reuss bound). Hill (1952) observed that arithmetic mean of the Voigt and Reuss bounds, sometimes called the Hill or Voigt-Reuss-Hill (VRH) average,

$$M_{\text{VRH}} = 1/2(M_{\text{voigt}} + M_{\text{Reuss}})$$

The VRH average is often close to experimental values, but it has no theoretical justification. As it is much easier to calculate the arithmetic mean of the Voigt and Reuss elastic tensors all authors have tended to apply the Hill average as an arithmetic mean. In earth sciences the Voigt, Reuss and Hill averages have been widely used for averages of oriented polyphase rocks (e.g. Crosson and Lin, 1971). Although the Voigt and Reuss bounds are often far apart for anisotropic materials, they still provide the limits within which the experimental data should be found (e.g., Watanabe et al., 2011).

1-3-2. Peridotite in the upper mantle

The major cause of seismic anisotropy in the upper mantle is the crystallographic preferred orientations (CPOs). Whereas the number of studies tried to understand its evolution from naturally deformed samples, experimentally deformed samples and numerical simulation, they are now undergoing to reveal the complex deformation histories of geodynamic interest. The CPOs do not only cause seismic anisotropy, but also record some aspects of the deformation history. Direct analysis of the uppermost mantle samples allows one to constrain the extent of these geodynamical mantle evolutions and their effect on seismic properties. Peridotite xenoliths are usually brought up by alkaline basalts or by kimberlites and represent the uppermost mantle beneath oceanic hotspots, continental rifts and continental cratons (e.g., Nixon, 1987). Such magmas can carry various rocks containing peridotite xenoliths, which may give us direct evidence of petrological and fabric characteristics (e.g., Arai et al., 2000).

Olivine is the major mineral of peridotites, and it is one of the most studied minerals. The number of experimental studies show the olivine CPOs classification to

illustrate the role of stress and water content as the controlling factors for the development of five CPO types (A, B, C, D and E) (Fig. 4). These five CPO types are assumed to represent the dominant slip system activity on A \equiv [100](010), B \equiv [001](010), C \equiv [001](100), D \equiv [100]{0kl}, and E \equiv [100](001). In the classification after Mainprice (2007), AG-type CPO added an additional class, which is quite common in naturally deformed samples.

The evolution of the uppermost mantle is strongly linked to partial melting and refertilization processes. Recent studies have shown that percolating melts may react with the mantle lithosphere, leading to enrichment in fusible components; i.e., refertilization via the crystallization of pyroxenes and spinel (e.g., Le Roux et al., 2007, 2008). Experimental deformation of partially molten assemblages reveals that the presence of melt, even in low fractions, results in a large reduction in viscosity (Hirth and Kohlstedt, 1995; Rosenberg and Handy, 2005; Takei, 2005). In addition, deformation may result in a higher transient permeability and facilitate melt segregation (Rosenberg and Handy, 2000; Holtzman et al., 2003). This feedback between melt percolation and deformation, as observed experimentally, has also been proposed, based on observations of geological structures, to be responsible for the development of shear zones in the middle and lower crust (e.g., Vauchez and Tommasi, 2003) and in the shallow mantle (Kelemen and Dick, 1995). At the plate scale, it has also been suggested (based on geodynamical models and seismic anisotropy data) that magmas play an essential role in the initiation of rifting (Buck, 2006; Kendall et al., 2006) and in erosion of the lithosphere above mantle plumes (Thoraval et al., 2006). Therefore, interactions between melt percolation and deformation in the mantle are important in the evolution of the lithosphere, controlling its composition and mechanical behavior.

1-4. Geological and seismological background of analyzed samples

Direct analysis of natural samples allows one to constrain the extent of these geodynamical mantle evolution and their effect on seismic properties. In order to understand the microstructural development in the uppermost mantle associated with melt/fluid rock interactions in peridotites induced by the back-arc spreading, as well as the implication for the seismic properties of the uppermost mantle, we used peridotite xenoliths from four localities; back-arc region and other tectonic setting for the comparison. Ichinomegata peridotites xenoliths preserved the normal seafloor spreading, whereas Oki-Dogo peridotites preserved the extension and the thinning of continental crust. For comparison, we have studied spinel peridotite xenoliths from another tectonic setting: Kilbourne Hole (New Mexico, USA) and Knippa peridotites (Texas, USA). Peridotite xenoliths from Kilbourne Hole represented the early stages of spreading in an active rift zone, whereas Knippa peridotites xenoliths were derived from the mantle lithosphere that could have recorded deformations in relation to the thinning of continental crust.

1-4-1. Ichinomegata, NE Japan

Subduction zones are regions where large chemical exchanges between the interior and surface of the Earth dominantly occur. Tectonic plate motion causes solid-state plastic corner flow between the subducting slab and the overriding plate and subsequently leads to the development of crystallographic preferred orientations (CPOs) of constituent olivine crystals within the mantle.

The northeast Japan arc is a typical subduction zone, where the Pacific plate subducting beneath the land area at a rate of ~ 10 cm/year and is one of the most

seismologically studied arcs. Shear-wave polarization anisotropy has been systematically investigated in the mantle wedge of the northeast Japan arc; Fast directions in the back-arc side are oriented nearly E-W, whereas fast directions in the fore-arc side are oriented approximately N-S (Nakajima and Hasegawa, 2004). Seismic anisotropy observations from the back-arc side of the northeast Japan arc are generally interpreted in terms of the CPO of mantle minerals arising from present-day mantle process such as mantle wedge convection and plate motion (Nakajima and Hasegawa, 2004; Ishise and Oda, 2005).

Ichinomegata volcano located at the Oga Peninsula, the northeast Japan arc (Fig. 5a). Here is very famous for the abundant deep-seated xenoliths and there are many petrological and geochemical studies previously (e.g., Kuno, 1967; Abe et al., 1995). The host magma is calc-alkali andesite to dacite, ca. 10,000 yr in age (Horie, 1964). Peridotites are most frequently lherzolite and sometimes veined by hornblendite with pargasite and rarely phlogopite (Abe et al., 1998). Those amphiboles, spinel-pyroxene symplectite and exsolution lamella of clinopyroxene in orthopyroxene are mantle metasomatic minerals, due to addition of hydrous melt/fluid to dry peridotite (e.g., Abe and Arai, 1993).

Peridotite xenoliths from the uppermost mantle lithosphere entrained by Ichinomegata volcano preserve strong asymmetric fabrics with intermediate seismic anisotropy. Furthermore, such seismic anisotropy in the uppermost mantle lithosphere could have been induced by back-arc spreading along the northeast Japan arc related to the normal seafloor spreading system during the Japan Sea opening.

1-4-2. Oki-Dogo, SW Japan

The uppermost mantle beneath the SW Japan arc is dry and has a steeper

geothermal gradient than that beneath the NE Japan arc, as deduced from petrologic studies of mafic and ultramafic xenoliths from Oki-Dogo Island, SW Japan, and Ichinomegata volcano, NE Japan (Takahashi, 1978a; Abe, 1997; Arai et al., 1998, 2000). This conclusion is supported by the results of recent studies on mantle xenoliths from many other localities throughout the Japan arcs. For example, Arai et al. (1998, 2000) proposed that the type of mantle peridotite beneath the SW Japan arc depends on the degree of metasomatism by Fe-rich melts superimposed on the primary residual characteristics.

Oki-Dogo Island is an important site in terms of xenoliths because it marks the most continent-ward occurrence of mantle peridotite xenoliths in the SW Japan arc, approximately 60 km offshore from Honshu Island (Fig. 5a). Numerous mafic and ultramafic xenoliths, including residual mantle peridotite, have been reported from the island (Takahashi, 1975, 1978a, 1978b). Kaneoka et al. (1978) and Nagao and Takahashi (1993) reported the Ar and Sr isotope geochemistry and noble gas geochemistry, respectively, of ultramafic xenoliths from Oki-Dogo Island.

Abe et al. (2003) presented petrological and mineral composition data, including trace-element data, for spinel lherzolite xenoliths from Oki-Dogo, following the publication of preliminary data by Abe et al. (1999). They discussed upper mantle processes beneath the Japan arcs and the Japan Sea, based on petrological data obtained from residual peridotite xenoliths from other localities such as Oshima-Oshima, Megata, Aratoyama, Kurose, Onyama, Takashima, Shingu, and Fukuejima, and based on trace element data from clinopyroxene within peridotite xenoliths from Kurose, located on the Japan Sea coast, within the SW Japan arc (Abe et al., 1998; Arai et al., 2001). Abe et al. (2003) argued that mantle metasomatism was induced by the intrusion of evolved melts beneath the SW Japan arc and the degree of

melting in the upper mantle during opening of the Japan Sea. With the exception of Takahashi (1978a, 1978b), no previous study has undertaken a petrophysical analysis of spinel lherzolite xenoliths, which represent residual mantle. Peridotite xenoliths from the uppermost mantle lithosphere in Oki-Dogo preserve fabrics and petrological characteristics, which could have been induced by back-arc spreading along the northeast Japan arc related to extension and thinning of the continental crust during the Japan Sea opening. Furthermore, changes in composition and texture of the uppermost mantle rocks can effect on the seismic properties.

1-4-3. Kilbourne Hole (New Mexio, USA)

Continental rifting is a complex process involving deformation of the lithosphere, asthenospheric flow, and partial melting; each of these processes can result in seismically anisotropic structures. As such, the significance of shear-wave splitting, in particular whether it represents lithospheric fabric or asthenospheric flow, remains controversial (Gao et al., 2008). Measurements of shear-wave splitting using P-to-S converted phase (SKS, SKKS, and PKS) play a crucial role in imaging the orientation and degree of polarization of mantle fabrics and in constraining models for the formation of these fabrics (Silver, 1996; Savage, 1999; Liu, 2009).

The Kilbourne Hole maar (Fig. 5b) exposes Quaternary basanites containing both crustal and mantle xenoliths (Hamblock et al., 2007). It is roughly elliptical in shape, almost 3 km in length, and from 100 to 125 m deep. Using ^3He surface exposure methods, the age of eruption has been constrained to 10–20 ka (Anthony and Poths, 1992; Williams, 1992); thus, the xenoliths represent essentially ambient conditions for the Rio Grande rift. Kilbourne Hole is a part of the Potrillo volcanic field (Anthony et al., 1992; Thompson et al., 2005), which consists of cinder cones,

maars, and fissure flows of basanitic and alkalic basalt composition. The Potrillo volcanic field is one of the largest silica-undersaturated volcanic fields in the Rio Grande rift, and has been interpreted as representing the products of small-degree partial melting of a volatile-charged asthenosphere. Based on their observation of olivine CPO in Kilbourne Hole peridotite xenoliths from the Rio Grande rift, Bussod and Irving (1981) proposed that deformation was accompanied by syntectonic recrystallization in the presence of intercrystalline fluid. However, these samples were analyzed using a universal stage, and the seismic properties of the mantle beneath the Rio Grande rift were not considered.

1-4-4. Knippa (Texas, USA)

The nature of ocean-continent transitional lithosphere is complicated. Recent passive seismological investigations provide fruitful avenues of inexpensive research to begin interrogating the lithosphere. Measuring shear-wave splitting (SKS) images the orientation and degree of polarization of mantle fabrics, and constrain models for the formation of these fabrics, including the mantle beneath south central North America (Gao et al., 2008). In spite of the robustness of SKS measurements, it is often not clear if anisotropy inferred from these measurements resides in the mantle lithosphere or asthenosphere (Fouch and Rondenay, 2006). Here we are interested in understanding fabrics for mantle xenoliths from southern Texas, and use this information to understand shear-wave splitting for upper mantle beneath the northern margin of the Gulf of Mexico (GoM). A previous study documented significant shear wave splitting beneath this region, with fast directions parallel to the Texas GoM continental margin (Gao et al., 2008). They noted that SKS splitting reached an apparent maximum where the crust was thinnest and discussed the parallelism of the

observed mantle anisotropy and the SE edge of the Laurentian cratonic keel.

A quarry near Knippa, Texas exposes Late Cretaceous basanites containing upper mantle xenoliths (Fig. 5b). This is the only known mantle peridotite locality in Texas (Young and Lee, 2009). Mantle xenoliths were carried up by Late Cretaceous (~87 Ma) quite primitive nephelinites of the Balcones Igneous Province (BIP) (Griffin et al., 2010). BIP volcanoes approximate the boundary between the ~1.1-1.4 Ga southernmost Laurentian (Texas) craton and Jurassic age transitional lithosphere along the GoM margin. The transitional lithosphere also involves the deformed rocks of the Ouachita fold belt (Keller et al. 1989).

The lithosphere that formed or was reworked during these tectonics events is preserved across a region that extends from the Grenville province of the craton (Anthony, 2005) to Jurassic oceanic crust in the GoM. Therefore, we consider it likely that the Knippa peridotite xenoliths are derived from the uppermost mantle lithosphere. We note that the region is dominated by alternate episodes of extension and compression. The associated mantle fabric could preserve some of this deformation, suggesting an important potential for tectonic inheritance and overprinting.

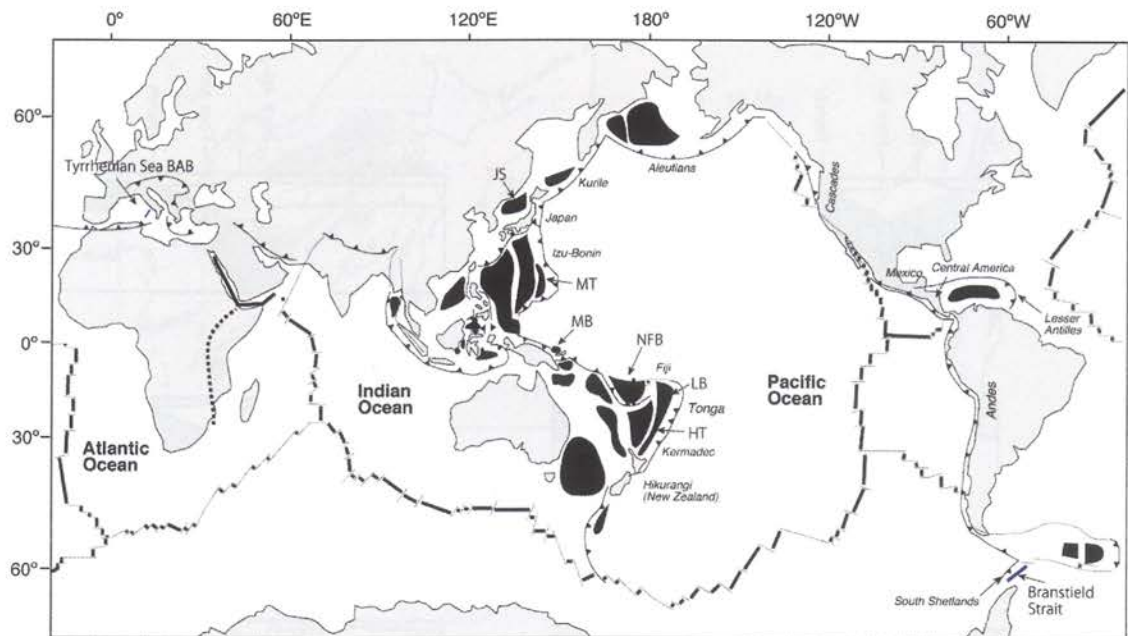


Figure 1. Locality map of back-arc basins (black parts) in the world. Modified after Tamaki and Honza (1991). More than 70 % of back-arc basins are located in the Western Pacific region. JS: Japan Sea; MT: Mariana trough; MB: Manus Basin; NFB: North Fiji Basin; LB: Lau Basin; HT: Havre trough, respectively.

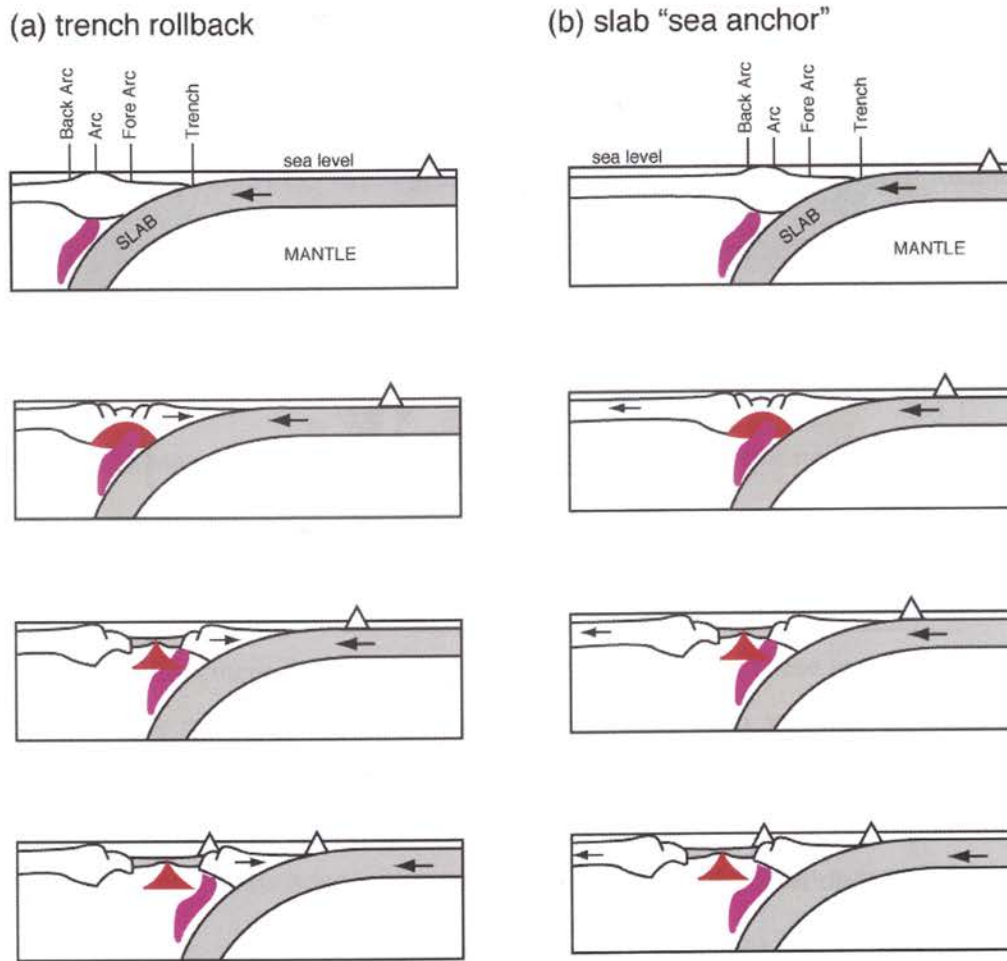


Figure 2. Schematic models to show back-arc spreading mechanism. (a) trench rollback model, (b) slab "sea anchor" model. Modified after Martinez et al. (2007).

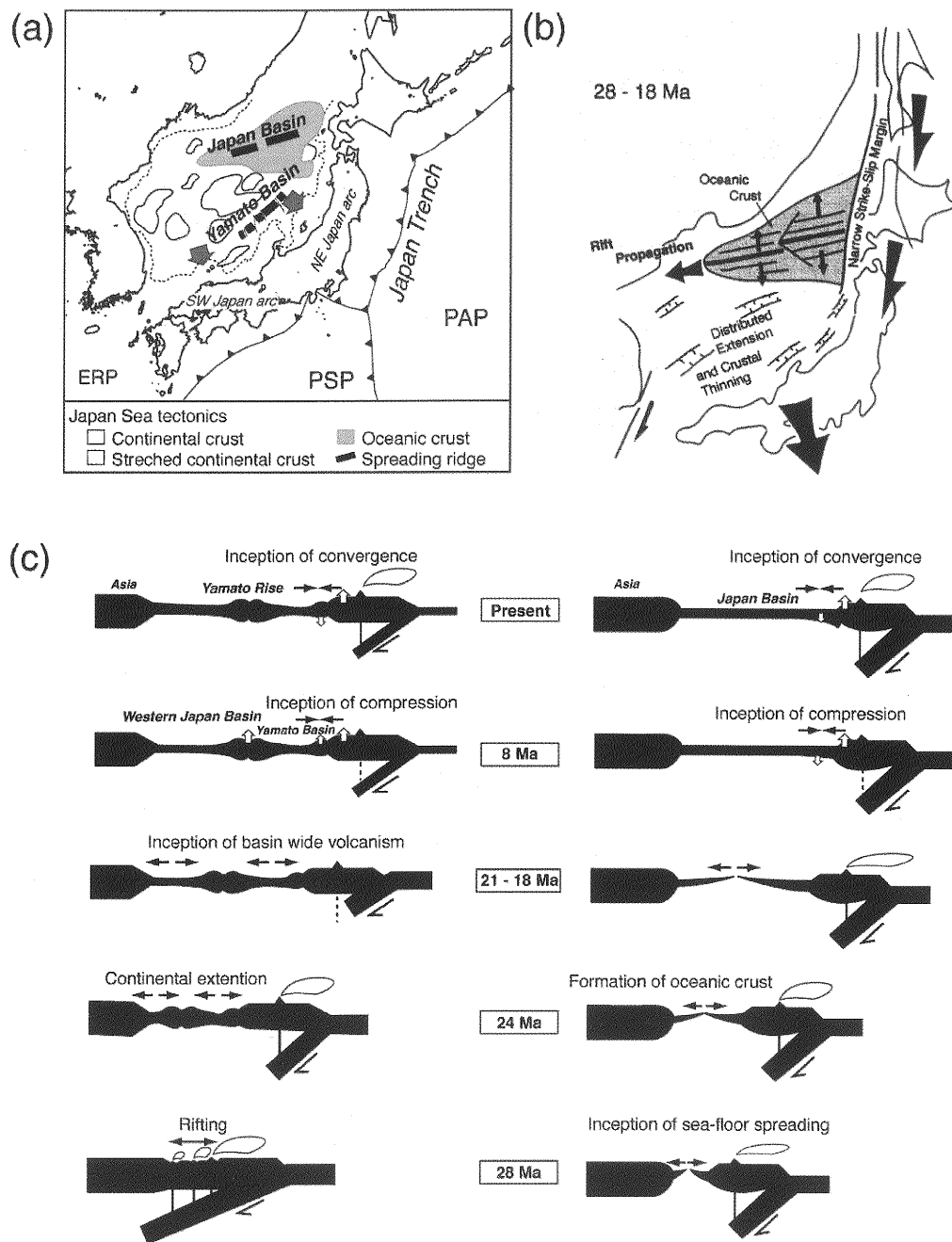


Figure 3. (a) Crustal component of the Japan Sea. NE part is consistent from oceanic crust, whereas SW part is consistent from continental and stretched continental crust. PSP: Philippine Sea Plate; PAP: Pacific Plate; ERP: Eurasia. Modified after Kimura et al. (2003). (b, c) Schematic model of the opening of the Japan Sea. Modified after Tamaki (1995). NE Japan was formed by the normal seafloor spreading system, whereas SW Japan was formed by the extension and thinning of the continental crust.

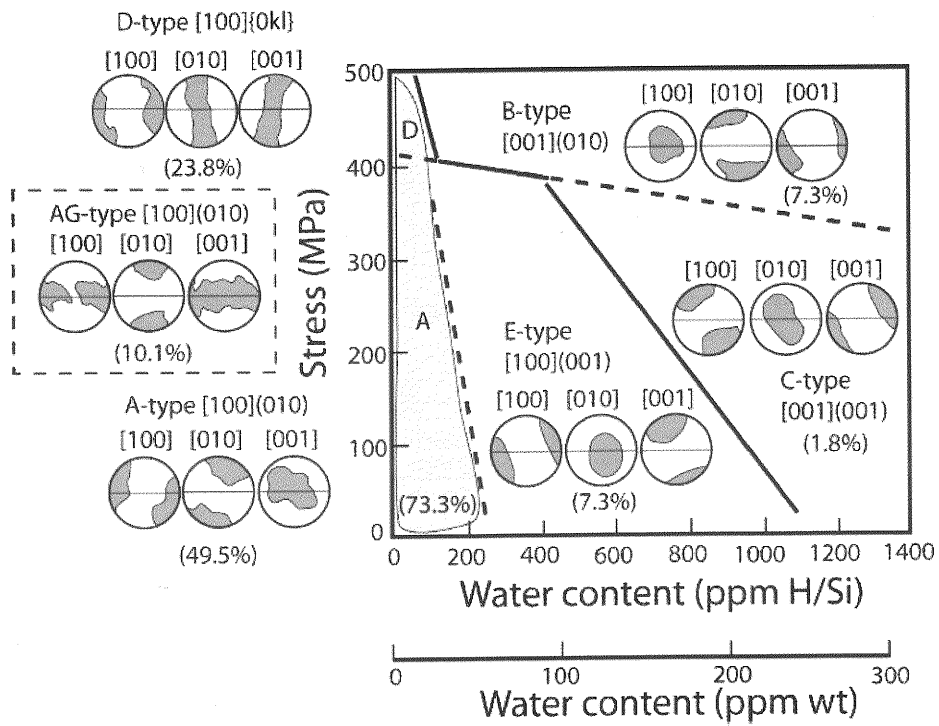


Figure 4. The classification of olivine CPOs as a function of stress and water content from Mainprice (2007). The water content scale in ppm H/Si is that originally used by Jung and Karato (2001). The numbers in brackets are the percentage of samples with the fabric types found in the database of Ben Ismaïl and Mainprice (1998).

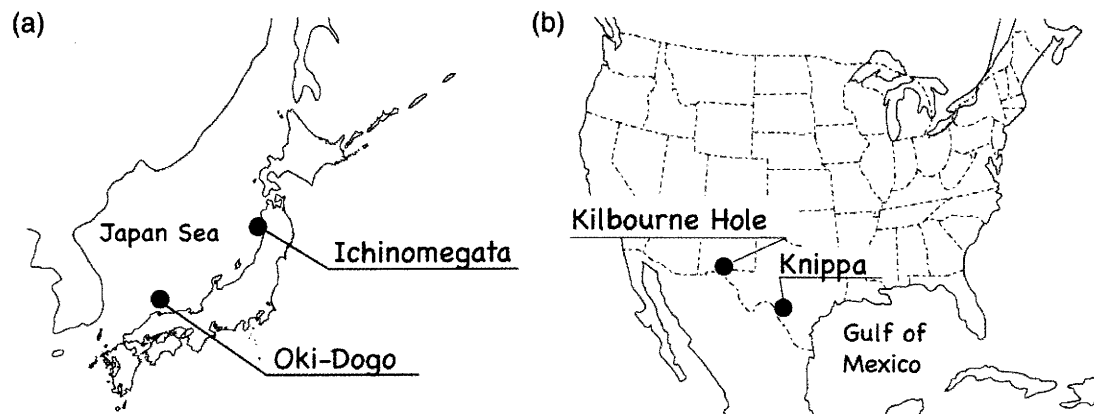


Figure 5. Locality map of mantle xenoliths in this study. (a) Ichinomegata (northeast Japan) and Oki-Dogo (southwest Japan). (b) Kilbourne Hole (New Mexico, USA) and Knippa (Texas, USA).

Chapter 2

Microstructures and melt/fluid rock interactions of the uppermost mantle beneath the back-arc region of Japan Sea: Peridotite xenoliths from Ichinomegata and Oki-Dogo

Originally Published in modified form as “Determination of Slip System in Olivine Based on Crystallographic Preferred Orientation and Subgrain-Rotation Axis: Examples from Ichinomegata Peridotite Xenoliths (Oga Peninsula, Akita Prefecture)” by T. Satsukawa and K. Michibayashi, *The Journal of the Geological Society of Japan*, **115**(6), 288-291. (In Japanese With English Abstract), 2009, All rights reserved.

Abstract	22
2-1. Introduction	23
2-2. Geological setting and petrography of peridotite xenoliths	26
2-2-1. Ichinomegata peridotite xenoliths	26
2-2-2. Oki-Dogo peridotite xenoliths	27
2-2-3. Shingu peridotite xenoliths	29
2-3. Mineral composition	30
2-3-1. Major elements	30
2-3-2. Trace elements	32
2-4. FTIR analyses of water contents in olivine and pyroxenes	33
2-4-1. Analytical procedures	33

2-4-2. Results	34
2-5. Microstructures of peridotite xenoliths	35
2-5-1. Methods of fabric analysis	35
2-5-2. Crystallographic preferred orientations (CPOs) of peridotite xenoliths	36
2-5-3. Analysis of subgrain rotation axes	38
2-5-4. Fabric strength of olivine	41
2-5-5. Microstructural analyses	42
2-6. Discussion	43
2-6-1. Evidence of fluid/melts rock interaction of peridotite xenoliths from Japan arc	43
2-6-2. Dominant slip systems of minerals in peridotite xenoliths	45
2-6-3. Implication for the dynamics of the back-arc region and development of oceanic lithosphere	47
2-6-4. Relationships between deformation and melt-rock interaction in the metasomatized peridotites	51
2-6-5. Structural history of the uppermost mantle in the back-arc of SW Japan	54
2-7. Conclusion	56
Figures and Tables	58

Abstract

The uppermost mantle in the back arc region of the subduction zone is the site of complex interactions between deformation, partial melting, fluid migration, and melts percolation. To constrain these interactions and their effects on olivine fabric, we analyze microstructures, geochemical analysis, crystallographic preferred orientations, and water contents of spinel peridotite xenoliths obtained from back arc region of Japan arc. The three sample locations correspond to slightly different geological settings from northeast Japan (Ichinomegata) to southwest Japan (Oki-Dogo and Shingu). The mineral chemistry of Ichinomegata peridotites shows a typical residual peridotite trend, depleted in LREE (light rare earth element). However, their strong Th-U positive anomaly indicates a possible metasomatic origin associated to the subduction of the Pacific plate. The chemical composition of Oki-Dogo peridotites shows that they were affected by various degree of metasomatism by melt, which might be related to back-arc spreading. Olivine CPO of Ichinomegata peridotites are consistent with slip on (010)[100] and {0kl}[100]. The angle between the [100] maximum concentration and the foliation decreases with increasing fabric strength, indicating that these samples record a strain gradient related to back-arc spreading. On the other hand, olivine CPO of Oki-Dogo peridotites are consistent with the (010)[100] slip system. Samples have low Mg# and show relatively high concentration in [010], however there were no strong relationships among them. Although peridotite xenoliths from Oki-Dogo Island could be deformed in the presence of melt, there was no strong interaction between deformation and melts percolation.

Key words: peridotite xenoliths, the uppermost mantle flow, back arc region, Japan Sea opening.

2-1. Introduction

The Japan Sea is the one of the back-arc basins which has a complicated geological structure (Tamaki et al., 1992), affected by its genesis of splitting the eastern margin of the Eurasian continent (e.g., Otofujii and Matsuda, 1984; Otofujii et al., 1985). Its floor is composed by oceanic crust, rifted continental crust and stretched continental crust (Tamaki et al., 1992). There are a few localities ever known that produce mantle-derived xenoliths, which will provide us with information on deep processes and materials beneath the Japan Sea.

Ichinomegata Crater is one of just a few localities where deep-level inclusions can be found in an island arc setting (Fig. 1a). Peridotite xenoliths preserved the possible occurrence of an anisotropic layer in the uppermost mantle lithosphere that might be related to 'frozen' deformation during back-arc spreading along the northeast Japan arc. Ichinomegata is very famous for the abundant deep-seated xenoliths and there are many petrological and geochemical studies previously (e.g., Kuno, 1967; Abe et al., 1995). The host magma is calc-alkali andesite to dacite, ca. 10,000 yr in age (Horie, 1964). Peridotites are most frequently lherzolite and sometimes veined by hornblendite with pargasite and rarely phlogopite (Abe et al., 1998). Those amphiboles, spinel-pyroxene symplectite and exsolution lamella of clinopyroxene in orthopyroxene are mantle metasomatic minerals, due to addition of hydrous melt/fluid to dry peridotite (e.g., Abe and Arai, 1993).

Peridotite xenoliths from the uppermost mantle lithosphere entrained by Ichinomegata volcano preserve strong asymmetric fabrics. Furthermore, such

anisotropic structure in the uppermost mantle lithosphere could have been preserved the deformation during the back-arc spreading along the northeast Japan arc related to the normal seafloor spreading system during the Japan Sea opening.

The evolution of the uppermost mantle is strongly linked to partial melting and refertilization processes. Recent studies have shown that percolating melts may react with the mantle lithosphere, leading to enrichment in fusible components; i.e., refertilization via the crystallization of pyroxenes and spinel (e.g., Le Roux *et al.*, 2007, 2008). Experimental deformation of partially molten assemblages reveals that the presence of melt, even in low fractions, results in a large reduction in viscosity (Hirth & Kohlstedt, 1995; Rosenberg & Handy, 2005; Takei, 2005). In addition, deformation may result in a higher transient permeability and facilitate melt segregation (Rosenberg and Handy, 2000; Holtzman *et al.*, 2003). This feedback between melt percolation and deformation, as observed experimentally, has also been proposed, based on observations of geological structures, to be responsible for the development of shear zones in the shallow mantle (Kelemen & Dick, 1995). Therefore, interactions between melt percolation and deformation in the mantle are important in the evolution of the lithosphere, controlling its composition and mechanical behavior.

The uppermost mantle beneath the SW Japan arc is dry and has a steeper geothermal gradient than that beneath the NE Japan arc, as deduced from petrologic studies of mafic and ultramafic xenoliths from Oki-Dogo Island, SW Japan, and Megata volcano, NE Japan (Takahashi, 1978a; Abe, 1997; Arai *et al.*, 1998, 2000). This conclusion is supported by the results of recent studies on mantle xenoliths from many other localities throughout the Japan arcs. For example, Arai *et al.* (1998, 2000) proposed that the type of mantle peridotite beneath the SW Japan arc depends on the degree of metasomatism by Fe-rich melts superimposed on the primary residual

characteristics.

Oki-Dogo Island is an important site in terms of xenoliths because it marks the most continent-ward occurrence of mantle peridotite xenoliths in the SW Japan arc, approximately 60 km offshore from Honshu Island (Fig. 1a). Numerous mafic and ultramafic xenoliths, including residual mantle peridotite, have been reported from the island (Takahashi, 1975, 1978a, 1978b). Kaneoka et al. (1978) and Nagao and Takahashi (1993) reported the Ar and Sr isotope geochemistry and noble gas geochemistry, respectively, of ultramafic xenoliths from Oki-Dogo Island. Many previous studies have investigated the petrology and geochemistry of residual peridotite xenoliths from the Japan arcs and Japan Sea (see Arai et al., 1998).

Abe et al. (2003) presented petrological and mineral composition data, including trace-element data, for spinel lherzolite xenoliths from Oki-Dogo, following the publication of preliminary data by Abe et al. (1999). Abe et al. (2003) discussed upper mantle processes beneath the Japan arcs and the Japan Sea, based on petrological data obtained from residual peridotite xenoliths from other localities such as Oshima-Oshima, Megata, Aratoyama, Kurose, Onyama, Takashima, Shingu, and Fukuejima, and based on trace element data from clinopyroxene within peridotite xenoliths from Kurose, located on the Japan Sea coast, within the SW Japan arc (Fig. 1) (Abe et al., 1998; Arai et al., 2001). Abe et al. (2003) argued that mantle metasomatism was induced by the intrusion of evolved melts beneath the SW Japan arc and the degree of melting in the upper mantle during opening of the Japan Sea. Moreover, Yamamoto et al. (2007) estimated the equilibrium pressure of mafic and ultramafic xenoliths from Oki-Dogo Island based on the pressure of CO₂ fluid inclusions preserved in minerals, yielding a depth of 25–29 km for lherzolites.

With the exception of Takahashi (1978a, 1978b), no previous study has undertaken a petrophysical analysis of spinel lherzolite xenoliths, which represent residual mantle. In the present paper, we describe the microstructure of peridotite xenoliths from Ichinomegata and Oki-Dogo Island with the aim of understanding the evolution of the uppermost mantle beneath the back-arc side of the Japan arc. For the comparison, we also show the fabric characteristic from Shingu (Fig. 1a), where is not back-arc region. Furthermore, we argue that such fabrics in the uppermost mantle lithosphere could have been induced by back-arc spreading along the northeast Japan arc related to the opening of the Japan Sea.

2-2. Geological setting and petrography of peridotite xenoliths

We briefly describe petrographical characteristics of peridotite xenoliths and their geological background of Ichinomegata, Oki-Dogo, and Shingu from the Japan arcs.

2-2-1. Ichinomegata peridotite xenoliths

Ichinomegata Volcano, located on Oga Peninsula, northeast Japan (Fig. 1a, b), is one of the few places on Earth where deep-level xenoliths occur in the back-arc region of an island arc. The host magma is calc-alkali andesite to dacite in composition and is ca. 10,000 yr in age. The Ichinomegata xenoliths suite is composed of peridotites, websterites, clinopyroxenites, gabbros, amphibolites, and other shallow-level rocks such as granitic and metavolcanic rocks and sediments (e.g., Abe et al., 1998). The peridotite xenoliths are up to 30 cm in diameter, but usually less than 10 cm (Fig. 2a). The xenoliths are generally lherzolite with some harzburgite that have

secondary pargasite and rare phlogopite of mantle metasomatic origin due to the addition of hydrous melt/fluid to dry peridotite (e.g., Abe et al., 1998).

In this study, we selected thirteen spinel peridotite xenoliths for detailed petrophysical analyses. Most of the peridotite xenoliths have a pervasive main foliation composed of compositional banding defined by pyroxene-rich and pyroxene-poor layers and a lineation defined by elongate pyroxene grains (Fig. 2a). We analyzed microstructures from XZ thin sections cut perpendicular to the foliation (XY plane) and parallel to the lineation (X). The lherzolites contain olivine, orthopyroxene, clinopyroxene, and spinel, and show equigranular texture (Fig. 2b). Large olivine grains commonly contain subgrain boundaries (Fig. 2c) and show undulose extinction. Triple-junction grain boundaries are observed (Fig. 2a), mainly among olivine grains. Orthopyroxene porphyroclasts contain exsolution lamellae of clinopyroxene (Fig. 2d). The pyroxenite xenoliths contain orthopyroxene, clinopyroxene, and minor olivine (Fig. 2e).

2-2-2. Oki-Dogo peridotite xenoliths

Oki-Dogo Island, located in the Japan Sea (Fig. 1a) upon a shelf that extends from Shimane Peninsula to Oki Bank. Basement on the island consists of a gneissic metamorphic complex (Fig. 1c). The metamorphic age of the basement complex is ca. 200 Ma, as determined by the Sm–Nd isochron method (Tanaka and Hoshino, 1987) and Pb–Pb analyses of zircon (Yamashita & Yanagi, 1994). The alkaline basalts that contain the xenoliths were erupted during the Pliocene–Pleistocene (from 4.38 ± 0.23 to 0.55 ± 0.09 Ma) (Uto et al., 1994), after the opening of the Japan Sea, which is thought to have occurred during the Oligocene–Miocene (28–18 Ma) as a consequence of back-arc spreading (e.g., Tamaki et al., 1992).

According to Takahashi (1978a, 1978b), five basalt lava flows on Oki-Dogo Island contain abundant ultramafic and mafic xenoliths, including mantle-derived spinel lherzolite. These basalts contain 2–15% normative nepheline, 45.0–49.1 wt% SiO₂, and yield FeO/MgO values of 0.60–1.15 (Uto et al., 1994). Takahashi (1978a) described approximately 70 ultramafic and mafic xenoliths in detail, and divided them into five groups based on mineral assemblage and microstructure. Takahashi (1975) reported that in Oku village, large amounts of angular ultramafic and mafic xenoliths are densely packed in a dyke (Fig. 3a) that represents a volcanic neck. The five groups of xenoliths identified by Takahashi (1978b) are as follows: (1) spinel lherzolite, (2) banded spinel peridotite, (3) banded plagioclase peridotite, (4) gabbro, and (5) granulite.

Xenoliths on the island are up to 10 cm in diameter (generally 1–3 cm). Spinel lherzolite xenoliths are the dominant xenolith type in the Kuroshima Basalt lava, whereas it is less abundant or absent in the other alkali basalt lavas. We collected 78 samples of spinel lherzolite from Kuroshima (KRB; a small island (<200 m across) near Oki-Dogo Island) and Oki-Dogo Island (OKD), along with several pyroxenites (e.g., OKD7-3) and gabbros (e.g., OKD08). Within samples greater than 3 cm in size, it is possible to recognize a foliation (XY plane) and lineation (X direction) defined by compositional banding and aligned spinel grains.

Thin sections were cut perpendicular to the foliation (Z) and parallel to the lineation (X; i.e., XZ-sections). For samples less than 3 cm in size, for which structures could not be identified, thin sections were cut at random orientations. For detailed analyses, we selected the 17 samples of lherzolite (of 78 in total) that contained the best-preserved peridotite microstructures, and selected one sample each of pyroxenite and gabbros.

The lherzolites contain olivine, orthopyroxene, clinopyroxene, and spinel, and show equigranular texture (Fig. 3b). Large olivine grains commonly contain subgrain boundaries (Fig. 3c) and show undulose extinction. Triple-junction grain boundaries are observed, mainly among olivine grains. Orthopyroxene porphyroclasts contain exsolution lamellae of clinopyroxene (Fig. 3d). The pyroxenite xenoliths contain orthopyroxene, clinopyroxene, and minor olivine (Fig. 3e), whereas the gabbro xenoliths contain plagioclase, orthopyroxene, clinopyroxene, and minor olivine (Fig. 3f).

2-2-3. Shingu peridotite xenoliths

Shingu in Shikoku Island is the locality of mantle xenoliths is very special on the Japan Island arcs (Takamura, 1978). There are two sheets of dikes of alkali basaltic composition that contain abundant crustal and mantle xenoliths, which are expected to have unique information that we cannot obtain from the xenoliths elsewhere on the Japan arcs (Arai et al., 2007). They cut crystalline schists of the Sambagawa metamorphic belt of high-pressure intermediate type (Miyashiro, 1973). Goto (1986) found several other dikes of similar chemical characteristics within the Sambagawa belt in Shikoku Island. The host alkali basalt characterized by abundance of carbonate minerals and hydrous minerals (biotite and amphibole), and the term “lamprophyre” is preferable, also taking the occurrence as dike into account. The age of host rock is 18 Ma, being older than the host rocks of other mantle-derived xenoliths from the Southwest Japan arc (Uto et al., 1987; Uto, 1990). We found a variety of ultramafic xenoliths (harzburgite, lherzolite, dunite, wehrlite, pyroxenite and kaersutite), and most of the pyroxenites and kaersutite (hornblendite) belong to Group II (Goto and Arai, 1987).

The peridotite xenoliths are mostly small (<5 cm across) and angular. They are rather fine-grained and show protogranular to porphyroclastic textures (Goto and Arai, 1987; Arai et al., 2000). Group I rocks are frequently penetrated by Group II rocks in individual xenoliths (=composite xenoliths; Irving, 1980). We can thus expect serious chemical effect on peridotite by the magma involved in the formation of Group II rocks (Goto and Arai, 1987; Arai et al., 2000).

2-3. Mineral composition

2-3-1. Major elements

The chemical compositions of olivine, orthopyroxene, clinopyroxene, and spinel were analyzed using a JEOL electron microprobe (JXA733) housed at the Center for Instrumental Analysis, Shizuoka University, Japan. Analytical conditions were 15 kV accelerating voltage and 12 nA probe current. Ferrous and ferric iron contents of spinel were calculated assuming spinel stoichiometry. Data are shown in Table 1 – 4. Cr# was calculated as the Cr/(Cr+Al) atomic ratio of spinel. Mg# was calculated as the Mg/(Mg+total Fe) atomic ratio for silicates and the Mg/(Mg+Fe²⁺) atomic ratio for spinel.

The relationship between the Mg# (Fo content) of olivine and the Cr# of spinel are plotted in Fig. 4 with previous studies. On an OSMA (olivine spinel mantle array) diagram, the samples plot in the field of residual peridotite of mantle origin (Arai, 1994). The Fo content of olivine grains of Ichinomegata peridotites ranges from 88 to 90 (Fig. 4a). The Cr# (= Cr/(Cr+Al)) of spinel is low (0.13–0.36; Fig. 4a). The spinel lherzolite from Ichinomegata volcano is quite normal in Mg relative to typical mantle peridotite xenoliths found in alkaline basalts (Abe et al., 2003).

The Fo content of olivine grains of Oki-Dogo peridotites ranges from 86 to

90 (Fig. 4b). The NiO content of olivine is relatively constant among grains, being ~0.30 wt% (range, 0.30–0.41 wt%), and shows a weak positive correlation with Fo content (Table 3). The Cr# (= Cr/(Cr+Al)) of spinel is low (0.17–0.45; Fig. 4b), and $Fe^{3+}/(Cr+Al+Fe^{3+})$ is < 0.1 (Table 3). Spinel in lherzolite from Oki-Dogo Island has the characteristics of mantle spinel, as defined by Dick and Bullen (1984). Orthopyroxene is enstatite (En 86.8–90.3), and contains moderate concentrations of CaO (1.01–1.29 wt%) and Al₂O₃ (2.81–4.94 wt%) (Table 4). Clinopyroxene is Cr-diopside to augite in composition, or Mg-rich augite containing 0.05–1.24 wt% Cr₂O₃. Clinopyroxene contains 3.61–6.18 wt% Al₂O₃ and 19.78–21.55 wt% CaO (Table 4).

The Fo content of olivine grains of Shingu peridotites ranges from 87 to 90 (Fig. 4c). The Cr# (= Cr/(Cr+Al)) of spinel is low (0.35–0.44; Fig. 4c). Some peridotites in Oki-Dogo and Shingu are plotted off the OSMA, which indicating that these are possibly metasomatized by melts (Arai et al., 2000).

Equilibrium temperatures of Ichinomegata peridotites were calculated using the Ca-Orthopyroxene thermometer of Brey and Köhler (1990), and estimated temperature conditions in the range 850 to 1000°C based on orthopyroxene thermometers (Table 5). This estimate is in good agreement with previous studies, which could represent a cooling event in the mantle lithosphere (Takahashi, 1986). It appears that the peridotite xenoliths are derived from relatively shallow levels in mantle, at 30 to 40 km depth (Takahashi, 1986), where the depth of the Moho is estimated to be approximately 28 km (Zhao et al., 1990).

Equilibrium temperatures of Oki-Dogo peridotites were calculated using the clinopyroxene thermometer of Nimis and Taylor (2000), the two-pyroxene and the Ca-Orthopyroxene thermometer of Brey and Köhler (1990), yielding temperatures of

1044–1134, 1040–1127, and 1021–1092 °C, respectively (Table 6).

2-3-2. Trace elements

In situ trace-element analyses of clinopyroxenes were performed by laser ablation induced coupled plasma mass spectroscopy (LA-ICP-MS) on thick (c. 150mm) sections at the AETE facility, Geosciences Montpellier, using a single-collector double-focusing sector field Element XR (eXtended Range) high-resolution (HR-) ICP-MS system, coupled with a Geolas (Microlas) automated platform housing a ArF 193 nm Compex 102 laser from LambdaPhysik. Measurements were conducted in an ablation cell of c. 30 cm³ in a He atmosphere, which enhances the sensitivity and reduces inter-element fractionation (Günther & Heinrich, 1999). The helium gas stream and particles from the sample were mixed with Ar before entering the plasma. Data were acquired in the fast E-scanmode at low resolution (M/DM1/4300). Signals were measured in Time Resolved Acquisition (TRA) mode, devoting 2 min for the blank, and 1min for cpx analysis. The laser was fired using an energy density of 15 J/cm² at a frequency of 5Hz and using a spot size of 77 mm. Oxide level, measured using the ThO/Th ratio, was below 0.7%. ⁴³Ca was used as an internal standard and the concentrations were calibrated against the NIST 612 rhyolitic glass using the values given by Pearce et al. (1997). Data were subsequently reduced using the GLITTER software (Van Achterbergh et al., 2001) by carefully inspecting the time-resolved analysis to check for absence of heterogeneities (inclusions or fractures) in the analysed volume. Representative mineral analyses are reported in Table 7 and 8.

For Ichinomegata peridotites, although fairly constant within samples, rare earth elements (REE) in clinopyroxene, orthopyroxene and olivine show extreme

variations between the different samples, in the range 0.001 - 10 times chondritic abundances (Fig. 5b). For all three minerals show depleted LREE (light rare earth elements) – depleted patterns. Figure 5(a) shows trace elements for three minerals. In clinopyroxene, there are high positive anomalies in Th-U.

REE in three minerals (clinopyroxene, orthopyroxene and olivine) of Oki-Dogo peridotites show extreme variations between the different samples, in the range 0.0001 - 100 times chondritic abundances (Fig. 6b). Clinopyroxene shows slightly enriched in LREE patterns, whereas orthopyroxene and olivine show depleted LREE – depleted patterns. Figure 6(a) shows trace elements for three minerals. There are high positive anomalies in Ce and Th in clinopyroxene, and Zr and Hf in orthopyroxene.

2-4. FTIR analyses of water contents in olivine and pyroxenes

2-4-1. Analytical procedures

Water contents in our samples were obtained using unpolarized mid-infrared radiation collected with a FTIR Bruker IFS66V/S spectrometer coupled with an Bruker Hyperion microscope at the Laboratoire des Colloïdes, Verres et Nanomatériaux (LCVN) at Université Montpellier 2, France. The technical setup of the IR microscope and the MCT detector are identical to those described by Demouchy et al. (2011), with a square aperture of 100 microns; and 200 scans were accumulated for each spectrum at a resolution of 4 cm^{-1} . The thickness of doubly polished sections of the samples for FTIR analyses ranges from 477 μm and 548 μm . Despite their infrequent occurrences, cracks and inclusions were strictly avoided. However, due to small grain size for two xenoliths (OKD04 and OKD69), pyroxenes could not be analyzed, also several grain boundaries were unfortunately included in

some olivine analyses. Although to avoid thickness interferences in some case (i.e., sinusoidal fringes), the crystals were put on a CaF₂ plate with a thin layer of fluorolube™ at the interface between the sample and the CaF₂ plate.

After background-baseline correction and thickness normalization to 1 cm, the hydroxyl content was determined for each spectrum using the empirical calibration from Paterson (1982):

$$C_{\text{OH}} = \frac{\varphi_i}{150\xi} \int \frac{k(\nu)}{3780 - \nu} d\nu \quad (1)$$

where C_{OH} is the concentration of hydroxyl, ξ is an orientation factor that equals 1/3 for unpolarized measurements, $k(\nu)$ is the absorption coefficient for a given wavenumber ν , φ_i is the density factor, which is chemistry and density dependent; its value for olivine and orthopyroxene is 2695 and 2769 wt ppm H₂O, respectively. (see calculation method in Bolfan-Casanova et al., 2000). Spectrum integration was performed between 2800 cm⁻¹ and 4000 cm⁻¹. The calibration from Paterson (1982) may underestimate the water content in some nominally anhydrous minerals (Libowitzky and Rossman 1997; Bell et al. 2003), Nevertheless the same calibration was used here for both sets of sample and for all the mineral phases to insure consistency during comparison of the water contents.

2-4-2. Results

Figure 7 shows typical unpolarized FTIR spectra for olivines and orthopyroxenes in Ichinomegata peridotites (TSI03, I892, I906, I702, TSI06) and Oki-Dogo peridotites (KRB15, OKD04, OKD45-2, OKD64 and OKD69). The olivine spectra are rather homogeneous. Water contents in the studied samples range from 2 to 7 ppm H₂O by weight for Ichinomegata, and from 2 to 6 ppm H₂O by weight for Oki-Dogo (Table 9). These values are in the same range as the water contents in

olivine from spinel-peridotite xenoliths sampling the continental lithosphere above the western North America, Patagonia and Carpathian subduction zones (Demouchy, 2004; Peslier & Luhr, 2006; Falus et al., 2008).

For Ichinomegata samples, orthopyroxene spectra are characterized by major O-H absorption bands at 3598 cm^{-1} and by broader minor peaks around 3424 cm^{-1} (Fig. 8). This pattern is typical for orthopyroxene from mantle xenoliths (Peslier et al., 2002; Grant et al., 2007). Water contents are however very heterogeneous, varying from 75 to 271 ppm (Table 9). There is abundant water in clinopyroxene. Clinopyroxene spectra is characterized by major O-H absorption bands at 3637 and 3472 cm^{-1} (Fig. 8). Water contents are however very heterogeneous, varying from 292 to 347 ppm (Table 9). Water contents in bulk rock are estimated using by modal composition, varying from 46 to 134 ppm (Table 9).

For Oki-Dogo samples, orthopyroxene spectra are characterized by major O-H absorption bands at 3571 and 3520 cm^{-1} and by broader minor peaks around 3523 cm^{-1} (Fig. 8). This pattern is typical for orthopyroxene from mantle xenoliths (Peslier et al., 2002; Grant et al., 2007). Water contents are however very heterogeneous, varying from 6 to 35 ppm (Table 9). There is abundant water in clinopyroxene. Clinopyroxene spectra is characterized by major O-H absorption bands at 3598 cm^{-1} (Fig. 8). Water contents are however very heterogeneous, varying from 8 to 98 ppm (Table 9). Water contents in bulk rock are estimated using by modal composition, varying from 4 to 10 ppm (Table 9).

2-5. Microstructures of peridotite xenoliths

2-5-1. Methods of fabric analysis

To examine the conditions of deformation in more detail, we have focused on the crystallographic preferred orientations (CPOs) of three common minerals: olivine, orthopyroxene, and clinopyroxene. These observations were obtained by electron backscatter diffraction (EBSD) using the SEM-EBSD facility at Géosciences Montpellier, France. The EBSD patterns were generated by the interaction of a vertical incident electron beam with a polished thin section, tilted at 70° , in a scanning electron microscope (JEOL JSM 5600). The diffraction pattern was projected onto a phosphor screen and recorded using a digital CCD camera. The resulting image was then processed and indexed in terms of crystal orientation using the CHANNEL5 software distributed by Oxford Instruments HKL.

For each sample, we obtained CPO maps covering almost the entire thin section (usually 35 mm long and 20 mm wide), with sampling steps from 25 to 40 μm , depending on grain size (Fig. 9); rates of indexation in the raw maps range from 50% to 80%. Post-acquisition data treatment allowed us to increase further the indexation rate by (1) filling the non-indexed pixels that have up to eight identical neighbors with this orientation, (2) identifying the grains (i.e. continuous domains characterized by an internal misorientation $< 12^\circ$), and (3) within each olivine crystal, searching and correcting for systematic indexation errors caused by the olivine hexagonal pseudo-symmetry, which results in similar diffraction patterns for orientations differing by a rotation of 60° around [100]. The resulting orientation maps were verified by the operator to avoid over extrapolation of the data at each step. To avoid over-representation of large crystals, CPOs are plotted as one measurement per grain (average orientation of the crystal).

2-5-2. Crystallographic preferred orientations (CPOs) of peridotite xenoliths

The measured CPOs are presented on equal-area, lower-hemisphere projections of peridotite xenoliths from Ichinomegata (Figs. 9, 10), Oki-Dogo (Fig. 11), and Shingu (Fig. 12).

For Ichinomegata peridotite xenoliths, Fig. 9 shows the EBSD maps and olivine CPOs. Olivine CPOs display a well-developed axial [100] pattern (Figs. 9, 10a) characterized by a strong point concentration of [100] axes sub-parallel to the lineation, which is systematically the dominant slip direction for olivine. This interpretation is corroborated by the predominance of (100) subgrain boundaries in the crystallographic orientation maps (Fig. 9d). Other axes, [010] and [001] show weak girdle normal to [100] (Fig. 10a). To infer a dominant slip system for the olivine, inverse pole figures were generated by plotting the direction of interest into the sample space. The inverse pole figures for the olivine in the direction of X (lineation), Y and Z (foliation normal) are shown in Fig. 10b. The inverse pole figures show that [100] of the olivine were aligned sub-parallel to the lineation and the [010] axes were aligned subnormal to the foliation, indicating that the [100] axis was a dominant slip direction and the (010) plane was a dominant slip plane: the (010)[100] slip system. For the sample I708 showing the [100] axes of the olivine were concentrated sub-parallel to the lineation. However, a weak distribution of the [010] and [001] axes of the olivine were observed in the direction of the foliation normal, indicating that the [100] axis was a dominant slip direction, but the slip plane was not well defined: the {0kl}[100] slip system. For orthopyroxene, although most of CPO patterns are weak, a (010)[001] pattern (shear direction is [001] and shear plane is (010)) occurs in two oriented samples (i.e. I667, I909 and I708) (Fig. 11a). Clinopyroxene CPO data show nearly random fabrics, whereas some samples show a weak (010)[001] slip (i.e. I909, I906 and I708) (Fig. 11b).

The CPOs of olivine, orthopyroxene, and clinopyroxene measured for Oki-Dogo peridotites and Shingu peridotites are shown in Figs. 12 and 13, in no structural frame. Because the foliation and lineation could not be determined macroscopically in samples, thin-sections were cut in random orientations, rather than parallel to the lineation and normal to the foliation. To allow a straightforward comparison between the CPO of the different have the maximum concentrations of olivine [100] and [010] axes parallel to the east - west and north - south directions, respectively. The olivine CPOs show a distinct alignment of [100] and [010]. The CPOs of orthopyroxene shows weak concentration, but [001] axes slightly sub-parallel to the olivine [100]. Otherwise, the CPOs of diopside shows random fabrics, whereas some samples show that [001] axes slightly sub-parallel to the olivine [100].

2-5-3. Analysis of subgrain rotation axes

To describe the CPO of a mineral, the orientations of the crystallographic axes of each crystal must be known with respect to an external reference frame (XYZ), which is usually defined in terms of the rock structure (e.g., X parallel to the lineation, Y normal to lineation within the foliation plane, and Z normal to the foliation). However, the external reference frame could not be determined for this sample because of their small size (< 3 cm) and lack of macroscopic structure. The orientations of many of the thin sections are therefore random or independent of the orientation of the foliation and lineation. Accordingly, to obtain the CPO data required to determine the slip system, we measured CPOs and calculated the axes of subgrain rotation, and compared the data obtained from the two methods.

We analyzed the characteristics of subgrain rotation with the aim of identifying the slip system that operated in olivine during deformation (e.g.,

Satsukawa and Michibayashi, 2009). Subgrains are formed by either edge dislocations (representing the edge of a half-plane in a distorted crystal lattice) or screw dislocations (representing a twisted lattice). A subgrain boundary can be thought of as a plane that separates two parts of an originally continuous crystal that have rotated slightly with respect to each other (Fig. 14). Such boundaries can therefore be classified according to the orientation of the rotation axis relative to the subgrain boundary. Subgrain boundaries that form with rotation axes oriented parallel to the boundary are known as tilt walls; those with axes oriented normal to the boundary are known as twist walls (Passchier and Trouw, 2005). A tilt wall (Fig. 14) consists of an array of edge dislocations with the same Burgers vector (slip direction). The slip direction is indicated by the axis oriented normal to the subgrain boundary. The rotation axis was calculated based on the orientations of the lattices of the paired subgrains (using the software HKL channel5, Oxford Instruments). The remaining axis of the three axes of olivine was interpreted to be oriented normal to the slip direction, upon the slip plane.

In order to confirm the differences of slip systems determined from CPO data and estimated from rotation axis analysis, we compare these two methods for samples, which is clearly identified its reference frame (X, Y, Z) from Ichinomegata peridotites. Three CPO of olivine are shown in Fig. 15. Olivine CPOs display a well-developed axial [100] pattern characterized by a strong point concentration of [100] axes sub-parallel to the lineation, which is systematically the dominant slip direction for olivine. [010] is normal to [100] (Fig. 15a), indicating that slip system is (010)[100] (Fig. 16a). For other samples, [010] and [001] show weak girdle normal to [100] (Fig. 15b, c), indicating that the [100] axis was a dominant slip direction and the (010) and (001) plane was a dominant slip plane: the {0kl} [100] slip system (Fig.

16b).

Figure 17(a) shows photomicrograph of an olivine subgrain boundary of Ichinomegata peridotites. Foliation is horizontal and lineation is E-W. A and B in Fig. 17(a) are points where crystallographic orientations were measured. In the Fig. 17(b) shows a great circle that indicates the orientation of the subgrain boundary, as measured on a universal stage, and circles that correspond to the orientation of olivine [100] (after Fig. 17(c) which shows CPO data at the point of A and B), representing the slip direction. When [100] is oriented subnormal to the subgrain boundary, with a rotation axis sub-parallel to the boundary, the boundary is identified as a tilt boundary. The axis of the misorientation between the subgrains is estimated to be [001], as plotted on an inverse pole figure in the figure 4(d). Thus, the slip direction is [100] and the axis of subgrain rotation is [001]; the remaining axis, [010], is interpreted to be oriented normal to the slip direction, upon the slip plane. Thus, the slip system is (010)[100].

Using the above method, subgrain rotation axis is determined for three samples. In the Fig. 18 shows a great circle that indicates the orientation of the subgrain boundary, and circles that correspond to the orientation of olivine [100] (after Fig. 15 which shows CPO data), representing the slip direction. The axis of the misorientation between the subgrains as plotted on an inverse pole figure (Fig. 19). For sample I909, misorientation axis is estimated to be [001], thus the slip system is (010)[100]. For others, misorientation axis is distributed from [001] to [010], indicate that slip system is $\{0kl\}[100]$. The slip system defined by subgrain rotation axes is consisted with that from CPO.

Oki-Dogo peridotites analyzed in this way, most of the subgrain-rotation axes are oriented parallel to [001] or [010] (Fig. 20a). All of the data regarding the

axes of subgrain rotation are shown in Fig. 20(b). The rotation axes of peridotite xenoliths of Oki-Dogo Island are mainly orientated parallel to [001], followed by [010].

2-5-4. Fabric strength of olivine

To characterize CPOs, we determined the fabric strength (*J*-index), distribution density (*pfJ*-index) and misorientation index (*M*-index) of the principal crystallographic axes (for definitions of the *J*-index, *pfJ*-index, and *M*-index, see Mainprice et al., 2000; Michibayashi and Mainprice, 2004; Skemer et al., 2005). Table 10 lists the number of measured olivine grains, the *J*-index values calculated for each xenoliths, *M*-index and the maximum density and *pfJ*-index value for each pole figure. The *J*-index is the volume-averaged integral of the squared orientation densities; it has a value of unity for a random CPO and is infinite for a single crystal. Most natural peridotites yield values between 2 and 20, with a peak around 8 (Ben Ismaïl and Mainprice, 1998), and those of the present study range from 2.56 to 7.94 (Table 10). Oki-Dogo: *J*-index values range from 5.30 to 24.76 (*M*-index: 0.068–0.319). *M*-index, which corresponds to the differences between the observed distribution of uncorrelated misorientation angles and that predicted for a random fabric. It has a value of zero for a random CPO and unity for a single crystal. Misorientation angle distribution and *M*-index are shown in Fig. 10(c).

J- and *M*- indices show a good linear correlation ($R^2=0.97$, Fig. 21), indicating that both indices correctly represent the CPO strength of the studied samples. As most published CPO data for natural peridotites and experimental aggregates have their strength expressed as *J*-indices, we choose to use this index in the following discussion.

2-5-5. Microstructural analyses

Ichinomegata peridotite xenoliths have main foliation composed of compositional banding defined by pyroxene-rich and pyroxene-poor layers and a lineation defined by elongate pyroxene grains. Thus, it is useful for detailed microstructural analysis because thin sections of these samples are made in XZ plane. Most of the peridotite xenoliths have medium- (<5 mm) to fine-grained (<1 mm) granular texture, whereas only two of the peridotite xenoliths have porphyroclastic textures.

From the EBSD mapping (Fig. 9), we can have several parameters about olivine microstructure from EBSD mapping; grain size, aspect ratio and angle of long axis of grain. Olivine grain size (diameter) histogram is shown in Fig. 22. Grain sizes are 34 μm to 4.67 mm (Fig. 22b). Mean grain size are 350 to 652 μm , and the fine-grained population is quite high (Fig. 22a). The J -index is correlated with the olivine grain size distribution and in Avacha peridotite xenoliths (Soustelle et al., 2010). They show that the fine-grained population has a strong influence on the estimation of the sample J -index if it is calculated by using one measurement per grains, as fine grains are more numerous on a given analyzed surface. The population of fine grains is relatively high in our samples (Fig. 22a). Thus, there may be strong grain-size heterogeneity in CPO intensity. Analysis of the J -indices for different grain size populations in sample also shows that fine (< 0.5 mm) and intermediate grains (0.5 - 1 mm) have lower J -indices than coarse grains, whereas J -indices calculated by using the EBSD mapping have higher values (Fig. 23). EBSD data of one measurement per grain, which are used in the calculation of J -indices, are generated from the full orientation dataset from mapping data. Here, we prefer to use

measurement per grains for later discussion, as to see the relation of CPOs to the microstructure.

The peridotite xenoliths with granular texture have shape-preferred orientations (SPOs) of olivine that are oriented oblique to the main foliation (Fig. 24a). Either olivine grains, which have large grain size or high aspect ratio, oriented closer to the foliation (Fig. 24b, c). There are no strong correlation between grain size and aspect ratio (Fig. 25a, b). Although the oblique foliation tends to weaken as olivine grain size decreases, the angle between the two foliations is constantly around 20°, indicating that these are steady-state microstructures. So-called 'oblique foliation' is a typical microstructure resulting from shear deformation (e.g., Nicolas and Christensen, 1987). The similar nature of the oblique foliations within all the peridotite xenoliths indicates that their origins are related to a pervasive event in the uppermost mantle lithosphere beneath the northeast Japan arc.

2-6. Discussion

2-6-1. Evidence of fluid/melts rock interaction of peridotite xenoliths from Japan arc

The spinel lherzolites from Oki-Dogo and Shingu show various trends in olivine Mg# and Spinel Cr#. On an OSMA (olivine spinel mantle array) diagram, the samples plot in the field of residual peridotite of mantle origin (Fig. 4) (Arai, 1994). The data provided by Abe et al. (2003) are plotted in Fig. 4. Combined with data from the present study, two trends of metasomatism are recognized, possibly reflecting the degree of melt extraction prior to metasomatism (Arai, 1994). Thus, the figure shows the degree of melt extraction using two different symbols. Samples with low Mg# show evidence of metasomatism. The spinel lherzolite from Oki-Dogo is rich in Fe relative to typical mantle peridotite xenoliths found in alkaline basalts (Abe et al.,

2003), and it is also similar in peridotites from Shingu (Goto and Arai, 1987). Such Fe-rich ($Fo < 88$) Cr-diopside series peridotites occur in several sites throughout the world, including New South Wales, Australia (Wilkinson and Binns, 1977), British Columbia, Canada (Brearly et al., 1984), Oahu, Hawaii (Sen and Leman, 1991), and SW Japan (Aratoyama: Fujiwara and Arai, 1982).

Other Fe-rich lherzolite xenoliths, modally metasomatized and containing phlogopite, have been reported in association with typical Mg-rich xenoliths at Salt Lake, Hawaii (Goto and Yokoyama, 1988). Some peridotite xenoliths from Megata volcano are also Fe-rich, as well as being strongly metasomatized and containing > 10 vol% sparsely distributed veinlets of amphibole and hornblende (Abe et al., 1992). The evidence of Th-U positive anomaly in clinopyroxene indicates that there is fluid metasomatism in Ichinomegata peridotites. Water contents of these samples are intermediate amounts; it is also consistent with the evidence of fluids interaction.

In contrast, Fe-rich peridotite xenoliths from Aratoyama (Fujiwara and Arai, 1982) and Shingu (Goto and Arai, 1987), as well as those from Oki-Dogo (SW Japan), do not contain hydrous phases and show no evidence of modal mantle metasomatism (Arai et al., 2000). Arai et al. (2000) proposed that Fe-rich peridotites (Cr-diopside series) in the upper mantle were intruded by Fe-rich cumulates and/or Fe-rich ultramafic rocks (Al-augite series), because they are found exclusively in regions that contain abundant Al-augite series and/or Fe-rich ultramafic xenoliths. Water content in pyroxenes was low, suggesting that water in peridotites was easily moved in melts if water was contained in rocks before the metasomatism. Because pyroxenes coexisting with olivine appear to retain their initial H contents than olivine even though the main minerals in the mantle (olivine, orthopyroxene and clinopyroxene) are nominally anhydrous (e.g., Peslier et al., 2002). Abe et al. (2003) explained the

origin of Fe-rich cumulates in terms of REE-enrichment metasomatism after depletion by melt extraction, based on the LREE-enriched U-shaped trace element patterns obtained for clinopyroxene. Moreover, we found that Oki-Dogo peridotites are influenced by various degrees of melts based on REE patterns varies from U-shaped pattern to enriched pattern.

2-6-2. Dominant slip systems of minerals in peridotite xenoliths

CPOs of olivine are well developed imply that peridotite xenoliths in this study deformed mainly by dislocation creep. The correlation between shape and crystal preferred orientation is a reliable tool to constrain the dominant slip systems in olivine. This results in alignment of the dominant slip direction with the shear direction and of the normal to the slip plane with the normal to the shear plane (or foliation) in simple shear (or pure shear) deformation (Zhang and Karato, 1995; Tommasi et al., 2000; Bystricky et al., 2000). In samples of Oki-Dogo and Shingu, however, the foliation and lineation cannot be easily identified, since the foliation and lineation could not be determined macroscopically in samples, thin-sections were cut in random orientations, rather than parallel to the lineation and normal to the foliation. Other observations are needed to constrain the dominant slip system. To constrain the active slip system, we use the analysis of subgrain rotation axes (to see 2-5-3. Analysis of subgrain rotation axes). The rotation axes accommodating low angle ($< 12^\circ$) misorientations within a crystal, because variations in crystallographic orientation within a grain or across a low angle grain boundary (subgrain boundary), as well as the orientation of subgrain boundaries, are directly related to the dislocations forming the boundary (Frank and Read, 1950; Amelinckx and Dekeyser, 1959).

Olivines of Ichinomegata have been deformed essentially by slip on the $\{0kl\}[100]$ systems, which occurred under the condition of high temperature (1200°C), low water contents and relatively low shear stress (e.g., Mainprice, 2007). The slip system of samples from Oki-Dogo and Shingu were estimated from the analysis of subgrain rotation axes. The olivine slip direction of these samples is mainly $[100]$, and (010) is normal to the $[100]$, indicating that olivines deform by slip on $(010)[100]$. For samples of Shingu, some samples have strong concentration in $[010]$ with girdle distribution of olivine $[100]$ and $[001]$. It suggests that slip direction is both $[100]$ and $[001]$, which are formed under presence of melts (Holtzman et al., 2003). We do not find $(001)[100]$, which system has been interpreted to dominate in olivine under low stress conditions in the presence of moderate water contents (Mehl et al., 2003; Katayama et al., 2004).

For orthopyroxene, most of the $[001]$ axes are more concentrated than $[100]$ or $[010]$ sub-parallel to the lineation, indicating dominantly $[001]$ slip (Fig. 11b). Combined with other axes, CPO data may indicate either or both $(100)[001]$ and $(010)[100]$ slip. Considering the pressure and temperature in the uppermost mantle, the dominant slip system in orthopyroxene is $(100)[001]$ (Doukhan et al., 1986); however, the $(100)[010]$ slip is the most readily activated, and thus the most common slip system (Naze et al., 1987). The obliquity between the olivine and orthopyroxene CPO is common in naturally deformed peridotites (e.g., Tommasi et al., 2004, 2006; Le Roux et al., 2008, Soustelle et al., 2010). It is usually interpreted as resulting from lower finite strains in stronger orthopyroxene crystals (Mackwell, 1991) at a given macroscopic strain.

Clinopyroxene CPO data suggest a nearly random fabric, with a weak concentration in (010) normal to the foliation and [001] parallel to the lineation. It is difficult to identify the slip system.

2-6-3. Implication for the dynamics of the back-arc region and development of oceanic lithosphere

Although the original orientations of the Ichinomegata peridotite xenoliths were lost during their volcanic transport to the surface, we are able to derive quantitative constraints on the structure within the lithospheric mantle. In this case, it is likely that regional-scale structures within the uppermost mantle lithosphere are oriented horizontally, as described below.

The opening of the Japan Sea is thought to have occurred over the period 25 to 13 Ma as a consequence of back-arc spreading within the northeast Japan arc; most of the basic geologic structure of the present Japanese Islands was accomplished during this time (Fig. 26) (e.g., Sato, 1994). The depth of the Moho beneath the Ichinomegata crater is approximately 28 km near the coast of the Japan Sea (Zhao et al., 1990), while the temperature of the Moho is thought to be about 850°C (Kushiro, 1987). The depth of the Moho becomes deeper, up to 38 km in depth, toward the northeast Japan arc (Zhao et al., 1990), where temperatures are 950 to 1000°C (Kushiro, 1987). The peridotite xenoliths analyzed in the present study came from relatively shallow levels in the mantle of 30 to 40 km depth at temperatures in the range 850 to 1000°C (Takahashi, 1986). Therefore, it is likely that the Ichinomegata peridotite xenoliths are derived from the uppermost mantle lithosphere in the region dominated by horizontal extension due to back-arc spreading (Fig. 26).

From the eight samples of Ichinomegata peridotite xenoliths, we found that

the angle between olivine [100] maximum and foliation decreases with increasing of J -index (Fig. 27a), and this relationship is independent of grain size (Fig. 27b). Figure 28 show the variation of temperature estimated from Ca-Orthopyroxene thermometer of Brey and Köhler (1990) at 1.0 GPa with J -index. The samples, which have high J -index, have lower temperature. Although temperature varies from approximately 830 to 1200 °C, we assume that the lowest temperature preserve the closet to the surrounding environment. From this assumption, this temperature variation suggests that J -index increases with decreasing of depth.

The correlation between shape and crystal preferred orientation is a reliable tool to constrain the deformation systems. There is one simple summary from our microstructural observations, SPO and CPO (Fig. 29a). The peridotite xenoliths have shape-preferred orientations (SPOs) of olivine that are oriented oblique to the main foliation and also have obliquity between the olivine [100] maximum and foliation. The relationships of these angles are results in olivine [100] – foliation – SPO (Fig. 29a). We have two models to define the shear plane, as follows.

Case 1) Slip plane is defined by foliation. The principle idea from experimental study (Zhang and Karato, 1995), which carried out simple shear experiments, olivine aggregates at 1200 °C and 1300 °C over a range of shear strains to investigate olivine fabric evolution. They found that the originally random fabric of their aggregates developed a CPO with a [100] maximum parallel to the flow direction.

Case 2) Slip direction is defined by olivine [100]. The principle idea from the field observation of Oman ophiolite (Ceuleneer et al., 1988) and experiments (Nicolas et al., 1973) which were performed in an axial geometry, but bubbles in olivine grains aligned with the flow direction at high strain and were interpreted to

have deformed by simple shear.

According to above two models and the assumption that Ichinomegata peridotite xenoliths preserved horizontal extension due to back-arc spreading, we show the geometry for the evolution of SPO and CPO (Fig. 29b). The combination of three independent angles is results in follows; SPO – olivine [100] - foliation (or olivine [100] - SPO – foliation) for case 1 and SPO – foliation - olivine [100] for case 2. As a result, case 2 is consistent with our observation.

Olivine CPOs can be used as a function of shear strain related to the kinematics of deformation. The geometric relationship of shear strain and the orientation of a marker layer are shown in Fig. 30(a). Shear strain is calculated from the change in pyroxene layer orientation in the kinematic reference frame, shown on the stereo net in Fig. 30(b). Following the method of Ramsay and Graham (1970) and Ramsay (1980), shear strain, γ , is given by:

$$\gamma = \cot(\alpha') - \cot(\alpha)$$

where α is the initial angle of the layering defined by the pyroxene rich compositional banding with respect to the shear plane, and α' is the deflection angle, as shown in Fig. 30(a). In this study, since we assume that shear direction is equal to the maximum direction of olivine [100], values for α' can consider as an angle between olivine [100] maximum and foliation (layer). Since xenoliths are usually lack of a well-defined finite strain marker, we have no evidence of pre-existing foliation. We calculated shear strain with changing initial direction of layering (α) from 45° to 90°, which provides a passive strain marker, as shown in Fig. 30(b). As a result, shear strain varies from 0.31 to 4.26, and decreases with increasing of α' (Fig. 30c). Moreover, shear strain increases with increasing of J -index (Fig. 30d).

The change in the angle of the olivine [100] maximum relative to the shear

plane with increasing strain is compared to naturally deformed sample, experimental results and models in Fig. 31(a). In comparison to experiments, the Ichinomegata peridotites are observed to require higher strain to align with the shear direction. Ichinomegata samples partly agree with predictions from VPSC ($\alpha 1$) (Tommasi et al., 2000), however they mostly do not agree with either VPSC or DRex models (Kaminski and Ribe, 2001).

The evolution of fabric strength with strain is also important for constraining models of CPO formation. The fabric strength of Ichinomegata peridotites is compared with naturally deformed sample, experimental results and models in Fig. 31(b). Although the Ichinomegata peridotites have higher shear strain than experimental dataset and model predictions, they are relatively similar to the Josephine peridotites. Ichinomegata peridotites have similar CPO type to Josephine peridotites, which have more girdle distribution in [010] and [001] compared to experimental samples. The rapid increase in J -index with shear strain observed in the experiments results from alignment of [010] and [001] axes. In the Josephine samples, [010] and [001] tend to have girdled patterns, leading to lower J -indices. CPO of Ichinomegata peridotites strengthens than predicted by the theoretical models.

According to above discussion, a schematic model of the mantle evolution beneath the Ichinomegata volcano is shown in Fig. 32. Peridotite xenoliths with higher J -index values tend to be more closely aligned to the main foliation, suggesting that these composite planar structures resulted from shearing in the uppermost mantle. These structures possibly indicate the occurrence of a strain gradient during back-arc spreading related to the opening of the Japan Sea (Fig. 32d). Although the original orientations of the Ichinomegata peridotite xenoliths were lost during their volcanic

transport to the surface (Fig. 32e), our results provide an improved framework for estimation of CPO evolution models from mantle xenoliths.

2-6-4. Relationships between deformation and melt-rock interaction in the metasomatized peridotites

Oki-Dogo and Shingu peridotites represent that part of the mantle affected by magma–rock interactions, as indicated metasomatism by melts. To understand the effects of metasomatism on the development of CPOs, the relationship between the Mg# of olivine and fabric strength (*J*-index) are shown in Fig. 33(b). CPO strength or intensity may be defined by the *J*-index, which represents the volume-averaged integral of the squared orientation distribution densities, and hence is sensitive to peaks in the orientation distribution function (Bunge, 1982). In the present samples, the *J*-index slightly increases with decreasing olivine Mg# (Fig. 33b). Because the *J*-index is a function of shear strain, the peridotites show increasing shear strain with degree of metasomatism. Le Roux et al. (2008) proposed that strain is localized by the occurrence of melts, whereas Tommasi et al. (2008) showed that the *J*-index decreases with decreasing olivine Mg# (Fo < 90). However, the three samples, which have low Fo contents (< 87), are inconsistent with this trend and record low strain.

Considering the above results, the observed small-scale variations in *J*-index may be explained by strain gradients or by a higher contribution of melt-enhanced diffusion processes compared with those samples that show a weaker CPO. The observed variations in CPO intensity may result from either the occurrence of a strain gradient or a change in the contribution of diffusion to deformation. The occurrence of high melts fractions favors diffusion-accommodated deformation and results in a decrease in CPO intensity (Hirth & Kohlstedt, 1995; Holtzman et al., 2003). In

contrast, at very low melt fractions, melt is essentially confined to triple-junctions grain boundaries and does not exist as an interconnected path that enables rapid diffusion. Nevertheless, such melt may reduce the contact area between grains, leading to a local increase in stress (Hirth & Kohlstedt, 1995). In turn, higher stress may enhance dislocation creep and CPO development. Therefore, the observed variation in *J*-index in peridotites may result from deformation in the presence of varying fractions of instantaneous melt.

To further assess the obtained CPO patterns in detail, we focused on the maximum density of CPOs (Fig. 33b-d), LS-index (Fig. 33e), and pfJ-index (Fig. 33f-h). LS-index is presented by Ulich and Mainprice (2005), which is used to quantify CPO variations. This method is based on well-established technique of eigenvalue analysis of pole figures. In the present case there is a clear case of the variation of the [100] and [010] from point maxima to girdles distributions in Fig. 12, for example sample KRB15. Hence in the present case one needs an LS index defined as $1/2[2-(P_{010}/(G_{010}+P_{010}))-(P_{100}/(G_{100}+P_{100}))]$, where P = eigenvalue for point maximum distribution and G = eigenvalue for girdle distribution. The correlation between the maximum densities of [010] relatively strengthens with decreasing Mg# (Fig. 33c), however there are not strong relationships among them. This finding indicates that the slip planes became stronger during Fe-enrichment metasomatism; otherwise, the slip directions would have become increasingly randomly oriented. The sample SNG0709, consisting from almost olivine, have the highest maximum density of [100] and [001]. Considering its modal composition, these characteristics might be due to the deformation mechanism with lack of secondary minerals.

These variations in CPO densities are also observed in the CPO patterns. The CPO pattern obtained for KRB15, OKD69 (Fig. 12), SNG0707 (Fig. 13) shows a

strong concentration of [010] axes compare to [100] and [001]. However, most of the olivine CPO has a strong concentration in [100], indicating the (010)[100] slip system. The [010] axes define a point maximum and the [100] axes form a girdle, together defining an AG-type pattern (Mainprice, 2007). AG-type olivine CPO patterns have been observed in peridotites worldwide, including in the Ronda massif (Vauchez & Garrido, 2001; Soustelle et al., 2009), the Lherz massif (Le Roux et al., 2008), Oman Ophiolite (Boudier & Nicolas, 1995), subcontinental xenoliths from Siberia (Tommasi et al., 2008), cratonic xenoliths (Ben Ismaïl et al., 2001; Vauchez et al., 2005), and xenoliths from the Canary Islands and the Kerguelen Islands (Vonlanthen et al., 2006; Bascou et al., 2008).

The “AG-type” CPO patterns measured in the present study are similar to the above pattern described by Holtzman et al. (2003), which reported that AG-type CPO patterns may also result from strain partitioning associated with melt segregation, as produced in a deformation experiment involving olivine in the presence of 4% MORB. Thus, it suggests that peridotite xenoliths from Oki-Dogo Island might be deformed in the presence of melt. This hypothesis is consistent with the above geochemical evidences proposed for the peridotites xenoliths. However, the Oki-Dogo peridotites show no clear change in microstructure and CPO with metasomatism, and the slip system is mostly (010)[100] rather than AG-type. Thus, we do not observe pronounced changes in olivine CPO following metasomatism.

It is important to consider the context of deformation and metasomatism in terms of the present samples, as we cannot infer the timing of these events based on the above analysis. If peridotites are metasomatized after the deformation event in which olivine CPOs developed, variations in olivine CPO or the intensity of the CPO would show no correlation with chemical composition. This observation, together with

our microstructural analysis, suggests that in the present case, reactive melt percolation postdated both deformation and static recrystallization. Indeed, an analysis of subgrain rotation axes reveals that subgrain boundaries in these peridotites are dominantly (100) tilt boundaries, indicating the dominant activation of [100] glide. Many olivine crystals retain well-defined subgrains, suggesting limited annealing. Thus, the absence of annealing features in olivine is inconsistent with the occurrence of static recrystallization.

2-6-5. Structural history of the uppermost mantle in the back-arc of SW Japan

Partial melting, percolation, and interaction of melt with host mantle rock are processes that affect the lithospheric mantle above a mantle plume. Abe et al. (2003) concluded that the Oki-Dogo peridotite xenoliths are slightly more Fe-rich than are other mantle peridotite xenoliths from around the world. Here, we consider the timing of deformation and metasomatism in the structural history of the uppermost mantle in the back-arc of the southwest Japan arc.

Kimura et al. (2005) provided an interpretation of the structure beneath SW Japan based on petrological analyses of volcanic rocks. The model proposed by Kimura et al. (2005), as shown in Fig. 34(b), involve four tectonic stages: 1) the Pacific Plate was subducted during 25–14 Ma; 2) the Philippine Sea Plate began to subduct during 17–12 Ma, the Japan Sea began to open, and upwelling of mantle asthenosphere occurred; 3) the rate of subduction decreased during 12–4 Ma; and 4) xenoliths were erupted and slab melting occurred at 4–0 Ma.

Given that the peridotite xenoliths from Oki-Dogo Island were affected by melts, we must consider the timing of melt-induced metasomatism of the peridotite xenoliths; i.e., whether it was related to asthenospheric upwelling or slab melting.

Kimura et al. (2005) argued that slab melting occurred below about 100 km depth, and the results of the present study indicate that melting was synchronous with deformation. Moreover, Yamamoto et al. (2007) proposed that lherzolite from Oki-Dogo Island originated at depths of 25–29 km; therefore, the peridotite xenoliths are likely to have originated from these depths. In turn, it is likely that the origin of the melts associated with the peridotite xenoliths was associated with asthenospheric upwelling (Fig. 34b, Stage II). Moreover, Abe et al. (2003) argued that mantle metasomatism was induced by the intrusion of evolved melts beneath the SW Japan arc and the degree of melting in the upper mantle during opening of the Japan Sea. Iwamori (1989) concluded that volcanism in SW Japan was caused by the upwelling of mantle material associated with the opening of the Japan Sea, as across-arc variations in basalt composition in the central Chugoku district show the opposite trend to those in the NE Japan arc, and cannot be explained by processes related to the subduction of oceanic lithosphere at the Nankai trough or Japan trench.

The opening of the Japan Sea is thought to have occurred during the period 20–15 Ma as a consequence of back-arc spreading within the Japan arc; most of the basic geological structure of the present Japanese Islands was formed during this time (e.g., Sato, 1993). During this period of back-arc spreading, SW Japan underwent clockwise rotation, whereas NE Japan underwent anticlockwise rotation (Fig. 34a). As a result, the Japan Sea adjacent to NE Japan consists of oceanic crust, whereas the Japan Sea adjacent to SW Japan consists of continental crust (locally stretched). Thus, it is important to compare NE and SW Japan in order to reconstruct the evolution of the uppermost mantle in association with back-arc spreading in the Japan arc.

Back-arc spreading within the Japan arc occurred progressively from NE to SW Japan (e.g., Sato, 1993; Kimura et al., 2005). Thus, based on the above discussion,

we argue that peridotite xenoliths from Oki-Dogo Island in SW Japan record an initial stage of back-arc spreading. In SW Japan, peridotites were influenced by melts generated in association with asthenospheric upwelling (Fig. 35).

Overall, peridotites from the uppermost mantle in SW Japan were deformed in the presence of inhomogeneously distributed melt produced by asthenospheric upwelling associated with back-arc spreading. The peridotites were subsequently erupted, although retaining the structures formed in association with back-arc spreading. Then we conclude that the Oki-Dogo peridotite xenoliths record a continuous history of back-arc spreading, especially from the beginning of this event.

2-7. Conclusion

Microstructures, geochemical analysis, crystallographic preferred orientations (CPOs), and water contents of spinel peridotite xenoliths obtained from back arc region of Japan arc (Ichinomegata and Oki-Dogo) was investigated.

The mineral chemistry of Ichinomegata peridotites showed a typical residual peridotite trend, depleted in LREE (light rare earth element). Olivine CPO of Ichinomegata peridotites were consistent with slip on (010)[100] and {0kl}[100], and the angle between the [100] maximum concentration and the foliation decreased with increasing fabric strength. By using those angles, shear strain was estimated to vary from 0.31 to 4.26, and temperature variation possibly suggested that *J*-index increased with decreasing of depth. These observations indicated that a strain gradient revealed by the peridotite xenoliths studied could be related to back-arc spreading. Three directions have been identified within thin sections of Ichinomegata peridotites: foliation defined by pyroxene rich layers, the [100] maximum concentration of olivine, and shape preferred orientation of olivine. From the relationships between these three

axes, shear plane was considered to be parallel to the [100] maximum concentration of olivine, not foliation. Those structural features were compatible with those found in the Oman ophiolite.

Oki-Dogo peridotites were affected by various degree of metasomatism by melt derived from the upwelling asthenosphere. Water content in pyroxenes was low, suggesting that water in peridotites was easily moved in melts if water was contained in rocks before the metasomatism. Because pyroxenes coexisting with olivine appear to retain their initial H contents than olivine even though the main minerals in the mantle (olivine, orthopyroxene and clinopyroxene) are nominally anhydrous (e.g., Peslier et al., 2002). Olivine CPO of Oki-Dogo peridotites was consistent with the (010)[100] slip system. Samples had low Mg# and showed relatively high concentration in [010], however there were no strong relationships among them. Although peridotite xenoliths from Oki-Dogo Island could be deformed in the presence of melt during the back-arc spreading, there was no strong interaction between deformation and melts percolation.

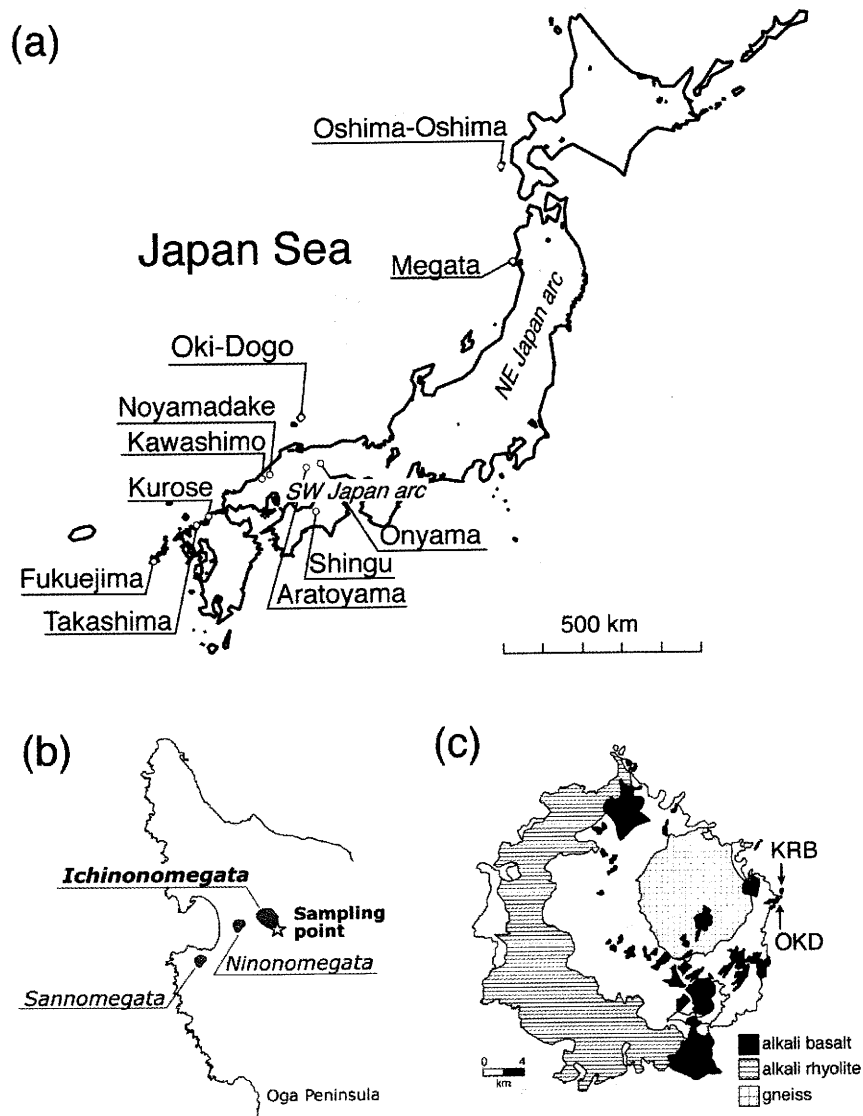


Figure 1. (a) Locality map of mantle xenoliths on the Japan arcs. Shown are selected localities of mantle xenoliths in the southwest (SW) and northeast (NE) Japan arcs. (b) Locality map of mantle xenoliths at Ichinomegata volcano (Oga peninsula, Akita prefecture) in the northeast (NE) Japan. A star shows the sampling point. (c) Locality map of mantle xenoliths on Oki-Dogo Island (Kuroshima basalt and OKD volcanic neck). The distributions of Plio-Pleistocene alkali basalt, and Miocene–Pliocene alkali rhyolite and basement gneiss complex are taken from Takahashi (1978a) and Uchimizu (1966). KRB: Kuroshima basalt; OKD: Oki-Dogo. Modified after Abe et al. (2003).

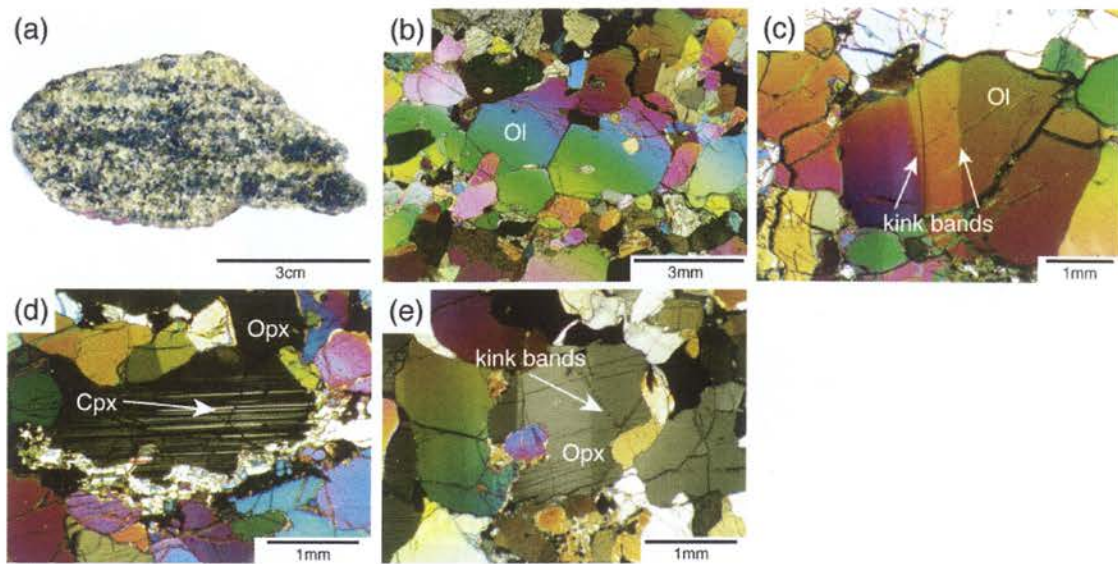


Figure 2. Photomicrographs of Ichinomegata peridotite xenoliths. (a) Slab samples show clear compositional banded structure. (b) Olivine grains with triple junction. (c) Large olivine grains showing subgrain boundaries. (d) Orthopyroxene porphyroclasts with clinopyroxene exsolution lamellas. (e) Large clinopyroxene grains showing subgrain boundaries.

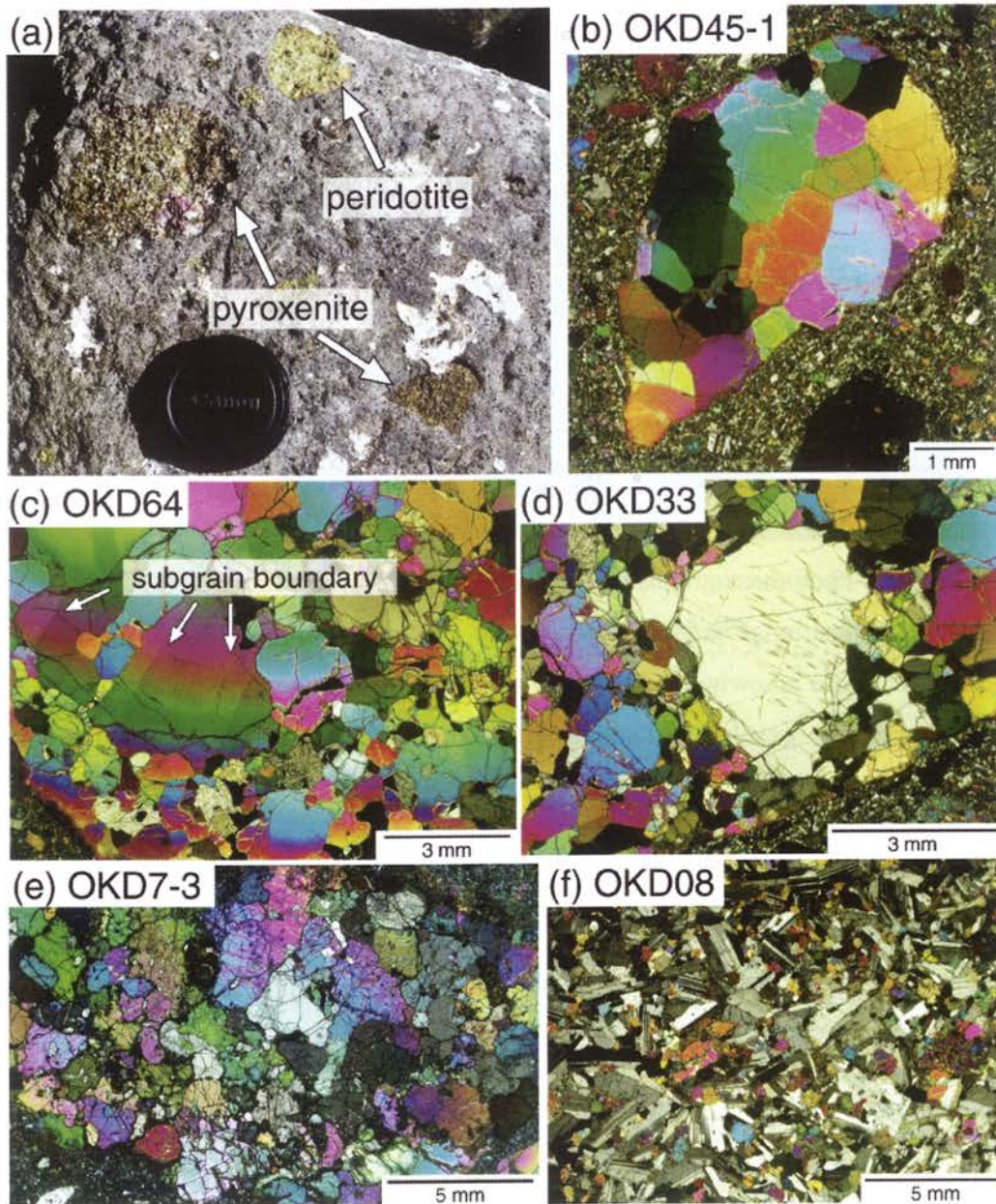


Figure 3. Photomicrographs of Oki-Dogo ultramafic and mafic xenoliths. (a) Boulder including ultramafic and mafic xenoliths at an outcrop of Kuroshima alkali basalt. Arrows indicate ultramafic and mafic xenoliths. (b)–(d) Peridotite xenoliths (samples OKD45-1, OKD64, OKD33). (c) Large olivine grains showing subgrain boundaries. (d) Orthopyroxene porphyroclasts with clinopyroxene exsolution lamellae. (e) Pyroxenite xenolith (OKD7-3). (f) Gabbro xenolith (OKD08). All photomicrographs were taken under cross-polarized light.

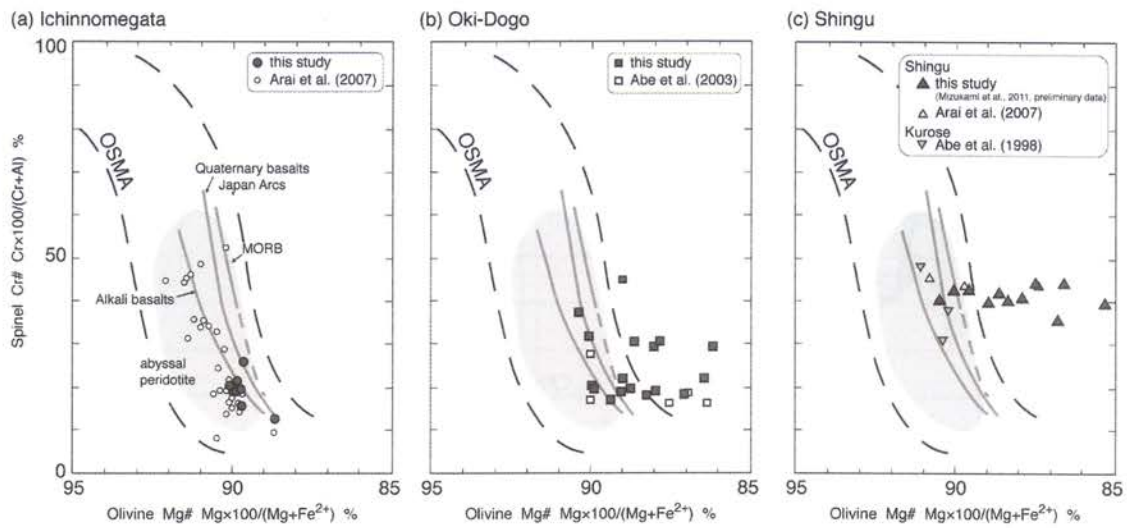


Figure 4. Relationship between the Mg# of olivine and the Cr/(Cr+Al) atomic ratio (Cr#) of spinel in analyzed samples of (a) Ichinomegata, (b) Oki-Dogo, and (c) Shingu. OSMA; olivine-spinel mantle array (Arai, 1994).

Ichinomegata

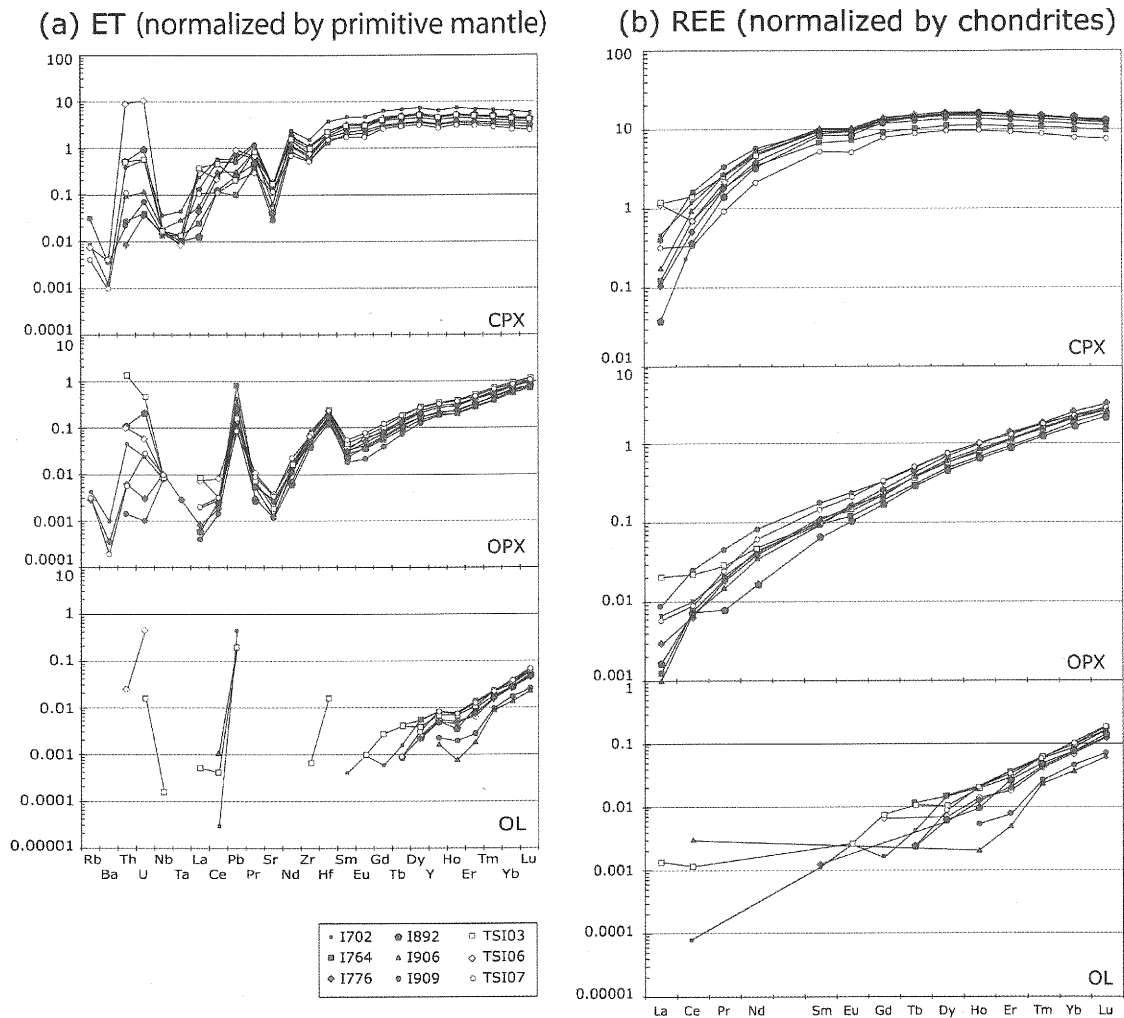


Figure 5. (a) Trace element patterns normalized Primitive mantle of clinopyroxene, orthopyroxene and olivine in nine Ichinomegata peridotite xenoliths. (b) Chondrite-normalized REE patterns of clinopyroxene, orthopyroxene and olivine in nine Ichinomegata peridotite xenoliths.

Oki-Dogo

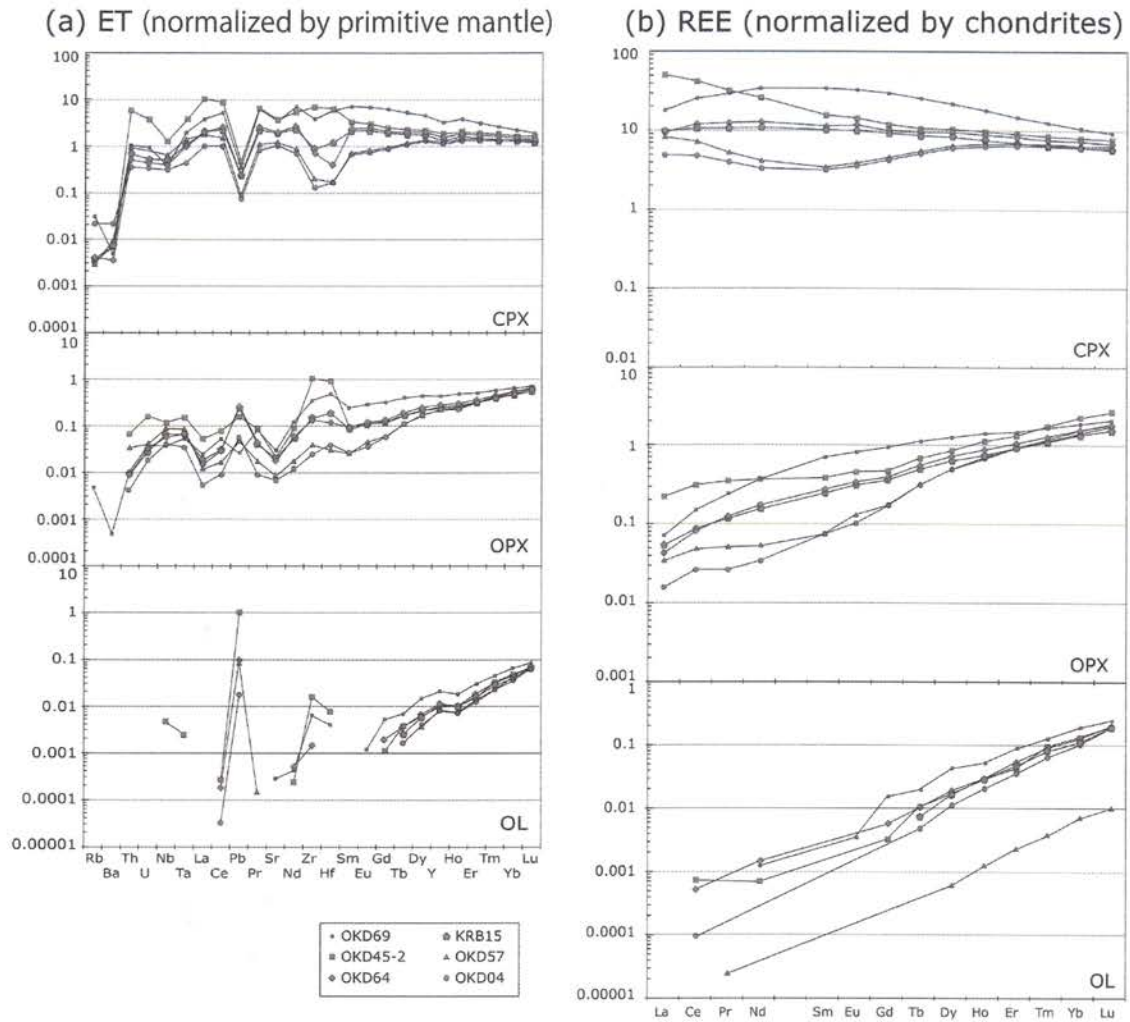


Figure 6. (a) Trace element patterns normalized Primitive mantle of clinopyroxene, orthopyroxene and olivine in six Oki-Dogo peridotite xenoliths. (b) Chondrite-normalized REE patterns of clinopyroxene, orthopyroxene and olivine in six Oki-Dogo peridotite xenoliths.

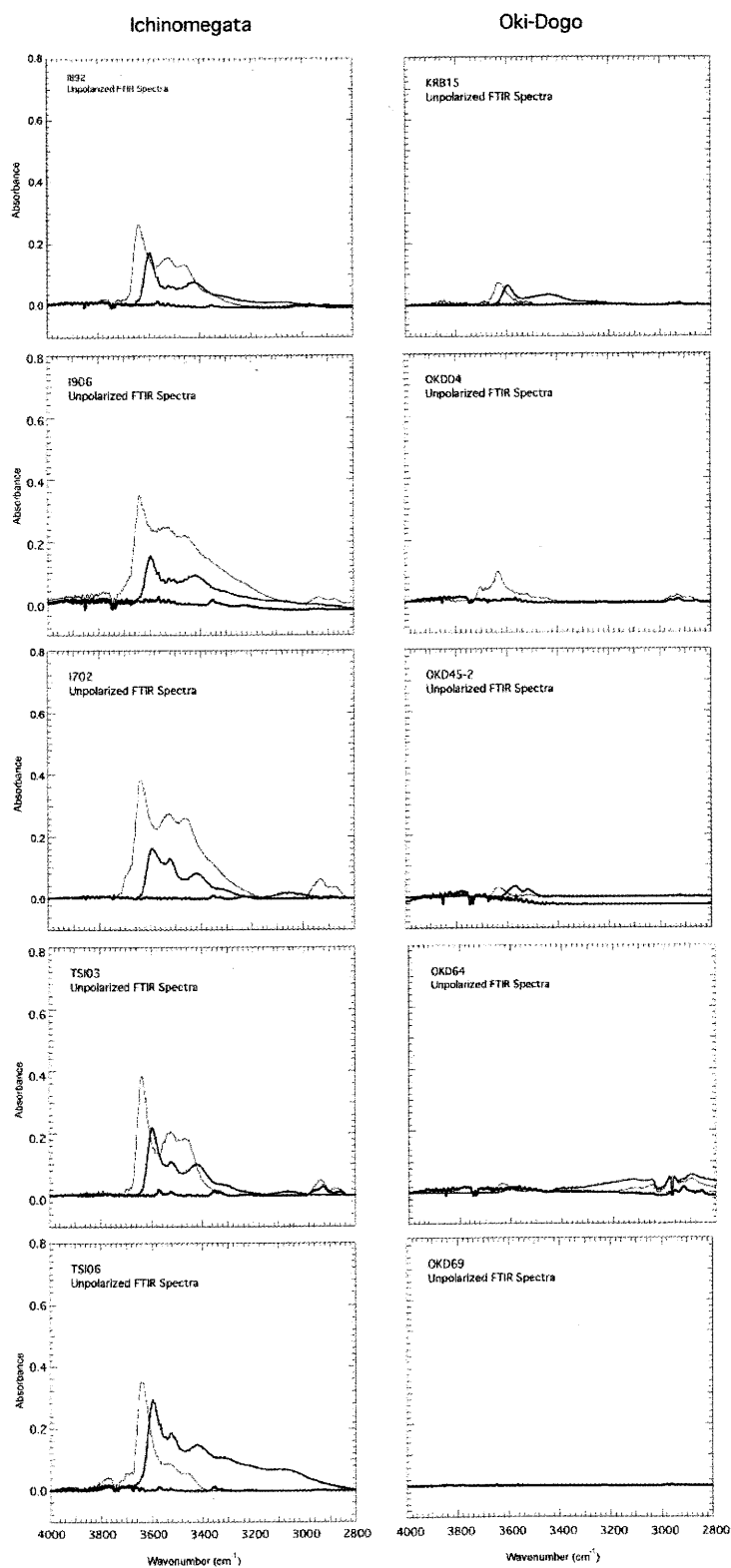


Figure 7. Unpolarized IR spectra for the most representative clinopyroxene, orthopyroxene and olivine in peridotite xenoliths. Spectra are normalized to 1cm⁻¹.

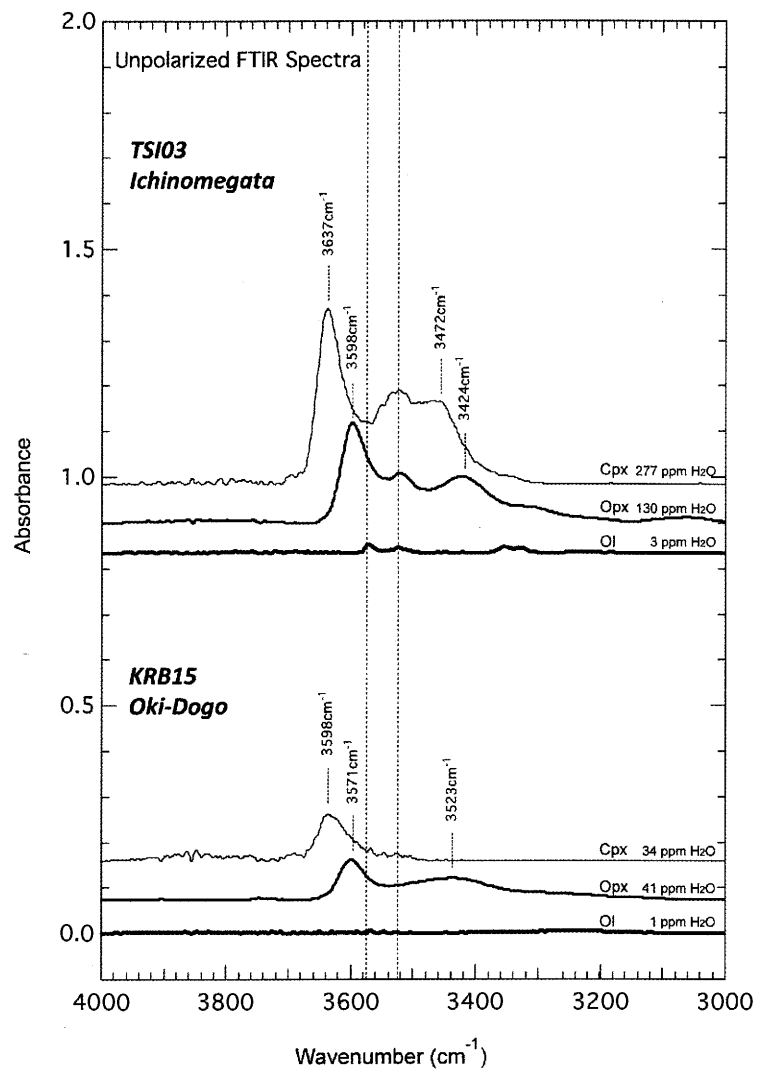


Figure 8. Unpolarized IR spectra for the most representative clinopyroxene, orthopyroxene and olivine in sample of TSI03 and KRB15. Spectra are normalized to 1cm^{-1} .

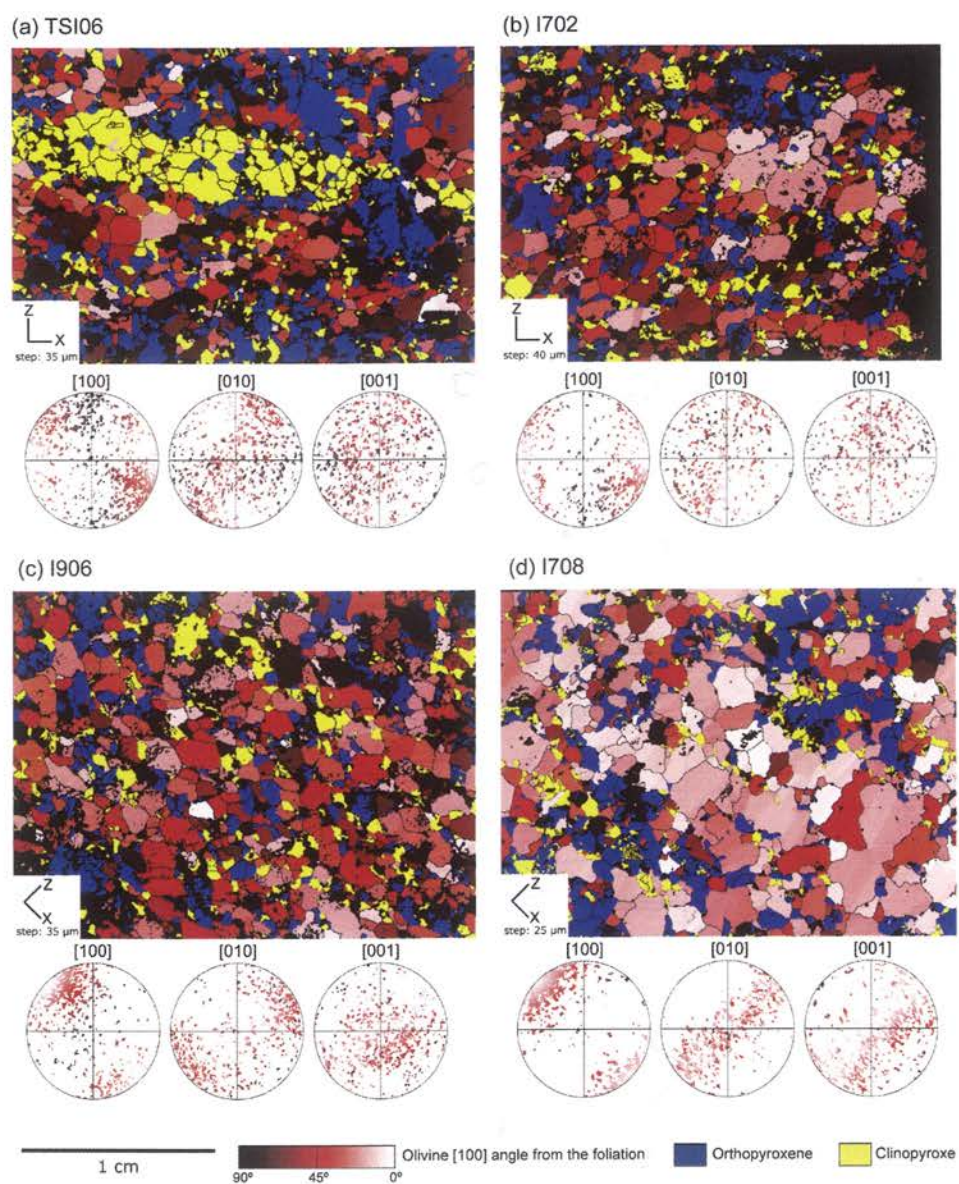


Figure 9. Crystallographic orientation map and equal-area lower hemisphere stereographic projections in the thin-section reference frame of [100], [010] and [001] axes of olivine. Red scale in the maps indicates the angle between the orientation of the [100] of olivine and the foliation plane indicated by pyroxene rich compositional banding.

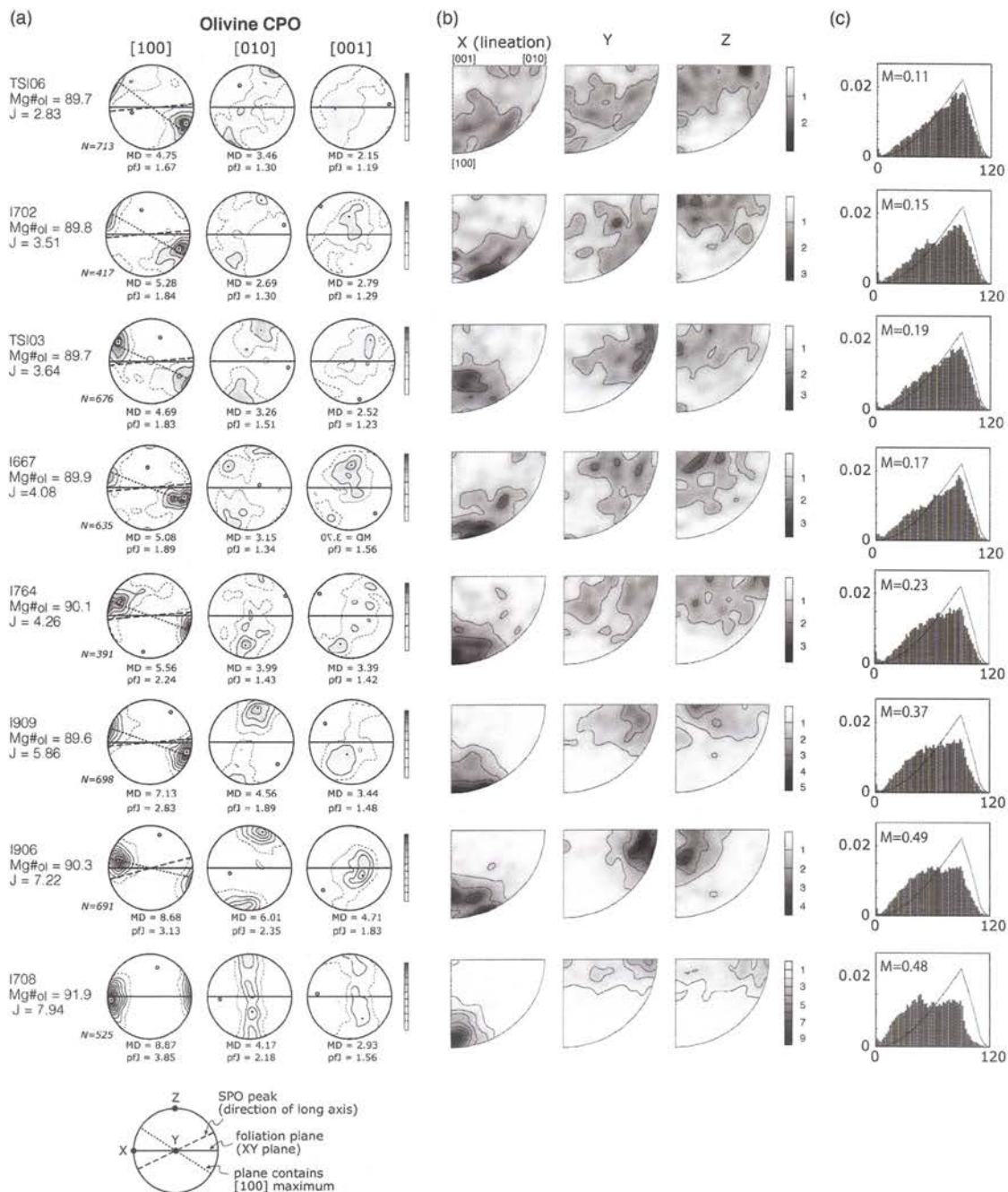


Figure 10. (a) Crystallographic preferred orientations (CPOs) of olivine. Lower hemisphere, equal-area stereographic projections, contours at one multiple of uniform distribution. N is number of measured grains. J , M_x and pfJ are indexes of fabric intensity, and MD is the maximum density (see Table 10) (b) Inverse pole figures of olivine. A half scatter width of 30° was used. The color coding refers to the density of the data points. (c) Misorientation distributions are for uncorrelated angles, with M -index values indicated. The solid line is the theoretical orthorhombic random distribution (Grimmer, 1979).

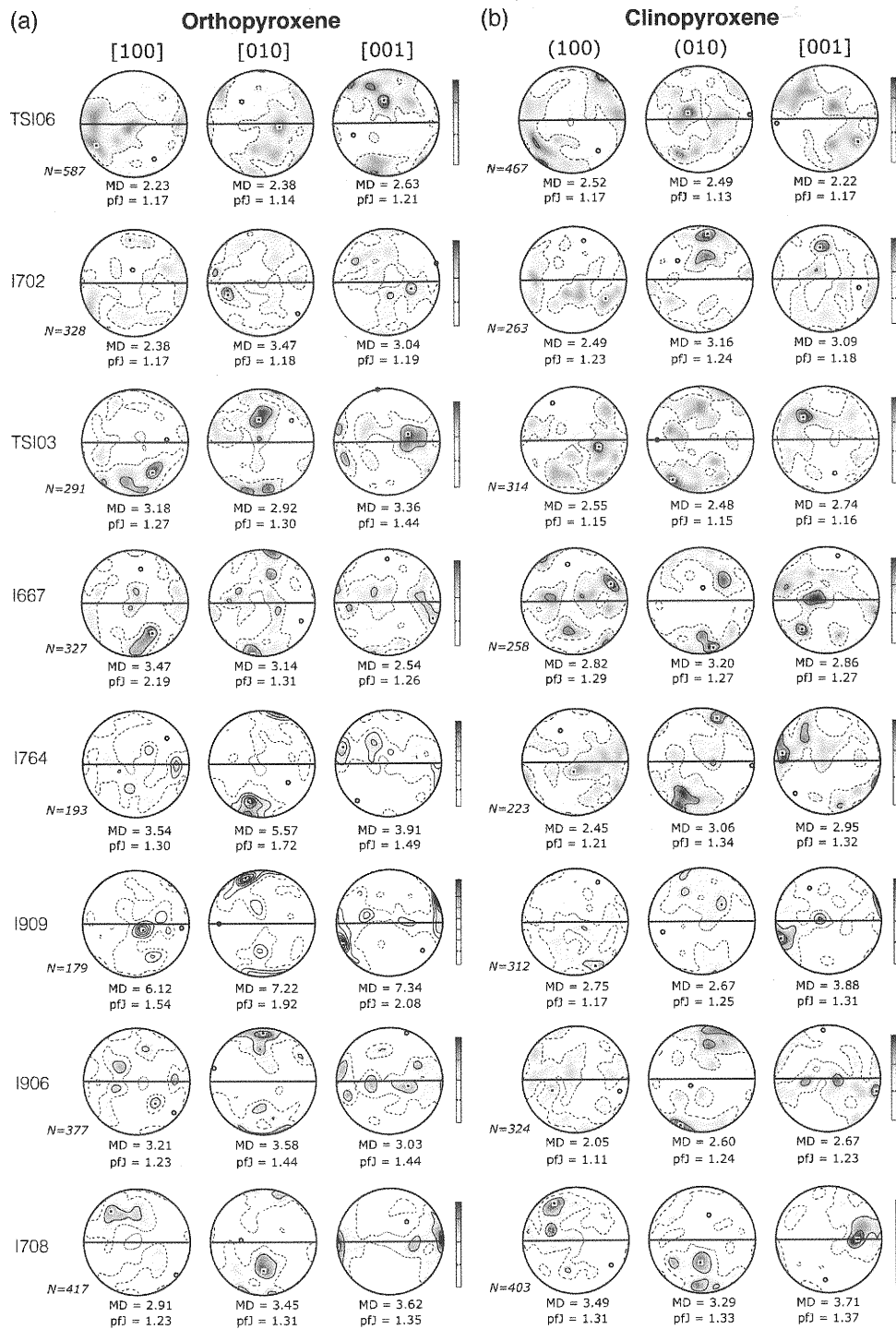


Figure 11. Crystallographic preferred orientations (CPOs) of orthopyroxene (a) and clinopyroxene (b). Lower hemisphere, equal-area stereographic projections, contours at one multiple of uniform distribution. N is number of measured grains.

Oki-Dogo peridotite

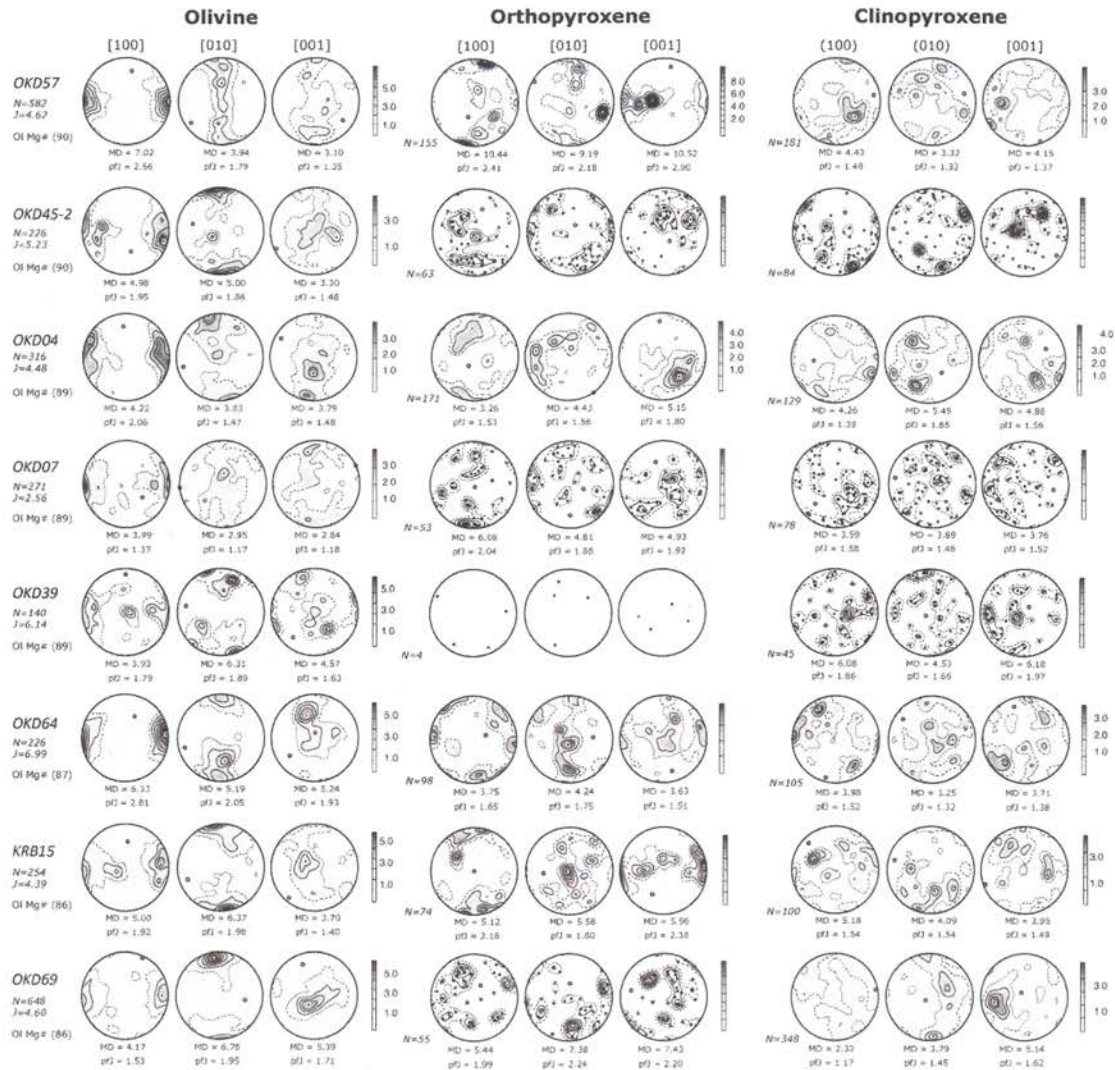


Figure 12. Crystallographic preferred orientations (CPOs) of olivine, orthopyroxene and clinopyroxene of Oki-Dogo peridotite xenoliths. Lower hemisphere, equal-area stereographic projections, contours at one multiple of uniform distribution. N is number of measured grains.

Shingu peridotite

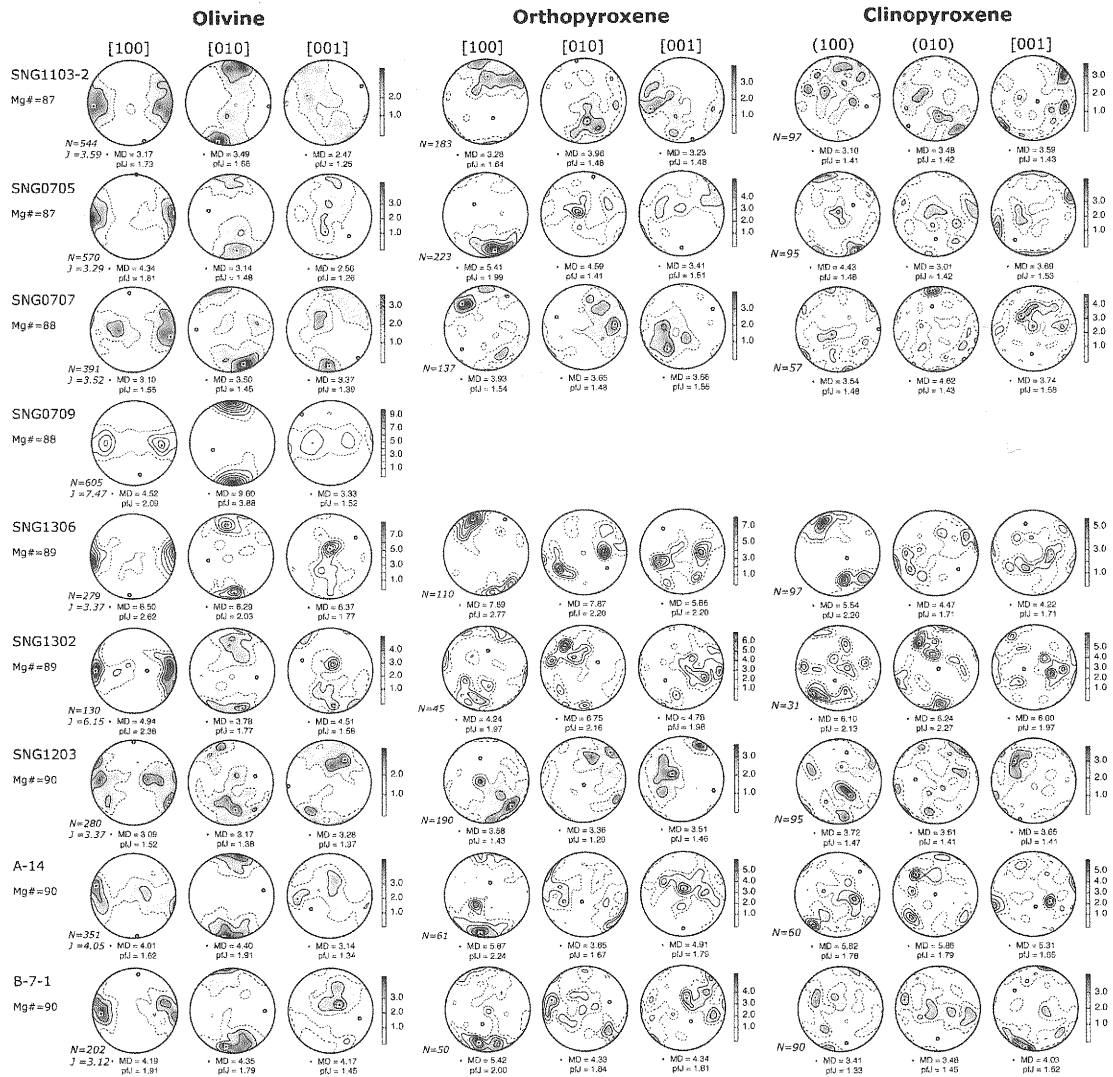


Figure 13. Crystallographic preferred orientations (CPOs) of olivine, orthopyroxene and clinopyroxene of Shingu peridotite xenoliths. Lower hemisphere, equal-area stereographic projections, contours at one multiple of uniform distribution. N is number of measured grains.

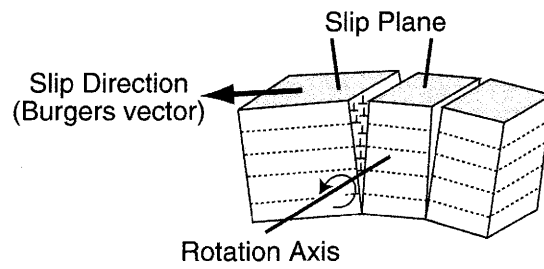


Figure 14. Crystal rotation and tiltwall orientations across an olivine single crystal. Slip direction (Burgers vector) is indicated by the axis normal to the subgrain boundary. Rotation axis is calculated by the two subgrain orientations. The remaining axis is interpreted to be normal to the slip plane. Modified after Mehl et al. (2003).

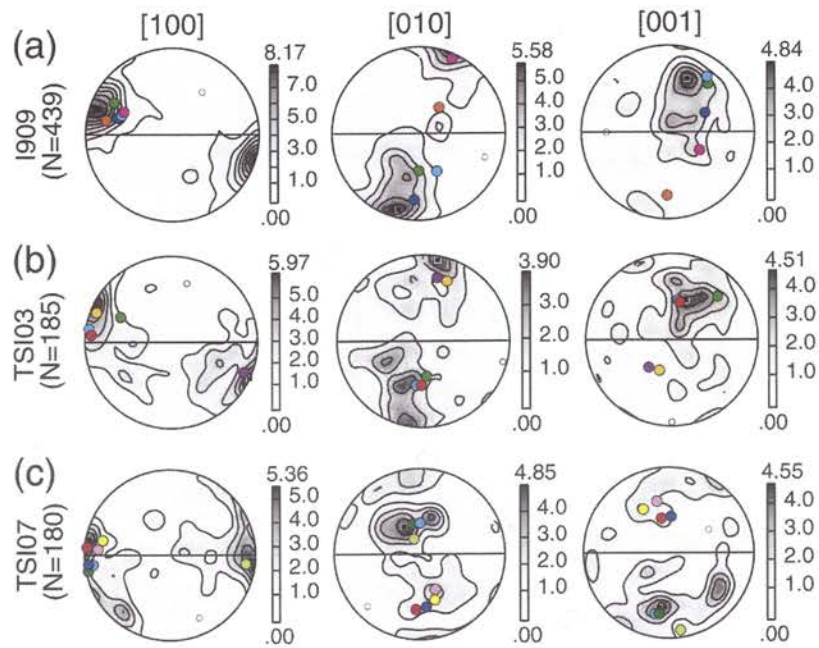


Figure 15. Olivine crystallographic preferred orientation (CPO) data obtained by the EBSD technique. Equal-area, lower-hemisphere projections. Contours at multiples of uniform distribution. Foliation is horizontal and lineation is E-W. N is the number of measurements. Symbols (color circles) correspond to those in Fig. 18 and Fig. 19.

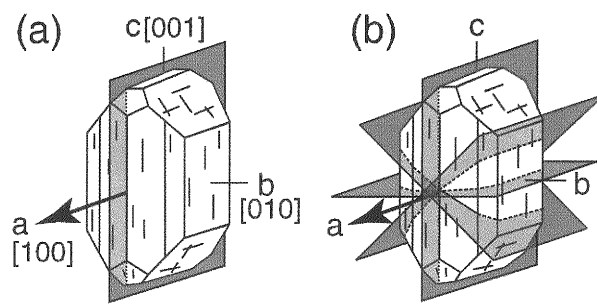


Figure 16. Slip systems in olivine single crystal. The bold arrows show slip direction, while the gray rectangles show slip planes. (a) $(010)[100]$. (b) $\{0kl\}[100]$.

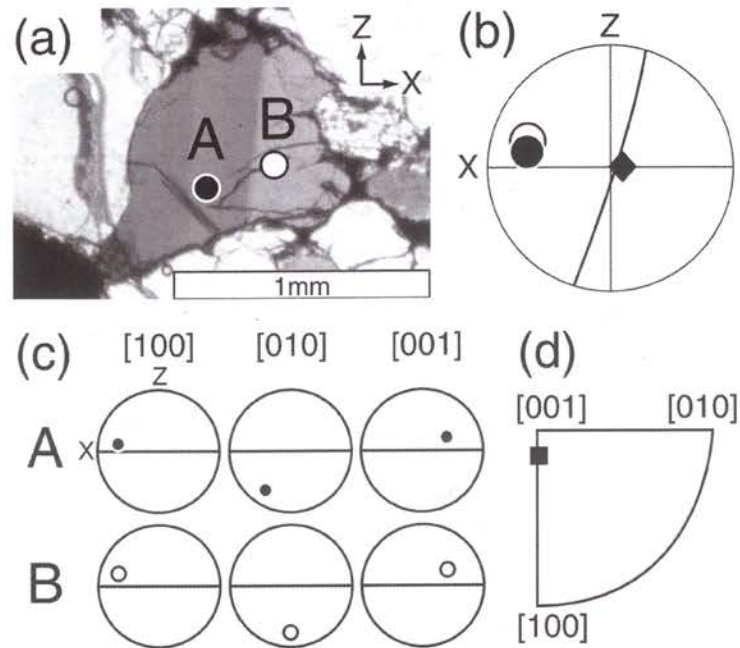


Figure 17. The subgrain-rotation axis method. (a) Photomicrograph of an olivine subgrain boundary in sample I909. Foliation is horizontal and lineation is E-W. Scale bar is 1mm. Crossed-polarized light. A and B are points where crystallographic orientations were measured. (b) A great circle indicates the subgrain-boundary orientation obtained by a universal stage. Circles correspond to the orientations of olivine. Diamond is the axis misorientation across the subgrain boundary. Provided that the slip direction is [100], this subgrain boundary is considered to be a tilt boundary with [100] edge dislocations, because the subgrain boundary is subnormal to [100] and subparallel to the misorientation axis. (c) Crystallographic orientation data at the points of A and B. Equal-area, lower-hemisphere projections. (d) The misorientation axis between subgrains A and B plotted on an inverse pole figure.

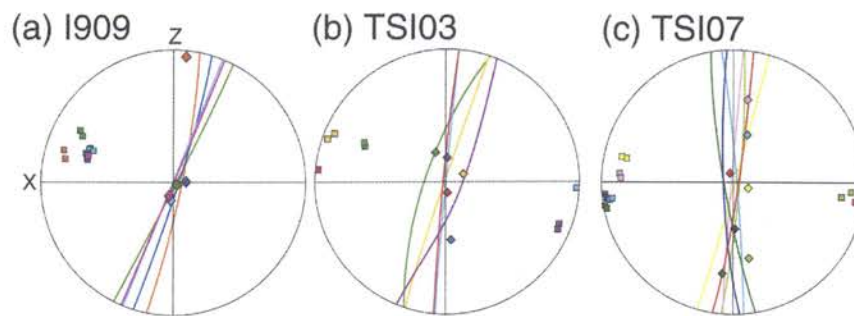


Figure 18. Great circles show subgrain-boundary orientations obtained by a universal stage. Squares correspond to the orientations of olivine [100], which is supposed to the slip direction. Diamonds are the orientations of misorientation axes across subgrain boundaries. Symbols (color circles) correspond to those in Fig. 15 and Fig. 19.

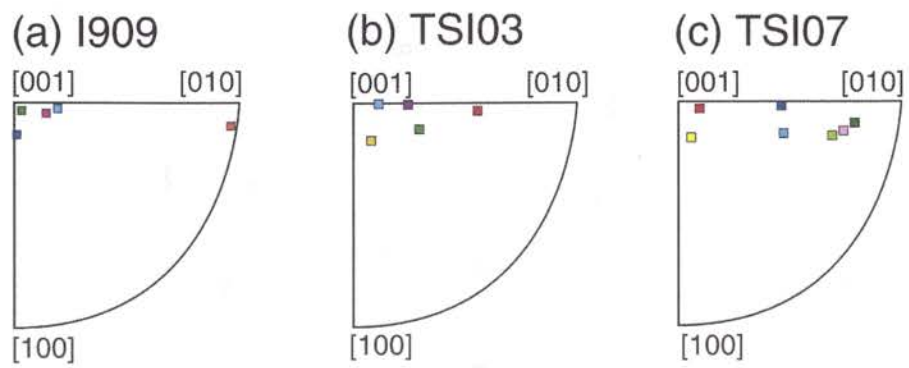


Figure 19. Misorientation axes across measured subgrain-boundaries plotted on inverse pole figures. (a) I909. (b) TSI03. (c) TSI07. Symbols (color circles) correspond to those in Fig. 15 and Fig. 18.

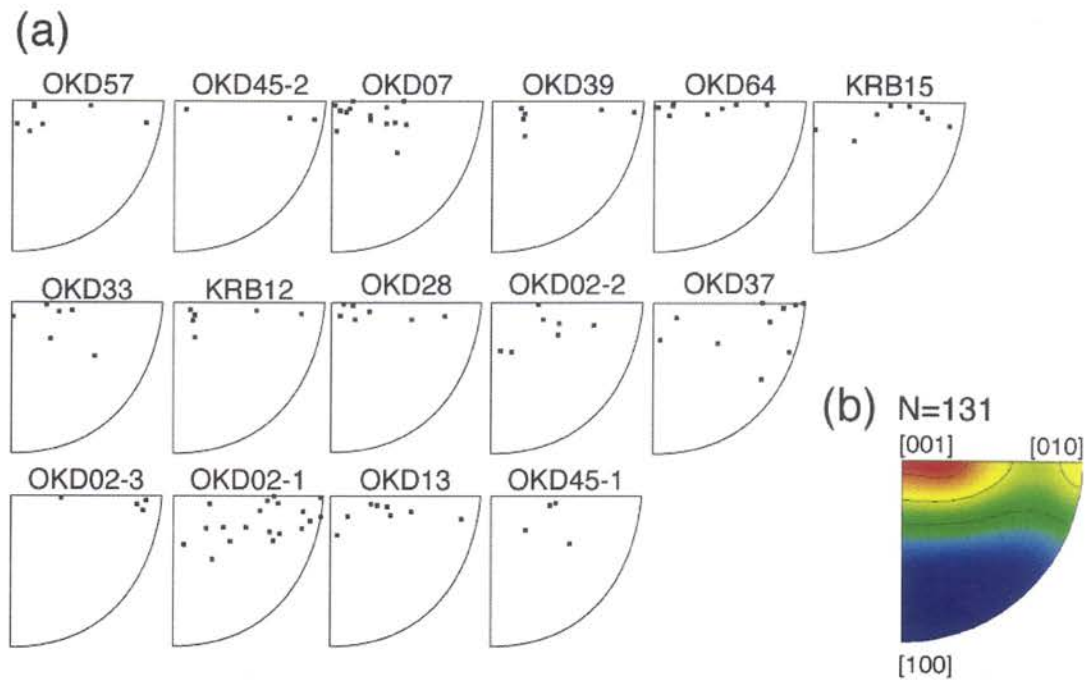


Figure 20. (a) Subgrain-rotation axes of measured subgrains plotted on inverse pole figures. (b) Subgrain-rotation axes of all measured subgrains of peridotite xenoliths from Oki-Dogo Island plotted on an inverse pole figure. Contours are multiples of uniform distribution.

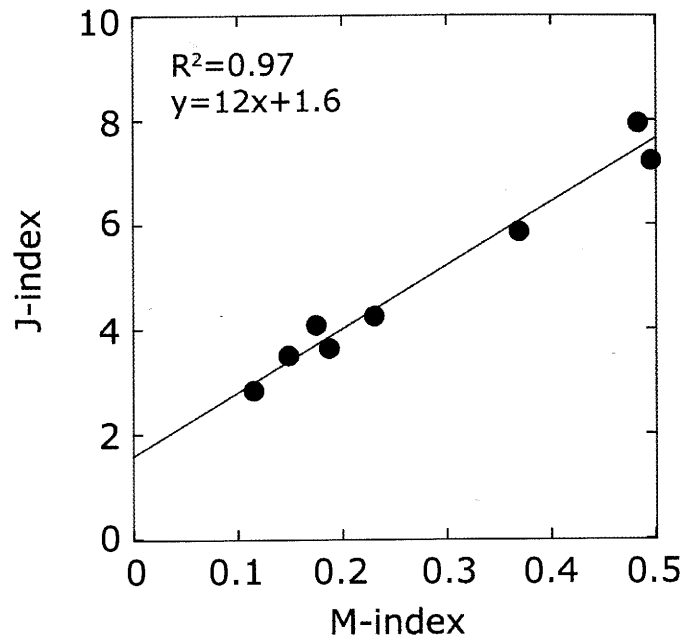


Figure 21. Strength of olivine crystallographic preferred orientation in the studied samples characterized by the J and the M indices. The high correlation coefficient (R^2) indicates that these two measures of the CPO strength are consistent.

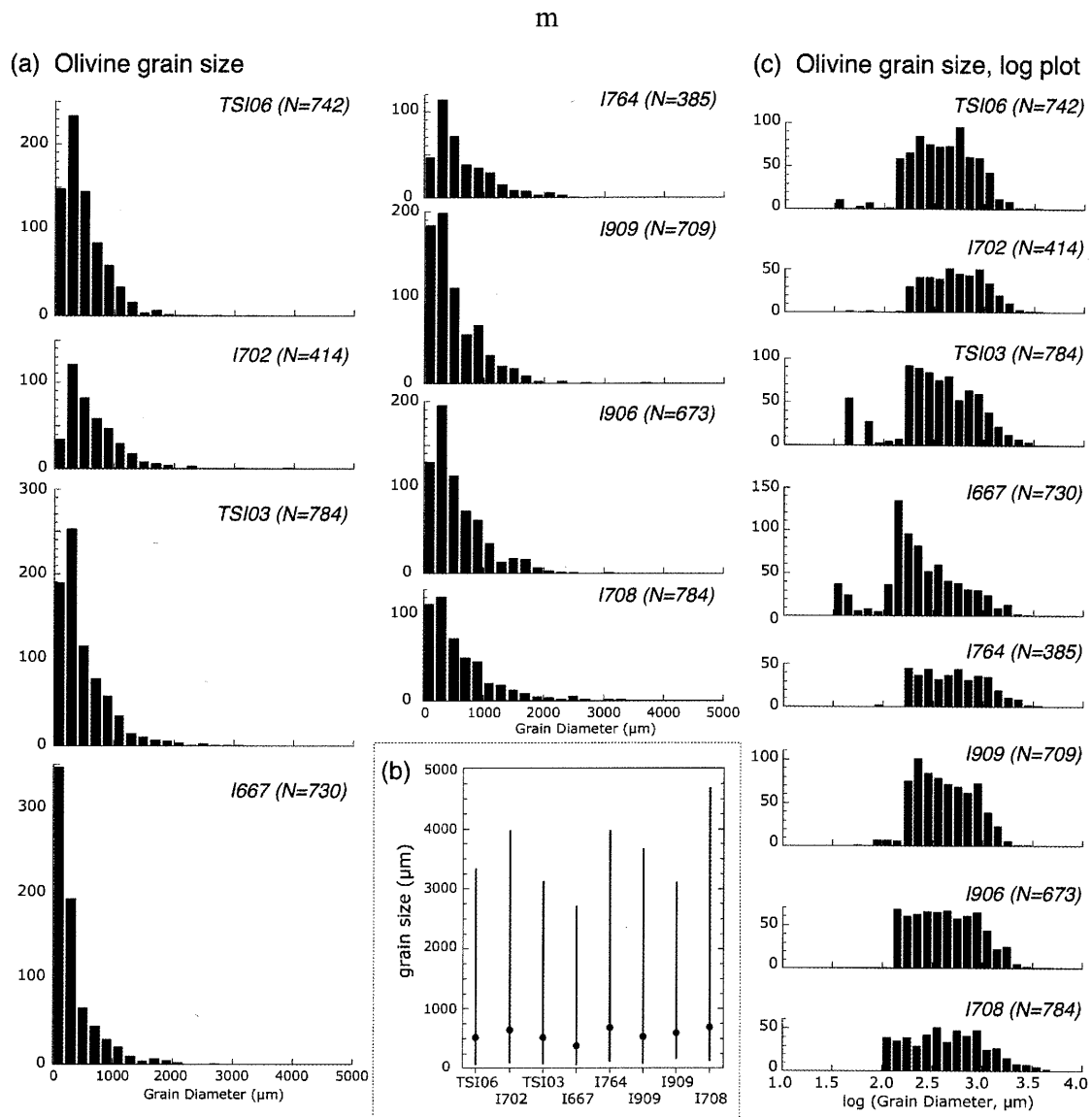
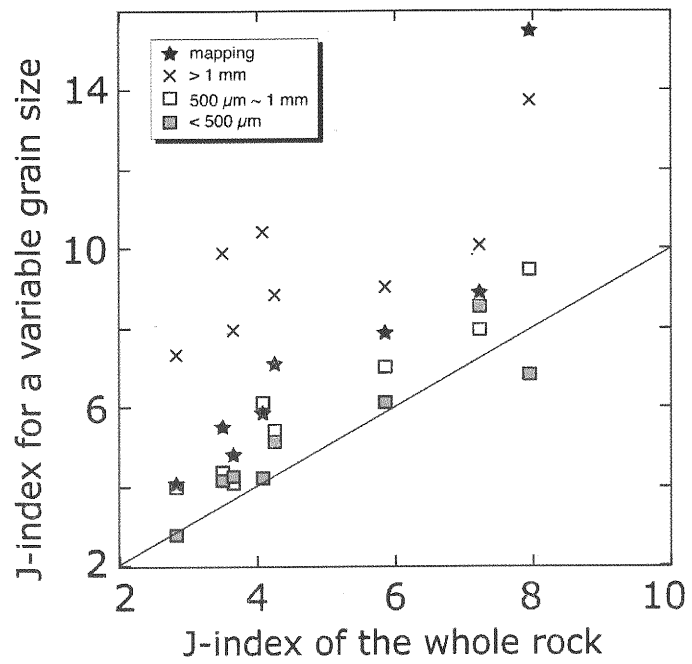


Figure 22. (a) Olivine grain size histogram for Ichinomegata peridotite xenoliths. Outlines of olivine grains were automatically traced by CHANNEL 5 software from crystallographic orientation map obtained by EBSD. We measured a total of 385 to 784 olivine grains per sample. (b) Range of grain size (diameter in μm) of olivine. Black circles show the average grain size. (c) Logarithmic grain-size distributions of olivine grains.



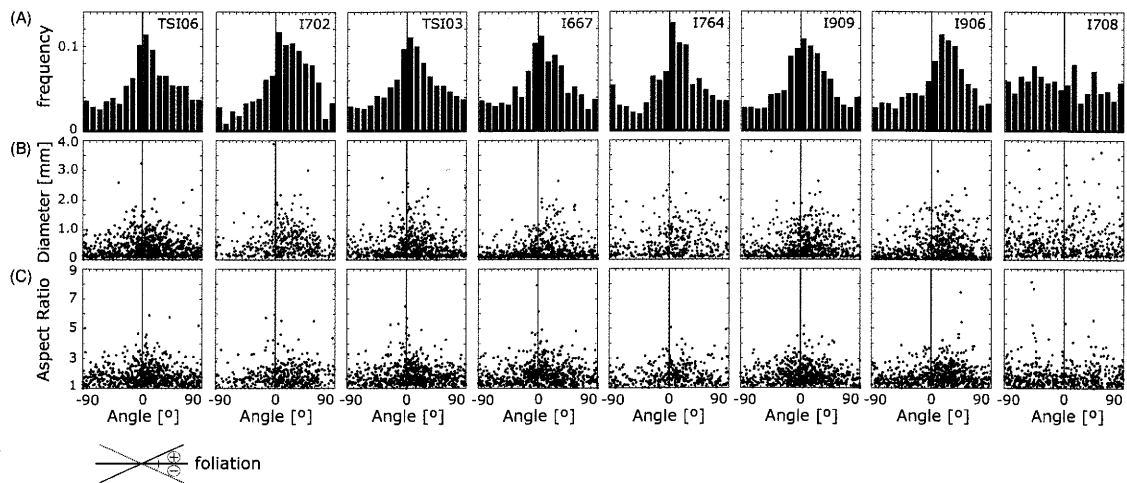


Figure 24. (a) Orientation distributions of olivine grains with respect to the main foliation (X). The angles between the shape-preferred orientation (SPO) and the main foliation are approximately $10 - 20^\circ$. (b) Relationship between orientation distribution of olivine grains with main foliation and grain size. (c) Relationship between orientation distribution of olivine grains with main foliation and aspect ratio.

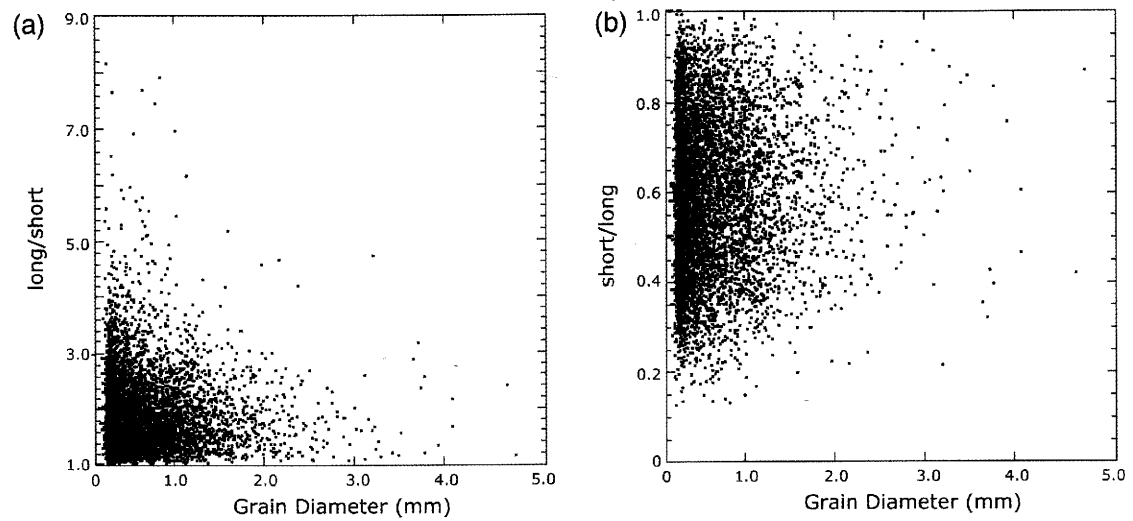


Figure 25. Relationship between olivine grain diameter and aspect ratio of long/short (a) and short/ long (b) of Ichinomegata peridotite xenoliths.

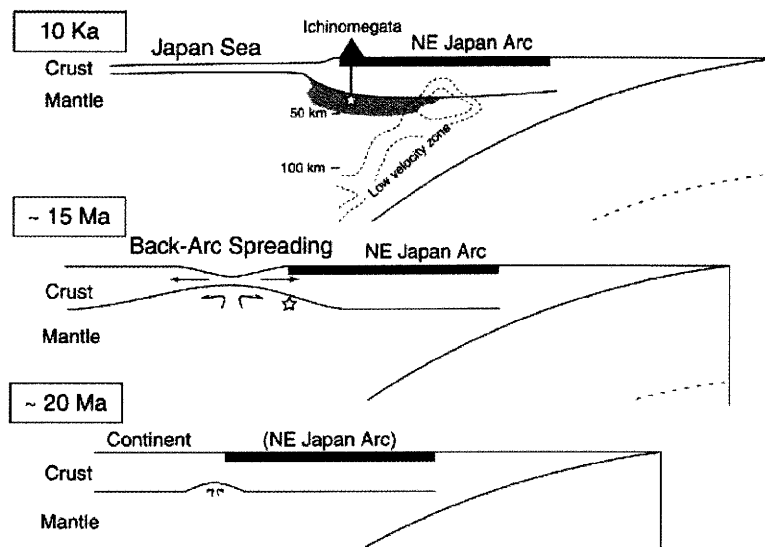


Figure 26. Schematic diagrams showing the tectonic evolution of the northeast Japan arc between ca 20 Ma and 10 Ka after Michibayashi et al. (2006). Star symbols indicate possible locations of the Ichinomegata peridotite xenoliths within the mantle. The shaded area in the vicinity of the star symbol at 10 Ka shows the possible thickness of the seismically anisotropic layer, from which the measured delay times of S-waves occurs.

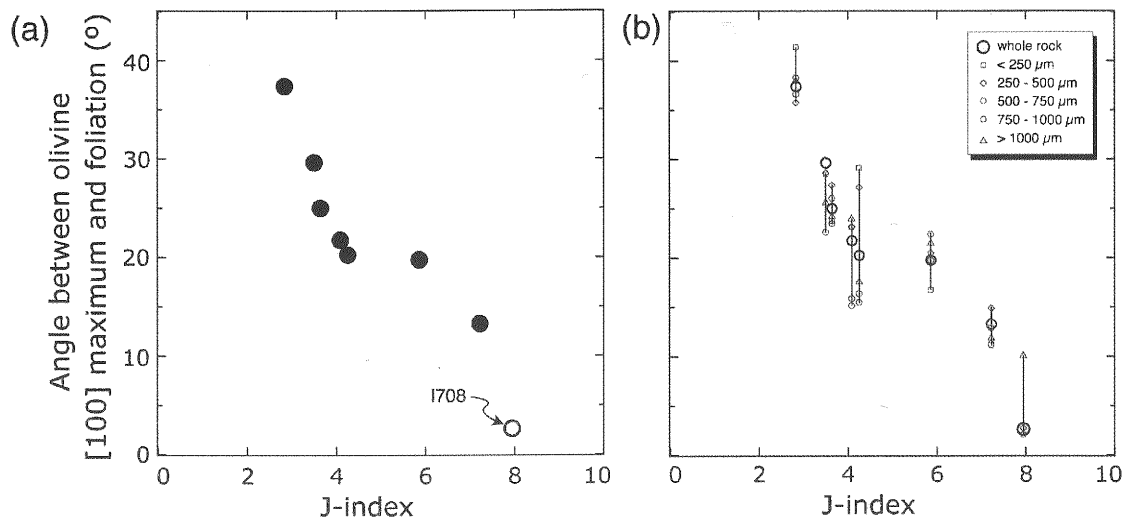


Figure 27. (a) Relationship between J-index and angle between olivine [100] maximum and foliation of Ichinomegata peridotite xenoliths. (b) Angle between olivine [100] maximum and foliation for various olivine grain size populations versus J-index of the whole rock. Gray circles, J-index calculated from whole rock data; triangles, coarse grains ($\phi > 1$ mm); circles, relatively coarse grains (ϕ between 1 and 0.75 mm); polygons, intermediate grains (ϕ between 0.50 and 0.75 mm); diamond shapes, relatively fine grains (ϕ between 0.25 and 0.50 mm); squares, fine grains ($\phi < 0.25$ mm).

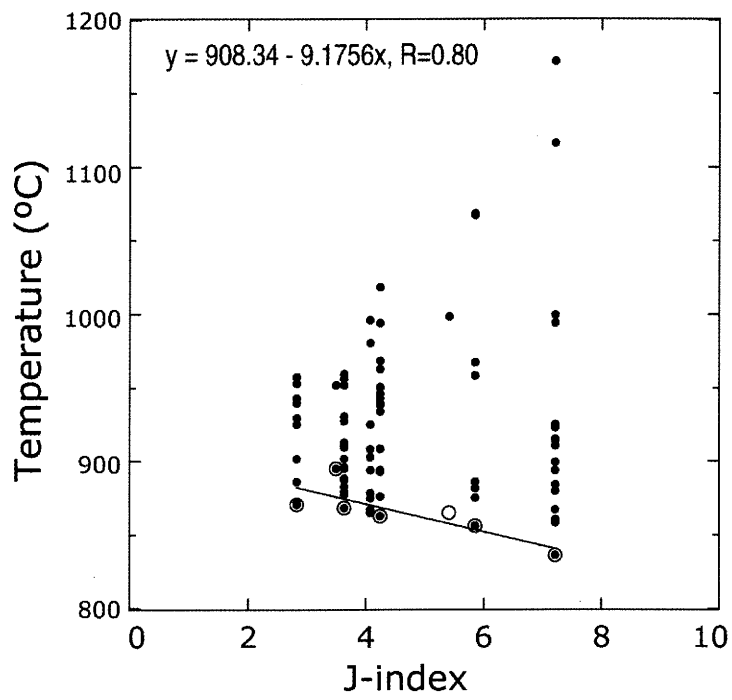


Figure 28. Relationships between J-index and temperature of Ichinomegata peridotite xenoliths.

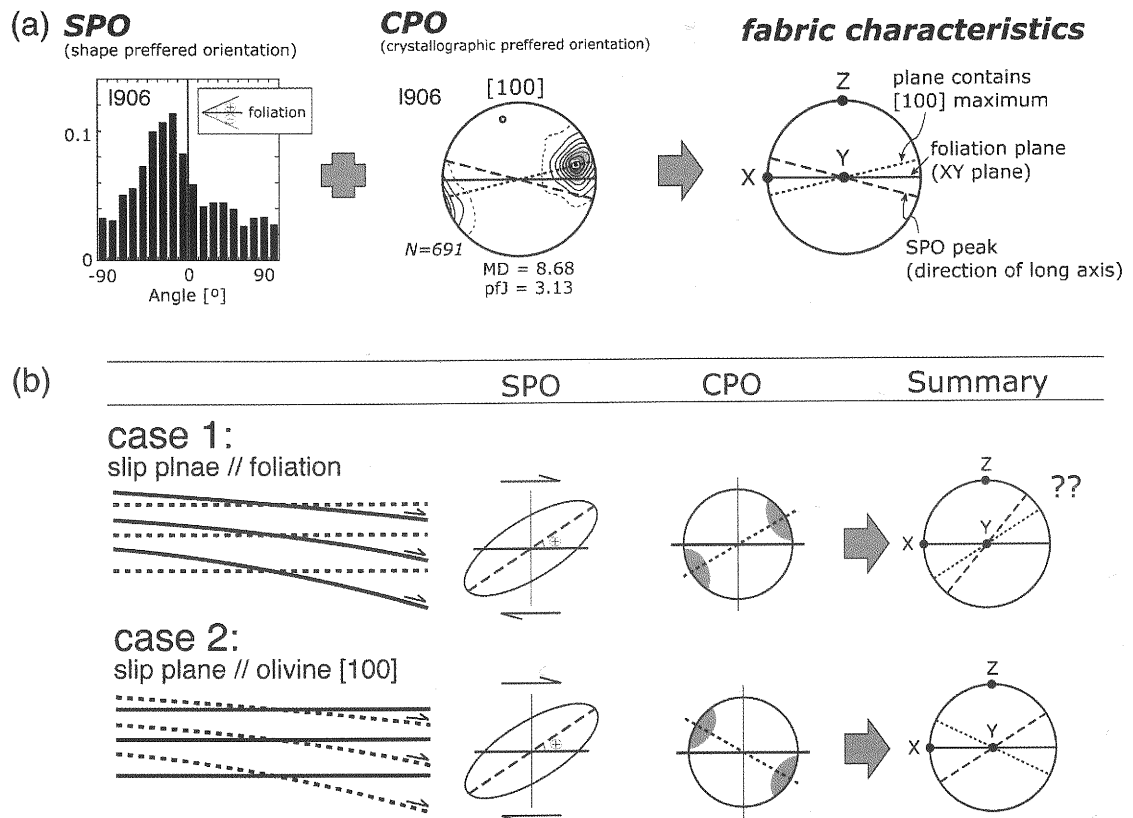


Figure 29. (a) Brief idea which show how to define fabric characteristics from SPO (shape preferred orientation) and CPO (crystallographic preferred orientation). (b) Schematic model for the estimation of shear sense of Ichinomegata peridotite xenoliths. Case 1: slip plane is defined by foliation; Case 2: slip plane is defined by olivine [100] axis.

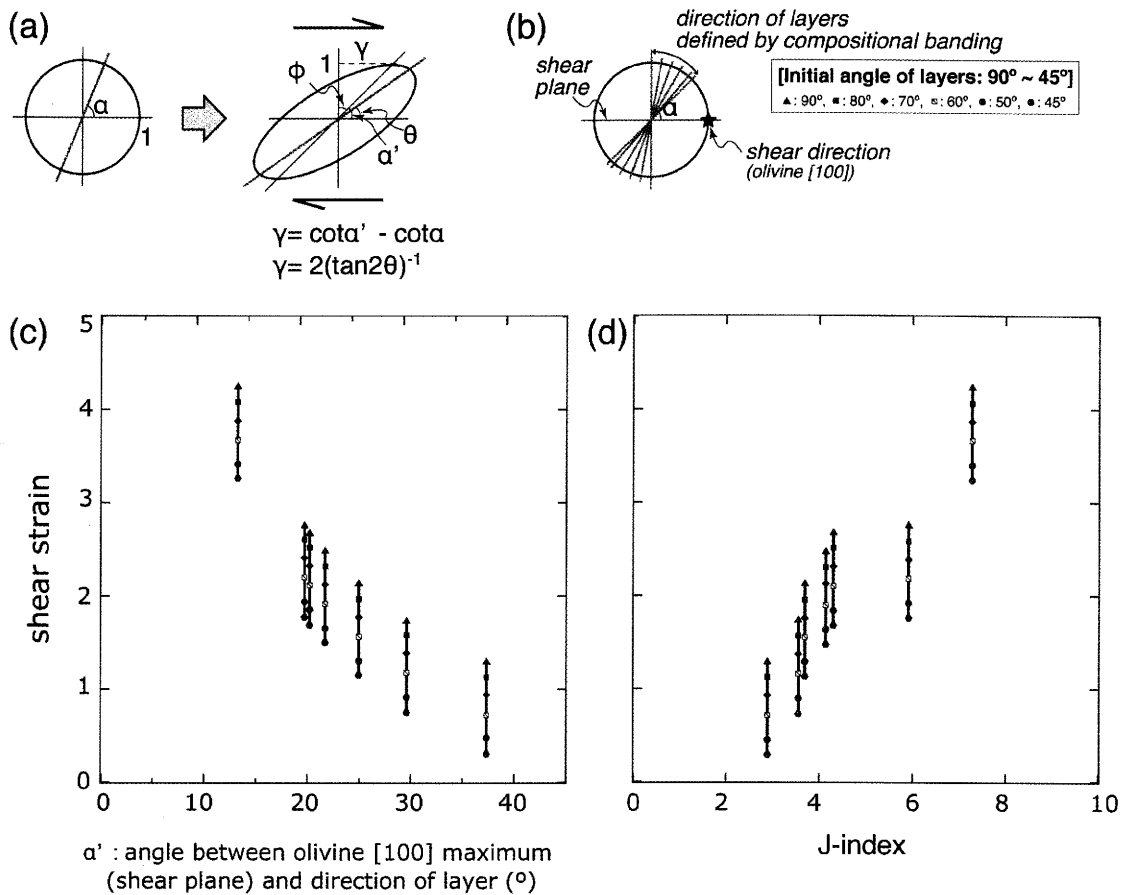


Figure 30. (a) The geometric relationship of shear strain, γ , to the orientation of a marker layer, which initially lies at an angle α to the shear plane and is deflected to a smaller angle, α' . The orientation of finite strain ellipsoid long axis is represented by the angle θ and is not coincident with the marker layer. Diagram adapted from Ramsay and Graham (1970). (b) Stereo net of the variation of layer (compositional banding) orientations with respect to the shear plane. (c) Calculated shear strain from equation shown in (a) with angle (α') from 45° to 90° . (d) Relationships between J-index and shear strain based on (c) results.

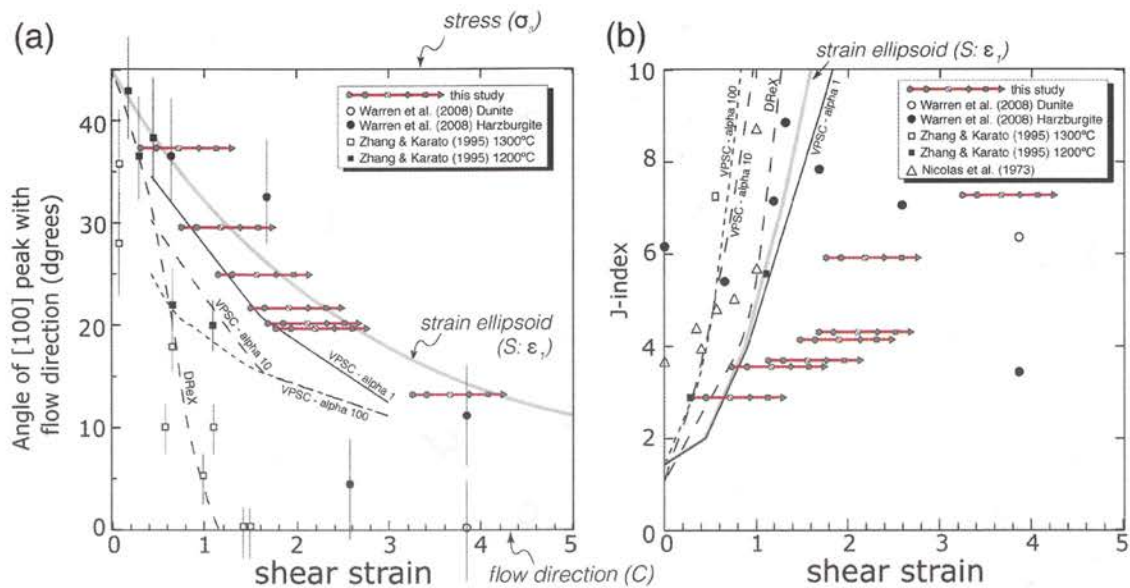


Figure 31. (a) Angle of the olivine [100] maximum to the shear plane as a function of shear strain in the Ichinomegata peridotite xenoliths (red bars), Josephine peridotites (Warren et al., 2008), experiments (Zhang and Karato, 1995), and models. The models and experiments initially have random fabrics, represented by an average angle of 45° to the shear direction. The simple model is finite strain ellipsoid and Shear, which follows the shear direction. VPSC is the best fit ($\alpha = 1, 10, 100$) of the viscoplastic self-consistent model (Tommasi et al., 2000) to the experiments. DRex is the best fit of the dynamic recrystallization model (Kaminski and Ribe, 2001) to the experiments. (b) Variation in the J-index as a function of shear strain. The results for the Ichinomegata peridotite xenoliths are shown as red bars. Also shown are Josephine peridotites (Warren et al., 2008), Nicolas et al. (1975) experiments, Zhang and Karato (1995) experiments (from the J-index calculation by Tommasi et al., 2000), the VPSC model and DRex model same in (a).

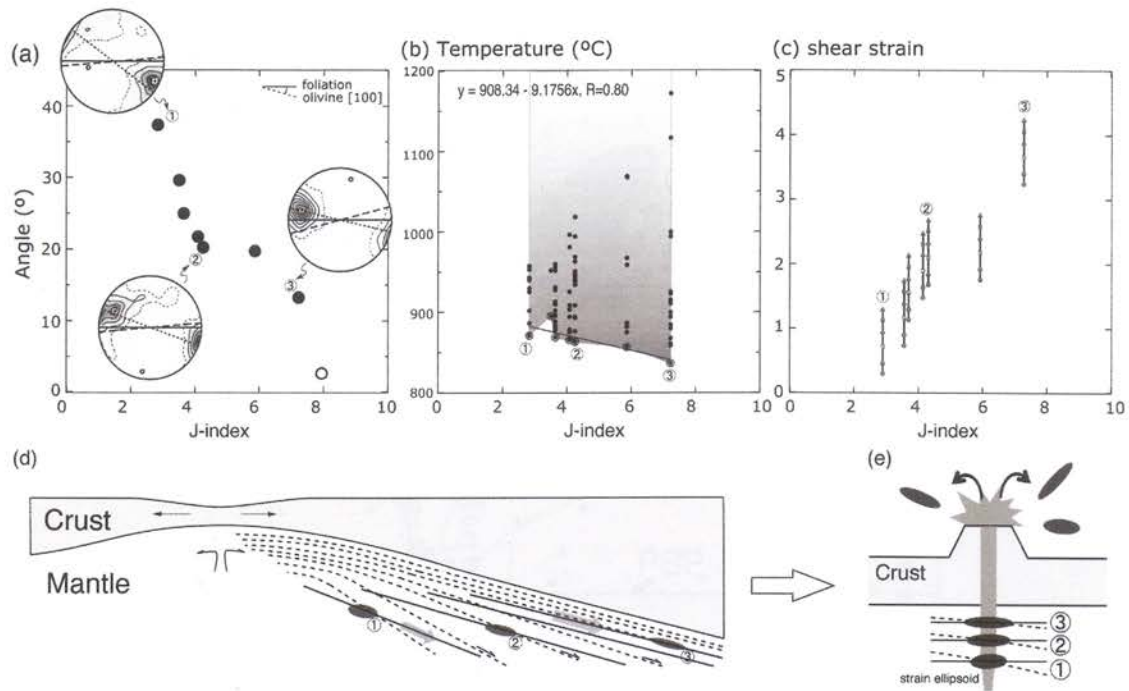


Figure 32. A schematic model of the mantle evolution beneath the Ichinomegata volcano. (a) ~ (c) show the summary of this study. (a) Angle between olivine [100] maximum and foliation decreases with increasing of J-index. (b) Minimum temperature is lower in the samples that have higher J-index. (c) Shear strain increases with increasing of J-index. (d) Mantle evolution during the back-arc spreading based on our observations. Peridotites in the uppermost mantle in the shallower part, where is assumed lower temperature, sheared higher than deeper part. At the present time, xenoliths which recorded frozen texture were erupted in the surface (e).

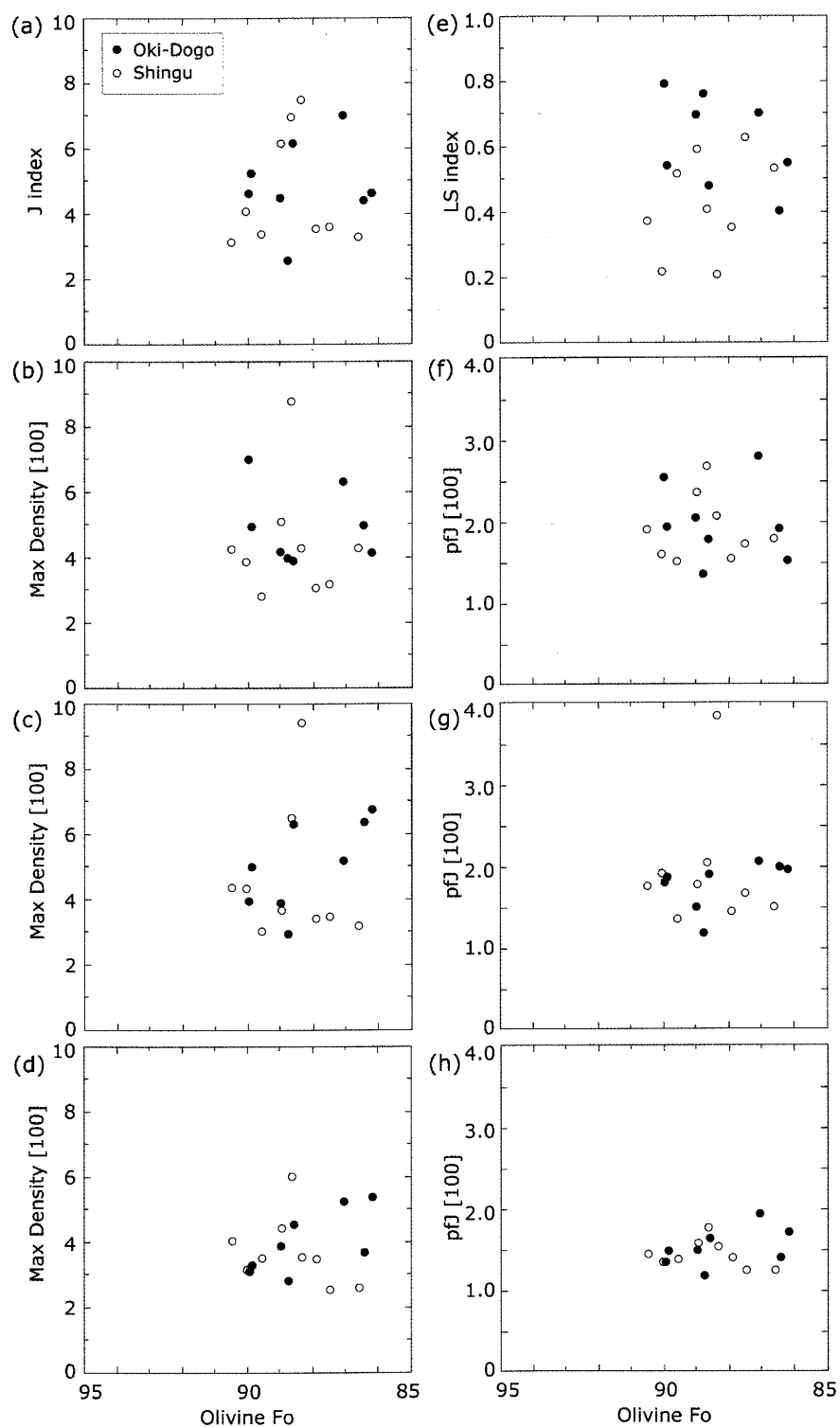


Figure 33. Evolution of olivine CPO as function of the Mg# of olivine. (a) CPO strength (J -index). (b)–(d) Maximum density of the distribution of the [100], [010], and [001] axes of olivine. (e) Ls-index. (f)–(h) pfJ-index of the [100], [010], and [001] axes of olivine.

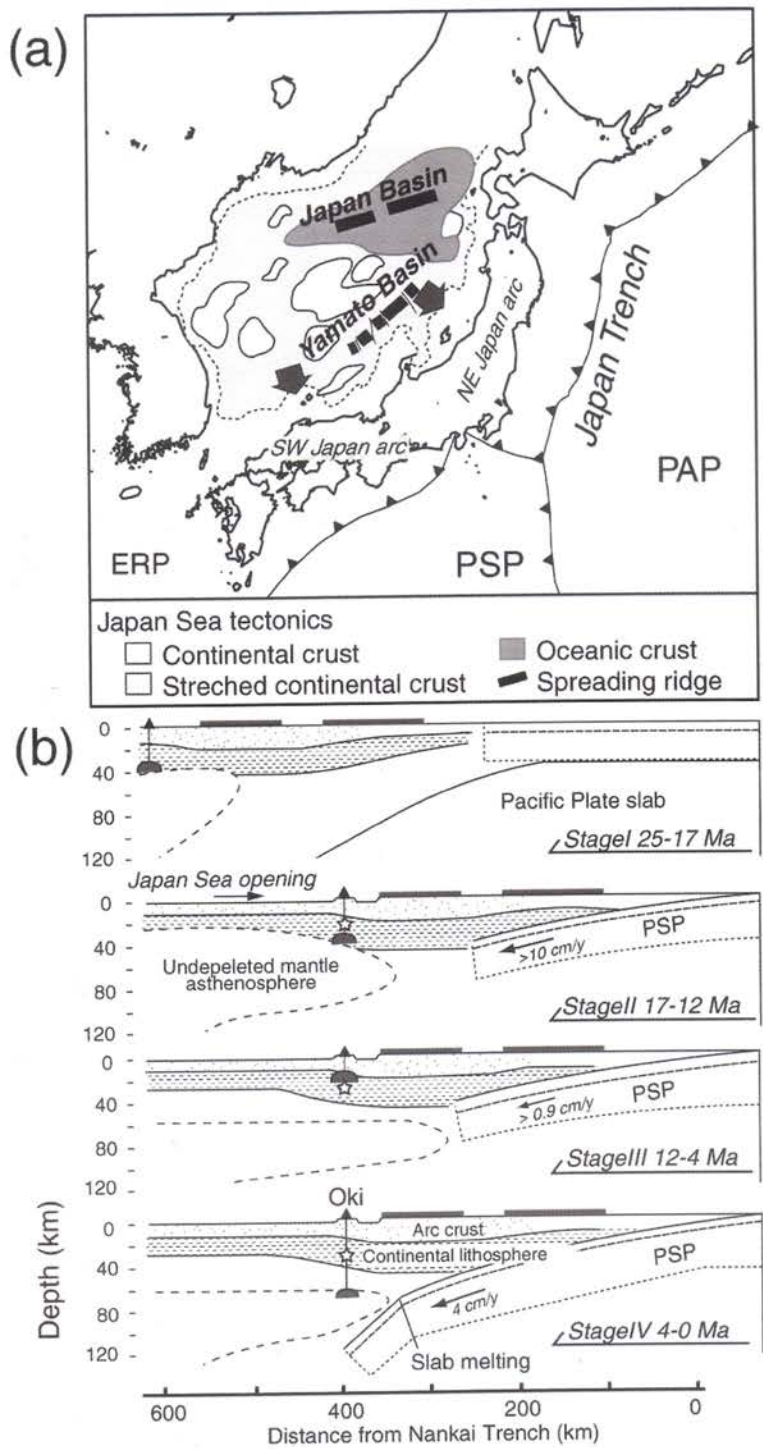


Figure 34. (a) Schematic model of the opening of the Japan Sea. (b) Development of the uppermost mantle beneath southwest (SW) Japan, based on petrological analyses of volcanic rocks. Star symbols indicate the possible location of the Oki-Dogo peridotite xenoliths within the mantle. Modified after Kimura et al. (2005). PSP: Philippine Sea Plate; PAP: Pacific Plate; ERP: Eurasia Plate.

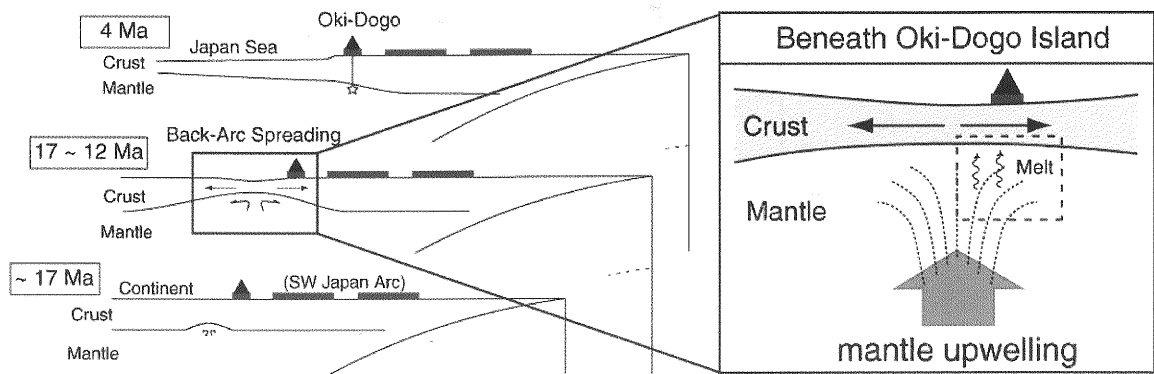


Figure 35. Schematic diagrams showing the tectonic evolution of the southwest Japan arc between ca. 17 and 4 Ma. The enlargement shows the evolution of the uppermost mantle during the period of back-arc spreading beneath the Japan Islands and Oki-Dogo Island. The dotted rectangle indicates the range of the uppermost mantle sampled as peridotite xenoliths in this study.

Table 1. Results of electron probe analyses of olivine and spinel within peridotite xenoliths from Ichinomegata.

	Sample number											
	I667	I702	I738	I764	I776	I777	I892	I906	I909	TSI03	TSI06	TSI07
<i>Olivine</i>												
SiO ₂	40.08	39.93	40.03	39.98	39.71	39.92	39.31	40.24	39.59	40.16	39.96	39.75
TiO ₂	0.00	0.00	0.04	0.00	0.00	0.00	0.00	0.01	0.06	0.00	0.01	0.04
Al ₂ O ₃	0.04	0.02	0.00	0.05	0.03	0.00	0.03	0.01	0.00	0.00	0.02	0.04
FeO ^a	10.12	10.11	11.32	9.85	9.99	9.85	9.93	9.12	10.30	10.16	10.34	10.10
MnO	0.04	0.08	0.08	0.12	0.06	0.06	0.20	0.11	0.04	0.14	0.08	0.10
MgO	50.52	50.16	49.71	50.04	50.30	49.34	49.82	50.13	49.97	49.79	50.53	50.20
CaO	0.10	0.07	0.03	0.08	0.07	0.11	0.03	0.01	0.04	0.07	0.08	0.10
Na ₂ O	0.00	0.01	0.00	0.00	0.00	0.00	0.00	0.00	0.00	0.00	0.00	0.00
K ₂ O	0.00	0.00	0.00	0.01	0.00	0.00	0.01	0.00	0.01	0.00	0.00	0.02
Cr ₂ O ₃	0.00	0.00	0.04	0.00	0.07	0.03	0.00	0.00	0.00	0.00	0.00	0.07
NiO	0.00	0.00	0.00	0.00	0.00	0.00	0.00	0.01	0.00	0.00	0.00	0.00
V ₂ O ₃	0.00	0.00	0.00	0.00	0.00	0.00	0.00	0.42	0.00	0.00	0.00	0.00
Total	100.90	100.39	101.26	100.11	100.21	99.32	99.33	100.06	100.01	100.34	101.02	100.41
Mg# ^b	0.90	0.90	0.89	0.90	0.90	0.90	0.90	0.91	0.90	0.90	0.90	0.90
<i>Spinel</i>												
SiO ₂	0.03	0.00	0.01	0.05	0.00	0.01	0.06	0.07	0.03	0.00	0.06	0.01
TiO ₂	0.15	0.10	0.06	0.03	0.00	0.04	0.09	0.04	0.22	0.18	0.08	0.09
Al ₂ O ₃	47.57	47.12	53.99	47.63	49.69	48.87	49.51	47.28	43.70	48.29	52.67	49.77
Fe ₂ O ₃	5.39	3.52	4.81	3.66	2.18	3.91	3.50	3.21	4.27	4.70	2.95	2.44
FeO	10.30	9.56	10.98	9.88	9.60	10.41	9.95	10.21	11.92	10.32	8.87	9.45
FeO ^a	15.16	12.73	15.31	13.18	11.56	13.93	13.09	13.10	15.76	14.55	11.53	11.64
MnO	0.03	0.10	0.07	0.20	0.02	0.00	0.15	0.18	0.09	0.05	0.05	0.11
MgO	19.20	19.15	19.43	18.89	19.46	19.10	19.38	18.76	17.66	19.11	20.42	19.55
CaO	0.00	0.01	0.00	0.01	0.02	0.00	0.01	0.01	0.00	0.00	0.02	0.00
Na ₂ O	0.00	0.00	0.00	0.00	0.00	0.00	0.00	0.00	0.04	0.02	0.00	0.00
K ₂ O	0.02	0.00	0.00	0.02	0.00	0.00	0.01	0.00	0.00	0.00	0.00	0.01
Cr ₂ O ₃	18.10	19.00	11.51	18.07	17.65	17.44	17.19	19.66	22.76	17.48	14.48	17.38
NiO	0.00	0.00	0.00	0.00	0.00	0.00	0.00	0.32	0.00	0.00	0.00	0.00
V ₂ O ₃	0.00	0.00	0.00	0.00	0.00	0.00	0.00	0.08	0.00	0.00	0.00	0.00
Total	100.80	98.56	100.86	98.43	98.61	99.78	99.84	99.82	100.68	100.14	99.60	98.79
Mg# ^b	0.77	0.78	0.76	0.77	0.78	0.77	0.78	0.72	0.73	0.77	0.80	0.79
Cr# ^c	0.20	0.21	0.13	0.20	0.19	0.19	0.19	0.22	0.26	0.20	0.16	0.19

^atotal Fe; ^bMg/(Mg+Fe²⁺) atomic ratio for silicate; ^cCr/(Cr+Al) atomic ratio; ^dtotal trivalent cation (Al+Cr+Fe³⁺).

Table 2. Results of electron probe analyses of orthopyroxene and clinopyroxene within peridotite xenoliths from Ichinomegata.

	Sample number											
	1667	1702	1738	1764	1776	1777	1892	1906	1909	TSI03	TSI06	TSI07
Orthopyroxene												
SiO ₂	53.88	54.43	54.78	53.77	53.24	53.76	53.69	54.68	54.46	54.06	54.40	53.83
TiO ₂	0.15	0.12	0.01	0.12	0.12	0.16	0.08	0.12	0.17	0.22	0.14	0.07
Al ₂ O ₃	3.99	3.82	3.64	3.40	3.68	4.19	3.64	3.61	3.84	3.93	3.99	3.87
FeO ^a	6.98	6.66	7.27	6.25	6.33	7.16	6.42	6.75	7.01	6.92	6.46	6.76
MnO	0.17	0.11	0.20	0.19	0.23	0.14	0.10	0.23	0.06	0.10	0.00	0.13
MgO	34.12	33.58	33.38	34.20	34.29	33.19	33.76	33.75	34.16	34.10	34.18	33.86
CaO	0.60	0.73	0.65	0.64	0.57	0.60	0.59	0.45	0.64	0.62	0.58	0.48
Na ₂ O	0.00	0.02	0.00	0.00	0.02	0.00	0.03	0.01	0.02	0.03	0.05	0.01
K ₂ O	0.03	0.00	0.00	0.00	0.02	0.01	0.00	0.00	0.01	0.02	0.01	0.02
Cr ₂ O ₃	0.59	0.66	0.42	0.45	0.39	0.61	0.53	0.04	0.61	0.69	0.34	0.63
NiO	0.00	0.00	0.00	0.00	0.00	0.00	0.00	0.41	0.00	0.00	0.00	0.00
V ₂ O ₃	0.00	0.00	0.00	0.00	0.00	0.00	0.00	0.08	0.00	0.00	0.00	0.00
Total	100.50	100.13	100.35	99.02	98.89	99.81	98.84	100.13	100.98	100.70	100.15	99.64
Mg ^{#b}	0.90	0.90	0.89	0.91	0.91	0.89	0.90	0.90	0.90	0.90	0.90	0.90
Clinopyroxene												
SiO ₂	50.49	50.96	51.02	51.07	51.32	53.76	50.88	51.09	50.92	50.49	50.75	50.57
TiO ₂	0.31	0.54	0.47	0.42	0.44	0.16	0.45	0.43	0.48	0.54	0.54	0.26
Al ₂ O ₃	6.38	5.06	4.86	4.37	4.52	4.19	4.85	5.12	4.63	5.12	5.42	4.39
FeO ^a	3.71	2.51	3.05	2.64	2.37	7.16	2.24	2.34	2.74	3.08	2.71	2.79
MnO	0.14	0.00	0.06	0.09	0.05	0.14	0.04	0.13	0.09	0.05	0.05	0.00
MgO	17.40	16.83	16.24	16.80	16.44	33.19	16.13	15.44	16.36	16.31	16.58	16.71
CaO	21.09	22.56	23.13	22.83	23.65	0.60	23.07	22.82	23.41	23.14	22.37	23.36
Na ₂ O	0.49	0.63	0.38	0.35	0.57	0.00	0.59	0.72	0.30	0.42	0.84	0.25
K ₂ O	0.00	0.00	0.02	0.00	0.03	0.01	0.00	0.00	0.02	0.01	0.00	0.01
Cr ₂ O ₃	0.77	1.09	0.95	0.81	0.99	0.61	0.95	0.07	1.07	1.17	1.21	0.68
NiO	0.00	0.00	0.00	0.00	0.00	0.00	0.00	1.07	0.00	0.00	0.00	0.00
V ₂ O ₃	0.00	0.00	0.00	0.00	0.00	0.00	0.00	0.06	0.00	0.00	0.00	0.00
Total	100.78	100.19	100.17	99.38	100.39	99.81	99.19	99.28	100.02	100.33	100.48	99.01
Mg ^{#b}	0.89	0.92	0.90	0.92	0.93	0.89	0.93	0.92	0.91	0.90	0.92	0.91

^atotal Fe; ^bMg/(Mg+Fe²⁺) atomic ratio for silicate.

Table 3. Results of electron probe analyses of olivine and spinel within peridotite xenoliths from Olki-Dogo.

	Sample number																
	OKD 33	OKD 69	KRB 15	OKD 57	OKD 45-2	KRB 12	OKD 28	OKD 04	OKD 39	OKD0 2-2	OKD 02-1	OKD 37	OKD 07	OKD0 2-3	OKD 64	OKD 13	OKD 45-1
<i>Olivine</i>																	
SiO ₂	40.19	39.64	39.26	39.85	39.95	40.15	40.06	39.63	39.30	39.68	39.71	39.25	40.70	39.98	39.45	40.18	40.16
TiO ₂	0.00	0.01	0.03	0.00	0.00	0.00	0.01	0.00	0.00	0.00	0.03	0.03	0.01	0.00	0.00	0.00	0.01
Al ₂ O ₃	0.02	0.03	0.04	0.03	0.04	0.01	0.03	0.03	0.05	0.04	0.02	0.03	0.03	0.03	0.04	0.02	0.03
FeO ^a	9.31	13.11	13.31	10.75	10.04	10.99	10.71	10.83	11.03	10.32	11.89	11.40	10.88	12.01	12.38	9.83	11.57
MnO	0.14	0.22	0.15	0.19	0.17	0.14	0.14	0.11	0.12	0.12	0.18	0.14	0.13	0.24	0.20	0.15	0.11
MgO	48.91	45.93	47.66	49.82	50.03	49.86	48.86	49.09	48.12	48.70	48.07	48.11	48.25	49.24	46.84	49.69	47.77
CaO	0.09	0.14	0.13	0.11	0.10	0.09	0.10	0.12	0.10	0.10	0.13	0.13	0.09	0.10	0.11	0.11	0.11
Na ₂ O	0.01	0.02	0.00	0.00	0.02	0.01	0.02	0.00	0.00	0.01	0.01	0.02	0.00	0.00	0.00	0.01	0.00
K ₂ O	0.00	0.00	0.01	0.00	0.00	0.00	0.00	0.00	0.01	0.01	0.00	0.01	0.00	0.00	0.00	0.00	0.01
Cr ₂ O ₃	0.07	0.06	0.09	0.02	0.00	0.02	0.03	0.03	0.03	0.03	0.01	0.02	0.00	0.03	0.03	0.05	0.02
NiO	0.36	0.30	0.33	0.33	0.38	0.39	0.41	0.33	0.39	0.33	0.35	0.33	0.39	0.32	0.32	0.40	0.34
V ₂ O ₃	0.01	0.00	0.00	0.00	0.00	0.00	0.00	0.00	0.00	0.03	0.01	0.00	0.01	0.02	0.01	0.01	0.00
Total	99.10	99.44	100.99	101.10	100.72	101.66	100.35	100.17	99.14	99.36	100.40	99.46	100.49	101.97	99.40	100.44	100.1
Mg# ^b	0.90	0.86	0.86	0.90	0.90	0.89	0.89	0.89	0.89	0.89	0.88	0.88	0.89	0.88	0.87	0.90	0.88
<i>Spinel</i>																	
SiO ₂	0.07	0.26	0.13	0.11	0.08	0.08	0.19	0.10	0.40	0.12	0.17	0.07	0.35	0.09	0.09	0.12	0.10
TiO ₂	0.02	1.37	0.29	0.13	0.26	0.35	0.12	0.13	0.61	0.10	0.19	0.73	0.09	0.26	0.37	0.22	0.43
Al ₂ O ₃	34.84	38.16	45.17	48.41	49.58	30.42	49.49	46.30	39.57	50.64	39.96	49.03	49.11	49.01	48.99	45.47	41.24
FeO ^a	17.32	19.38	17.16	13.55	13.35	16.67	12.92	14.90	15.93	12.68	16.39	14.74	13.54	14.85	15.99	15.15	15.99
MnO	0.17	0.14	0.17	0.08	0.07	0.16	0.10	0.10	0.09	0.12	0.18	0.09	0.11	0.08	0.10	0.22	0.15
MgO	14.62	15.54	17.31	18.65	19.54	15.74	19.44	18.60	16.97	19.79	16.96	18.87	18.96	18.56	18.79	18.00	16.80
CaO	0.01	0.01	0.00	0.01	0.01	0.00	0.00	0.01	0.01	0.01	0.00	0.00	0.01	0.01	0.01	0.01	0.01
Na ₂ O	0.00	0.00	0.00	0.00	0.00	0.02	0.00	0.01	0.00	0.00	0.01	0.01	0.00	0.01	0.00	0.01	0.00
K ₂ O	0.01	0.00	0.00	0.00	0.00	0.00	0.01	0.00	0.00	0.00	0.00	0.01	0.00	0.00	0.01	0.00	0.00
Cr ₂ O ₃	30.89	23.75	18.67	18.42	18.15	36.81	17.12	19.35	25.76	15.50	25.95	15.73	17.89	16.95	16.47	21.19	25.27
NiO	0.23	0.24	0.27	0.36	0.28	0.18	0.37	0.33	0.23	0.37	0.26	0.33	0.33	0.28	0.33	0.29	0.29
V ₂ O ₃	0.11	0.10	0.08	0.12	0.10	0.13	0.10	0.12	0.14	0.10	0.13	0.13	0.10	0.09	0.09	0.10	0.13
Total	98.63	99.57	99.81	99.82	101.77	101.01	100.21	100.43	100.14	99.82	100.67	100.20	100.82	100.60	101.78	101.18	100.7
Mg# ^b	0.65	58.85	0.72	0.76	0.77	0.69	0.78	0.76	0.72	0.79	0.71	0.76	0.76	0.75	0.75	0.74	0.70
Cr ^{III} ^c	0.37	0.29	0.22	0.20	0.20	0.45	0.19	0.22	0.30	0.17	0.30	0.18	0.20	0.19	0.18	0.24	0.29
Fe ²⁺ /Y ^d	0.04	0.07	0.06	0.03	0.04	0.05	0.04	0.05	0.05	0.04	0.05	0.05	0.03	0.04	0.05	0.04	0.04

^atotal Fe; ^bMg/(Mg+Fe²⁺) atomic ratio for silicate; ^cCr/(Cr+Al) atomic ratio; ^dtotal trivalent cation (Al+Cr+Fe³⁺).

Table 4. Results of electron probe analyses of orthopyroxene and clinopyroxene within peridotite xenoliths from Olki-Dogo.

	Sample number														
	OKD 33	KRB 15	OKD 57	OKD 45-2	KRB 12	OKD 28	OKD 04	OKD 02-2	OKD 02-1	OKD 37	OKD 07	OKD 02-3	OKD 64	OKD 13	OKD 45-1
<i>Orthopyroxene</i>															
SiO ₂	55.85	53.44	54.05	54.33	55.63	54.29	54.29	54.44	53.35	52.74	54.54	53.87	53.17		
TiO ₂	0.02	0.14	0.05	0.16	0.08	0.06	0.11	0.03	0.09	0.29	0.05	0.12	0.11		
Al ₂ O ₃	3.18	4.52	4.44	4.62	2.81	4.56	4.39	4.49	4.18	4.94	4.52	4.72	4.55		
FeO ^a	6.17	8.30	6.51	6.42	6.58	6.62	7.06	6.73	7.87	9.31	6.93	7.47	7.90		
MnO	0.14	0.13	0.13	0.12	0.09	0.14	0.18	0.15	0.14	0.16	0.16	0.18	0.18		
MgO	32.77	30.72	32.07	32.70	33.70	32.50	32.02	32.61	31.42	30.97	31.71	31.97	31.76		
CaO	1.01	1.29	1.13	1.14	1.11	1.15	1.15	1.12	1.28	1.26	1.13	1.14	1.30		
Na ₂ O	0.07	0.08	0.05	0.08	0.05	0.05	0.08	0.06	0.07	0.11	0.06	0.05	0.09		
K ₂ O	0.00	0.00	0.01	0.01	0.01	0.00	0.00	0.01	0.00	0.00	0.01	0.00	0.00		
Cr ₂ O ₃	0.75	0.59	0.65	0.59	0.75	0.55	0.57	0.51	0.68	0.44	0.62	0.53	0.56		
NiO	0.12	0.09	0.15	0.12	0.12	0.07	0.08	0.13	0.09	0.05	0.13	0.07	0.13		
V ₂ O ₅	0.01	0.03	0.02	0.05	0.01	0.02	0.01	0.00	0.02	0.01	0.04	0.01	0.04		
Total	100.08	99.33	99.25	100.33	100.93	100.01	99.95	100.28	99.19	100.27	99.89	100.13	99.78		
Mg ^{#b}	0.90	0.87	0.90	0.90	0.90	0.90	0.89	0.90	0.88	0.86	0.89	0.88	0.88		
<i>Clinopyroxene</i>															
SiO ₂	52.51	51.13	51.93	51.59	52.74	51.71	52.14	50.38	52.00	50.91	52.54	52.26	52.06	51.09	51.59
TiO ₂	0.07	0.37	0.19	0.48	0.24	0.44	0.28	1.08	0.16	1.00	0.14	0.34	0.28	0.29	0.51
Al ₂ O ₃	3.75	5.87	5.34	5.57	3.61	5.75	5.52	6.06	4.67	6.18	5.13	5.78	5.81	4.73	5.10
FeO ^a	2.94	4.31	3.35	3.43	2.93	3.39	3.69	3.48	3.81	3.67	3.47	4.05	4.10	3.21	3.72
MnO	0.08	0.10	0.11	0.12	0.09	0.13	0.12	0.09	0.13	0.09	0.12	0.10	0.06	0.15	0.12
MgO	17.04	16.24	16.85	16.45	17.65	16.63	16.56	16.84	16.72	-16.06	16.41	16.65	16.31	17.07	16.53
CaO	21.55	19.78	21.03	20.96	20.77	20.55	20.74	20.83	20.85	19.79	20.96	20.16	20.52	21.27	19.90
Na ₂ O	0.69	1.04	0.56	0.81	0.78	0.77	0.90	0.43	0.71	1.09	0.57	0.79	0.95	0.56	1.02
K ₂ O	0.00	0.02	0.00	0.00	0.00	0.00	0.00	0.00	0.01	0.00	0.00	0.00	0.00	0.01	0.01
Cr ₂ O ₃	1.13	0.07	0.84	0.87	1.16	0.84	0.88	0.81	0.05	1.19	0.80	0.88	0.86	1.06	1.24
NiO	0.08	0.02	0.07	0.05	0.09	0.07	0.07	0.11	0.04	0.00	0.06	0.08	0.04	0.07	0.06
V ₂ O ₅	0.02	1.08	0.00	0.02	0.04	0.00	0.23	0.03	1.06	0.02	0.03	0.04	0.06	0.02	0.02
Total	99.87	100.01	100.28	100.36	100.11	100.28	100.92	100.13	100.20	100.01	100.25	101.12	101.06	99.51	99.82
Mg ^{#b}	0.91	0.87	0.90	0.90	0.91	0.90	0.89	0.90	0.89	0.89	0.89	0.88	0.88	0.90	0.89

^atotal Fe; ^bMg/(Mg+Fe²⁺) atomic ratio for silicate.

Table 5. Calculated equilibrium temperatures (°C) of peridotite xenoliths from Ichinomegata volcano.

Geothermometer	Brey&Köhler (1990) Ca in opx
Pressure (GPa)	1.0
Sample number	
I667	911
I702	954
I708	883
I738	927
I764	927
I777	913
I892	910
I906	942
I909	925
TSI03	918
TSI06	904
TSI07	867

Table 6. Calculated equilibrium temperatures (°C) of peridotite xenoliths from Oki-Dogo.

Geothermometer	N&T ^a	B&K ^b	B&K ^b
Pressure (GPa)	cpx	2px ^c	opx
	0.8	0.8	0.8
Sample number			
OKD33	1044	1040	1021
OKD69	-	-	-
KRB15	1117	1109	1091
OKD57	1096	1089	1054
KRB12	1101	1096	1051
OKD45-2	1070	1083	1043
OKD28	1105	1109	1056
OKD04	1095	1094	1057
OKD02-2	1080	1100	-
OKD37	1101	1096	1048
OKD39	-	-	1089
OKD07	1102	1088	1083
OKD64	1099	1094	1050
OKD02-3	1134	1127	1053
OKD02-1	1088	1072	1092
OKD13	1074	1070	1046
OKD45-1	1113	-	-

^aNims and Taylor (2000); ^bBrey and Köhler (1990).

Table 7. Trace element concentrations in olivine and orthopyroxene mineral separates in samples of Ichinomegata peridotite xenoliths.

Sample	I702	I764	I776	I892	I906	I909	TSI03	TSI06	TSI07
<i>Clinopyroxene</i>									
Ti	3011.135	2447.637	2749.193	2833.410	3288.353	3118.050	3104.857	3083.603	2365.198
Rb	0.004	0.005	0.007	0.011	0.006	0.019	0.006	0.005	0.003
Sr	2.183	2.423	0.836	0.812	1.354	2.861	3.261	3.876	2.462
Y	19.968	15.410	20.210	19.970	23.127	17.643	20.147	21.693	12.538
Zr	11.418	8.077	8.183	6.855	13.040	11.493	10.680	8.993	5.792
Nb	0.017	0.011	0.014	0.012	0.014	0.010	0.011	0.014	0.010
Ba						0.022		0.028	0.006
La	0.104	0.028	0.023	0.008	0.041	0.087	0.254	0.258	0.073
Ce	0.679	0.416	0.286	0.208	0.580	0.883	0.797	0.415	0.199
Pr	0.241	0.168	0.152	0.126	0.255	0.297	0.229	0.198	0.084
Nd	2.169	1.560	1.638	1.442	2.488	2.449	2.033	2.104	0.973
Sm	1.370	0.991	1.222	1.178	1.596	1.314	1.344	1.470	0.783
Eu	0.528	0.406	0.490	0.456	0.603	0.504	0.513	0.554	0.289
Gd	2.482	1.828	2.391	2.328	2.941	2.234	2.505	2.730	1.574
Tb	0.495	0.371	0.488	0.494	0.582	0.438	0.508	0.554	0.324
Dy	3.660	2.767	3.627	3.655	4.287	3.220	3.743	4.050	2.400
Ho	0.808	0.618	0.811	0.832	0.938	0.706	0.841	0.900	0.537
Er	2.247	1.759	2.280	2.351	2.599	1.971	2.326	2.472	1.489
Tm	0.328	0.261	0.329	0.346	0.372	0.287	0.342	0.368	0.215
Yb	2.063	1.678	2.061	2.149	2.305	1.830	2.124	2.264	1.320
Lu	0.288	0.241	0.290	0.311	0.321	0.258	0.303	0.322	0.185
Hf	0.776	0.529	0.572	0.539	0.740	0.578	0.715	0.632	0.494
Ta	0.001		0.001	0.000	0.001	0.000	0.001	0.000	
Pb	0.075	0.145	0.025	0.045	0.060	0.088	0.038	0.188	0.037
Th	0.022	0.001	0.003	0.044	0.008	0.002	0.042	0.829	0.010
U	0.008	0.001	0.001	0.020	0.003	0.001	0.012	0.239	
<i>Orthopyroxene</i>									
Ti	813.755	730.980	807.237	776.017	969.973	948.125	894.610	989.597	990.090
Rb	0.003		0.002					0.002	0.002
Sr	0.050	0.058	0.026	0.000	0.025	0.054	0.073	0.037	0.070
Y	0.968	0.821	1.188	0.910	1.302	1.211	1.186	1.515	1.429
Zr	0.713	0.510	0.589	0.423	0.888	0.839	0.775	0.777	0.744
Nb	0.006	0.006	0.007	0.006	0.006	0.006	0.006	0.006	0.007
Ba	0.007		0.002						0.001
La	0.001		0.001	0.000		0.002	0.005	0.006	0.001
Ce	0.005	0.004	0.003	0.005	0.004	0.013	0.014	0.006	0.006
Pr	0.002	0.001	0.001	0.001	0.001	0.004	0.003	0.002	0.002
Nd	0.016	0.017	0.015	0.008	0.016	0.031	0.023	0.020	0.029
Sm	0.014	0.012	0.013	0.010	0.015	0.022	0.016	0.020	0.023
Eu	0.007	0.006	0.008	0.006	0.010	0.011	0.009	0.011	0.013
Gd	0.038	0.033	0.045	0.036	0.047	0.056	0.050	0.060	0.072
Tb	0.012	0.010	0.013	0.011	0.015	0.015	0.015	0.019	0.020
Dy	0.121	0.103	0.145	0.119	0.162	0.158	0.150	0.194	0.197
Ho	0.036	0.032	0.046	0.037	0.050	0.047	0.047	0.061	0.060
Er	0.152	0.128	0.188	0.149	0.196	0.184	0.193	0.242	0.221
Tm	0.032	0.027	0.038	0.032	0.042	0.037	0.040	0.050	0.047
Yb	0.309	0.260	0.354	0.290	0.366	0.320	0.365	0.435	0.394
Lu	0.056	0.051	0.066	0.058	0.069	0.059	0.071	0.081	0.075
Hf	0.060	0.044	0.052	0.039	0.067	0.059	0.066	0.070	0.071
Ta			0.000						
Pb	0.075	0.148	0.044	0.054	0.024	0.032	0.025	0.029	0.014
Th	0.004	0.000	0.001	0.009	0.001		0.008	0.112	0.000
U	0.000		0.000	0.004		0.000	0.001	0.009	0.001

Table 7. (Continued)

Sample	I702	I764	I776	I892	I906	I909	TSI03	TSI06	TSI07
<i>Olivine</i>									
Ti	6.640	7.833	6.903	7.242	2.088	12.967	10.200	4.156	9.027
Rb	0.000								
Sr	0.000								
Y	0.036	0.036	0.022	0.022	0.007	0.010	0.030	0.023	0.036
Zr	0.005	0.022	0.002	0.012		0.004	0.007	0.033	0.003
Nb	0.000						0.000		
Ba	0.000								
La	0.000						0.000		
Ce	0.000				0.002		0.001		
Pr	0.000								
Nd	0.000								
Sm	0.000		0.000						
Eu	0.000						0.000		
Gd	0.000						0.002	0.001	
Tb	0.000	0.000		0.000			0.000		0.000
Dy	0.004	0.004	0.002	0.002			0.003	0.002	0.002
Ho	0.001	0.001	0.001	0.001	0.000	0.000	0.001	0.001	0.001
Er	0.006	0.006	0.003	0.004	0.001	0.001	0.005	0.003	0.006
Tm	0.002	0.002	0.001	0.001	0.001	0.001	0.002	0.001	0.002
Yb	0.017	0.015	0.013	0.013	0.006	0.008	0.017	0.012	0.018
Lu	0.004	0.004	0.003	0.004	0.002	0.002	0.005	0.003	0.005
Hf	0.000						0.005		
Ta	0.000								0.000
Pb	0.079	0.436	0.085	0.061	0.037	0.091	0.034	0.145	0.033
Th	0.000							0.002	
U	0.000			0.000			0.000	0.010	

Table 8. Trace element concentrations in olivine and orthopyroxene mineral separates in samples of Ichinomegata peridotite xenoliths.

Sample	KRB15	OKD04	OKD45-2	OKD57	OKD64	OKD69
<i>Clinopyroxene</i>						
Ti	2844.120	1005.617	3122.057	1157.693	2877.410	7460.133
Rb	0.004	0.023	0.004	0.003	0.004	0.033
Sr	67.310	37.330	133.207	42.617	71.420	124.845
Y	10.180	8.537	14.127	9.327	11.990	24.708
Zr	16.620	2.422	129.050	3.737	13.380	72.533
Nb	0.610	0.373	1.543	0.758	0.467	0.444
Ba	0.083	0.251	0.080	0.109	0.042	0.057
La	2.374	1.176	12.140	2.026	2.298	4.400
Ce	6.710	3.005	26.410	4.510	7.465	15.768
Pr	1.023	0.384	3.133	0.510	1.216	2.848
Nd	5.185	1.587	12.363	1.967	6.170	16.158
Sm	1.599	0.490	2.463	0.534	1.789	5.315
Eu	0.595	0.211	0.852	0.230	0.694	1.940
Gd	1.928	0.888	2.483	0.952	2.083	6.238
Tb	0.331	0.198	0.411	0.207	0.364	0.961
Dy	2.151	1.570	2.706	1.674	2.463	5.658
Ho	0.442	0.366	0.556	0.391	0.511	1.055
Er	1.163	1.078	1.533	1.139	1.384	2.497
Tm	0.167	0.166	0.222	0.174	0.199	0.325
Yb	1.061	1.063	1.406	1.127	1.271	1.836
Lu	0.149	0.152	0.201	0.165	0.176	0.243
Hf	0.611	0.088	3.330	0.087	0.198	3.055
Ta	0.070	0.030	0.238	0.098	0.067	0.135
Pb	0.072	0.022	0.147	0.027	0.075	0.107
Th	0.097	0.052	0.821	0.132	0.073	0.148
U	0.019	0.012	0.130	0.028	0.016	0.033
<i>Orthopyroxene</i>						
Ti	838.150	381.935	919.673	409.703	975.645	1596.440
Rb						0.003
Sr	0.432	0.145	0.513	0.181	0.364	0.627
Y	1.121	1.003	1.355	1.049	1.325	2.012
Zr	1.678	0.279	13.323	0.444	1.517	4.115
Nb	0.048	0.030	0.096	0.064	0.041	0.027
Ba						0.003
La	0.013	0.004	0.043	0.008	0.010	0.017
Ce	0.055	0.017	0.158	0.030	0.051	0.094
Pr	0.011	0.003	0.027	0.005	0.012	0.023
Nd	0.074	0.016	0.139	0.025	0.083	0.177
Sm	0.038	0.012	0.048	0.012	0.043	0.110
Eu	0.019	0.006	0.022	0.008	0.021	0.049
Gd	0.076	0.035	0.080	0.037	0.083	0.196
Tb	0.019	0.012	0.021	0.012	0.021	0.044
Dy	0.166	0.129	0.178	0.128	0.190	0.334
Ho	0.044	0.039	0.052	0.040	0.051	0.082
Er	0.155	0.155	0.181	0.158	0.181	0.256
Tm	0.029	0.030	0.036	0.031	0.034	0.044

Table 8. (Continued)

Sample	KRB15	OKD04	OKD45-2	OKD57	OKD64	OKD69
Yb	0.238	0.246	0.312	0.273	0.273	0.325
Lu	0.041	0.046	0.055	0.049	0.048	0.054
Hf	0.060	0.013	0.323	0.009	0.037	0.155
Ta	0.003	0.001	0.007	0.004	0.003	0.002
Pb	0.047	0.011	0.034	0.009	0.053	0.005
Th	0.001	0.000	0.007	0.003	0.001	0.001
U	0.001	0.000	0.004	0.001	0.001	0.001
<i>Olivine</i>						
Ti	36.250	15.097	36.445	17.160	31.097	92.520
Rb						0.049
Sr	0.016	0.019				0.919
Y	0.047	0.037	0.045	0.038	0.051	0.115
Zr	0.023	0.007	0.177	0.008	0.016	0.708
Nb	0.001	0.001	0.003	0.002	0.002	0.063
Ba						0.122
La						0.009
Ce		0.000	0.000		0.000	0.029
Pr				0.000		0.001
Nd			0.000		0.001	0.005
Sm						0.001
Eu						0.000
Gd			0.001		0.001	0.003
Tb	0.000	0.000	0.000		0.000	0.001
Dy	0.004	0.003	0.004	0.003	0.005	0.013
Ho	0.002	0.001	0.002	0.001	0.002	0.004
Er	0.008	0.006	0.007	0.007	0.009	0.016
Tm	0.002	0.002	0.002	0.002	0.002	0.003
Yb	0.019	0.017	0.023	0.021	0.022	0.031
Lu	0.005	0.005	0.005	0.004	0.005	0.008
Hf			0.002			0.015
Ta			0.000			0.004
Pb	0.058	0.003	0.187	0.015	0.018	0.048
Th						0.006
U						0.006

Table 9. Water contents in olivines and pyroxenes in samples of Ichinomegata and Oki-Dogo peridotite xenoliths.

	sample#	water content [ppm] (number of measurements)			
		olivine	orthopyroxene	clinopyroxene	bulk
Ichinomegata	I-892	4 (10)	175 (3)	298 (3)	68
	TSI06	7 (8)	271 (4)	292 (3)	134
	I-906	5 (7)	75 (4)	347 (6)	60
	I-702	4 (7)	155 (3)	304 (3)	70
	TSI03	2 (3)	137 (7)	208 (7)	46
Oki-Dogo	OKD64	6 (3)	6 (2)	8 (2)	6
	KRB15	2 (10)	35 (6)	30 (4)	10
	OKD45-2	2 (3)	17 (4)	10 (2)	5
	OKD04	4 (7)	-	98 (2)	7
	OKD69	4 (4)	-	-	4

Table 10. Characteristics of crystallographic preferred orientations in samples of Ichinomegata peridotite xenoliths.

sample#	N	J	M	MD			pfJ		
				[100]	[010]	[001]	[100]	[010]	[001]
<i>Ichinomegata</i>									
I-667	635	4.08	0.17	5.08	3.15	3.70	1.89	1.34	1.56
I-702	417	3.51	0.15	5.28	2.69	2.79	1.84	1.30	1.29
I-708	525	7.94	0.48	8.87	4.17	3.01	3.89	2.18	1.58
I-738	527	5.88		6.62	4.20	3.65	2.73	1.91	1.51
I-764	391	4.26	0.23	5.58	3.99	3.39	2.24	1.43	1.42
I-777	117	4.43		3.79	3.86	3.74	1.50	1.52	1.36
I-892	330	5.78		6.90	4.09	4.35	2.45	1.64	1.66
I-906	691	7.22	0.49	8.68	6.01	4.71	3.13	2.35	1.83
I-909	698	5.86	0.37	7.13	4.56	3.44	2.83	1.89	1.48
TSI03	676	3.64	0.19	4.69	3.26	2.52	1.83	1.51	1.23
TSI06	713	2.83	0.11	4.75	3.46	2.15	1.67	1.30	1.19
TSI07	380	4.10		6.71	3.35	2.66	2.13	1.43	1.31
<i>Oki-Dogo</i>									
OKD04	316	4.48	0.22	4.20	3.88	3.90	2.06	1.49	1.49
OKD07	271	2.56	0.21	4.00	2.95	2.84	1.37	1.17	1.18
OKD39	140	6.14	0.10	3.93	6.31	4.57	1.79	1.89	1.63
OKD45-2	226	5.23	0.18	4.98	5.00	3.30	1.95	1.86	1.48
OKD57	582	4.62	0.19	7.02	3.94	3.10	2.56	1.79	1.35
OKD64	226	6.99	0.22	6.33	5.19	5.24	2.81	2.05	1.93
OKD69	648	4.60	0.08	4.17	6.76	5.39	1.53	1.95	1.71
KRB15	254	4.39	0.13	5.00	6.37	3.70	1.92	1.98	1.40

N: Number of measurements; J: J-index; M: M-index; MD: Max density; pfJ: pJ-index

Chapter 3

Seismic anisotropy of the uppermost mantle beneath the back-arc region of Japan Sea: Evidence from Ichinomegata and Oki-Dogo peridotite xenoliths

Abstract.....	106
3-1. Introduction	107
3-2. Geological setting and samples	108
3-3. Rock seismic properties.....	109
3-4. Interpretation and discussion.....	112
Figures and Tables	115

Abstract

A dense network of seismic stations has been deployed across the northeast Japan arc to investigate mantle wedge structures. To attain independent petrophysical constraints, we determined the seismic properties of peridotite xenoliths from the back-arc region, Ichinomegata and Oki-Dogo, which were brought to the surface from the mantle lithosphere by volcanic eruptions. We calculated the seismic properties of the xenoliths from olivine and pyroxene crystallographic preferred orientations (CPOs) and single crystal elastic constants. The small magnitude of measured S-wave splitting (delay time of 0.22 s in the area where the xenoliths were entrained) beneath Ichinomegata can be explained by the average seismic properties of mantle xenoliths for an approximately 20-km thick horizontal anisotropic layer, indicating that the mantle lithosphere could be one of the dominant sources of seismic anisotropy. To constrain the effects of metasomatism on the seismic anisotropy, we explore the calculation of seismic properties for Oki-Dogo peridotites, which have affected by Fe enrichment with lower Mg# ($=\text{Mg}/\text{Mg}+\text{Fe}$) of olivine than that in typical residual peridotites of the upper mantle. CPO and seismic anisotropy are little affected by the percolation of melts, even though reactions change their composition. Our results revealed systematic across arc variations in both fast directions and delay times, with implications for the different in anisotropic structures between the northern and the southern parts of back-arc region of Japan Sea.

Key words: peridotite xenoliths; Ichinomegata; Oki-Dogo Island; Fe-enrichment metasomatism; seismic anisotropy

3-1. Introduction

Measurements of shear-wave splitting play a crucial role in imaging flow patterns within mantle wedges (e.g., Nakajima and Hasegawa, 2004; Audoin et al., 2004); however, observed shear-wave splitting from earthquakes of intermediate depth may be affected by anisotropy in the mantle wedge, the crust, and the slab. If shear-wave splitting occurs due to mineral CPOs, it is necessary to understand the strength of strain in the mantle wedge and the elastic coefficients of minerals to evaluate the delay time along ray paths.

In the northeast Japan, shear-wave polarization anisotropy has been systematically investigated in the mantle wedge of the northeast Japan arc; Fast directions in the back-arc side are oriented nearly E-W, whereas fast directions in the fore-arc side are oriented approximately N-S (Nakajima and Hasegawa, 2004). Although seismic anisotropy observations from the back-arc side of the northeast Japan arc are generally interpreted in terms of the CPO of mantle minerals arising from present-day mantle process such as mantle wedge convection and plate motion (Nakajima and Hasegawa, 2004; Ishise and Oda, 2005), we show peridotite xenoliths from the uppermost mantle lithosphere entrained by Ichinomegata Volcano in the back-arc region of northeast Japan. This anisotropy could be one of the dominant sources in explaining the observed delay times of shear-wave velocity in this region.

In the southwest Japan, a large low velocity zone is observed from seismic tomography images (Nakajima and Hasegawa, 2007), where it is suggested that there are interaction between melts and rocks. Tommasi et al. (2004) investigated seismic anisotropy in peridotite xenoliths from French Polynesia, and shows that increasing interaction with plume-related melts results in significant Fe-enrichment of the

peridotites, but it does not modify seismic anisotropy. Also, Lee (2003) proposed that thermal anomaly and the Fe-enrichment of olivine would produce a negative seismic anomaly. In this chapter, we calculated the seismic properties of Oki-Dogo peridotite xenoliths to constrain the relationships between seismic anisotropy and melt-rock interaction preserved in peridotite xenoliths in the back-arc region.

3-2. Geological setting and samples

The studied samples were eight peridotite xenoliths from Ichinomegata volcano and eight peridotites Oki-Dogo Island, located in the Japan Sea (Fig. 1). These peridotites were the subject of detailed microstructural studies in Chapter 2.

The depth of the Moho beneath the Ichinomegata crater is approximately 28 km near the coast of the Japan Sea (Zhao et al., 1990), while the temperature of the Moho is thought to be about 850°C (Kushiro, 1987). The depth of the Moho becomes deeper, up to 38 km in depth, toward the northeast Japan arc (Zhao et al., 1990), where temperatures are 950 to 1000°C (Kushiro, 1987). The peridotite xenoliths analyzed in the present study came from relatively shallow levels in the mantle of 30 to 40 km depth at temperatures in the range 850 to 1000°C (Takahashi, 1986).

The origin of Oki-Dogo peridotites was estimated by Yamamoto et al. (2007). They show that the equilibrium pressure of mafic and ultramafic xenoliths from Oki-Dogo Island based on the pressure of CO₂ fluid inclusions preserved in minerals, yielding a depth of 25–29 km for lherzolites, just below the Moho. The chemical composition of Oki-Dogo peridotites shows that they were affected by various degree of metasomatism by melt, which might be related to back-arc spreading (Chapter 2).

Olivine CPO obtained by SEM-EBSD facility at Géosciences Montpellier,

France are used as the same data in Chapter 2. The details of results of CPOs are shown in Figs. 2 and 3. For the maximization of the average seismic anisotropy, the CPO data for each sample were adjusted to an external reference frame in which the maximum V_p is parallel to the reference direction X, and the minimum V_p is parallel to the Z-axis as the same method in Satsukawa et al. (2011).

3-3. Rock seismic properties

Seismic properties were computed by averaging individual grain elastic-constant tensors as a function of the CPO and modal composition of a sample. This method enables the calculation of the three-dimensional distribution of seismic velocities in an anisotropic polycrystalline aggregate (Mainprice and Humbert, 1994). In the present calculations, we used Voigt–Reuss–Hill averaging of single-crystal elastic constants at ambient conditions (Abramson et al., 1997; Chai et al., 1997; Collins and Brown, 1998).

Since olivine Mg# is varying from 86 to 90 in Oki-Dogo samples, we calculated the olivine density and its elastic constants to constrain the effect of the compositional changes induced by melt-rock interactions on the seismic properties. By using the same method reported Tommasi et al. (2004) with taking into account the dependence of olivine single crystal elastic constants and density of olivine (Bass, 1995), these factors are calculated as follows:

$$\text{Density: } -10.977 \times \text{Ol Mg\# (0~100)} + 4329.1$$

$$C_{11}: 0.0061 \times \text{Fo} + 2.6589$$

$$C_{22}: 0.0032 \times \text{Fo} + 1.6795$$

$$C_{33}: 0.0003 \times \text{Fo} + 2.3193$$

$$C_{44}: 0.0035 \times \text{Fo} + 0.3203$$

$$C_{55}: 0.0034 \times Fo + 0.4643$$

$$C_{66}: 0.0024 \times Fo + 0.5699$$

$$C_{12}: -0.0028 \times Fo + 0.9374$$

$$C_{13}: -0.0023 \times Fo + 0.9200$$

$$C_{23}: -0.0017 \times Fo + 0.9219$$

Figure 4 shows the calculated density as a function of the forsterite content of olivine in each sample compare with the previous studies in Tommasi et al. (2004).

Based on the geothermobarometric analysis, we calculated the seismic properties assuming conditions of 900°C and 1.0 GPa for Ichinomegata peridotites (Fig. 5 and Table 1), and 1000 °C and 0.8 GPa for Oki-Dogo peridotites (Fig. 6 and Table 1). This method has been described in detail previously (Pera et al., 2003; Tasaka et al., 2008).

By combining data from each of the eight xenoliths, the average of the sample was then calculated, with the same weighting applied to each measurement, regardless of the number of measurements acquired from each xenoliths (Fig. 7a, c).

Olivine CPO of Ichinomegata data show a-axis fiber patterns characterized by a strong concentration in [100], with a weak girdle of [010] and [001]. For orthopyroxene, CPO data may indicate (100)[001] slip. In contrast, clinopyroxene CPO data suggest a nearly random fabric, with a weak concentration in [001] parallel the foliation (Fig. 7a). Olivine CPO of Oki-Dogo data show a-axis fiber patterns characterized by a strong concentration in [100], with a weak point maximum of [010] and weak girdle of [001]. For orthopyroxene, CPO data may indicate (100)[001] slip. In contrast, clinopyroxene CPO data suggest a nearly random fabric, with a weak concentration in [001] parallel the foliation (Fig. 7c).

On average, olivine CPOs have P-wave propagation that is fastest parallel to

the highest density of [100], and is slowest parallel to the highest density of [010]; polarization anisotropies are highest in directions approximately normal to the highest density of [010]. The orientation of the polarization plane of the fastest S-wave (V_{s1}) indicates the orientation of the great circle containing the [100] maximum.

For Ichinomegata samples, the V_p of olivine range from 7.59 to 8.49 km/s; their anisotropy is 11.2% and $AV_{s_{max}}$ is 7.85%. Orthopyroxene CPOs, the average anisotropies are small: V_p range between 7.60 and 7.72 km/s, their anisotropy is 1.5%, and $AV_{s_{max}}$ is 1.82%. Although clinopyroxene has weaker CPOs and smaller measured values than orthopyroxene, its seismic anisotropy is larger: V_p range between 8.25 and 8.56 km/s, their anisotropy is 3.6%, and $AV_{s_{max}}$ is 1.64% (Fig. 7b).

The V_p of olivine of Oki-Dogo samples range from 7.56 to 8.35 km/s; their anisotropy is 9.7% and $AV_{s_{max}}$ is 6.96%. For orthopyroxene CPOs, the average anisotropies are small: V_p range between 7.52 and 7.74 km/s, their anisotropy is 2.9%, and $AV_{s_{max}}$ is 3.24%. Although clinopyroxene has weaker CPOs and smaller measured values than orthopyroxene, its seismic anisotropy is larger: V_p range between 8.29 and 8.43 km/s, their anisotropy is 1.7%, and $AV_{s_{max}}$ is 2.26% (Fig. 7d).

Based on the modal composition of peridotites, we recalculated the seismic properties for mean compositions of lherzolite ($Ol_{70}Opx_{16}Cpx_{14}$; Fig. 8a) for Ichinomegata, and lherzolite ($Ol_{84}Opx_9Cpx_8$; Fig. 8b) for Oki-Dogo. Using this approach, P-wave propagation is fastest parallel to the highest density of [100] and is slowest parallel to the highest density of [010], and polarization anisotropies are highest at directions approximately normal to the highest density of [010]. V_p/V_{s1} and V_p/V_{s2} ratios are highest for propagation directions that are normal and parallel, respectively, to the highest density of [100] of olivine. Although these anisotropy patterns do not change significantly as olivine volume fraction decreases, P- and

S-wave velocities and anisotropies decrease. Because olivine is the primary mineral in peridotites, it is likely that peridotite anisotropy is defined mainly by the characteristics of olivine.

We have calculated variations in seismic properties as a function of modal composition for the structural planes of XY for horizontal shear, XZ for lateral shear, and YZ for vertical shear (Fig. 9 and 10); in these Figures, gray shaded squares represent ranges in the modal compositions of peridotite xenoliths from this study. To estimate the effect of modal composition on seismic properties, we varied the mineral composition from 100% olivine to 50% olivine + 50% pyroxene, by the alternating stepwise addition of 10% orthopyroxene or clinopyroxene. We have extrapolated variations in Vp anisotropy, the maximum Vs anisotropy (Figs. 9a, 10a), Vp (Figs. 9b, 10b), the anisotropy of Vs (Figs. 9c, 10c), the average of Vp (Figs. 9d, 10d), the deviation of Vp (Figs. 9e, 10e), and Vp/Vs (Figs. 9f, 10f) with respect to the olivine volume fraction, assuming propagation direction of seismic wave is vertical. As a result, the effect of the second most abundant phase on seismic properties is highly dependent on structural orientation. Vp anisotropy decreases as the volume fraction of olivine decreases (Figs. 9a, 10a), whereas average Vp, unlike other factors, increases with the addition of clinopyroxene (i.e., decreasing olivine abundance; Figs. 9b, d and 10b, d). Vp/Vs does not differ significantly as a function of modal olivine abundance.

3-4. Interpretation and discussion

Although the original orientations of the Ichinomegata peridotite xenoliths were lost during their volcanic transport to the surface, we are able to derive quantitative constraints on the intrinsic anisotropy within the lithospheric mantle but not constrain the trend of the fast split shear waves (Ben Ismaïl and Mainprice, 2001).

If the structures within the uppermost mantle lithosphere beneath the Ichinomegata volcano were randomly oriented, the peridotite xenoliths analyzed in the current study would make no contribution to the observed shear-wave splitting; however, it is likely that regional-scale structures within the uppermost mantle lithosphere are oriented horizontally, as described in Chapter 2. The thickness (T) of an anisotropic layer is given by $T = (100dtV_{s_{\text{mean}}})/AV_s$, where dt is the delay time of S-waves, $V_{s_{\text{mean}}}$ is the average velocity of the fast and slow velocities, and AV_s is the anisotropy for a specific propagation direction expressed as a percentage (e.g., Pera et al., 2004). Accordingly, the observed delay times (e.g., 0.22 s at Oga Peninsula where Ichinomegata Volcano is located) can be explained by the seismic properties of our average peridotite xenolith for an approximately 20-km thick anisotropic layer with a horizontal foliation and lineation. It is noted that the bulk anisotropy should be less than that in each individual sample due to destructive interferences (e.g., Ben Ismail and Mainprice, 2001), so that it might be necessary to have a thicker anisotropic layer.

S-wave seismograms of intermediate-depth earthquakes show small delay times but regionally coherent polarizations, where the E-W fast anisotropy occurs from the back-arc region to the volcanic front above the low velocity zones (Nakajima and Hasegawa, 2004). Although the low velocity zones are commonly attributed to the zones of partially melted mantle (Kushiro, 1987), the propagation of a partial-melting front across the lithosphere would not erase the pre-existing CPO and related seismic anisotropy, even if it does modify the microstructure (Vauchez and Garrido, 2001). Consequently, mantle lithosphere in the back-arc region is possibly one of the dominant sources of seismic anisotropy, which is presently commonly attributed to corner flow.

Oki-Dogo Island is an important site in terms of xenoliths because it marks

the most continent ward occurrence of mantle peridotite xenoliths in the back-arc region of the southwest Japan arc. Peridotite xenoliths modified by melt percolation demonstrate the possible occurrence of an anisotropic layer in the uppermost mantle lithosphere that might be related to 'frozen' deformation during back-arc spreading along the southwest Japan arc. To constrain the effect of the compositional changes induced by melt-rock interactions on the seismic properties, analysis of P- and S-waves velocities as a function of the olivine forsterite content in each sample shows that S-waves velocities decrease with Fe-enrichment in olivine (Fig. 11a). However, P-waves velocities are not sensitive to the olivine forsterite content (Fig. 11b). Figure 11(c, d) shows the P- and S-waves anisotropy as a function of the olivine forsterite content in each sample. Lherzolite which have low Mg# have relatively high anisotropy for S-wave, particularly (Fig. 11d). Since Oki-Dogo samples do not show any structure defined by a foliation or a lineation, seismic anisotropy may only be related to flow in the uppermost mantle by assuming that olivine [100] and [010] axes alignment, respectively. The production of S-wave anisotropy in lherzolite consisted with the evidence that samples which have low Mg# and showed relatively high concentration in [010] (Chapter 2). Over all, CPO and seismic anisotropy are little affected by the percolation of melts, even though reactions change their composition. The Fe enrichment results in an increase in density and decrease in S-wave velocity, however, P-wave and S-wave anisotropies showed few significant changes. Our results revealed systematic across arc variations in both fast directions and delay times, with implications for the different in anisotropic structures between the northern and the southern parts of back-arc region of Japan Sea.



Figure 1. Locality map of mantle xenoliths on the Japan arcs. Shown are selected localities of mantle xenoliths in the southwest (SW) and northeast (NE) Japan arcs. Ichinomegata volcano is located in Oga Peninsula (Akita prefecture, NE Japan), and Oki-Dogo Islands is located in Shima prefecture (SW Japan).

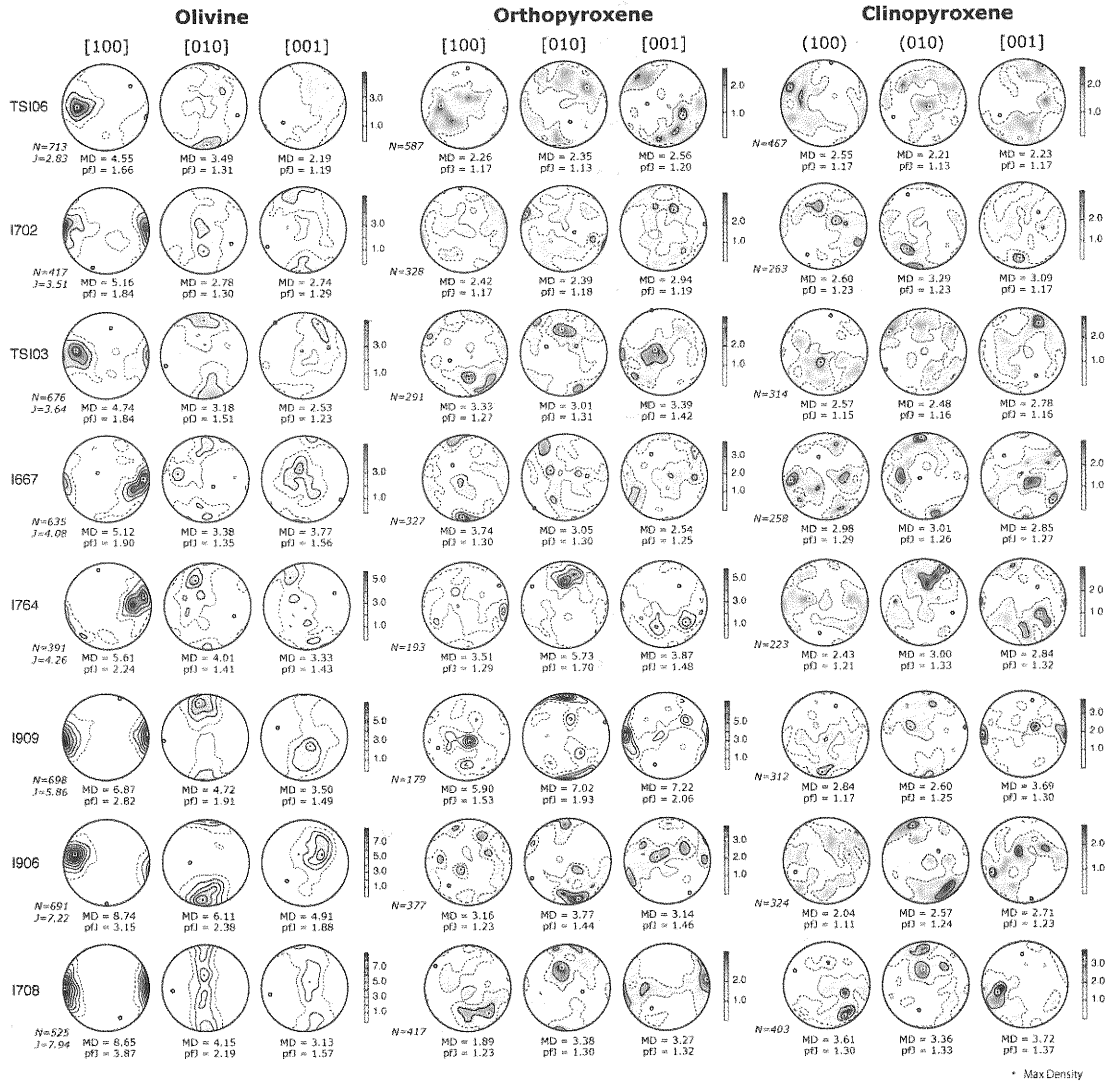


Figure 2. Olivine, orthopyroxene and clinopyroxene CPOs. To maximize the average seismic anisotropy the orientation data for each sample were rotated with the result that the maximum Vp is parallel to the reference direction X (east or west in the pole figure) and the minimum Vp is parallel to Z (north or south in the pole figure).

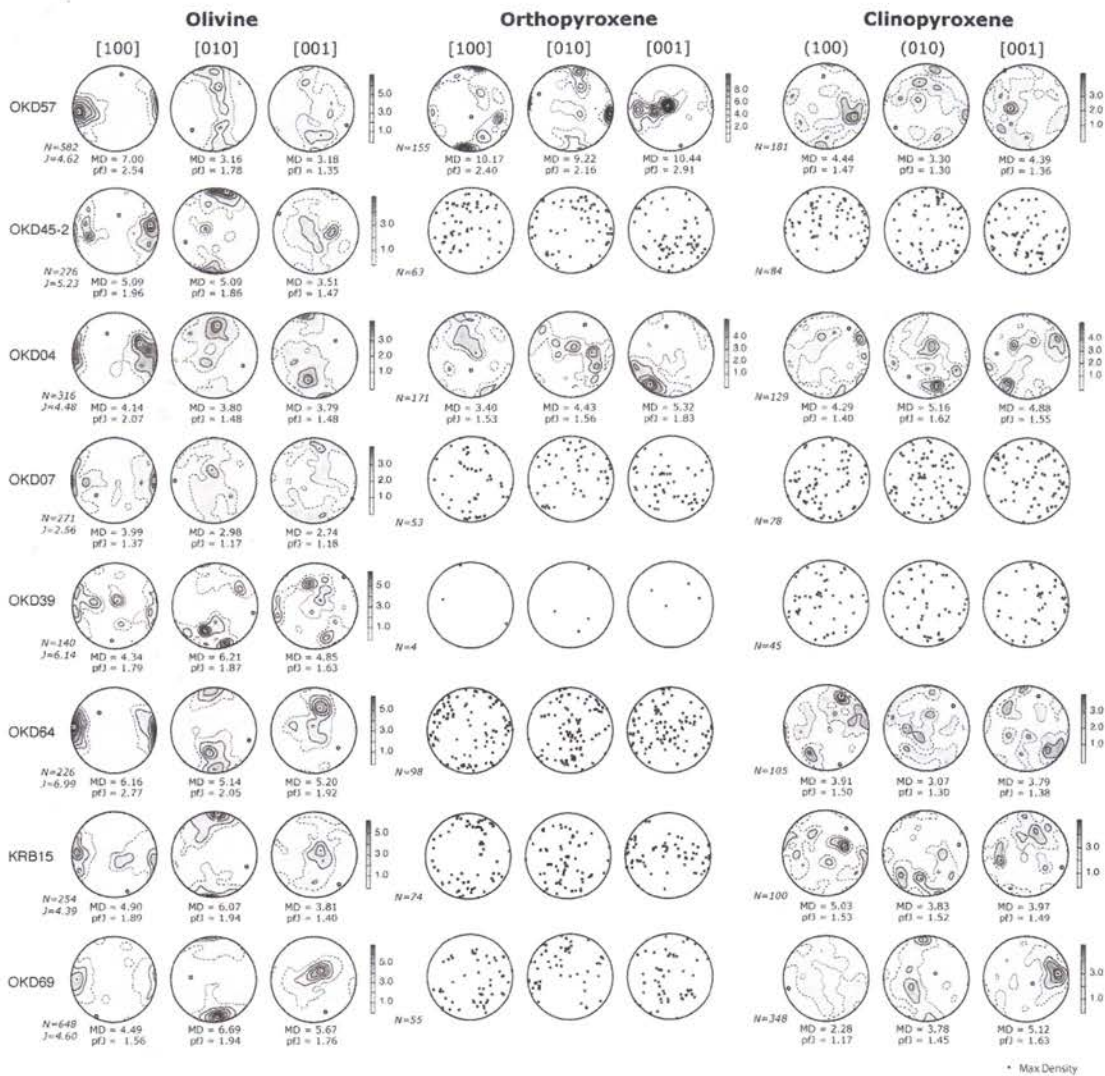


Figure 3. Olivine, orthopyroxene and clinopyroxene CPOs. To maximize the average seismic anisotropy the orientation data for each sample were rotated with the result that the maximum V_p is parallel to the reference direction X (east or west in the pole figure) and the minimum V_p is parallel to Z (north or south in the pole figure).

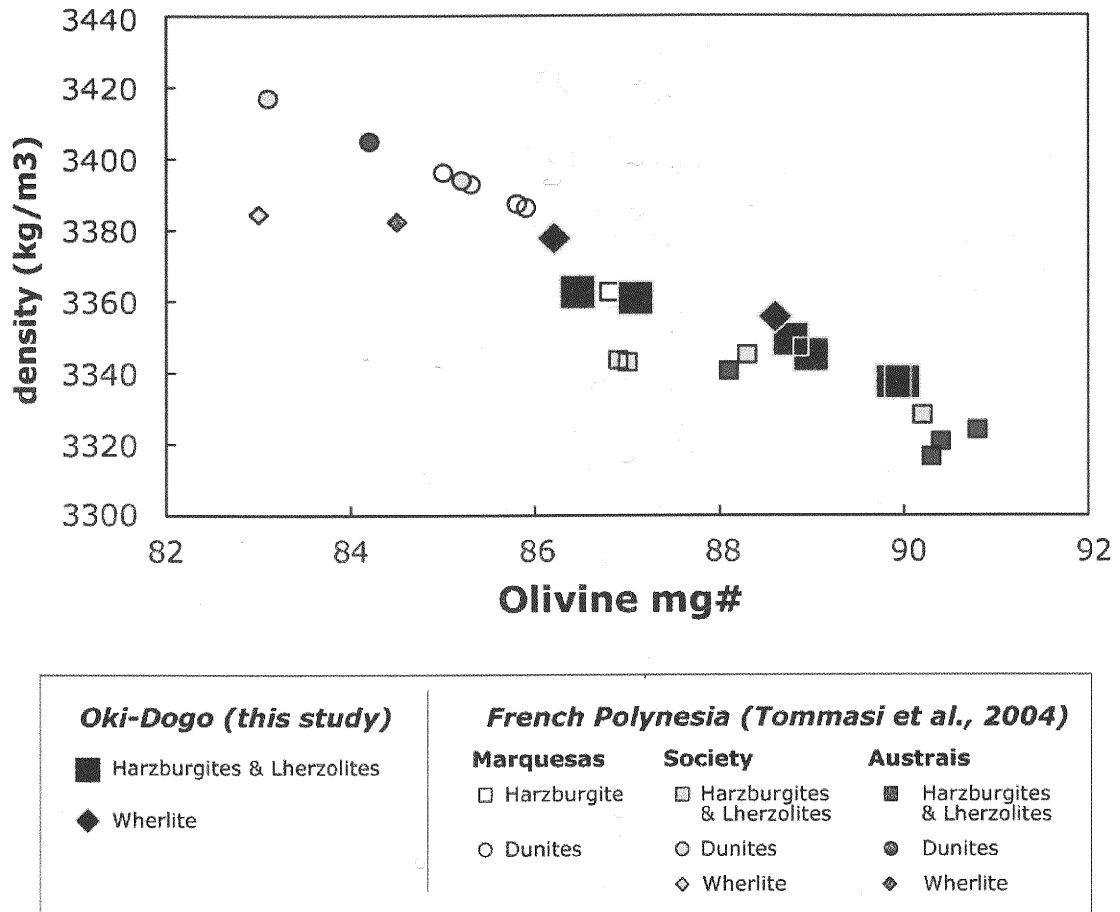


Figure 4. Density as a function of the forsterite content of olivine in each sample.

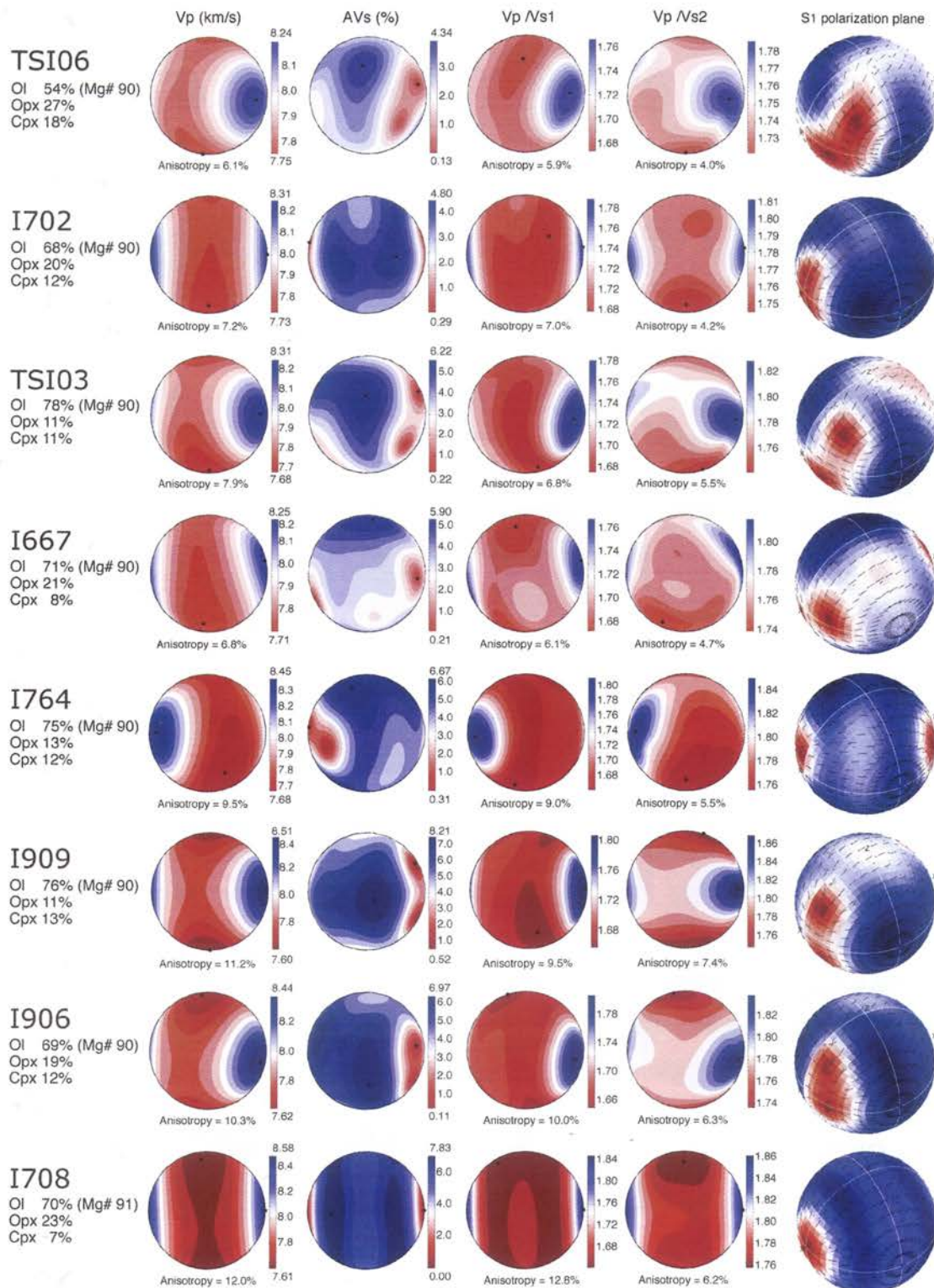


Figure 5. Seismic properties. These data were calculated based on crystallographic preferred orientation data in Fig. 2. From left to right: P-wave velocity, S-wave anisotropy, V_p/V_{s1} , V_p/V_{s2} , and the polarization of the fast shear wave S_1 .

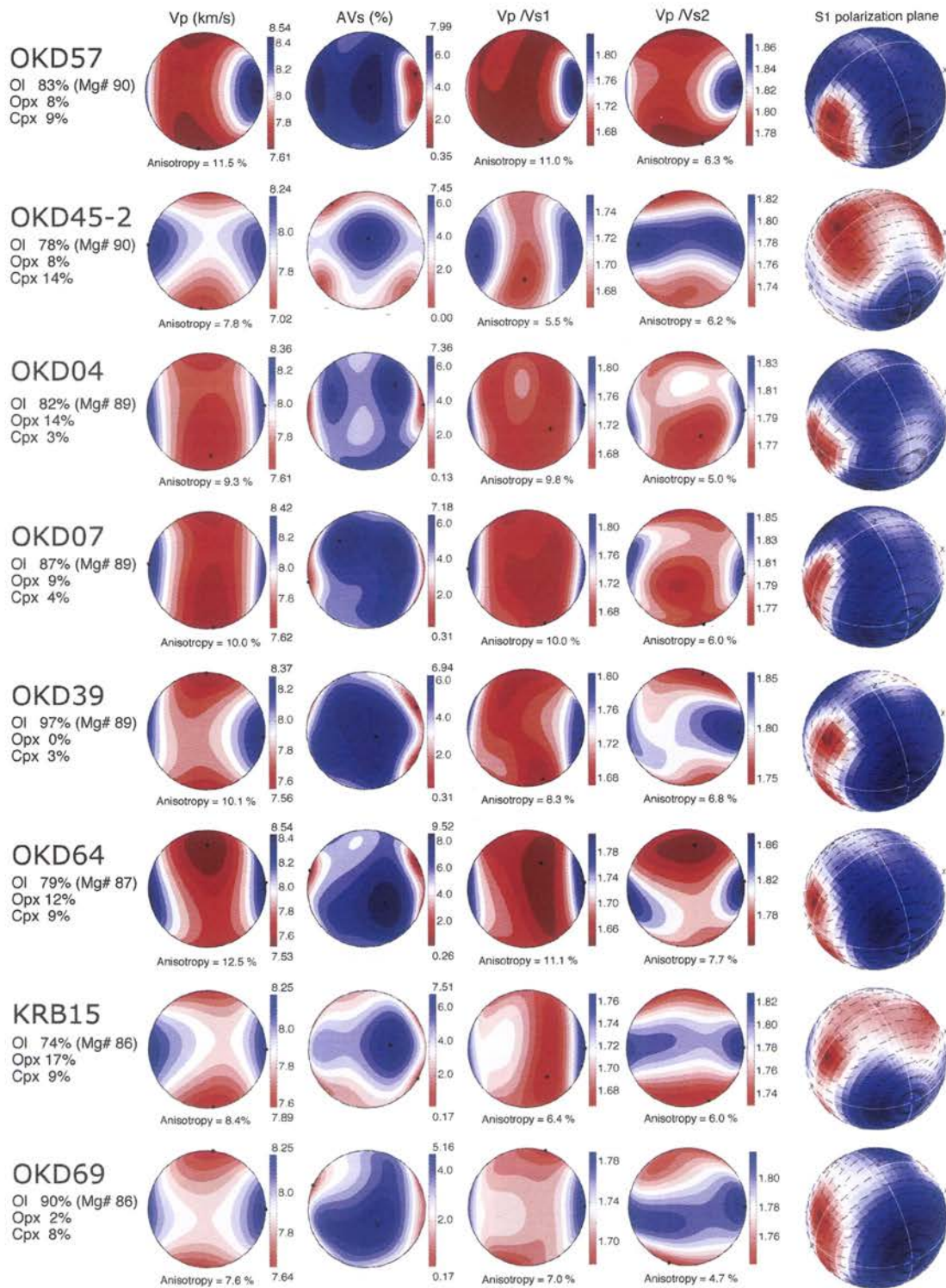


Figure 6. Seismic properties. These data were calculated based on crystallographic preferred orientation data in Fig. 3. From left to right: P-wave velocity, S-wave anisotropy, V_p/V_{s1} , V_p/V_{s2} , and the polarization of the fast shear wave S_1 .

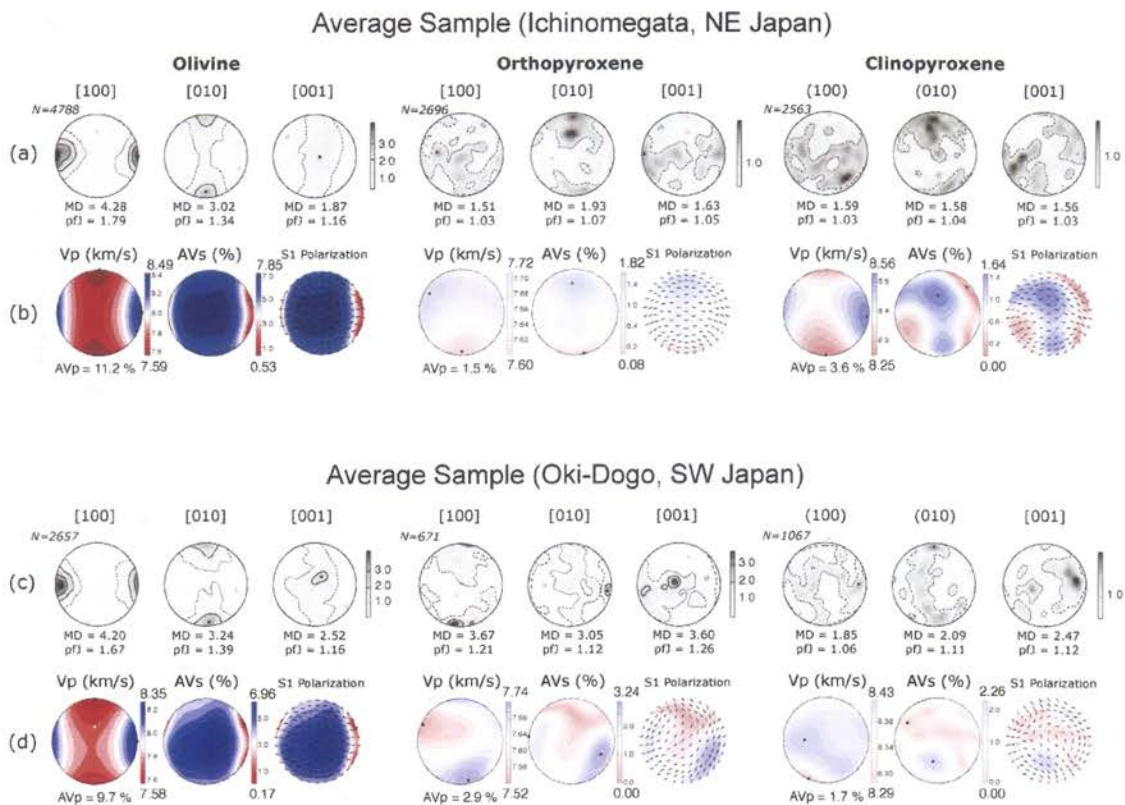


Figure 7. (a, c) Crystallographic preferred orientation (CPO) data for the average sample, obtained by summing the CPO of six peridotite xenoliths. CPOs are plotted on equal-area, lower hemisphere projections, contours are multiples of the uniform distribution, N is the number of measurements, pfJ is an index of fabric intensity, and MD is the maximum density. (b, d) Seismic properties of the average sample for each mineral (olivine, orthopyroxene and clinopyroxene) computed from the average CPOs based on grid data at a temperature of 1000°C and pressure of 1.0 GPa (b) and a temperature of 1000°C and pressure of 0.8 GPa (d). Contours are multiples of uniform density; Vp is the three-dimensional distribution of the P-wave velocity; anisotropy is $(V_{p_{\max}} - V_{p_{\min}}) / (V_{p_{\text{mean}}})$; AVs is the three-dimensional distribution of the polarization plane of the fast split S-wave (S1), as a function of the orientation of the incoming wave relative to the structural frame of the sample. Each small represents the trace of the polarization plane at the point at which S1 penetrates the hemisphere.

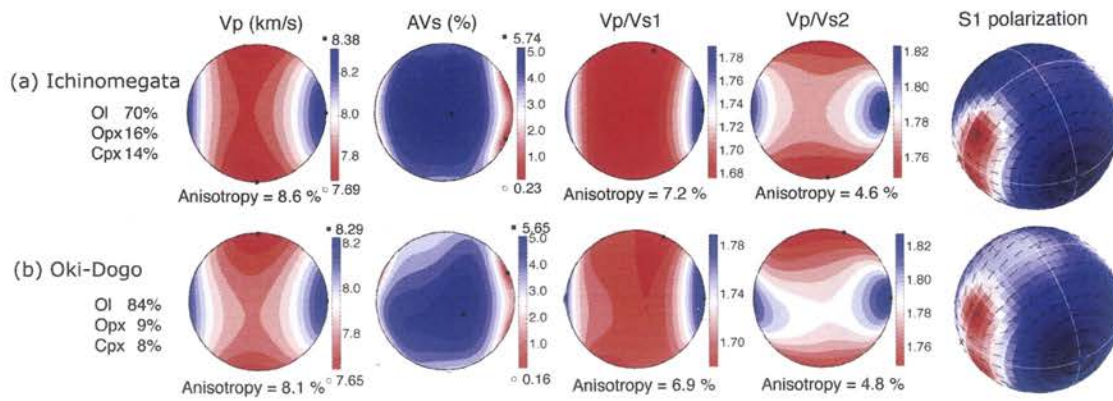


Figure 8. Seismic properties of average samples. From left to right: P-wave velocity, S-wave anisotropy, V_p/Vs_1 , V_p/Vs_2 , and the polarization of the fast shear wave S_1 . (a) Ichinomegata. (b) Oki-Dogo.

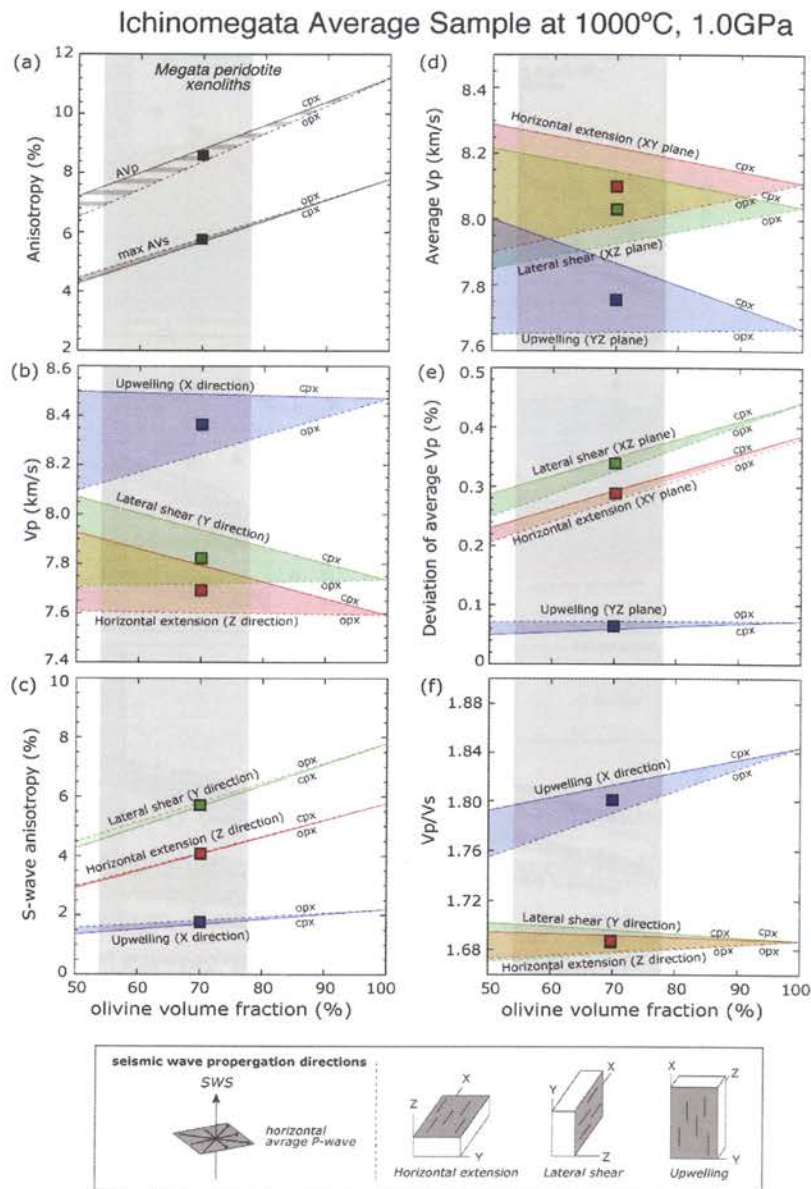


Figure 9. Variations in (a) Vp anisotropy and the maximum Vs anisotropy, (b) Vp, (c) S-wave anisotropy, (d) Average Vp, (e) Deviation of average Vp and (f) Vp/Vs as a function of mantle composition at a temperature of 1000 °C and pressure of 1.0 GPa. Solid lines represent compositions ranging from 50% olivine + 50 % clinopyroxene to 100% olivine; broken lines represent compositions ranging from 50% olivine + 50 % orthopyroxene to 100% olivine. Contours are shown for three geodynamic models: red for horizontal extension, green for lateral shear, and blue for upwelling. Within the box, the shaded area represents the plane of the foliation, and lines indicate lineation. Symbols relate to the mean composition of the peridotites: squares for lherzolite and circles for harzburgite.

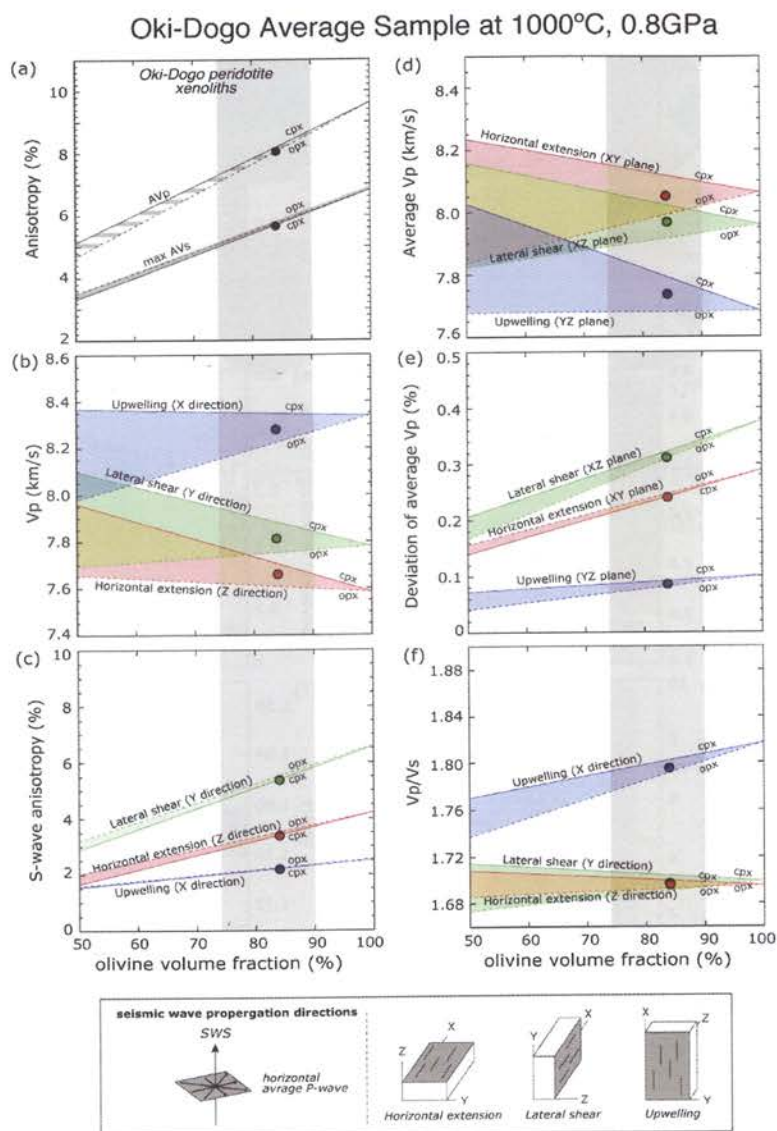


Figure 10. Variations in (a) Vp anisotropy and the maximum Vs anisotropy, (b) Vp, (c) S-wave anisotropy, (d) Average Vp, (e) Deviation of average Vp and (f) Vp/Vs as a function of mantle composition at a temperature of 1000 °C and pressure of 0.8 GPa. Solid lines represent compositions ranging from 50% olivine + 50 % clinopyroxene to 100% olivine; broken lines represent compositions ranging from 50% olivine + 50 % orthopyroxene to 100% olivine. Contours are shown for three geodynamic models: red for horizontal extension, green for lateral shear, and blue for upwelling. Within the box, the shaded area represents the plane of the foliation, and lines indicate lineation. Symbols relate to the mean composition of the peridotites: squares for lherzolite and circles for harzburgite.

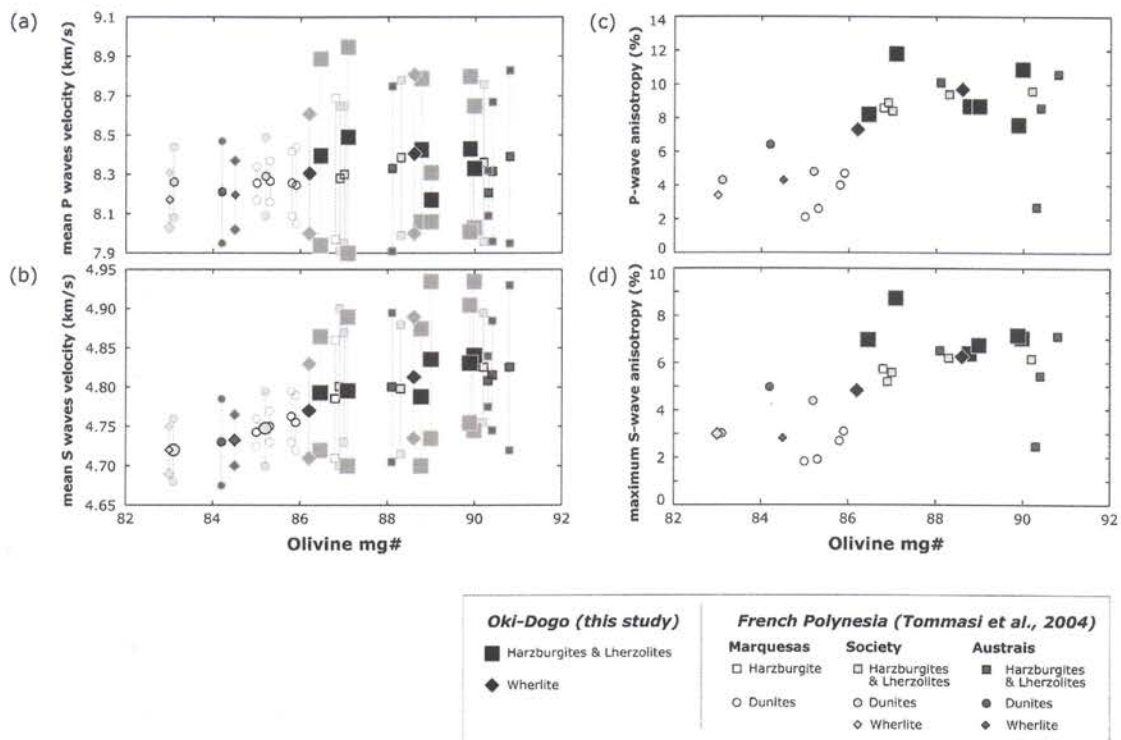


Figure 11. P-wave velocity (a), S-wave velocity (b), P-wave anisotropy (c) and maximum S-wave anisotropy (d) as a function of the forsterite content of olivine in each sample. The maximum and minimum P-wave velocities (a) or the mean fast and slow S-wave velocities (b) calculated for the actual anisotropic samples are represented as light symbols.

Table 1. Seismic velocity and anisotropy in samples of Ichinomegata and Oki-Dogo peridotite xenoliths.

Sample #	Vp Max (km/s)	Vp Min (km/s)	AVp (%)	AVs Max (%)	Vs1 max (km/s)	Vs1 min (km/s)	Vs2 max (km/s)	Vs2 min (km/s)
<i>Ichinomegata</i>								
I667	8.25	7.71	6.80	5.90	4.67	4.52	4.60	4.38
I702	8.31	7.73	7.20	4.89	4.69	4.57	4.59	4.41
I708	8.58	7.61	12.00	7.83	4.77	4.58	4.58	4.31
I738	8.79	7.92	10.40	6.18	4.95	4.81	4.86	4.61
I764	8.45	7.68	9.50	6.87	4.74	4.55	4.60	4.36
I777	8.45	7.93	6.30	4.57	4.93	4.75	4.79	4.71
I892	8.74	8.03	8.40	5.69	4.98	4.81	4.88	4.64
I906	8.44	7.62	10.30	6.97	4.75	4.56	4.61	4.36
I909	8.51	7.60	11.20	8.21	4.75	4.53	4.60	4.34
TSI03	8.31	7.68	7.90	6.20	4.70	4.52	4.60	4.38
TSI06	8.24	7.75	6.10	4.34	4.70	4.59	4.62	4.47
TSI07	8.64	8.09	6.60	4.42	4.95	4.82	4.86	4.69
<i>Oki-Dogo</i>								
OKD04	8.36	7.61	9.29	7.35	4.72	4.53	4.55	4.31
OKD07	8.42	7.62	10.03	7.18	4.70	4.52	4.56	4.29
OKD39	8.81	8.00	9.70	6.26	4.98	4.80	4.86	4.61
OKD45-2	8.24	7.62	7.84	7.46	4.72	4.51	4.56	4.38
OKD57	8.54	7.61	11.49	7.99	4.74	4.53	4.58	4.30
OKD64	8.54	7.53	12.55	9.51	4.75	4.52	4.61	4.28
OKD69	8.25	7.64	7.63	5.16	4.64	4.51	4.56	4.36
KRB15	8.25	7.59	8.39	7.51	4.73	4.50	4.57	4.37

AVp: P-wave anisotropy; AVs: S-wave anisotropy.

Chapter 4

Seismic anisotropy of the uppermost mantle beneath the Rio Grande rift: Evidence from Kilbourne Hole peridotite xenoliths, New Mexico

Originally Published in modified form as “Seismic anisotropy of the uppermost mantle beneath the Rio Grande rift: Evidence from Kilbourne Hole peridotite xenoliths” by T. Satsukawa, K. Michibayashi, E. Y. Anthony, R. J. Stern, S. G. Stephen and H. L. Kelly, *Earth and Planetary Science Letters*, **331**, 172-181, 2011, All rights reserved.

Abstract.....	128
4-1. Introduction	129
4-2. Geological setting	130
4-3. Seismic data	131
4-4. Mineral compositions, microstructures, and fabric analyses.....	132
4-5. Rock seismic properties.....	135
4-6. Variation in seismic properties as a function of modal composition	136
4-7. Discussion: Seismic anisotropies beneath the Rio Grande rift.....	137
4-8. Conclusions	143
Figures and Tables	145

Abstract

Peridotite xenoliths from the Kilbourne Hole maar, New Mexico, consist of spinel lherzolite, harzburgite, and dunite. Because Kilbourne Hole erupted at approximately 10 ka, these xenoliths represent essentially current conditions beneath the Rio Grande rift. In this study, we present detailed petrofabric data and seismic properties obtained from peridotite xenoliths from Kilbourne Hole to illuminate the origin and significance of shear-wave splitting in the uppermost mantle beneath this active rift. Using phase relations and the temperature of equilibration, we infer that these xenoliths were derived from the uppermost mantle, from depths of 35 – 60 km. Their crystallographic preferred orientations indicate the preservation of olivine b-axis fiber fabrics with a strong concentration of [010] with girdles of [100] and [001]. We consider three geodynamic models for the source region of these xenoliths: horizontal extension, lateral shear, and upwelling. After calculating seismic properties using a volume fraction of olivine, orthopyroxene and clinopyroxene appropriate to each model, we conclude that these xenoliths are derived from a lateral shear zone (vertical foliation (XY plane) and horizontal lineation within the plane of the foliation (X-axis)). However, the degree of seismic anisotropy generated by peridotite xenoliths alone is limited, so that the existence of melt in thin cracks or dikes could be required to cause a significant increase; the orientation of such melt pockets parallel to the XY plane in either model would result in an increase in anisotropy. These results indicate that the shear-wave splitting observed in the Rio Grande rift is a reflection of the lithospheric fabric and the presence of melts as thin cracks or dikes.

Key words: peridotite xenolith; Kilbourne Hole maar; Rio Grande rift; rifting; mantle flow; crystallographic preferred orientation (CPO); seismic anisotropy.

4-1. Introduction

Continental rifting is a complex process involving deformation of the lithosphere, asthenospheric flow, and partial melting; each of these processes can result in seismically anisotropic structures. As such, the significance of shear-wave splitting, in particular whether it represents lithospheric fabric or asthenospheric flow, remains controversial (Gao et al., 2008). Recent passive seismological investigations, combined with CPO (crystallographic preferred orientation) studies of xenolith fabrics, have provided an inexpensive and fruitful avenue for addressing this question (e.g., Satsukawa et al., 2010). Measurements of shear-wave splitting using P-to-S converted phase (SKS, SKKS, and PKS) play a crucial role in imaging the orientation and degree of polarization of mantle fabrics and in constraining models for the formation of these fabrics (Silver, 1996; Savage, 1999; Liu, 2009). Numerous laboratory and field studies suggest that seismic anisotropy in the uppermost mantle results mainly from olivine CPO which tends to show a maximum seismic velocity parallel to the direction of plastic flow within the upper mantle (Nicolas and Christensen, 1987). This study is aimed at understanding mantle fabrics and their formation mechanisms beneath the Rio Grande rift by combining petrological and seismological measurements (Fig. 1).

The upwelling of asthenospheric mantle in rift zones provides an abundance of melts. Recent petrophysical studies of both natural (e.g., Le Roux et al., 2008) and experimentally generated (e.g., Holtzman et al., 2003) peridotites indicate that partial melting and refertilization processes may affect CPO. CPOs for peridotite xenoliths from the Kerguelen Islands, which are strongly affected by the Kerguelen plume,

differ between harzburgites and dunites as a result of melt–rock interaction; these petrographic differences correspond with the distribution of CPO-induced S-wave anisotropy (Bascou et al., 2008).

Previous studies have highlighted correlations between seismic properties and the modal composition of orthopyroxene and olivine, based on modeling (e.g., Mainprice, 1997), and analyses of natural sample of continental peridotite (e.g., Lee, 2003; Matsukage et al., 2005) and natural peridotite xenoliths (e.g., Pera et al., 2003; Soustelle and Tommasi, 2010). However, the effect of clinopyroxene on seismic properties is poorly understood, despite it having the third-highest modal abundance in peridotite.

Based on their observation of olivine CPO in Kilbourne Hole peridotite xenoliths from the Rio Grande rift, Bussod and Irving (1981) proposed that deformation was accompanied by syntectonic recrystallization in the presence of intercrystalline fluid. However, these samples were analyzed using a universal stage, and the seismic properties of the mantle beneath the Rio Grande rift were not considered. In this study, we present detailed petrofabric data for spinel peridotite xenoliths from Kilbourne Hole, New Mexico, determined using electron backscatter diffraction. Using these results, we illuminate the origin and significance of shear-wave splitting in the upper mantle beneath this active rift (Fig. 1).

4-2. Geological setting

The Kilbourne Hole maar exposes Quaternary basanites containing both crustal and mantle xenoliths (Hamblock et al., 2007). It is roughly elliptical in shape, almost 3 km in length, and from 100 to 125 m deep. Using ^3He surface exposure methods, the age of eruption has been constrained to 10–20 ka (Anthony and Poths,

1992; Williams, 1999); thus, the xenoliths represent essentially ambient conditions for the Rio Grande rift. Kilbourne Hole is a part of the Potrillo volcanic field (Anthony et al., 1992; Thompson et al., 2005), which consists of cinder cones, maars, and fissure flows of basanitic and alkalic basalt composition. The Potrillo volcanic field is one of the largest silica-undersaturated volcanic fields in the Rio Grande rift, and has been interpreted as representing the products of small-degree partial melting of a volatile-charged asthenosphere.

4-3. Seismic data

For the study, we use all available broadband seismic data recorded in the 2° by 2° area approximately centered at Kilbourne Hole. The data were recorded by 7 stations (Fig. 1) and were archived at the IRIS (Incorporated Research Institutions for Seismology) Data Management Center. Station KIDD is operated by the University of Texas at El Paso (UTEP) and is located near the UTEP campus, and the rest of the stations belong to the Transportable Array of the USArray. A robust shear-wave splitting parameter measuring and ranking procedure (Liu et al., 2008; Liu, 2009; Gao and Liu, 2009; Gao et al., 2010) developed based on the approach of Silver and Chan (1991) was applied to the broadband seismograms to obtain the polarization direction of the fast wave and the splitting time. A total of 84 pairs of well-defined splitting parameters were obtained (Fig. 1). The average fast direction is $22.0 \pm 11.7^\circ$ from the North, which is sub-parallel to the strike of most regional tectonic features including the Rio Grande rift and Cenozoic faults in the area (Fig. 1). The average splitting time is 1.2 ± 0.3 s that is similar to the global average for continental areas (Silver, 1996). The waveforms, particle motion patterns and all the other related information for each of the measurements can be found at

<http://web.mst.edu/~sgao/XKS/KilHole/all/meas.html>.

4-4. Mineral compositions, microstructures, and fabric analyses

We have studied six Kilbourne Hole peridotites, which span the modal ranges of lherzolite and harzburgite. In all samples the aluminous accessory phase was spinel, as is common for Cenozoic North American peridotite xenoliths (Wilshire et al., 1988). The silicate minerals have high Mg# ($\text{Mg}^{2+}/(\text{Mg}^{2+} + \text{Fe}^{2+})$), with Fo = 89–91 for olivine, En = 89–92 for orthopyroxene, and Mg# = 90–93 for clinopyroxene. Spinel exhibits a moderate depletion in Cr# ($\text{Cr}^{3+}/(\text{Cr}^{3+} + \text{Al}^{3+})$), ranging from 0.06 to 0.21 for lherzolite and from 0.22 to 0.51 for harzburgite. Based on texture, modal mineralogy, and chemical composition, the samples can be divided into three distinct groups. The first group comprises fine-grained (<2 mm) lherzolite with a tabular, equigranular texture (Fig. 2a). The second group consists of protogranular lherzolite (Fig. 2b); although its chemistry is still fertile, the fabric of these rocks is different from those of the first group. Although most previous studies of Kilbourne Hole xenoliths (e.g., Bussod and Irving, 1981) have considered only these two groups, we also identified a third group comprising porphyroclastic harzburgite (Fig. 2c). Xenoliths in this group are characterized by strong foliation and the whole-rock and mineral chemistries (Cr# in spinel) are consistent with melt depletion (Perkins and Anthony, 2011; Table 1). Using the thermometers of Brey and Köhler (1990), the equilibration temperatures (calculated at 2 GPa) of the three groups are also distinct: fine-grained lherzolite (KH41, KH29) has the lowest temperature (1009–1040°C), protogranular to porphyroclastic lherzolite (KH43, KH54) has temperatures of 1049–1102°C, and porphyroclastic olivine-rich peridotites (KH22, KH25) have the highest temperatures (1094–1152°C; Table 1). Together with phase relations

(Perkins and Anthony, 2011; Takahashi et al., 1993), these ranges imply that Kilbourne Hole xenoliths were derived from depths of 35 – 60 km, within the uppermost mantle. The difference in temperature in three textural types suggests that the subcontinental mantle beneath Kilbourne Hole is rheologically and chemically layered.

The peridotite xenoliths contain a foliation and a lineation defined by the alignment of spinel crystals; we have analyzed their microstructures using thin sections cut perpendicular to the foliation and parallel to the lineation (i.e., XZ sections). To examine the conditions of deformation in more detail, and to evaluate the effects of the seismic properties on rocks beneath the rift zone, we have focused on the CPOs of three common minerals: olivine, orthopyroxene, and clinopyroxene. These observations were obtained by electron backscatter diffraction (EBSD) using the SEM-EBSD facility at Géosciences Montpellier, France. The EBSD patterns were generated by the interaction of a vertical incident electron beam with a polished thin section, tilted at 70°, in a scanning electron microscope (JEOL JSM 5600). The diffraction pattern was projected onto a phosphor screen and recorded using a digital CCD camera. The resulting image was then processed and indexed in terms of crystal orientation using the CHANNEL5 software distributed by Oxford Instruments HKL. For each sample, we obtained CPO maps covering almost the entire thin section (usually 35 mm long and 20 mm wide), with sampling steps of 30 or 35 μm , depending on grain size; rates of indexation in the raw maps range from 50% to 80%. The measured CPOs are presented on equal-area, lower-hemisphere projections (Fig. 3). Most of the analyzed samples show a strong concentration in [010], with weak girdle of [100] and [001] in olivine. For orthopyroxene, although most of CPO patterns are weak, a (010)[001] pattern (shear direction is [001] and shear plane is

(010)) occurs in two oriented samples (i.e. KH22 and 25). Clinopyroxene CPO data show nearly random fabrics, except for KH22, which show a weak (010)[001] slip.

To characterize CPOs, we determined the fabric strength (J -index) and distribution density (pfJ -index) of the principal crystallographic axes (for definitions of the J -index and pfJ -index, see Mainprice et al., 2000; Michibayashi and Mainprice, 2004). Table 1 lists the number of measured olivine grains, the J -index values calculated for each xenoliths, and the maximum density and pfJ -index value for each pole Fig.. The J -index is the volume-averaged integral of the squared orientation densities; it has a value of unity for a random CPO and is infinite for a single crystal. Most natural peridotites yield values between 2 and 20 (Ben Ismaïl and Mainprice, 1998), and those of the present study range from 2.81 to 9.65 (Table 1).

To maximize the average seismic anisotropy, the orientation data for each sample were adjusted to an external reference frame in which the maximum V_p is parallel to the reference direction X, and the minimum V_p is parallel to the Z-axis (see also Fig. 4). Seismic properties for each samples are shown in Fig. 5. By combining data from each of the six xenoliths, the average of the sample was then calculated, with the same weighting applied to each measurement, regardless of the number of measurements acquired from each xenolith (Fig. 6a). Using this approach, olivine CPO data show b-axis fiber patterns characterized by a strong concentration in [010], with a weak girdle of [100] and [001]. For orthopyroxene, CPO data may indicate either or both (100)[001] and (010)[100] slip; the (100)[010] slip is the most readily activated, and thus the most common, slip system (Naze et al., 1987). In contrast, clinopyroxene CPO data suggest a nearly random fabric, with a weak concentration in (010) normal to the foliation (Fig. 6a).

4-5. Rock seismic properties

Seismic properties were computed by averaging individual grain elastic-constant tensors as a function of the CPO and modal composition of a sample. This method enables the calculation of the three-dimensional distribution of seismic velocities in an anisotropic polycrystalline aggregate (Mainprice and Humbert, 1994). In the present calculations, we used Voigt–Reuss–Hill averaging of single-crystal elastic constants at ambient conditions (Abramson et al., 1997; Chai et al., 1997; Collins and Brown, 1998). Because the geothermobarometric analysis in this study yielded temperatures of 950–1200°C and pressures of 1.3–1.8 GPa (Perkins and Anthony, 2011), we calculated the seismic properties assuming conditions of 1000°C and 1.5 GPa (Fig. 6b). This method has been described in detail previously (Pera et al., 2003; Tasaka et al., 2008).

On average, olivine CPOs have P-wave propagation that is fastest parallel to the highest density of [100], and is slowest parallel to the highest density of [010]; polarization anisotropies are highest in directions approximately normal to the highest density of [010]. The orientation of the polarization plane of the fastest S-wave (V_{s1}) indicates the orientation of the great circle containing the [100] maximum. The V_p of olivine range from 7.58 to 8.24 km/s; their anisotropy is 8.4% and $AV_{s_{max}}$ is 6.88%. For orthopyroxene CPOs, the average anisotropies are small: V_p range between 7.72 and 7.78 km/s, their anisotropy is 0.8%, and $AV_{s_{max}}$ is 1.72%. Although clinopyroxene has weaker CPOs and smaller measured values than orthopyroxene, its seismic anisotropy is larger: V_p range between 8.28 and 8.61 km/s, their anisotropy is 3.9%, and $AV_{s_{max}}$ is 2.22%.

To assess the effect of grain size, we also calculated seismic properties from grid data obtained from CPO maps (Fig. 6c). The distributions of seismic properties

calculated in this way are very similar to those listed above based on a single measurement per grain (Fig. 6b), although individual velocity and anisotropy values calculated from grid data shown an increase compared to that from single measurement data per grain (e.g., for olivine, V_p range between 7.45 and 8.42 km/s, their anisotropy is 12.3%, and $AV_{S_{max}}$ is 9.17%). In this paper, we prefer the seismic properties based on the grid data (Fig. 6c) to those based on a single measurement per grain (Fig. 6b) for the following interpretations, which contains the effect of grain size, and thus it will provide more realistic seismic properties.

4-6. Variation in seismic properties as a function of modal composition

Based on the modal composition of peridotites (four lherzolites and two harzburgites), we recalculated the seismic properties for mean compositions of dunite (Ol_{100}), harzburgite ($Ol_{78}Op_{16}Cpx_6$), and lherzolite ($Ol_{64}Op_{23}Cpx_{13}$; Fig. 7). Using this approach, P-wave propagation is fastest parallel to the highest density of [100] and is slowest parallel to the highest density of [010], and polarization anisotropies are highest at directions approximately normal to the highest density of [010]. V_p/V_{s_1} and V_p/V_{s_2} ratios are highest for propagation directions that are normal and parallel, respectively, to the highest density of [100] of olivine. Although these anisotropy patterns do not change significantly as olivine volume fraction decreases, P- and S-wave velocities and anisotropies decrease. Because olivine is the primary mineral in peridotites, it is likely that peridotite anisotropy is defined mainly by the characteristics of olivine.

We have calculated variations in seismic properties as a function of modal composition for the structural planes of XY for horizontal shear, XZ for lateral shear, and YZ for vertical shear (Fig. 8); in these figures, gray shaded squares represent

ranges in the modal compositions of peridotite xenoliths from this study. To estimate the effect of modal composition on seismic properties, we varied the mineral composition from 100% olivine to 50% olivine + 50% pyroxene, by the alternating stepwise addition of 10% orthopyroxene or clinopyroxene. In Fig. 8, we have extrapolated variations in V_p anisotropy, the maximum V_s anisotropy, V_p , the anisotropy of V_s , the average of V_p , the deviation of V_p , and V_p/V_s with respect to the olivine volume fraction, assuming propagation direction of seismic wave is vertical. As a result, the effect of the second most abundant phase on seismic properties is highly dependent on structural orientation. V_p anisotropy decreases as the volume fraction of olivine decreases (Fig. 8a), whereas average V_p , unlike other factors, increases with the addition of clinopyroxene (i.e., decreasing olivine abundance; Fig. 8b, d). V_p/V_s does not differ significantly as a function of modal olivine abundance.

4-7. Discussion: Seismic anisotropies beneath the Rio Grande rift

Because the peridotite xenoliths in this study erupted recently (10 ka), they provide a snapshot of the “present” mantle composition beneath the region in central New Mexico known as the Rio Grande rift. Isotopic studies suggest that all lithosphere that formed or was reworked during past tectonics events are preserved (Anthony, 2005). Kilbourne Hole peridotite xenoliths come from a depth range of 35 – 60 km, the lowest-temperature samples potentially represent lithospheric mantle, whereas those from higher temperatures may represent the asthenosphere. CPO patterns are characterized by a strong concentration of [010], which show normal distribution compared to another peridotite xenoliths from a continental margin setting in Knippa, Texas (Satsukawa et al., 2010). In addition, some seismic properties are different

between the two sets of xenoliths, such as polarization anisotropies, which have maximums approximately parallel to the foliation for Kilbourne Hole peridotite xenoliths, but normal to foliation for Knippa peridotite xenoliths (Satsukawa et al., 2010).

The geometry and strength of seismic anisotropies are generally estimated using measurements of shear-wave splitting, which can place constraints on both the delay time and polarization direction of fast shear-wave propagation. Shear-wave splitting results indicate a delay time of 0.45–2.13 s with the average splitting time 1.2 ± 0.3 s within the Rio Grande rift (Fig. 1).

Continental rifting is a complex process involving deformation of the lithosphere, asthenospheric flow, and partial melting. Because each of these processes may result in seismically anisotropic structures, it is difficult to discriminate between the effects of rock anisotropy, recent mantle flow, and aligned cracks (Gao et al., 1997). In addition, Vauchez et al. (2000) showed that an anisotropy due to preferentially oriented anisometric melt pockets may add to the asthenospheric CPO-induced anisotropy beneath the active part of a rift. In this paper, we present seismic properties obtained from peridotite xenoliths from Kilbourne Hole, which we use to discuss rock seismic properties, as well as other mineral phases.

Lherzolite xenoliths generally contain orthopyroxene in higher abundances than clinopyroxene, which is a result of the selective removal of clinopyroxene from primary mantle lherzolite by partial melting. In spite of its small volume fraction, clinopyroxene has a significant effect on seismic properties (Fig. 8). It is also interesting to note that in the case of harzburgite ($Ol_{78}Opx_{16}Cpx_6$) and lherzolite ($Ol_{64}Opx_{23}Cpx_{13}$) mineral compositions, S-wave anisotropy is lower than results calculated from either orthopyroxene or clinopyroxene alone (Fig. 8c). This may

reflect an offset of the S-wave anisotropy (AVs) caused by interactions between orthopyroxene and clinopyroxene (Fig. 6b, c).

The magnitude of the delay time depends on the strength of the anisotropy and the thickness of the anisotropic layer. To explain the variability in splitting times near Kilbourne Hole, the thickness (T) of an anisotropic layer can be described by $T = (100 \text{ dt} \langle V_s \rangle) / AV_s$ (e.g., Pera et al., 2003). Although the original orientation of the Kilbourne Hole xenoliths was lost during transport to the surface, we know from their mineral compositions that they were derived from the uppermost lithospheric mantle (Perkins and Anthony, 2011). We have calculated the thickness of the anisotropic layer with our averaged sample (Fig. 6) using the average splitting time (1.2 s) for three different structural orientations. This allowed us to assess the degree to which the CPO data are consistent with models in which horizontal extension, lateral shear, or upwelling are invoked to explain the observed delay time (Fig. 9). Using this approach, we obtain anisotropic layer thicknesses (for models of lateral shear, upwelling, and horizontal extension, respectively) of 70-110, 100-180 and 260-350 km for a delay time of 1.2 s (Fig.). Of these results, only the lateral shear and upwelling models yield thicknesses consistent with geothermobarometric evidence that the peridotite xenoliths came from a depth of 35 – 60 km. Because the study region is an active rift zone, these two models are also suitable from a geological perspective. For example, Vauchez et al. (2000) proposed that anisotropies measured in the Rio Grande rift were caused by a transtensional deformation of the lithospheric mantle during rifting, as indicated by the consistent obliqueness of the polarization direction of the fast shear wave to the rift trend. However, it should be noted that when a delay time of 1.2 s is used, our calculated thicknesses of the anisotropic layer are still greater than those indicated by geothermobarometric evidence (25 km; Fig. 9).

Other factors, such as the alignment of melt lenses in the low-velocity zone, or cracks infilled by fluid, may provide a more likely explanation for the observed seismic anisotropy, and seismological studies do favor the existence of melts beneath the Rio Grande rift. A wide zone of low velocity situated beneath the Rio Grande rift, at a depth of 65 to 125 km, is clearly visible in LA RISTRA data obtained using both surface wave inversions (West et al., 2004) and tomography (Gao et al., 2004). Velocities from depths of 55 to 90 km beneath the rift axis are 10% slower than those beneath the Great Plains, which is consistent with the presence of small amounts of partial melt (West et al., 2004). Thus, SKS splitting measurements in the Rio Grande rift could also be caused by magma-filled cracks (e.g., Gao et al., 1997).

Seismological studies using travel-time tomography reveal the existence of a low-velocity zone within the mantle wedge (e.g., Nakajima and Hasegawa, 2004). The V_p/V_s ratio provides constraints on mantle composition, in particular for low-velocity zones in the mantle wedges (e.g., Nakajima et al., 2001). Several models have been proposed to explain spatial variation of V_p/V_s ratios, including the presence of fluids or melts for high ratios of V_p/V_s (Takei, 2002), or changes in mineralogical composition (e.g., orthopyroxene enrichment) for low ratios of V_p/V_s (Wagner et al., 2006).

Enrichment in orthopyroxene is widely reported for peridotite xenoliths (Griffin et al., 2008; Soustelle et al., 2010); V_p/V_s ratios calculated from spinel peridotite xenoliths from Avacha volcano in Kamchatka, vary from 1.72 to 1.75, and decrease with increasing orthopyroxene content (Soustelle and Tommasi, 2010). In addition, V_p/V_s ratios from different tectonic settings show a better correlation with the abundance of orthopyroxene than that of olivine (Afonso et al., 2010). In our model, V_p/V_s ratios vary from 1.68 to 1.78 (Fig. 8f) and decrease with increasing of

orthopyroxene composition, but the ratios are almost insensitive to the degree of clinopyroxene enrichment in all of our models (upwelling, lateral shear, and horizontal extension). As a result, the variability in V_p/V_s ratios is minimal for our natural peridotite compositions (harzburgite: $Ol_{78}Opx_{16}Cpx_6$; lherzolite: $Ol_{64}Opx_{23}Cpx_{13}$). Thus, we predict that for most of the upper mantle, compositional variations are unlikely to alter V_p/V_s ratios to a detectable degree in terms of current seismological methods.

As discussed above, the use of models that consider only mineral CPOs makes it difficult to produce realistic thicknesses for the anisotropic layer, or meaningful V_p/V_s ratios from rock seismic anisotropies. Another possibility is to use the preferential orientation of melt-lenses as an additional phase in the models. By applying the approach developed by Mainprice (1997), Vauchez et al. (2000) used simulations to show that if melt is contained in isometric or weakly anisometric pockets, an increase in melt fraction alone does not significantly increase the anisotropy of an aggregate. In contrast, if even small amounts of melt (e.g., 4%) collect in thin lenses parallel to the foliation, they can double the anisotropy produced by the mineral CPO, indicating that melt lenses may contribute significantly to seismic anisotropy within the rift itself. Nakajima et al. (2005) evoked the existence of melt-filled pores, combined with a specific effective aspect ratio and volume fraction for the pores, to explain the observed low-velocity anomalies in NE Japan, which cannot be explained by the thermal effect alone. For a depth of 40 km, this approach results in 1–2 vol.% melts, present as thin cracks or dikes with aspect ratios of 0.02–0.04, whereas a depth of 65 km yields 0.04–0.05 vol.% melt with an aspect ratio of ~ 0.001 .

We can compare the shear wave splitting of $dt = 1.2 (\pm 0.3)$ s for the Rio

Grande rift to another well-studied rift zone in Ethiopia (where the splitting is greater and varies from 1.7 to 2.5 s; Kendall et al., 2005). In addition, APM (absolute plate motion) direction is nearly parallel to the rift for the Rio Grande, whereas in Ethiopia, it is almost perpendicular. Considering these observations and that degree of melting is rather small in the Rio Grande rift, the model that has the maximum CPO related shear wave splitting with Y vertical (i.e., the lateral shear model) is more realistic for the Rio Grande, even if a small amount of melt is present. The orientation of APM direction with respect to the rift axis is also more compatible with lateral shear.

In this study, we propose a schematic model for the structure of the uppermost mantle beneath the Rio Grande rift, based on evidence from peridotite xenoliths from the Kilbourne Hole maar, derived from depths of 35 – 60 km (Fig. 10). Model of lateral shear is likely to contribute to the thickness of the anisotropic layer (Fig. 9). Moreover, the vertically planar structure of these models is in good agreement with the observed high concentrations of [010] in olivine, parallel to the Z direction. In the lateral shear model (considered relative to the XZ plane), the polarization direction of V_{s1} (the fastest S-wave) is in the XY plane (Fig. 4). Because the shear-wave splitting direction is parallel to the rift axis, we assume that the Z direction is normal to the rift axis (Fig. 10), which is most reasonable from a geological perspective.

The degree of S-wave anisotropy generated by peridotite xenoliths alone is limited; it is 4.81 to 8.82 %, however it requires approximately 13 to 17 % to produce the realistic thickness (25km). Therefore the existence of melt in thin cracks or dikes could be required to cause a significant increase. It is well established that melt reduces shear-wave velocity; consequently, seismic anisotropy is sensitive to the orientation of melt pockets. It is likely that melt pockets could be ideally oriented parallel to the XY plane in either model, so that the velocity of S2 may be lower,

resulting in an increase in anisotropy (Fig. 10). In contrast, the orientation of such melt pockets parallel to the YZ plane would reduce the velocity of S1 but would not affect S2 velocities (Fig. 10), resulting in lower anisotropies. We can estimate the melt fractions and shape of melts pocket to produce high S-wave anisotropy (13 to 17 %) if we apply the result of simulation by Vauchez et al. (2000) to this study. In case of 20 (shape ratio; 20:20:1), melt fraction is 1.5 to 2.5%. On the other hand, it requires 6 to 9 % of melt fraction for the case of 5 (5:5:1).

4-8. Conclusions

Continental rifting is a complex process involving deformation of the lithosphere, asthenospheric flow, and partial melting. Because each of these processes may result in seismically anisotropic structures, it is difficult to discriminate between the effects of rock anisotropy, recent mantle flow, and aligned cracks. In this paper, we present detailed petrofabric data and seismic properties obtained from peridotite xenoliths from Kilbourne Hole to illuminate the origin and significance of shear-wave splitting in the uppermost mantle beneath this active rift. Peridotite xenoliths from the Kilbourne Hole maar consist of spinel lherzolite, harzburgite, and dunite, which were derived from the uppermost mantle, from depths of 35 to 60 km. Since Kilbourne Hole erupted at approximately 10 ka, these xenoliths represent essentially current conditions beneath the Rio Grande rift. Their crystallographic preferred orientations indicate the preservation of olivine b-axis fiber fabrics with a strong concentration of [010] with girdles of [100] and [001].

We consider three geodynamic models for the source region of these xenoliths: horizontal extension, lateral shear, and upwelling, using a volume fraction of orthopyroxene and clinopyroxene appropriate to each model. Although lherzolite

xenoliths generally contain orthopyroxene in higher abundances than clinopyroxene, clinopyroxene has a significant effect on seismic properties, in spite of its small volume fraction. After calculating seismic properties and consideration of absolute plate motion direction, we conclude that these xenoliths are derived from a lateral shear zone (vertical foliation (XY plane) and horizontal lineation within the plane of the foliation (X-axis)). However, the degree of seismic anisotropy generated by peridotite xenoliths alone is limited, so that the existence of melt in thin cracks or dikes could be required to cause a significant increase. If melt pockets are oriented parallel to the XY plane in either model, the velocity of S2 may be lower, resulting in an increase in anisotropy. In contrast, the orientation of such melt pockets parallel to the YZ plane would reduce the velocity of S1 but would not affect S2 velocities, resulting in lower anisotropies.

Overall, the peridotite xenoliths demonstrate the possible presence of an anisotropic layer within the uppermost mantle lithosphere, which could be related to 'frozen' deformation. We have calculated the maximized seismic properties of peridotite xenoliths in order to determine their contribution to seismic observations of the active region of the Rio Grande rift. In summary, the seismic properties determined for the mantle beneath the rift suggest that the region has a complex tectonic pattern, with probable lateral shear, in addition to the presence of melt as thin cracks or dikes.

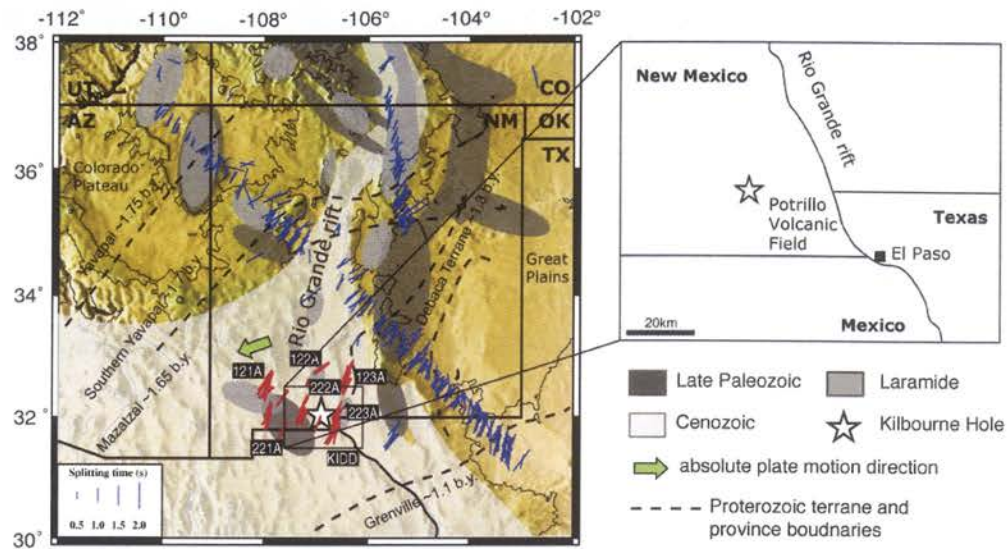


Figure 1. Location of Kilbourne Hole maar in New Mexico, USA and shear-wave splitting parameters plotted above the XKS ray-piercing points at 100 km depth. The red bars are new splitting data in this study, and the blue bars are from the first uniform shear-wave splitting database (Liu, 2009). Note that in the original paper (Liu, 2009), the data were plotted above 200 km piercing points. To be consistent with the new results, we re-calculated the locations to 100 km depth. Absolute plate motion direction (green arrow) of North America calculated based on the HS3-NUVEL1A model (Gripp and Gordon, 2002). The orientation of the red bars represents the polarization direction of the fast wave, and the length of the bars is proportional to the splitting time which ranges from 0.45 s to 2.13 s, and the average splitting time is 1.2 ± 0.3 s. Uplift traces are modified after Wilson et al. (2003).

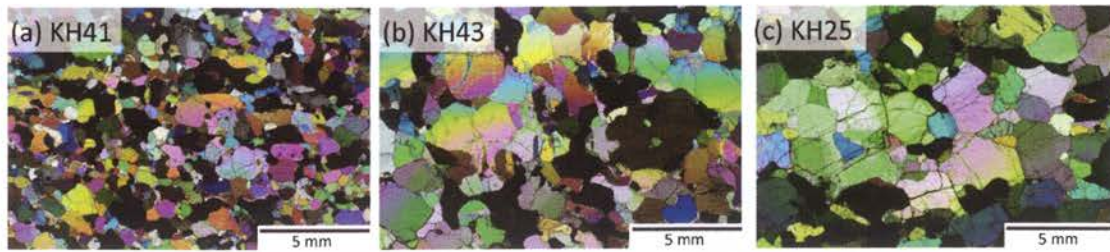


Figure 2. Photomicrographs of peridotite xenoliths from Kilbourne Hole (scale bar is 5 mm). (a) KH41, fine grained lherzolite. (b) KH43, protogranular lherzolite. (c) KH25, porphyroclastic harzburgite.

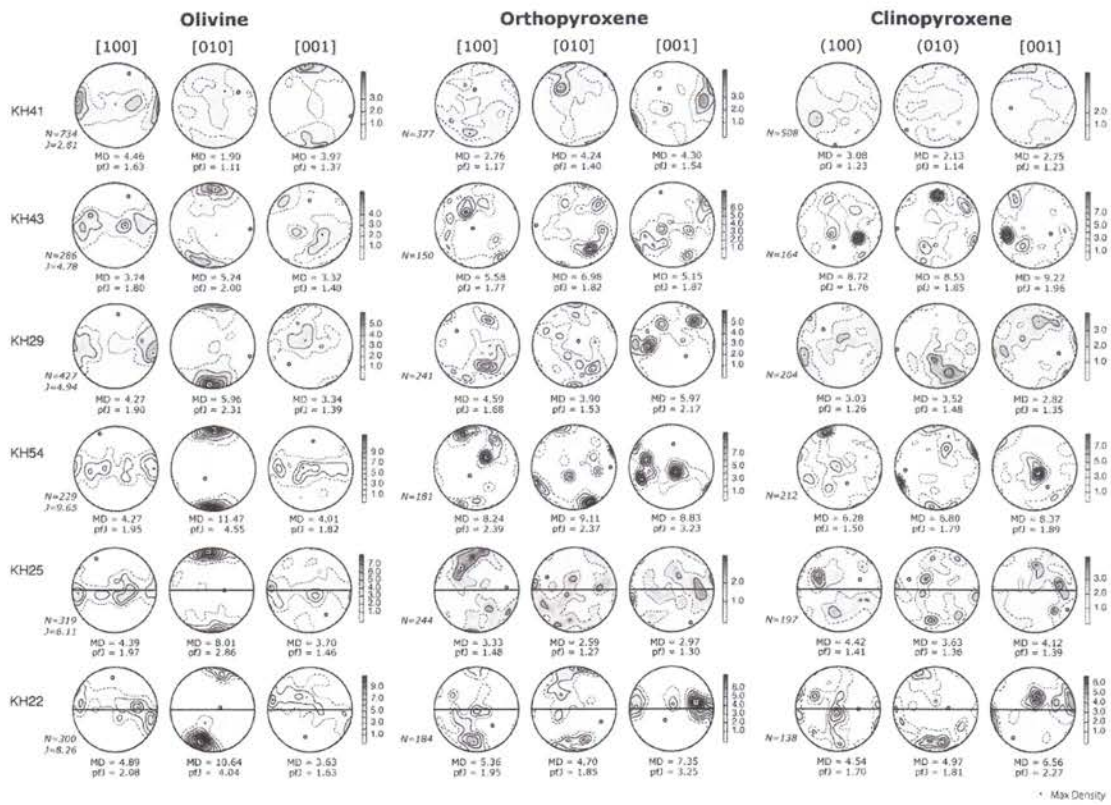


Figure 3. Crystallographic preferred orientations (CPOs) of olivine, orthopyroxene and clinopyroxene. Lower hemisphere, equal-area stereographic projections, contours at one multiple of uniform distribution. N is number of measured grains.

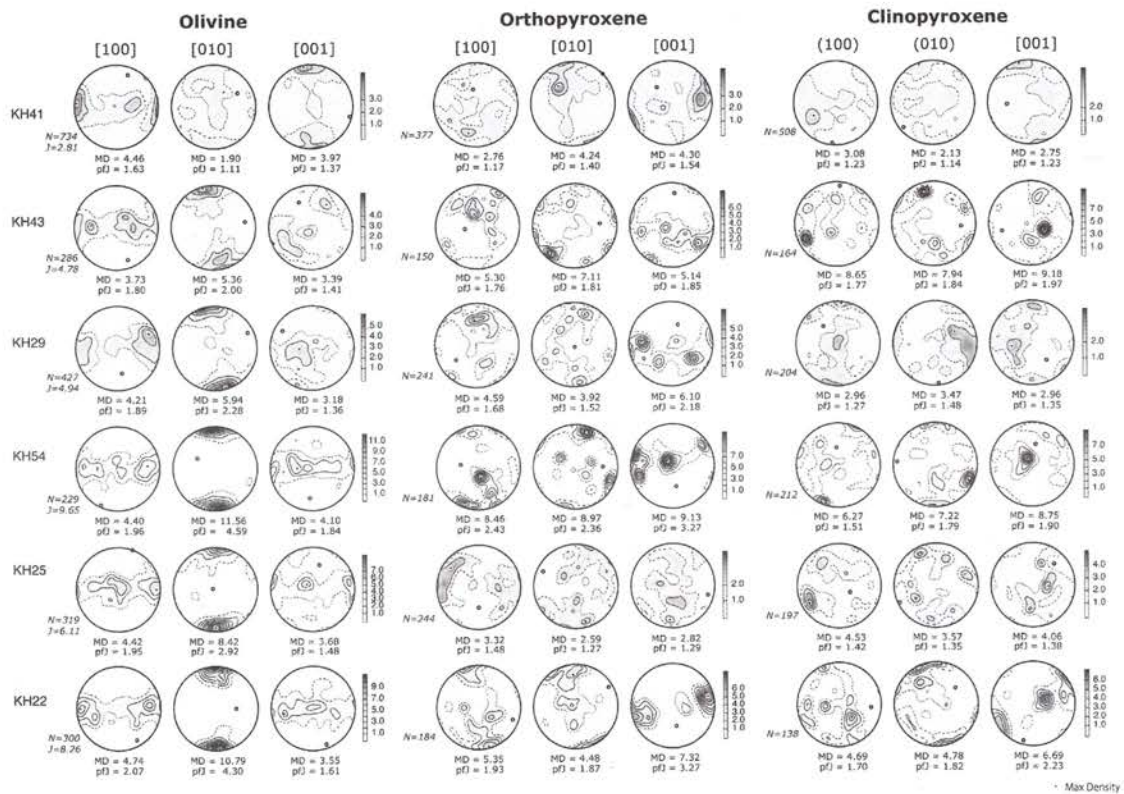


Figure 4. Olivine, orthopyroxene and clinopyroxene CPOs. To maximize the average seismic anisotropy in Fig. 6 the orientation data for each sample were rotated with the result that the maximum V_p is parallel to the reference direction X (east or west in the pole figure) and the minimum V_p is parallel to Z (north or south in the pole figure).

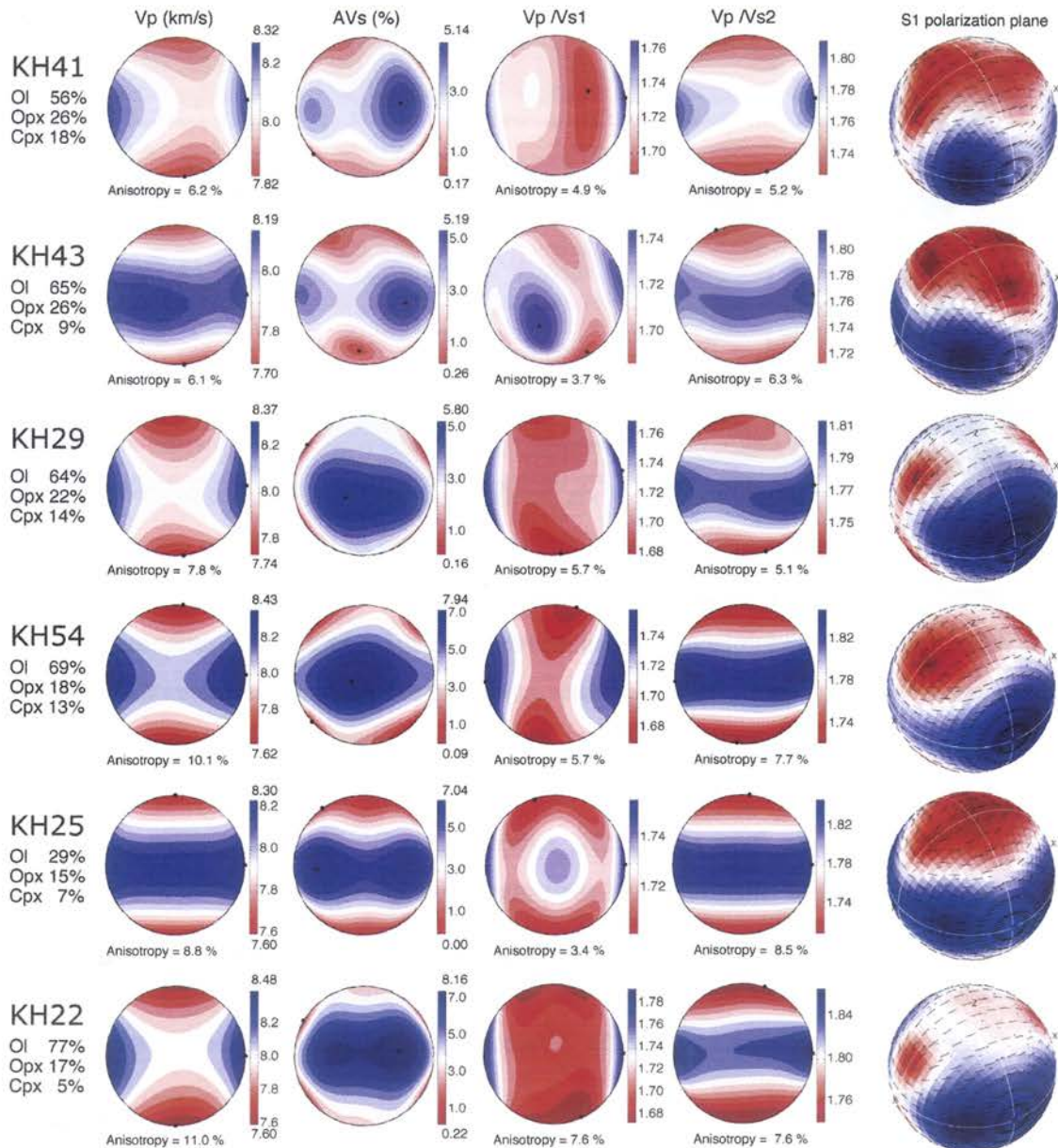


Figure 5. Seismic properties. From left to right: P-wave velocity, S-wave anisotropy, V_p/V_{s1} , V_p/V_{s2} , and the polarization of the fast shear wave S_1 .

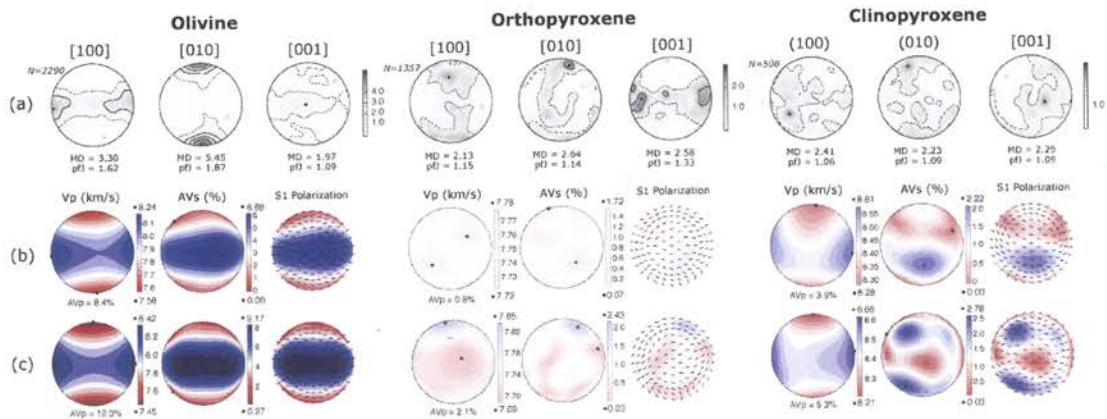


Figure 6. (a) Crystallographic preferred orientation (CPO) data for the average sample, obtained by summing the CPO of six peridotite xenoliths. CPOs are plotted on equal-area, lower-hemisphere projections, contours are multiples of the uniform distribution, N is the number of measurements, pfJ is an index of fabric intensity, and MD is the maximum density. (b, c) Seismic properties of the average sample for each mineral (olivine, orthopyroxene, and clinopyroxene) computed from the average CPOs based on one-point-per grain data (b), and grid data (c), at a temperature of 1000 °C and pressure of 1.5 GPa. Contours are multiples of uniform density; V_p is the three-dimensional distribution of the P-wave velocity; anisotropy is $(V_{p_{max}} - V_{p_{min}})/(V_{p_{mean}})$; AVs is the three-dimensional distribution of the polarization anisotropy of S-waves due to S-wave splitting; and S1 is the polarization plane of the fast split S-wave (S1), as a function of the orientation of the incoming wave relative to the structural frame of the sample. Each small segment represents the trace of the polarization plane at the point at which S1 penetrates the hemisphere.

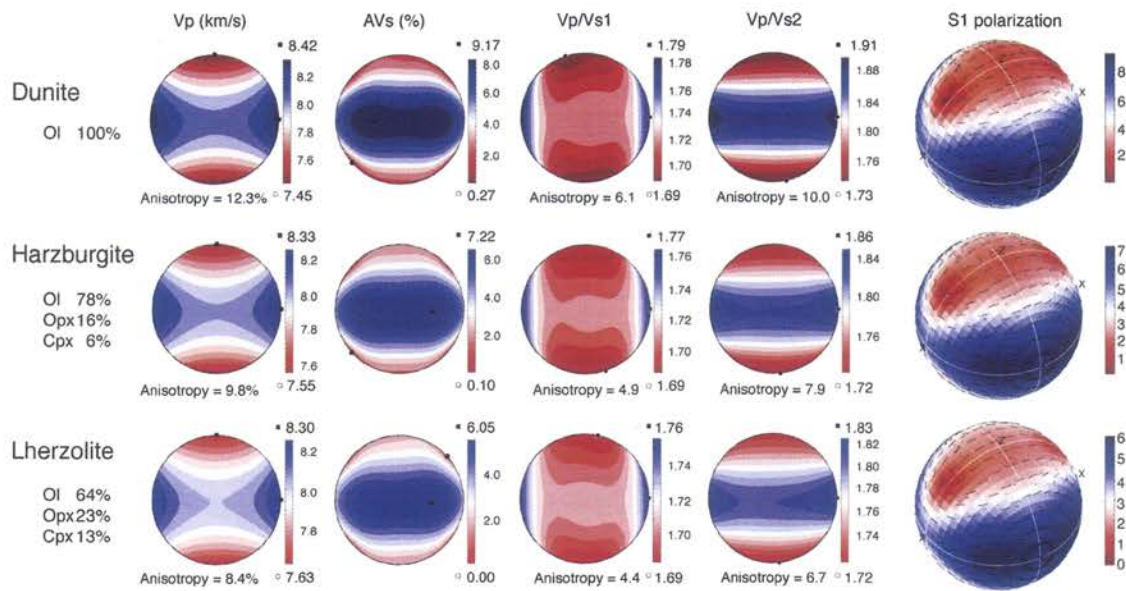


Figure 7. Seismic properties of the average dunite, harzburgite, and lherzolite (from Fig. 6a) at a temperature of 1000 °C and a pressure of 1.5 GPa. From left to right: P-wave velocity, S-wave anisotropy, V_p/V_{s1} , V_p/V_{s2} , and the polarization of the fast shear wave S_1 .

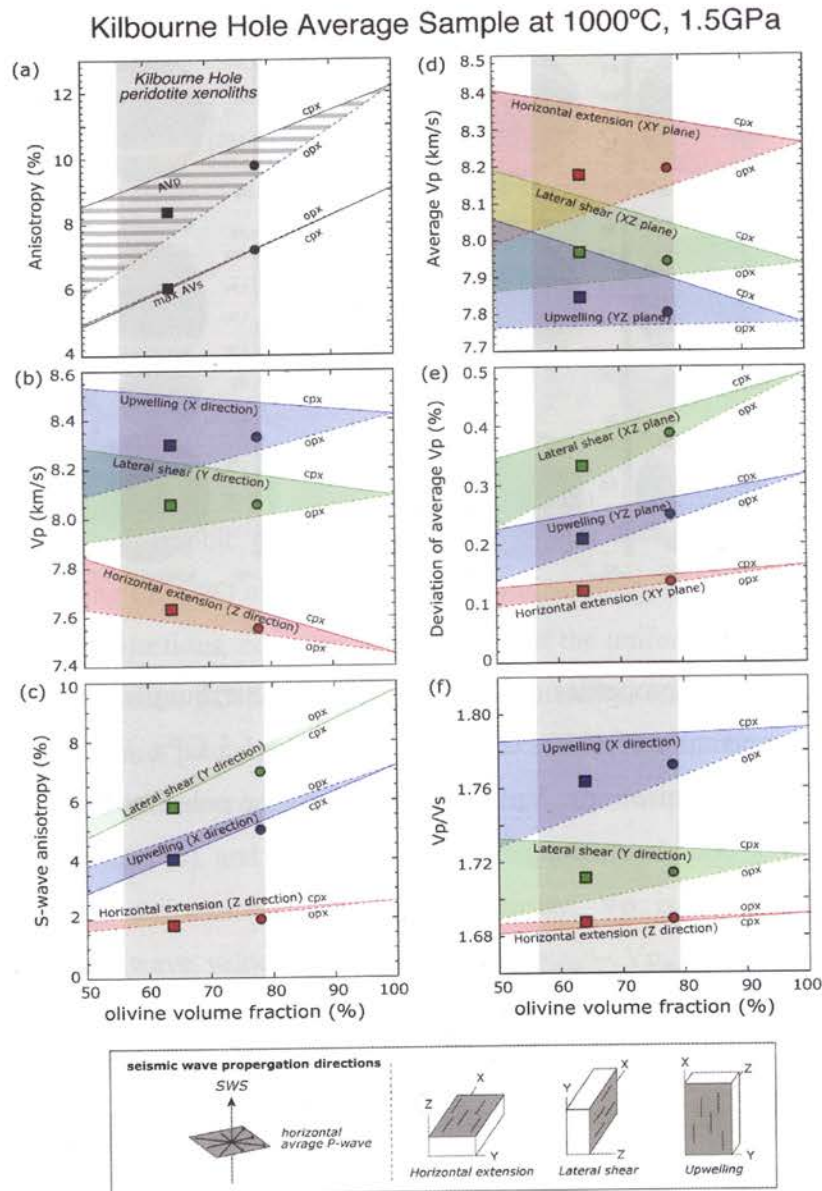


Figure 8. Variations in (a) V_p anisotropy and the maximum V_s anisotropy, (b) V_p , (c) S-wave anisotropy, (d) Average V_p , (e) Deviation of average V_p and (f) V_p/V_s as a function of mantle composition at a temperature of 1000 °C and pressure of 1.5 GPa. Solid lines represent compositions ranging from 50% olivine + 50 % clinopyroxene to 100% olivine; broken lines represent compositions ranging from 50% olivine + 50 % orthopyroxene to 100% olivine. Contours are shown for three geodynamic models: red for horizontal extension, green for lateral shear, and blue for upwelling. Within the box, the shaded area represents the plane of the foliation, and lines indicate lineation. Symbols relate to the mean composition of the peridotites: squares for lherzolite and circles for harzburgite.

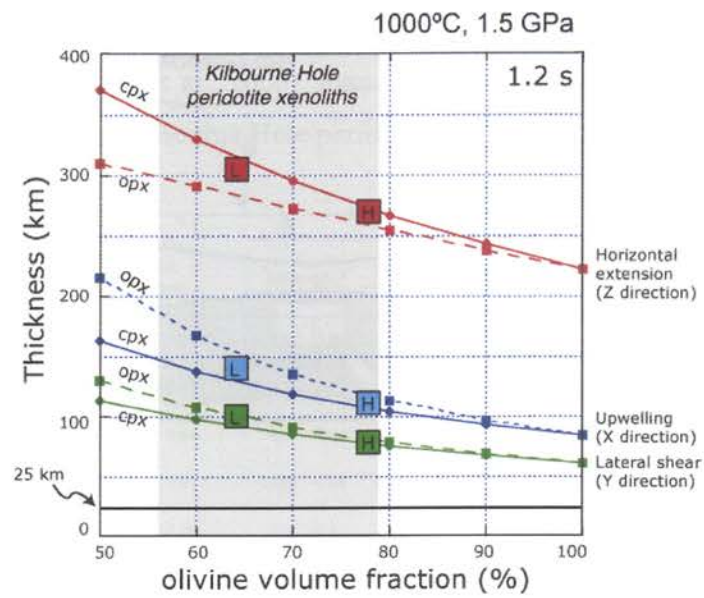


Figure 9. Relationship between olivine volume fraction and required thickness of the anisotropic layer in Kilbourne Hole, as indicated by peridotite xenoliths. Delay times is 1.2 s. H and L are the harzburgite and lherzolite shown in Fig. 7, respectively.

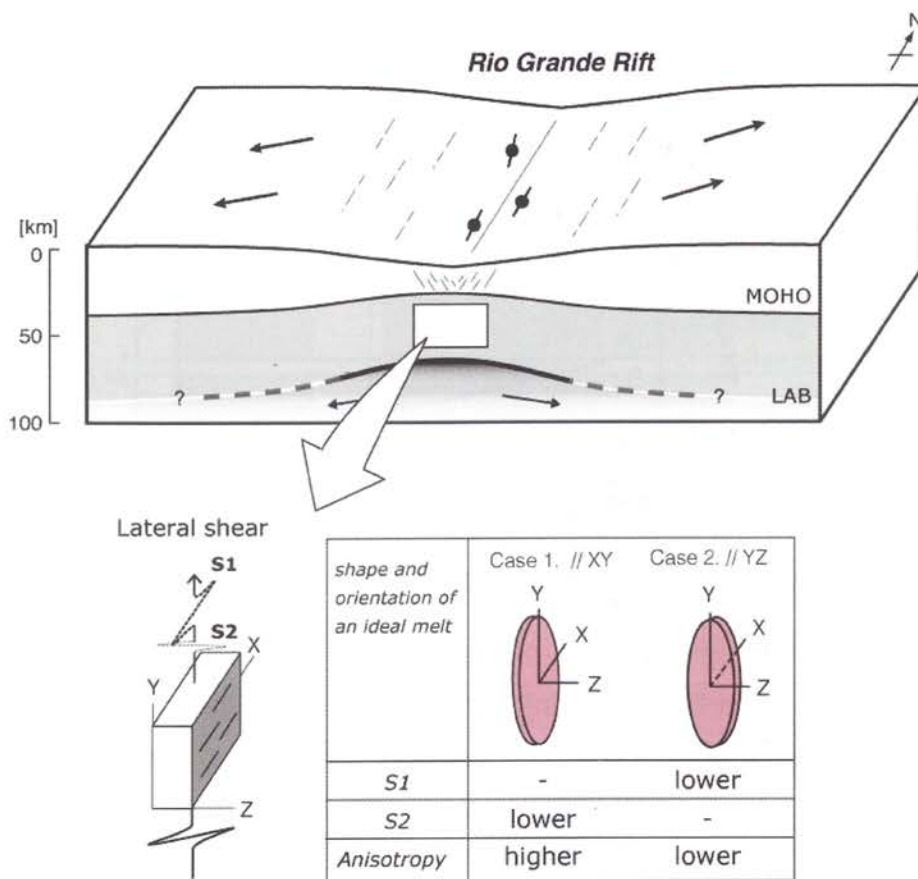


Figure 10. Schematic summary of results showing the possible type of model (lateral shear zone), and the shape and orientation of an ideal melts beneath the Rio Grande rift.

Table 1. Lithology, modal composition (%), number of measurements, J-index values (calculated after Mainprice et al., 2000), max density (MD), pJ values, and temperature (Na/Opx-Cpx) for the six Kilbourne Hole peridotite xenoliths studied here.

Sample number	lithology	mode (%)			grain size (mm)	CPO olivine									T (°C)	Ol Mg#	Sp Cr#
		ol	opx	cpx		N	J	[100] axis		[010] axis		[001] axis					
								MD	pJ	MD	pJ	MD	pJ				
KH41	fine-grained lherzolite	56	26	18	0.52	734	2.81	4.46	1.63	1.90	1.11	3.97	1.37	1009	0.90	0.10	
KH29	fine-grained lherzolite	64	22	14	0.49	286	4.78	3.74	1.80	5.24	2.00	3.32	1.40	1040	0.89	0.07	
KH43	protogranular lherzolite	65	26	9	0.69	427	4.94	4.94	1.90	5.96	2.31	3.34	1.39	1049	0.89	0.10	
KH54	protogranular lherzolite	69	18	13	0.91	229	9.65	4.27	1.95	11.47	4.55	4.01	1.82	1102	0.89	0.11	
KH22	porphyroclastic harzburgite	77	17	5	1.20	319	6.11	4.39	1.97	8.01	2.86	3.70	1.46	1152	0.91	0.32	
KH25	porphyroclastic harzburgite	78	15	7	1.02	300	8.26	4.89	2.08	10.64	4.04	3.63	1.63	1094	0.91	0.22	

Ol: olivine; Opx; orthopyroxene; Cpx: clinopyroxene; Sp: spinel; N: Number of measurements; J: J-index; MD: Maximum density; T: temperature, respectively.

Chapter 5

Uppermost mantle anisotropy beneath the southern Laurentian margin: Evidence from Knippa peridotite xenoliths, Texas

Originally Published in modified form as “Uppermost mantle anisotropy beneath the southern Laurentian margin: Evidence from Knippa peridotite xenoliths” by T. Satsukawa, K. Michibayashi, R. Urmidola, E. Y. Anthony, J. Pulliam and R. Stern, *Geophysical Research Letters*, **37** (L20312), doi:10.1029/2010GL044538, 2010, All rights reserved.

Abstract.....	157
5-1. Introduction	157
5-2. Geological setting	158
5-3. Microstructural and Fabric Analyses.....	159
5-4. Rock Seismic Properties	162
5-5. Seismic data	162
5-6. Discussion and Conclusions.....	163
Figures and Tables	167

Abstract

Peridotite xenoliths from southern Texas consist of spinel lherzolite, harzburgite and minor dunite. Based on phase relations and temperature of equilibration, Knippa xenoliths come from the uppermost mantle, 40-70 km deep. Knippa xenoliths provide rare snapshots of upper mantle processes and compositions beneath south-central Laurentia. They preserve olivine a-axis fiber fabrics with a strong concentration of (100) and girdles of (010) and (001). Assuming a lithospheric mantle having a horizontal flow direction parallel to fast directions, the mantle lithospheric fabric revealed by the xenoliths mostly explains the magnitude of shear-wave splitting observed along the southern margin of the Laurentian craton.

Key words: peridotite xenoliths; Texas, mantle flow; crystallographic preferred orientation; seismic anisotropy

5-1. Introduction

The nature of ocean-continent transitional lithosphere is complicated. Recent passive seismological investigations provide fruitful avenues of inexpensive research to begin interrogating the lithosphere. Measuring shear-wave splitting (SKS) images the orientation and degree of polarization of mantle fabrics, and constrain models for the formation of these fabrics, including the mantle beneath south central North America (Gao et al., 2008). In spite of the robustness of SKS measurements, it is often not clear if anisotropy inferred from these measurements resides in the mantle lithosphere or asthenosphere (Fouch and Rondenay, 2006). Here we are interested in understanding fabrics for mantle xenoliths from southern Texas, and use this

information to understand shear-wave splitting for upper mantle beneath the northern margin of the Gulf of Mexico (GoM) (Fig. 1). A previous study documented significant shear wave splitting beneath this region, with fast directions parallel to the Texas GoM continental margin (Fig. 1; Gao et al., 2008). They noted that SKS splitting reached an apparent maximum where the crust was thinnest and discussed the parallelism of the observed mantle anisotropy and the SE edge of the Laurentian cratonic keel.

In this study, we present new SKS results and petrofabric data for spinel peridotite xenoliths from Knippa, Texas, and use these results illuminate the origin and significance of shear wave splitting beneath southern Laurentia (Fig. 1). The seismic anisotropy resulting mainly from olivine crystallographic preferred orientations (CPO) tends to show a maximum seismic velocity parallel to the direction of plastic flow within the upper mantle (Nicolas and Christensen, 1987). Assuming that shear-wave splitting reflects mineral CPO, we can use CPO measured in mantle xenoliths to better understand uppermost mantle structure beneath south central North America and the elastic coefficients of minerals to evaluate the delay time along ray paths.

5-2. Geological setting

A quarry near Knippa, Texas (Fig. 1) exposes Late Cretaceous basanites containing upper mantle xenoliths. This is the only known mantle peridotite locality in Texas (Young and Lee, 2009). Mantle xenoliths were carried up by Late Cretaceous (~87 Ma) quite primitive nephelinites of the Balcones Igneous Province (BIP) (Griffin et al., 2010). BIP volcanoes approximate the boundary between the ~1.1-1.4 Ga southernmost Laurentian (Texas) craton and Jurassic age transitional lithosphere along

the GoM margin. The transitional lithosphere also involves the deformed rocks of the Ouachita fold belt (Keller et al. 1989).

Knippa peridotites are spinel lherzolite and harzburgite (plus minor dunite) consisting of olivine (Ol), orthopyroxene (Opx), clinopyroxene (Cpx) and spinel (Sp). Minerals have high Mg#: Ol (Fo_{89-91.6}), Opx (En_{89.3-92.3}) and Cpx (Mg#=90.4-93.4). Cr# (atomic Cr/(Cr+Al)) in Sp show moderate depletion, ranging from 0.14-0.21 for lherzolite to 0.25-0.36 for harzburgite, indicating that lherzolite experienced 5-9% melt depletion compared to 11-14% for harzburgite. Temperatures determined using the Ca in Opx thermometer (Brey and Köhler, 1990) range between 900 and 1000 °C. Based on the ubiquitous presence of spinel and absence of garnet (Takahashi et al., 1993), and temperature of equilibration, Knippa xenoliths come from the uppermost mantle, from depths of 40-70 km. These temperatures are high for a steady state geotherm, except for a lithosphere enriched in heat-producing elements (HPE) near the base of the lithosphere (Stein et al., 1993). Alternatively, the temperatures may represent transient conditions associated with BIP magmatism. Young and Lee (2009) note that Knippa peridotites are enriched in fluid-mobile trace elements (e.g., La) relative to fluid-immobile trace elements (e.g., Nb). They inferred that such fractionation reflects subduction-related metasomatism of Laurentian lithospheric mantle due to ~1 Ga plate convergence.

5-3. Microstructural and Fabric Analyses

In this study, we selected eight peridotite xenoliths for detailed petrophysical analyses to evaluate the effect of olivine CPO on seismic-wave properties. The xenoliths are coarse-grained and equigranular, with grain boundaries that range from triple junctions to smoothly curving boundaries. The spinels are elongate, bleb-shaped

and dark brown in plane-polarized light. Some spinels and Cpx show corroded rims. Olivine grains are large and commonly contain subgrain boundaries (Fig. 2a). Serpentine veins occur in two peridotite xenoliths and cut olivine grains (Fig. 2a). These serpentine veins are identified as lizardite by Raman spectroscopy at the University of Tokyo, Japan.

To examine deformation conditions in more detail, we measured the CPOs of olivine grains from highly polished thin sections using a scanning electron microscope equipped with an electron backscatter diffraction system (EBSD), housed at the Center for Instrumental Analysis, Shizuoka University, Japan. We determined Ol, Opx and Cpx crystal orientations, and visually checked the computerized indexation of the diffraction pattern for each crystal orientation.

The dominant slip system in olivine was determined from the orientations of the axes of subgrain rotation and CPO data (e.g., Satsukawa and Michibayashi, 2009). We rotated the CPO data based on the orientations of the axes of subgrain rotation, such that the “foliation” became horizontal and the “lineation” became E-W. From Subsequently, using data from the eight xenoliths, we calculated the average sample (1740, 533 and 282 measurements for Ol, Opx and Cpx, respectively), giving the same weight to each measurement, independently of the number of measurements in each xenoliths (Fig. 2b, Table 1). As a result, olivine CPO data show a-axis fiber patterns characterized by a strong concentration in (100) with weak girdles of (010) and (001), whereas the CPOs of enstatite and diopside show nearly random fabrics (Fig. 2b).

We analyzed the characteristics of subgrain rotation with the aim of identifying the slip system that operated in olivine during deformation (e.g., Satsukawa and Michibayashi, 2009). Subgrains are formed by either edge dislocations (representing the edge of a half-plane in a distorted crystal lattice) or screw

dislocations (representing a twisted lattice). A subgrain boundary can be thought of as a plane that separates two parts of an originally continuous crystal that have rotated slightly with respect to each other. Such boundaries can therefore be classified according to the orientation of the rotation axis relative to the subgrain boundary. Subgrain boundaries that form with rotation axes oriented parallel to the boundary are known as tilt walls; those with axes oriented normal to the boundary are known as twist walls (Passchier & Trouw, 2005). A tilt wall (see below Fig. 1 from Satsukawa and Michibayashi, 2009) consists of an array of edge dislocations with the same Burgers vector (slip direction). The slip direction is indicated by the axis oriented normal to the subgrain boundary. The rotation axis was calculated based on the orientations of the lattices of the paired subgrains (using the software HKL channel5, Oxford Instruments). The remaining axis of the three axes of olivine was interpreted to be oriented normal to the slip direction, upon the slip plane. As an example of an analysis of subgrain rotation described in Satsukawa and Michibayashi (2009).

To describe the CPO of a mineral, the orientations of the crystallographic axes of each crystal must be known with respect to an external reference frame (XYZ), which is usually defined in terms of the rock structure (e.g., X parallel to the lineation, Y normal to lineation within the foliation plane, and Z normal to the foliation). However, the external reference frame could not be determined for this sample because of their small size (< 3 cm) and lack of macroscopic structure. The orientations of many of the thin sections are therefore random or independent of the orientation of the foliation and lineation. Accordingly, to obtain the CPO data required to determine the slip system, we measured CPOs and calculated the axes of subgrain rotation, and compared the data obtained from the two methods.

For this sample, the two methods yielded consistent results; therefore, we

rotated the CPO data based on the orientations of the axes of subgrain rotation, such that the “foliation” became horizontal and the “lineation” became E–W.

5-4. Rock Seismic Properties

We calculated the seismic properties of the peridotite xenoliths from single crystal elastic constants, crystal density, and the CPO of Ol, Opx, and Cpx, assuming different scenarios: either a composition of 100 % Ol (for each sample as well as the mean), or the actual modal composition of the rock (dunite, lherzolite and harzburgite). The elastic constants and averaging scheme used in our calculations are same in *Michibayashi et al. (2009)*.

Fig. 2(c) and Table 1 presents the seismic properties of the peridotite xenoliths. The maximum seismic anisotropy of S-waves varies between 5.09 and 8.26% for 100% olivine, whereas average samples vary between 4.35 and 6.12% along with variations of mineral composition (Table 1). Polarization anisotropies of most samples have two maxima girdles on each side of a plane normal to the (100) maximum, whereas the minimum birefringence occurs for propagation directions close to the (100) maximum (Fig. 2c). The orientation of the polarization plane of the fastest S-wave systematically marks the orientation of the great circle that contains the maximum concentration of (100) (Fig. 2b). These anisotropic patterns are quite common globally, as previously reported (e.g., Mainprice et al., 2000).

5-5. Seismic data

Five broadband, three-component seismographs were deployed between Junction and San Antonio, TX from February through August 2008 at an average spacing of 28 km (Table 2) (Pulliam et al., 2009). The transect extended from the

Laurentian craton to the edge of the craton and, possibly, onto the stretched and thinned transitional crust of the Texas Gulf Coastal Plain. Receiver function results for the same stations indicate crustal thickness of 32 km at GCP05 vs. 45 km at GC01 (Pulliam et al., 2009).

For each temporary station, as well as for the permanent ANSS station JCT, SKS splitting measurements were made for 22 deep-focus ($h > 50$ km) teleseismic events with magnitudes greater than 6.0 using the Matlab-based SplitLab software (Wüstefeld et al., 2008). SplitLab simultaneously computes splitting parameters via three independent techniques: (a) the rotation-correlation method (e.g. Bowman and Ando, 1987), which maximizes the cross-correlation between the radial and transverse component of the SKS phase, (b) the minimum energy method (Silver and Chan, 1991), which minimizes the energy on the transverse component, and (c) the minimum eigenvalue method (Silver and Chan, 1991).

For measurements to be accepted we required that results for both the minimum energy and rotation-correlation methods each display clear minima in their error surfaces and be consistent with each other, i.e., within 0.2 s of delay time and 20° with respect to fast polarization direction. On average, only five events satisfied these criteria for our stations during their seven-month deployment. Fig. 1 shows averaged results for the best five events at each station, including the permanent station JCT, located near Junction, TX. Our results for Junction (Table 2) confirm the results reported previously by Gao et al. (2008). Results from the five temporary stations show rapidly increasing delay times but only small changes in the fast polarization direction as one progresses from Junction toward the southeast.

5-6. Discussion and Conclusions

The region that spans the northern GoM margin underwent two complete cycles of continental rifting (ca. 540 and 170 Ma) and collisional orogeny (ca. 1000 and 350 Ma) along the southern flank of Laurentia (e.g., Thomas, 2006). These events include the late Mesoproterozoic Grenville orogeny, early Cambrian rifting and passive margin formation, late Paleozoic Ouachita orogeny during the final stages of assembly of Pangaea, and formation of the modern continental margin accompanied by brief seafloor spreading and oceanic crust formation during the Jurassic (ca. 165 Ma).

The lithosphere that formed or was reworked during these tectonics events is preserved across a region that extends from the Grenville province of the craton (Anthony, 2005) to Jurassic oceanic crust in the GoM. The Moho beneath the Texas passive margin is approximately 40 km deep (Gao et al., 2008). As described above, Knippa peridotites come from 40-70 km deep (Raye et al., 2009). Therefore, we consider it likely that the Knippa peridotite xenoliths are derived from the uppermost mantle lithosphere. We note that the region is dominated by alternate episodes of extension and compression (Fig. 1). The associated mantle fabric could preserve some of this deformation, suggesting an important potential for tectonic inheritance and overprinting.

The strong gradient in shear wave splitting observed along the traverse near Knippa implies a shallow, i.e. lithospheric, source for the anisotropy. One possible explanation invokes flow in the lithospheric mantle as a mechanism for aligning olivine fast axes: the Coastal Plain appears to have a crust that is on the order of 10 km thinner than the craton (Mickus et al., 2009). This would allow a correspondingly thicker lithospheric mantle and, therefore, longer paths for SKS to accumulate splitting times, assuming flow channeled around the cratonic keel aligns crystals'

a-axes effectively.

Gao et al. (2008) argued that the magnitude of anisotropy must be 5.5–10% (Fig. 3) in order to produce the observed 0.9 to 1.6 s splitting time, assuming that the lithosphere beneath the region is 70 km thick (Fig. 1). Our measurements constrain the intrinsic anisotropy within the lithospheric mantle, although the original orientations of the peridotite xenoliths were lost during their volcanic transport to the surface (e.g. Michibayashi et al., 2009). As noted above, the average Knippa peridotite shows 4.35 to 6.12% anisotropy depending on mineral compositions, whereas individual samples vary range from 5.09 to 8.26% in case of Ol 100% (Fig. 3). Consequently, the observed delay times are mostly explained by the seismic properties of the mantle lithosphere sampled by Knippa peridotite xenoliths.

To explain the variation of splitting time near station JCT is complicated. The thickness (T) of an anisotropic layer is given by $T = (100dt\langle V_s \rangle) / AV_s$, (e.g., Pera et al., 2004). Accordingly, the observed delay time (0.5 – 1.5 s at JCT) can be explained by the seismic properties of our peridotite xenoliths for an approximately 50 to 150 km thickness. However, it is difficult to produce the observed variation in split times over lateral distances of a few tens of km with this explanation alone. For example, if we use the AVs of a highly deformed sample (sample number; 10 shown in Table 1), the long delay time (1.5 s) requires 85 km thickness. Therefore, a more likely candidate is deformation caused by collision between Laurentia and Gondwana during the late Paleozoic, which produced large amounts of deformation, including the folded Ouachita mountain chain. Varying amounts of deformation would produce corresponding variations in the alignment of olivine fast directions in the lithospheric mantle. Such deformation can both vary significantly over short distances and can vary in its effectiveness in aligning crystals. In the case of Oman ophiolites, major

shear zones seem to have developed at the contact between a flowing asthenosphere (young) and a frozen lithospheric (old) wall, a thermal boundary inducing a characteristic asymmetry (Nicolas and Boudier, 2008). Consequently, the long delay time can be explained by fabric variation, that is, peridotites beneath the transitional crust could preserve greater deformation from the Paleozoic Ouachita orogeny (young) rather than the lithosphere beneath the Mesoproterozoic craton (old). Overall, the Knippa peridotite xenoliths demonstrate the possible occurrence of an anisotropic layer in the uppermost mantle lithosphere that could be related to 'frozen' deformation associated with the alternate processes of extension and compression beneath the southern Laurentian margin.

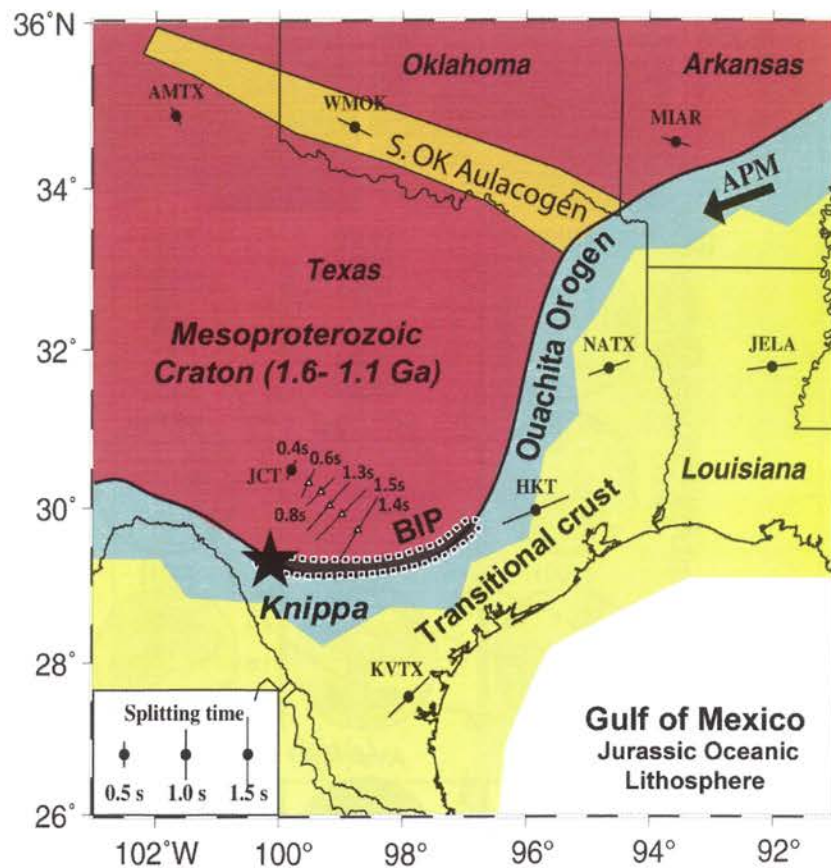


Figure 1. Location of Knippa and principal tectonic features of the south central USA. The peridotite xenoliths are from Knippa quarry in Uvalde County, TX (star). SKS results shows shear-wave splitting time and shear-wave fast directions. Circles; results after Gao et al. (2008), triangles; results from this study (Table 2). The arrow represents the absolute plate motion (APM).

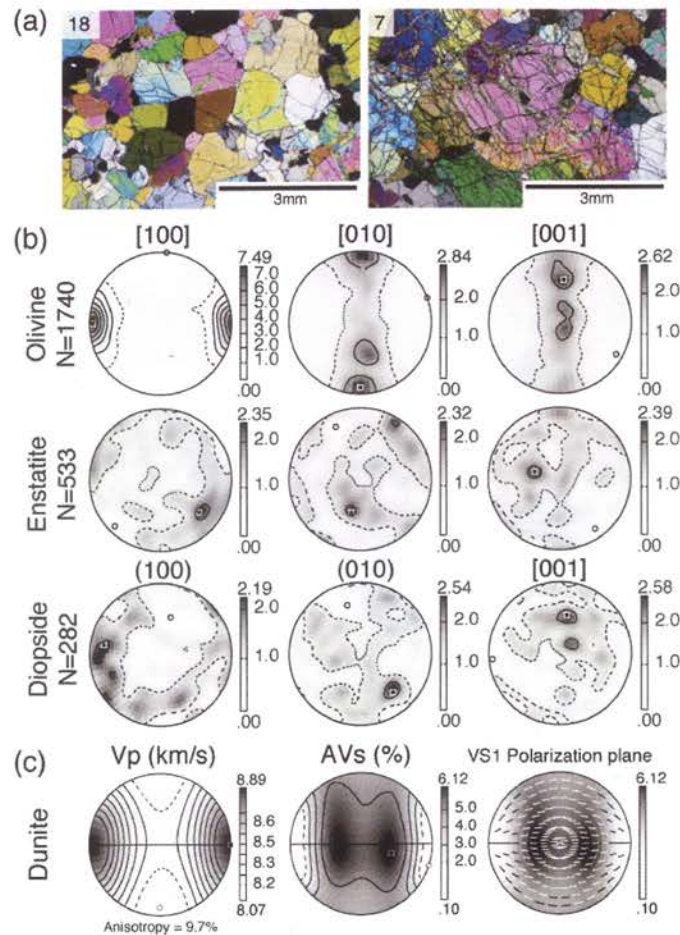


Figure 2. (a) Photomicrographs of Knippa peridotite xenoliths. In some samples, olivines are cut by serpentine veins. Scale bar is 3 mm, 18 and 7 are sample number. (b) CPOs data of the average sample (Table 1) obtained by the EBSD technique. CPOs are plotted on equal-area, lower hemisphere projections. Contours are multiples of the uniform distribution. N is the number of measurements. (c) Seismic properties of the average sample computed from single crystal elastic constants, crystal density, and the average CPOs of olivine. Contours are multiples of uniform density. Vp is 3D distribution of the P-wave velocity. Anisotropy is $(V_{pmax} - V_{pmin}) / V_{pmean}$. AVs (seismic anisotropy of S-waves) is 3D distribution of the polarization anisotropy of S-waves owing to S-wave splitting. Vs1 plane is polarization plane of the fast split S-wave (S1) as a function of the orientation of the incoming wave relative to the structural frame of the sample. Each small segment represents the trace of the polarization plane on the point at which S1 penetrates the hemisphere.

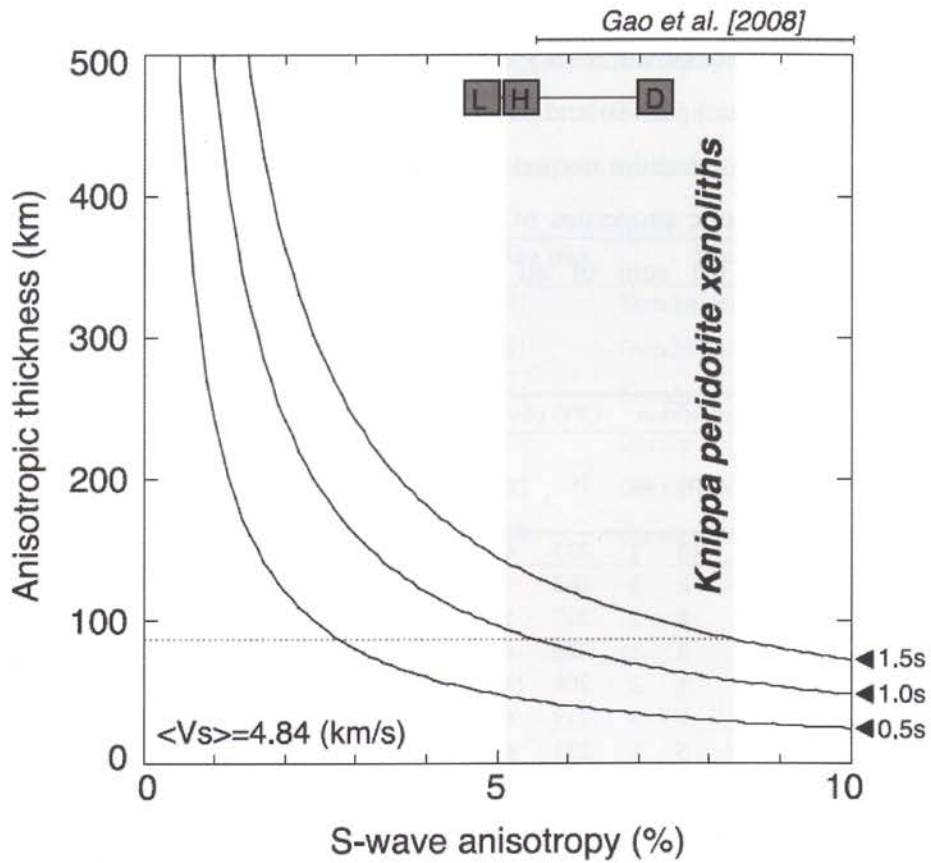


Figure 3. Relationship between S-wave anisotropy (AVs) and required thickness of anisotropic layer in Knippa peridotite xenoliths calculated as 100% olivine. Shear-wave splitting time is 0.5 to 1.5 s, from Gao et al. (2008). Gray area shows the range of AVs obtained by individual samples. D, H and L are dunite harzburgite, lherzolite of average sample shown in Table 1.

Table 1. Modal composition (%), number of measurements, J-index values (calculated after Mainprice et al., 2000) and seismic properties (V_p , AV_p , AV_s , V_{s1} , V_{s2}) for the 8 Knippa peridotite xenoliths studied here. The last three lines report, the crystallographic data and the seismic properties of the average sample. The average sample has been calculated from the sum of all measurements, giving the same weight to each measurement.

Sample number	Modal composition				CPO olivine		Seismic Anisotropy							
	ol	opx	cpx	sp	N	J	V_p (km/s)		AV_p (%)	AV_s (%)	V_{s1} (km/s)		V_{s2} (km/s)	
							Max	Min			Max	Min	Max	Min
1	63	25	10	2	225	4.60	8.81	8.09	8.4	5.09	4.97	4.86	4.86	4.66
3	69	20	8	3	202	5.29	8.83	8.09	8.7	5.59	5.01	4.84	4.85	4.64
6	70	20	8	2	217	5.55	8.98	8.06	10.8	7.35	5.03	4.84	4.87	4.60
9	82	15	2	1	220	4.61	8.82	8.07	8.9	6.13	4.98	4.84	4.88	4.64
10	80	13	5	2	208	11.42	9.04	8.07	11.3	8.26	5.06	4.82	4.87	4.59
13	68	20	9	3	219	6.05	8.98	8.02	11.4	7.34	5.03	4.86	4.89	4.59
16	81	14	5	1	231	6.67	8.94	8.02	10.8	6.81	5.00	4.85	4.90	4.60
18	75	20	4	1	218	5.94	8.79	7.97	9.8	6.36	5.03	4.80	4.85	4.66
AS (D)	100	0	0	0	1740	-	8.89	8.07	9.7	6.12	5.01	4.84	4.87	4.63
AS (H)	80	15	5	0	-	-	8.75	8.08	7.9	4.92	4.97	4.84	4.86	4.67
AS (L)	70	18	12	0	-	-	8.89	8.07	7.1	4.35	4.95	4.83	4.85	4.68

Ol: olivine; Opx; orthopyroxene; Cpx: clinopyroxene; Sp: spinel; N: Number of measurements; J: *J*-index; MD: Maximum density; AS: Average sample. D, H and L are dunite, harzburgite, lherzolite, respectively.

Table 2. Station locations and SKS splitting results from the 2008 broadband deployment. Delay times between the fast and slow polarization directions are indicated by δt ; the orientation of the fast polarization direction, with respect to north, is indicated by Φ .

Station	Latitude (°)	Longitude (°)	Elevation (m)	Sensor	δt	Φ
JCT	30.48	-99.8	581	Streckeisen STS2	0.42	28
GC01	30.33	-99.53	681	Guralp CMG-3ESP	0.57	24
GC02	30.2	-99.34	634	Guralp CMG-3ESP	0.8	44
GC03	30.02	-99.21	598	Guralp CMG-3T	1.3	42
GC04	29.91	-99.01	487	Guralp CMG-3ESP	1.5	46
GC05	29.73	-98.74	468	Guralp CMG-3ESP	1.44	34

Chapter 6

Microstructure and seismic properties at the spreading/rifting zone

6-1. Microstructural and petrological characteristics in the four peridotite xenoliths localities: a summary.....	173
6-2. The uppermost mantle evolution during the back-arc spreading ...	176
Figures	179

6-1. Microstructural and petrological characteristics in the four peridotite xenoliths localities: a summary

The uppermost mantle in the back arc region is the site of complex interactions between deformation, partial melting, fluid migration, and melts percolation. In order to constrain these interactions and their effects on olivine fabric, we have presented the detailed fabric analysis and calculated the seismic properties induced by rock anisotropies in Chapter 2-5. Figure 1 shows average olivine CPOs of each sample.

In Chapter 2, we analyzed microstructures, geochemical analysis, crystallographic preferred orientations (CPOs), and water contents of spinel peridotite xenoliths obtained from back arc region of Japan arc: Ichinomegata (NE Japan) and Oki-Dogo (SW Japan).

The mineral chemistry of Ichinomegata peridotites showed a typical residual peridotite trend, depleted in LREE (light rare earth element). Olivine CPO of Ichinomegata peridotites were consistent with slip on $(010)[100]$ and $\{0kl\}[100]$ (Fig. 1a), and the angle between the $[100]$ maximum concentration and the foliation decreased with increasing fabric strength. By using those angles, shear strain was estimated to vary from 0.31 to 4.26, and temperature variation possibly suggested that J -index increased with decreasing of depth. These observations indicated that a strain gradient revealed by the peridotite xenoliths studied could be related to back-arc spreading. Three directions have been identified within thin sections of Ichinomegata peridotites: foliation defined by pyroxene rich layers, the $[100]$ maximum concentration of olivine, and shape preferred orientation of olivine. From the relationships between these three axes, shear plane was considered to be parallel to the

[100] maximum concentration of olivine, not foliation. Those structural features were compatible with those found in the Oman ophiolite (Ceuleneer et al., 1988).

Oki-Dogo peridotites were affected by various degree of metasomatism by melt derived from the upwelling asthenosphere. Water content in pyroxenes was low, suggesting that water in peridotites was easily moved in melts if water was contained in rocks before the metasomatism. Because pyroxenes coexisting with olivine appear to retain their initial H contents than olivine even though the main minerals in the mantle (olivine, orthopyroxene and clinopyroxene) are nominally anhydrous (e.g., Peslier et al., 2002). Olivine CPO of Oki-Dogo peridotites was consistent with the (010)[100] slip system (Fig. 1b). Samples had low Mg# and showed relatively high concentration in [010], however there were no strong relationships among them. Although peridotite xenoliths from Oki-Dogo Island could be deformed in the presence of melt, there was no strong interaction between deformation and melts percolation.

In Chapter 3, we presented seismic properties obtained from peridotite xenoliths from Ichinomegata and Oki-Dogo to illuminate the origin and significance of shear-wave splitting in the uppermost mantle in the back arc region of Japan arc. Since the estimation of thickness of an anisotropic layer was about 20 km, Ichinomegata peridotite xenoliths demonstrated the possible occurrence of an anisotropic layer in the uppermost mantle lithosphere. Olivine forsterite contents in Oki-Dogo peridotites varied continuously from 86 to 90, so that seismic properties were calculated by taking into account the elastic constants and mineral density. Although the rock density and S-wave velocity decreased with increasing of olivine forsterite content, P-wave and S-wave anisotropies showed few significant changes.

In Chapter 4, we presented detailed petrofabric data and seismic properties obtained from peridotite xenoliths from Kilbourne Hole maar, New Mexico, to illuminate the origin and significance of shear-wave splitting in the uppermost mantle beneath the Rio Grande rift. Peridotite xenoliths consisted of spinel lherzolite, harzburgite, and dunite. Olivine CPOs indicated the preservation of b-axis fiber fabrics with a strong concentration of [010] with girdles of [100] and [001] (Fig. 1c). We consider three geodynamic models for the source region of these xenoliths: horizontal extension, lateral shear, and upwelling. After calculating seismic properties, we concluded that these xenoliths were derived from a lateral shear zone (vertical foliation (XY plane) and horizontal lineation within the plane of the foliation (X-axis)). However, the degree of seismic anisotropy generated by peridotite xenoliths alone was limited, so that the existence of melt in thin cracks or dikes could be required to cause a significant increase; the orientation of such melt pockets parallel to the XY plane in either model would result in an increase in anisotropy. As a result, the shear-wave splitting observed in the Rio Grande rift was a reflection of the lithospheric fabric and the presence of melts as thin cracks or dikes.

Knippa xenoliths provided rare snapshots of upper mantle processes and compositions beneath south-central Laurentia. In Chapter 5, we presented new SKS results and petrofabric data for spinel peridotite xenoliths from Knippa, Texas, and used these results to illuminate the origin and significance of shear wave splitting beneath southern Laurentia. Peridotite xenoliths consisted of spinel lherzolite, harzburgite and minor dunite. They preserved olivine a-axis fiber fabrics with a strong concentration of [100] and girdles of [010] and [001] (Fig. 1d). Assuming a lithospheric mantle having a horizontal flow direction parallel to fast directions, the mantle lithospheric fabric revealed by the xenoliths mostly explained the magnitude of

shear-wave splitting observed along the southern margin of the Laurentian craton. Consequently, the long delay time could be explained by fabric variation, that was, peridotites beneath the transitional crust could preserve greater deformation from the Paleozoic Ouachita orogeny (young) rather than the lithosphere beneath the Mesoproterozoic craton (old). Overall, the Knippa peridotite xenoliths demonstrated the possible occurrence of an anisotropic layer in the uppermost mantle lithosphere that could be related to 'frozen' deformation associated with the alternate processes of extension and compression beneath the southern Laurentian margin.

6-2. The uppermost mantle evolution during back-arc spreading

For the contribution to the understanding of back-arc spreading, the four localities have been chosen in this study. Schematic models showing the uppermost mantle during the back-arc spreading are presented in Fig. 2. Ichinomegata and Oki-Dogo peridotite xenoliths have documented distinct stages of spreading of the Japan Sea back-arc region, respectively.

Ichinomegata peridotites xenoliths preserved the normal seafloor spreading (Chapter 2), whereas Oki-Dogo peridotites preserved the extension and the thinning of continental crust (Fig. 2) (Chapter 2). For comparison, we have studied spinel peridotite xenoliths from another tectonic setting: Kilbourne Hole (New Mexico, USA; Chapter 4) and Knippa peridotites (Texas, USA; Chapter 5) (Fig. 3). Peridotite xenoliths from Kilbourne Hole represented the early stages of spreading in an active rift zone (Fig. 3a and Chapter 4), whereas Knippa peridotites xenoliths were derived from the mantle lithosphere that could have recorded deformations in relation to the thinning of continental crust (Fig. 3b and Chapter 5).

The uppermost mantle evolution in Ichinomegata peridotite xenoliths shows

possible evidence that preserved strain gradient field during the latest geological event, back-arc spreading (Chapter 2). Oki-Dogo peridotites show no clear change in microstructure and CPO with metasomatism, and the slip system is mostly (010)[100] rather than AG-type (Chapter 2). Thus, we do not observe pronounced changes in olivine CPO following metasomatism and there is no strong interaction between percolation of melts and deformation (Chapter 2). In contrast, there is strong concentration of [010] from Kilbourne Hole samples (Fig. 3a), which documents the deformation under the existence of fundamental melts due to the present continental rifting (Chapter 4).

The differences between the peridotite xenoliths from the Japan Sea side and Kilbourne Hole in Texas, USA, may result from differences of periods of time and a scale between them; whereas the scale of back-arc spreading is several hundreds kilometers and it had been continued for about 10 million years in Japan Sea (Chapter 2), Kilbourne Hole is located to Rio Grande rift where has been widespread extended during the past 35 million years (Chapter 4). The microstructure and geochemical characteristics observation in Oki-Dogo peridotite xenoliths were affected by the supply of upwelling-derived melts, in the end of the back-arc spreading, which may supply the trigger the termination of back-arc spreading and basins (Chapter 2). Olivine CPO of Knippa peridotites is consistent with slip on {0kl}[100] with strong concentration in [100] (Chapter 5). Knippa is located in Laurentian continental margin and records the deformation related to alternate extension and compression (Fig. 3c and Chapter 5). There are no samples in back-arc region that show strong fabrics like Knippa, indicating that this strong CPO could be developed during these continuous deformations.

Overall, in the initial stage of the back-arc spreading, the active spreading

starts (from the northeast parts in the case of Japan Sea) where the uppermost mantle deformed similar system to the mid ocean ridge spreading (Fig. 2b). After that, passive extension, which depending on the surrounding environments, was induced in the southwest region (Fig. 2b). There are no strong reactions between melt percolation and deformation in comparison with the continental rift zone, probably due to its small size and short period. In conclusion, this study showed the uppermost mantle evolution during the back-arc spreading, which is one of the keys for the understanding of its process, and provided several aspects of the contrasts between the back-arc spreading and the mid ocean ridge/continental rifting.

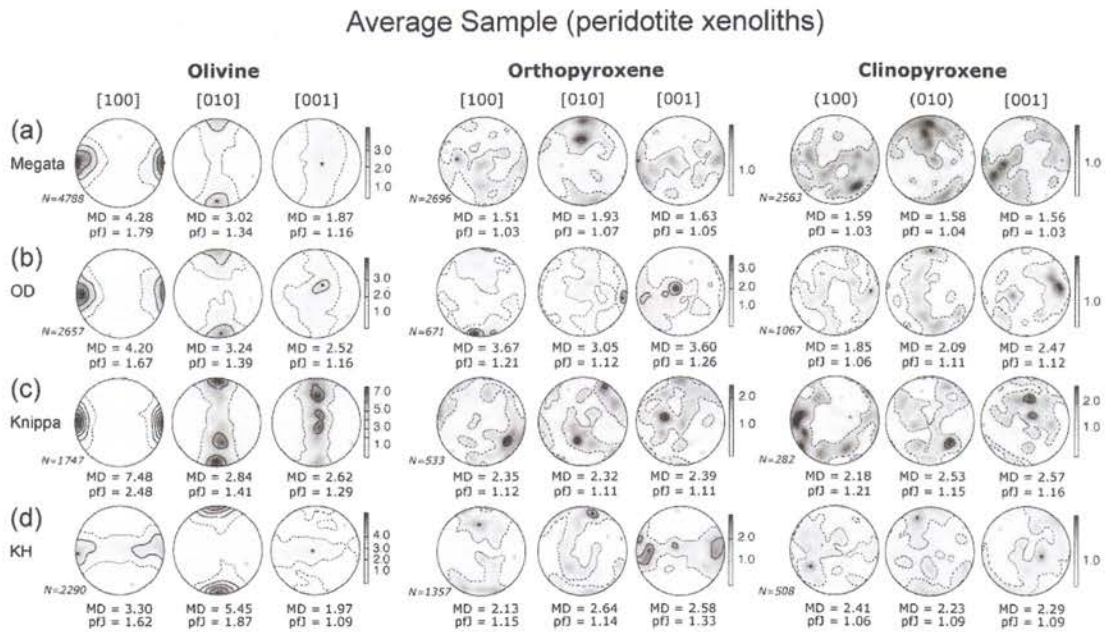


Figure 1. Crystallographic preferred orientation (CPO) data for the average sample, obtained by summing the CPO of each peridotite xenolith from (a) Ichinomegata, (b) Oki-Dogo, (c) Knippa, (d) Kilbourne Hole. CPOs are plotted on equal-area, lower-hemisphere projections, contours are multiples of the uniform distribution, N is the number of measurements, pfJ is an index of fabric intensity, and MD is the maximum density.

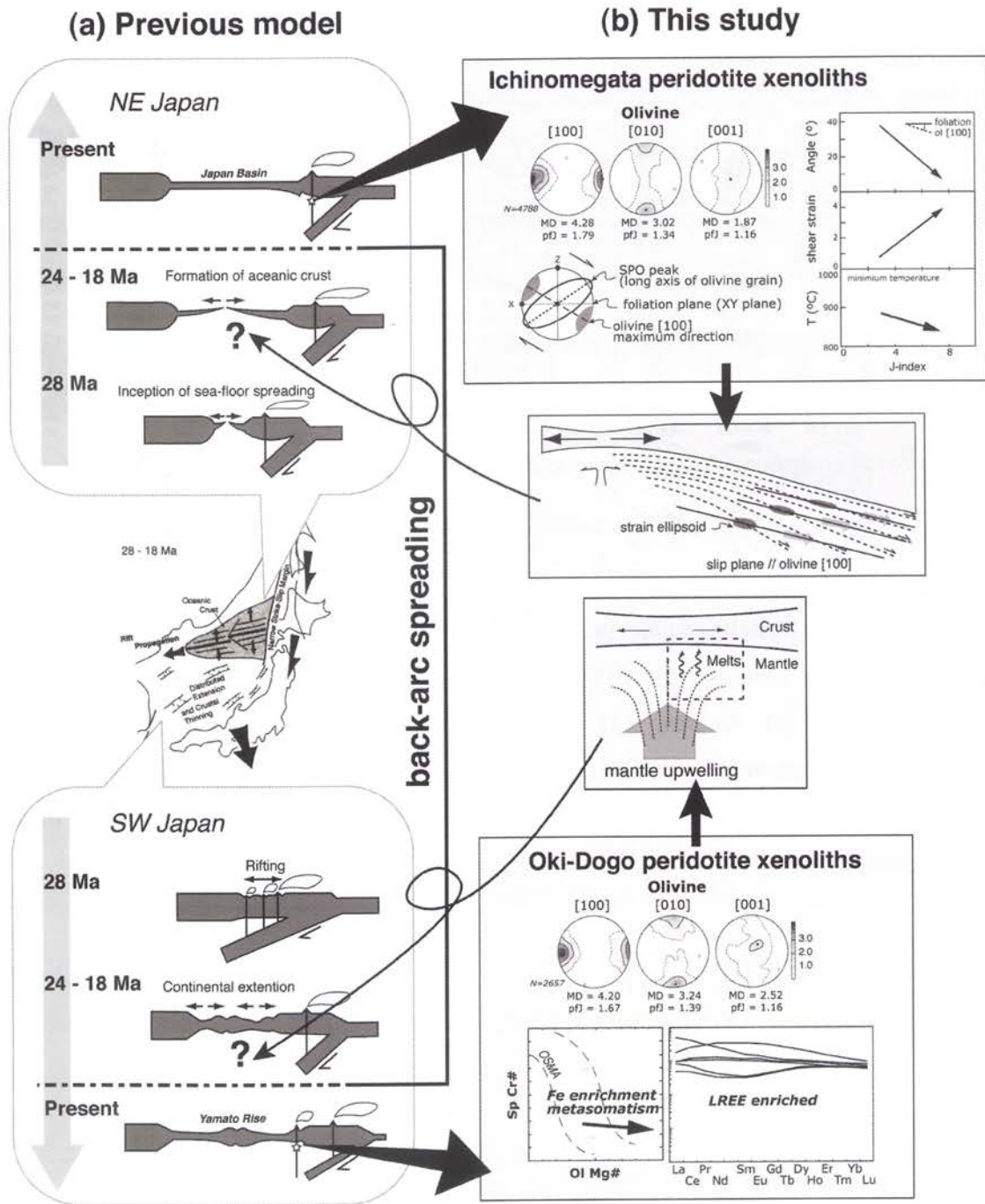
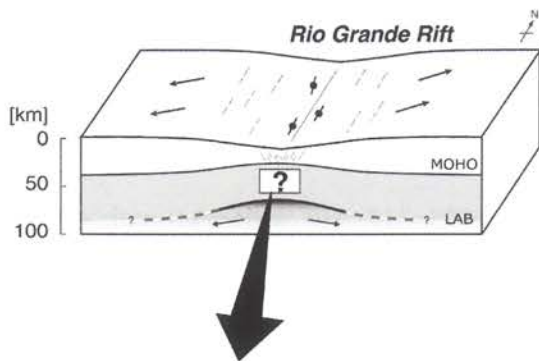
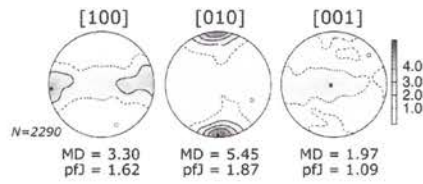


Figure 2. (a) Schematic model of the opening of the Japan Sea. Modified after Tamaki (1995). (b) A summary of microstructural and petrological characteristics in the Ichinomegata and Oki-Dogo peridotite xenoliths and a schematic model of the uppermost mantle evolution during the back-arc spreading.

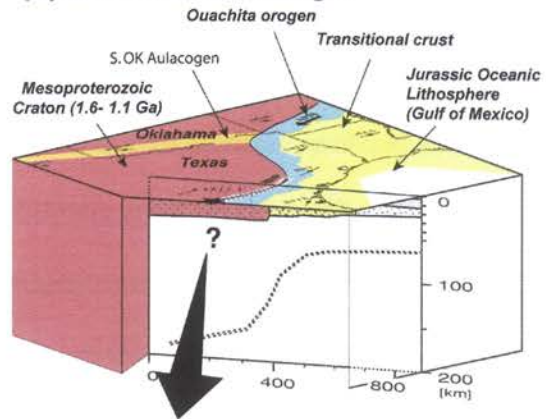
(a) Continental rifting



Kilbourne Hole peridotite xenoliths



(b) Continental margin



Knippa peridotite xenoliths

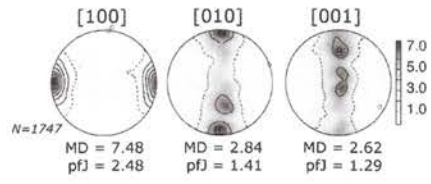


Figure 3. Fabric characteristics in the continental rifting (a) and continental margin (b) and a schematic model of its tectonic setting.

References

- Abe, N., Arai, S. and Saeki, Y., 1992, Hydration processes in the arc mantle; petrology of the Megata peridotite xenoliths, the Northeast Japan arc. *Journal of Mineralogy, Petrology and Economic Geology*, **87**, 305–317. (in Japanese with an English abstract)
- Abe, N. and Arai, S., 1993, Petrographical characteristics of ultramafic xenoliths from the Megata volcano, the Northeast Japan arc. *Sci. Rep. Kanazawa Univ.*, **38**, 1–24.
- Abe, N., Arai, S. and Ninomiya, A., 1995, Peridotite xenoliths and essential ejecta from the Ninomegata crater, the Northeastern Japan arc. *J. Mineral. Petrol. Econ. Geol.*, **90**, 41–49 (in Japanese with English abstract).
- Abe, N., 1997, Petrology of mantle xenoliths from the arcs: Implications for the petrochemical evolution of the wedge mantle. Doctoral Thesis, Kanazawa University, Kanazawa, Japan.
- Abe, N., Arai, S. and Yurimoto, H., 1998, Geochemical characteristics of the uppermost mantle beneath the Japan island arcs; implications for the upper mantle evolution. *Phys. Earth Planet. Int.*, **107**, 233–248.
- Abe, N., Tamaki, M. and Arai, S., 1999, Geochemistry of the ultramafic xenoliths from Oki-Dogo island: Implications for the wedge mantle evolution. *Ophioliti*, **24**, 47.
- Abe, N., Takami, M. and Arai, S., 2003, Petrological feature of spinel lherzolite xenoliths from Oki-Dogo Island: An implication for variety of the upper mantle peridotite beneath southwestern Japan. *Island Arc*, **12**, 219–232.
- Abramson, E. H., Brown, J. M., Slutsky, L. J. and Zang, J. J., 1997, The elastic constants of San Carlos olivine to 17 GPa, *J. Geophys. Res.*, **102**, 12253– 12263.

- Afonso, J. C., Ranalli, G., Fernandez, M., Griffin, W. L., O'Reilly, S. Y. and Faul, U., 2010, On the Vp/Vs-Mg# correlation in mantle peridotites: Implication for the identification of thermal and compositional anomalies in the upper mantle. *Earth Planet. Sci. Lett.*, **289**, 606-618.
- Aki, K. and Lee, W. H. L., 1976, Determination of three dimensional velocity anomalies under a seismic array using first P arrival times from local earthquakes, 1, A homogeneous initial model. *J. Geophys. Res.*, **81**, 4381-4399.
- Amelinckx, S. and Dekeyser, W., 1959, The structure and properties of grain boundaries. *Solid State Physics*, **8**, 325-499.
- Anthony, E. Y., Hoffer, J. M., Wagner, W. K. and Chen, W., 1992, Compositional diversity in late Cenozoic mafic lavas in the Rio Grande rift and Basin and Range province, southern New Mexico. *Geol. Soc. America Bull.*, **104**, 973-979.
- Anthony, E. Y. and Poths, J., 1992, ³He surface exposure dating and its implications for magma evolution in the Potrillo volcanic field, Rio Grande Rift, New Mexico, USA. *Geochim Cosmochim Acta*, **56**, 4105-4108.
- Anthony, E. Y., 2005. Source regions of granites and their links to tectonic environment: Examples from the western United States. *Lithos* (Ilmari Haapala Retirement Special Volume), **80**, 61-74.
- Arai, S., 1994, Characterization of spinel peridotites by olivine-spinel compositional relationships: Review and interpretation. *Chemical Geology*, **113**, 191-204.
- Arai, S., Abe, N. and Hirai, H., 1998, Petrological characteristics of the sub-arc mantle: An overview on petrology of xenoliths from the Japan arcs. *Trends in Mineralogy (Indeia)*, **2**, 39-55.
- Arai, S., Hirai, H., and Uto, K., 2000, Mantle peridotite xenoliths from the Southwest Japan arcs: A model for the sub-arc upper mantle structure and composition of the

- Western Pacific rim. *Journal of Mineralogical and Petrological Sciences*, **95**, 9–23.
- Arai, S., Abe, N., Hirai, H. and Shimizu, Y., 2001, Geological, petrographical and petrological characteristics of ultramafic-mafic xenoliths in Kurose and Takashima, northern Kyushu, southwestern Japan. *Sci. Rep. Kanazawa Univ.*, **46**, 9–38.
- Bascou, J., Deipech, G., Vauchez, A., Moine, B. N., Cottin, J. Y. and Barruol, G., 2008, An integrated study of microstructural, geochemical, and seismic properties of the lithospheric mantle above the Kerguelen plume (Indian Ocean). *Geochem. Geophys. Geosyst.*, **9**, Q04036, doi:10.1029/2007GC001879.
- Bell, D. R., Rossman, G. R., Maldener, A., Endisch, D. and Rauch, F., 2003, Hydroxide in olivine: A quantitative determination of the absolute amount and calibration of the IR spectrum. *J. Geophys. Res.*, **108**, doi: 10.1029/2001JB000679.
- Ben Ismaïl, W. and Mainprice, D., 1998, An olivine fabric database: An overview of upper mantle fabrics and seismic anisotropy. *Tectonophysics*, **296**, 145–157.
- Bolfan-Casanova, N., Keppler, H. and Rubie, D. C., 2000, Water partitioning between nominally anhydrous minerals in the MgO-SiO₂-H₂O system up to 24GPa: implications for the distribution of water in the Earth's mantle. *Earth Planet. Sci. Lett.*, **182**(3-4), 209-221.
- Bowman, J. R. and Ando, M., 1987, Shear-wave splitting in the upper-mantle wedge above the Tonga subduction zone. *Geophys. J. R. Astron. Soc.*, **88**, 25–41.
- Brearily, M., Scarfe, C. M., Fujii, T., 1984. The petrology of ultramafic xenoliths from Summit Lake, near Prince George, British Columbia. *Contrib. Mineral. Petrol.*, **88**, 53-63.
- Brey, G. P. and Köhler, T., 1990. Geothermobarometry in four-phase lherzolites II. New thermobarometers, and practical assessment of existing thermobarometers. *J.*

- Petrology*, **31**, 1535-1378.
- Buck, W. R., 2006, The role of magma in the development of the Afro–Arabian rift system. *Geological Society of London, Special Publications*, **259**, 43–54.
- Bunge, H. J., 1982, *Texture Analysis in Materials Sciences*. Butterworth, London.
- Bussod, G. Y. A. and Irving, A. J., 1981, Thermal and rheologic history of the upper mantle beneath the Southern Rio Grande Rift: evidence from Kilbourne Hole xenoliths, Conference on the Processes of Planetary Rifting. *Lunar and Planetary Institute*, pp. 145-148.
- Bystricky, M., Kunze, K., Burlini, L. and Burg, J.-P., 2000, High shear strain of olivine aggregates: rheological and seismic consequences. *Science*, **290**, 1564–1567.
- Ceuleneer, G., Nicolas, A. and Boudier, F., 1988, Mantle flow patterns at an oceanic spreading centre: The Oman peridotites record, *Tectonophysics*, **151**, 1-26.
- Chai, M., Brown, J. M., Slutsky, L. J. and Zang, J., 1997, The elastic constants of an aluminous orthopyroxene to 12.5 GPa. *J. Geophys. Res.*, **102**, 14779-14785.
- Clark, S. R., Stegman, D. and Müller, R. D., 2008, Episodicity in back-arc tectonic regimes, *Phys. Earth Planet. Int.*, Special Volume on Computational Geology and Geodynamics, edited by B. J. P. Kaus, T. V. Gerya and D.W. Schmid, 171, 265-279.
- Crampin, S., 1984, Effective anisotropic elastic constants for wave propagation through cracked solids. *Geophys. J. Royal Astro. Soc.*, **76**, 135-145.
- Collins, M. D. and Brown, J. M., 1998, Elasticity of an upper mantle clinopyroxene. *Phys. Chem. Miner.*, **26**, 7 – 13.
- Crosson, R. S. and Lin J. W., 1971, Voigt and Reuss prediction of anisotropic elasticity of dunite. *J. Geophys. Res.*, **76**, 570-578.

- Demouchy, S., 2004, Water in the Earth's interior: Thermodynamics and kinetics of hydrogen incorporation in olivine and wadsleyite. Universität Bayreuth.
- Demouchy, S., Mainprice, D., Tommasi, A., Couvy, H., Barou, F., Frost, D. J. and Cordier, P., 2011, Forsterite to wadsleyite phase transformation under shear stress and consequences for the Earth's mantle transition zone, *Earth Planet. Sci. Lett.*, **184**, 91-104.
- Dick, H. J. B. and Bullen, T., 1984, Chromian spinel as a petrogenetic indicator in abyssal and alpine-type peridotites and spatially associated lavas. *Contrib. Mineral. Petrol.*, **86**, 54-76.
- Doukhan, J. -C., Doukhan, N., Naze, L. and Van Duysen, J. -C., 1986, Défauts de réseau et plasticité cristalline dans les pyroxenes: Une revue. *Bulletin de Minéralogie*, **109**, 377-374.
- Dvorkin, J., Nur, A., Mavko, G. and Ben-Avraham, Z., 1993, Narrow subducting slabs and the origin of backarc basins. *Tectonophysics*, **227**, 63-79.
- Faccenna, C., Davy, P., Brun, J. P., Funicello, R., Giardini, D., Mattei, M. and Nalpas, T., 1996, The dynamic of backarc basins: An experimental approach to the opening of the Tyrrhenian Sea. *Geophys. J. Int.*, **126**, 781-795.
- Falus, G., Tommasi, A., Ingrin, J. and Szabo, C., 2008, Deformation and seismic anisotropy of the lithospheric mantle in the southeastern Carpathians inferred from the study of mantle xenoliths. *Earth Planet. Sci. Lett.*, **272**, 50-64.
- Fouch, M. J. and S. Rondenay, 2006, Seismic anisotropy beneath stable continental interiors. *Phys. Earth Planet. Int.*, **158**, 292-320.
- Frank, F. C. and Read, W. T. J., 1950, Multiplication processes for slow moving dislocations. *Physical Review*, **79**, 722-723.
- Fujiwara, M., and Arai, D., 1982, Ultramafic xenoliths in Aratoyama alkali basalt,

- Okayama Prefecture, as upper mantle materials beneath a typical island arc. *Journal of Mineralogy, Petrology and Economic Geology*, **3**, 219–227. (in Japanese with an English abstract)
- Gao, S., Davis, P. M., Liu, H., Slack, P. D., Rigor, A. W., Zorin, Y. A., Mordvinova, V. V., Kozhevnikov, V. M. and Logatchev, N. A., 1997, SKS splitting beneath continental rift zones. *J. Geophys. Res.*, **102**, B10, 22781-22797.
- Gao, W., Grand, S. P., Baldrige, W. S., Wilson, D., West, M., Ni, J. F. and Aster, R., 2004, Upper mantle convection beneath the central Rio Grande rift imaged by P and S wave tomography. *J. Geophys. Res.*, **109**(B03305), doi:10.1029/2003JB002743.
- Gao, S. S., Liu, K. H., Stern, R. J., Keller, G. R., Hogan, J. P., Pulliam, J. and Anthony, E. Y., 2008, Characteristics of mantle fabrics beneath the south-central United states: Constraints from shear-wave splitting measurements. *Geosphere*, **4**(2), 411-417.
- Gao, S. S. and Liu, K. H., 2009, Significant seismic anisotropy beneath the southern Lhasa Terrane, Tibetan Plateau. *Geochem. Geophys. Geosyst.*, **10**(Q02008), doi:10.1029/2008GC002227.
- Gao, S. S., Liu, K. H. and Abdelsalam, M. G., 2010, Seismic anisotropy beneath the Afar Depression and adjacent areas: Implications for mantle flow. *J. Geophys. Res.*, **115**(B12330), doi:10.1029/2009JB007141.
- Goto, K., 1986, Lamprophyre dikes and mafic-ultramafic xenoliths at Shingu, the outer zone of southwestern Japan. Master's thesis, University of Tsukuba, Japan.
- Goto, K. and Arai, S., 1987, Petrology of peridotite xenoliths in lamprophyre from Shingu, Southwestern Japan: Implications for origin of Fe-rich mantle peridotite. *Mineralogy and Petrology*, **37**, 137–155.

- Goto, A. and Yokoyama, K., 1988, Lherzolite inclusions in olivine nephelinite tuff from Salt Lake Crater, Hawaii. *Lithos*, **21**, 67–80.
- Grant, K., Ingrin, J., Lorand, J. and Dumas, P., 2007, Water partitioning between mantle minerals from peridotite xenoliths. *Contrib. Mineral. Petrol.*, **154**(1), 15-34.
- Griffin, W. L., O'Reilly, S. Y., Afonso, J. C. and Begg, G., 2008, The composition and evolution of lithospheric mantle: a re-evaluation and its tectonic implications. *J. Petrol.*, doi:10.1093/petrology/egn033.
- Griffin, W. R., Foland, K. A., Stern, R. J. and Leybourne, M. L., 2010, Geochronology of Bimodal Alkaline Volcanism in the Balcones Igneous Province, Texas: Implications for Cretaceous Intraplate Magmatism in the Northern Gulf of Mexico Magmatic Zone. *Journal of Geology*, **118**, 1-23.
- Grimmer, H., 1979, The distribution of disorientation angles if all relative orientations of neighbouring grains are equally probable. *Scripta Metallurgica*, **13**(2), 161-164.
- Gripp, A. E. and Gordon, R. G., 2002, Young tracks of hotspots and current plate velocities. *Geophys. J. Int.*, **150**, 321 – 361.
- Günther, D. and Heinrich, C. A., 1999, Enhanced sensitivity in LAICP-MS using helium-argon mixtures as aerosol carrier. *Journal of Analytical Atomic Spectrometry*, **14**, 1369-1374.
- Hamblock, J. M., Andronicos, C. L., Miller, K. C., Barnes, C. G., Ren, M. -H., Averill, M. G. and Anthony, E. Y., 2007, A composite geologic and seismic profile beneath the southern Rio Grande rift, New Mexico, based on xenoliths mineralogy, temperature, and pressure. *Tectonophysics*, **442**, 14-48.
- Hill, R., 1952, The elastic behaviour of a crystalline aggregate. *Proc. Phys. Soc. London Ser. A*, **65**, 349-354.

- Hirth, G. and Kohlstedt, D. L., 1995, Experimental constraints on the dynamics of the partially molten upper mantle: deformation in the dislocation creep regime. *J. Geophys. Res.*, **100**, 15441–15449.
- Holtzman, B. K., Kohlstedt, D. L., Zimmerman, M. E., Heidelbach, F., Hiraga, T. and Hustoft, J., 2003, Melt segregation and strain partitioning: Implications for seismic anisotropy and mantle flow. *Science*, **301**, 1227–1230, doi:10.1126/science.1087132.
- Irving, A. J., 1980, Petrology and geochemistry of composite ultramafic xenoliths in alkalic basalts and implications for magmatic processes within the mantle. *Am. J. Sci.*, **280-A**, 389–426.
- Ishise, M., and Oda, H., 2005, Three-dimensional structure of P-wave anisotropy beneath the Tohoku district, northeast Japan. *J. Geophys. Res.*, **110**(B07304), doi:10.1029/2004JB003599.
- Iwamori, H., 1989, Compositional zonation of Cenozoic basalts in the Central Chugoku district, Southwestern Japan: Evidence for mantle upwelling. *Bulletin of the Volcanological Society of Japan*, **34**(2), 105–123.
- Jung, H. and Karato, S., 2001, Water-induced fabric transitions in olivine. *Science* **293**, 24–27.
- Jolivet, L., Tamaki, K. and Fournier, M., 1994, Japan Sea, opening history and mechanism: A synthesis. *J. Geophys. Res.*, **99**(B11), 22,237–22,259.
- Kaminski, É., Ribe, N. M., 2001, A kinematic model for recrystallization and texture development in olivine polycrystals. *Earth Planet. Sci. Lett.*, **189**, 253–267.
- Kaneoka, I., Matsuda, J., Xashu, D., Takahashi, E. and Aoki, K., 1978, Ar and Sr isotopes of mantle-derived rocks from the Japanese islands. *Bulletin of Volcanology*, **41**, 424–433.

- Karato S. -I., 1998, Seismic anisotropy in the deep mantle, boundary layers and the geometry of mantle convection. *Pure and Applied Geophysics*, **151**, 565-587.
- Katayama, I., Jung, H. and Karato, S. -I., 2004, New type of olivine fabric from deformation experiments at modest water content and low stress. *Geology*, **32** (12), 1045–1048.
- Kelemen, P. B. and Dick, H. J. B., 1995, Focused melt flow and localized deformation in the upper mantle: juxtaposition of replacive dunite and ductile shear zones in the Josephine peridotite, SW Oregon. *J. Geophys. Res.*, **100**, 423–438.
- Keller, G. R., Kruger, J. M., Smith, K. J. and Voight, W. M., 1989, The Ouachita system: A geophysical overview, in *The Appalachian–Ouachita Orogen in the United States (The Geology of North America F2)*, Edited by R. D. Hatcher Jr., W. A. Thomas, G. W. Viele, pp. 689-694, Geol. Soc. Am.
- Kendall, J. -M., Stuart, G. W., Ebinger, C. J., Bastow, I. D. and Keir, D., 2005, Magma-assisted rifting in Ethiopia. *Nature*, **433**, 146-148.
- Kendall, J. -M., Pilidou, S., Keir, D., Bastow, I. D., Stuart, G. W. and Ayele, A., 2006, Mantle upwellings, melt migration and the rifting of Africa: insights from seismic anisotropy. *Geological Society of London, Special Publications*, **259**, 55–72.
- Kimura, J., Stern, R. J. and Yoshida, T., 2005, Reinitiation of subduction and magmatic responses in SW Japan during Neogene time. *GSA Bulletin*, **117**(7/8), 989–986.
- Kuno, H., 1967, Mafic and ultramafic nodules from Itinome-gata, Japan. In: Wyllie, P.J. (Ed.), *Ultramafic and Related Rocks*. John Wiley & Sons, New York, pp. 337–346.
- Lee, C. -T. A., 2003, Compositional variation of density and seismic velocities in natural peridotites at STP conditions: implications for seismic imaging of

- compositional heterogeneities in the upper mantle. *J. Geophys. Res.*, **108**. doi:10.1029/2003JB002413.
- Le Roux, V., Bodinier, J. -L., Tommasi, A., Alard, O., Dautria, J. -M., Vauchez, A. and Riches, A. J. V., 2007, The Lherz spinel lherzolite: refertilized rather than pristine mantle. *Earth Planet. Sci. Lett.*, **259**, 599–612.
- Le Roux, V., Tommasi, A. and Vauchez, A., 2008, Feedback between melt percolation and deformation in an exhumed lithosphere-asthenosphere boundary. *Earth Planet. Sci. Lett.*, **274**, 401-413.
- Libowitzky, E. and Rossman, G. R., 1997, An IR absorption calibration for water in minerals. *Am. Mineral.*, **82**, 1111–1115.
- Liu, K. H., Gao, S. S., Gao, Y. and Wu, J., 2008, Shear wave splitting and mantle flow associated with the deflected Pacific slab beneath northeast Asia. *J. Geophys. Res.*, **113**(B01305), doi:10.1029/2007JB005178.
- Liu, K. H., 2009, NA-SWS-1.1: A uniform database of teleseismic shear wave splitting measurements for North America. *Geochem. Geophys. Geosyst.*, **10**, Q05011, doi:10.1029/2009GC002440.
- Mackwell, S. J., 1991, High-temperature rheology of enstatite: implications for creep in the mantle. *Geophys. Res. Lett.*, **18**(11), 2027–2030.
- Mainprice, D. and Humbert, M., 1994, Methods of calculating petrophysical properties from lattice preferred orientation data. *Surv. Geophys.*, **15**, 575-592.
- Mainprice, D., 1997, Modelling anisotropic seismic properties of partially molten rocks found at mid-ocean ridges. *Tectonophysics*, **279**, 161-179.
- Mainprice, D., 2007, Seismic anisotropy of the deep Earth from a mineral and rock physics perspective, In: Schubert, G. (ed.), *Treatise on Geophysics*, vol. 2. Elsevier, Oxford, pp. 437–492.

- Mainprice, D., Barruol, G. and Ben Ismail, W., 2000, The anisotropy of the Earth's mantle: From single crystal to polycrystal. *in Mineral Physics and Seismic Tomography: From Atomic to Global*, Geophys. Monogr. Ser., vol. 117, edited by S. Karato et al., pp. 237–264, AGU, Washington, D. C.
- Martinez, F., Okino, K., Ohara, Y., Reysenbach, A., and Goffredi, S., 2007, Back-Arc Basins. *Oceanography*, **20**(1), 116-127.
- Martinod, J., Hatzfeld, D., Brun, J. -P., Davy, P., Gautier, P., 2000, Continental collision, gravity spreading, and kinematics of Aegean and Anatolia. *Tectonics*, **19**, 290–299.
- Matsukage, K. N., Nishihara, Y. and Karato, S. I., 2005, Seismological signature of chemical differentiation of Earth's upper mantle. *J. Geophys. Res.*, **110**(B12305), doi:10.1029/2004JB003504.
- Mehl, L., Hacker, B. R., Hirth, G. and Kelemen, P. B., 2003, Arc-parallel flow within the mantle wedge: Evidence from the accreted Talkeetna arc, south central Alaska. *J. Geophys. Res.*, **108**(B8, 2375), doi:10.1029/2002JB002233.
- Michael, A. H., 1988, Effects of three-dimensional velocity structure on the seismic of the seismicity of the 1984 Morgan Hill, California, aftershock sequence. *Bull. Seismol. Soc. Am.*, **78**, 1199-1221.
- Michibayashi, K. and Mainprice, D., 2004, The role of pre-existing mechanical anisotropy on shear zone development within oceanic mantle lithosphere: and example from the Oman ophiolites. *J. Petrol.*, **45**(2), 405-414, doi: 10.1093/petrology/egg099.
- Michibayashi, K., Ina, T. and Kanagawa, K., 2006, The effect of dynamic recrystallization on olivine fabric and seismic anisotropy: insight from a ductile shear zone, Oman ophiolite. *Earth Planet. Sci. Lett.*, **244**, 695–708.

- Michibayashi, K., Oohara, T., Satsukawa, T., Ishimaru, S., Arai, S. and Okrugin, V. M., 2009, Rock seismic anisotropy of the low velocity zone beneath the volcanic front in the mantle wedge. *Geophys. Res. Lett.*, **36**(L12305), doi:10.1029/2009GL038527.
- Mickus, K., Stern, R. J., Keller, G. R. and Anthony, E. Y., 2009, Potential field evidence for a volcanic rifted margin along the Texas Gulf Coast. *Geology*, **37**, 387-390.
- Miyashiro, A., 1973, *Metamorphism and Metamorphic Belts*. George Allen & Unwin, London.
- Nagao, K., and Takahashi, E., 1993, Noble gases in the mantle wedge lower crust: An inference from the isotopic analyses of xenoliths from Oki-Dogo and Ichinomegata, Japan. *Geochemical Journal*, **27**, 229–240.
- Nakajima, J., Matsuzawa, T., Hasegawa, A. and Zhao, D., 2001, Threedimensional structure of Vp, Vs, and Vp/Vs beneath the northeastern Japan arc: implications for arc magmatism and fluids. *J. Geophys. Res.*, **106**, 21843–21857.
- Nakajima, J. and Hasegawa, A., 2004. Shear-wave polarization anisotropy and subduction-induced flow in the mantle wedge of northeastern Japan. *Earth Planet. Sci. Lett.*, **225**, 365-377.
- Nakajima, J., Takei, Y. and Hasegawa, A., 2005, Quantitative analysis of the inclined low-velocity zone in the mantle wedge of northeastern Japan: A systematic change of melt-filled pore shapes with depth and its implications for melt migration. *Earth Planet. Sci. Lett.*, **234**, 59-70.
- Naze, L., Doukhan, N., Doukhan, J. C. and Latrous, K., 1987, TEM study of lattice defects in naturally and experimentally deformed orthopyroxenes. *Bull. Mineral.*, **110**, 497–512.

- Nicolas, A., Boudier, F. and Boullier, A. M., 1973, Mechanisms of flow in naturally and experimentally deformed peridotites. *Am. J. Sci.*, **273**, 853–876.
- Nicolas, A. and Christensen, N. I., 1987, Formation of anisotropy in upper mantle peridotites: A review, in *Composition, Structure and Dynamics of the Lithosphere-Asthenosphere System*. Geodyn. Ser., vol. 16, edited by K. Fuchs and C. Froidevaux, pp. 111 – 123, AGU, Washington, D. C.
- Nicolas, A., and Boudier, F., 2008, Large shear zones with no relative displacement. *Terra Nova*, **20**(3), 200-205.
- Nimis, P. and Taylor, W. R., 2000, Single clinopyroxene thermobarometry for garnet peridotites. Part I. Calibration and testing of a Cr-rich-Cpx barometer and an enstatite-in Cpx thermometer. *Contrib. Mineral. Petrol.*, **139**, 541–554.
- Nixon, P. H., 1987. *Mantle Xenoliths*. John Wiley & Sons, New York.
- Otofuji, Y. and Matsuda, T., 1984, Timing of rotational motion of Southwest Japan inferred from paleomagnetism. *Earth Planet. Sci. Lett.*, **70**, 373–382.
- Otofuji, Y., Matsuda, T. and Nohda, S., 1985. Paleomagnetic evidence from the Miocene counter-clockwise rotation of Northeast Japan—rifting process of the Japan Sea. *Earth Planet. Sci. Lett.*, **75**, 265–277.
- Passchier, C. W. and Trouw, R. A. J., 2005, *Microtectonics*. Springer Berlin Heidelberg, New York.
- Paterson, M. S., 1982, The determination of hydroxyl by infrared absorption in quartz, silicate-glasses and similar materials. *Bulletin de Minéralogie*, **105**(1), 20-29.
- Pera, E., Mainprice, D. and Burlini, L., 2003, Anisotropic seismic properties of the upper mantle beneath the Torre Alfina area (northern Apennines, central Italy). *Tectonophys*, **370**, 11 –30.
- Perkins, D. and Anthony, E. Y., 2011, The evolution of spinel lherzolite xenoliths and

- the nature of the mantle at Kilbourne Hole, New Mexico. *Contrib. Mineral. Petrol.*, doi: 10.1007/s0410-011-0644-1.
- Peslier, A. H., Francis, D. and Ludden, J., 2002, The lithospheric mantle beneath continental margins: melting and melt-rock reaction in Canadian Cordillera xenoliths. *J. Petrol.*, **43**, 2013-2047.
- Peslier, A. and Luhr, J., 2006, Hydrogen loss from olivines in mantle xenoliths from Simcoe (USA) and Mexico: Mafic alkalic magma ascent rates and water budget of the sub-continental lithosphere. *Earth Planet. Sci. Lett.*, **242**(3-4), 302-319.
- Pulliam, J., Suhardja, S., Stern, R. J., Anthony, E. Y., Gao, S., Keller, G. R. and Mickus, K., 2009, Broadband Seismic Study of the Texas Continent-Ocean Boundary: A Pilot Project. Geological Society of America, South-Central Section – 43rd Annual Meeting, Richardson, TX, 16-17 March 2009.
- Ramsay, J. G. and Graham, R. H., 1970, Strain variation in shear belts. *Can. J. Earth Sci.*, **7**, 786–813.
- Ramsay, J. G., 1980, Shear zone geometry: a review. *J. Struct. Geol.*, **2**(1/2), 83–99.
- Raye, U., Stern, R. J., Anthony, E. Y., Ren, M., Kimura, J., Tani, K. and Qing, C., 2009, Characterization of mantle beneath Texas: Constraints from Knippa xenoliths, *GSA Abstracts*, **41**(2), 29.
- Reuss, A., 1929, Berechnung der Fließgrenze von Mischkristallen auf Grund der Plastizitätsbedingung für Einkristalle. *Z. Angew. Math. Mech.* **9**, 49-58.
- Rosenberg, C. L. and Handy, M. R., 2000, Syntectonic melt pathways during simple shearing of a partially molten rock analogue (Norcampher–Benzamide). *J. Geophys. Res.*, **105**, 3135–3149.
- Rosenberg, C. L. and Handy, M. R., 2005, Experimental deformation of partially melted granite revisited: implications for the continental crust. *J. Metamor. Geol.*,

23, 19–28.

Sato, H., 1993, The relationship between late Cenozoic tectonic events and stress field and basin development in NE Japan. *J. Geophys. Res.*, **99**(B11), 22261–22274.

Sato, H., 1994, The relationship between late Cenozoic tectonic events and stress field and basin development in northeast Japan. *J. Geophys. Res.*, **99**, 22,261– 22,274.

Satsukawa, T. and Michibayashi, K., 2009, Determination of slip system in olivine based on crystallographic preferred orientation and subgrain-rotation axis: examples from Ichinomegata peridotite xenoliths, Oga peninsula, Akita prefecture. *J. Geol. Soc. Jpn.*, **115**, 288-291.

Satsukawa, T., Michibayashi, K., Raye, U., Anthony, E. Y., Pulliam, J. and Stern, R., 2010, Uppermost mantle anisotropy beneath the southern Laurentian margin: Evidence from Knippa peridotite xenoliths, Texas. *Geophys. Res. Lett.*, **37**(L20312), doi:10.1029/2010GL044538.

Satsukawa, T., Michibayashi, K., Anthony, E. Y., Stern, R. J., Gao, S. S. and Liu, K. H., 2011, Seismic anisotropy of the uppermost mantle beneath the Rio Grande rift: Evidence from Kilbourne Hole peridotite xenoliths, New Mexico. *Earth Planet. Sci. Lett.*, **311**(1-2), 172-181, doi:10.1016/j.epsl.2011.09.013.

Sen, G. and Leman, W. P., 1991, Iron-rich lherzolitic xenoliths from Oahu: Origin and implications for Hawaiian magma sources. *Earth Planet. Sci. Lett.*, **102**, 45–57.

Savage, M. K., 1999, Seismic anisotropy and mantle deformation: what have we learned from shear wave splitting? *Rev. Geophys.*, **37**, 65-106.

Silver, P. G. and Chan, W. W., 1991, Shear wave splitting and subcontinental mantle deformation. *J. Geophys. Res.*, **96**, 16429–16454

Silver, P. G., 1996, Seismic anisotropy beneath the continents: Probing the depths of geology. *Ann. Rev. Earth. Planet. Sci.*, **24**, 385-432.

- Skemer, P., Katayama, I., Jiang, Z. and Karato, S., 2006, The misorientation index: development of a new method of olivine lattice preferred orientations. *Tectonophysics*, **411**, 157–167.
- Soustelle, V., Tommasi, A., Bodinier, J. I., Garrido, C. J. and Vauchez, A., 2009, Deformation and reactive melt transport in the mantle lithosphere above a large-scale partial melting domain: the Ronda peridotite massif, southern Spain. *J. Petrol.*, **50**(7), 1235–1266.
- Soustelle, V., Tommasi, A., Demouchy, S. and Ionov, D. A., 2010, Deformation and Fluid-Rock Interaction in the Supra-subduction Mantle: Microstructures and Water Contents in Peridotite Xenoliths from the Avacha Volcano, Kamchatka. *J. Petrol.*, **51**(1&2), 363-394, doi:10.1093/petrology/egp085.
- Soustelle, V. and Tommasi, A., 2010, Seismic properties of the supra-subduction mantle: Constraints from peridotite xenoliths from the Avacha volcano, southern Kamchatka. *Geophys. Res. Lett.*, **37**(L13307), doi:10.1029/2010GL043450.
- Stein, M., Garfunkel, Z. and Jagoutz, E., 1993, Chronothermometry of peridotitic and pyroxenitic xenoliths: Implications for the thermal evolution of the Arabian lithosphere. *Geochim Cosmochim Acta*, **57**, 1325-1337.
- Takahashi, E., Shimazaki, T., Tsuzaki, Y. and Yoshida, H., 1993, Melting study of a peridotite KLB-1 to 6.5 GPa, and the origin of basaltic magmas. *Phil. Trans. R. Soc. Lond. A.*, **342**, 105-120.
- Takahashi, E., 1975, Finding of spinel-lherzolites inclusions in Oki-Dogo Island, Japan. *J. Geol. Soc. Jpn.*, **81**, 81–83. (in Japanese)
- Takahashi, E., 1978a, Petrologic model of the crust and upper mantle of the Japanese Island arcs. *Bulletin of Volcanology*, **41**, 529–547.
- Takahashi, E., 1978b, Petrology of the upper mantle and lower crust of the Japanese

- Island arcs. Doctoral Thesis, University of Tokyo, Tokyo, Japan.
- Takahashi, E., 1986, Genesis of calc-alkali andesite magma in a hydrous mantle–crust boundary: petrology of lherzolite xenoliths from the Ichinomegata crater, Oga Peninsula, Northeast Japan, Part II. *J. Volcanol. Geotherm. Res.*, **29**, 355–395.
- Takamura, H., 1978, Finding of spinel–lherzolite xenolith in basaltic sheets from Shingu, Ehime Prefecture, Japan. *J. Geol. Soc. Jpn.*, **84**, 475–479 (in Japanese).
- Takei, Y., 2002, Effect of pore geometry on VP/VS: From equilibrium geometry to crack. *J. Geophys. Res.*, **107**(B2), 2043, doi:10.1029/2001JB000522.
- Takei, Y., 2005, Deformation-induced grain boundary wetting and its effects on the acoustic and rheological properties of partially molten rock analogue. *J. Geophys. Res.*, **110**, doi:10.1029/2005JB003801.
- Tamaki, K., Suyehiro, K., Allam, J., Ingle, J. C. and Pisciotto, K. A., 1992, *Tectonic synthesis and implication of Japan Sea ODP Drilling*, IN: Tamaki, K., et al. (eds.), Proceedings of the Ocean Drilling Program, Scientific Results 127/128, Part 2. Ocean Drilling Program, College Station, pp. 1333–1348.
- Tamaki, K., 1995, Opening tectonics of the Japan-Sea in Backarc Basins: Tectonics and Magmatism. Edited by B. Taylor 407-450, Plenum Press New York.
- Tamaki, K. and Honza, E., 1991, Global tectonics and formation of marginal basins: role of the western Pacific. *Episodes*, **14**, 224–230.
- Tanaka, T., Hoshino, M., 1987, Sm–Nd ages of Oki metamorphic rocks and their geological significance. In 94th Annual Meeting, Geological Society of Japan., Osaka, Japan, pp. 492.
- Tasaka, M., Michibayashi, M. and Mainprice, D., 2008, B-type olivine fabrics developed in the fore-arc side of the mantle wedge along a subducting slab. *Earth Planet. Sci. Lett.*, **272**, 747-757.

- Thomas, W. A., 2006, Tectonic inheritance at a continental margin, *GSA Today*, **16**, 4-11.
- Thompson, R. N., Ottley, C. J., Smith, P. M., Pearson, D. G., Dickin, A. P., Morrison, M. A., Leat, P. T. and Gibson, S. A., 2005, Source of the quaternary alkalic basalts, picrites and basanites of the Potrillo Volcanic Field, New Mexico, USA: Lithosphere or convecting mantle? *J. Petrol.*, **46**, 1603-1643.
- Thoraval, C., Tommasi, A. and Doin, M. -P., 2006, Plume–lithosphere interactions beneath a fast-moving plate. *Geophys. Res. Lett.*, **33**(L01301), doi:01310.01029/02005GL024047.
- Tommasi, A., Mainprice, D., Canova, G. and Chastel, Y., 2000, Viscoplastic self-consistent and equilibrium-based modeling of olivine lattice preferred orientations: Implications for the upper mantle seismic anisotropy. *J. Geophys. Res.*, **105**(B5), 7893–7908.
- Tommasi, A., Godard, M., Coromina, G., Dautria, J. M. and Barseczus, H., 2004, Seismic anisotropy and compositionally induced velocity anomalies in the lithosphere above mantle plumes: a petrological and microstructural study of mantle xenoliths from French Polynesia. *Earth Planet. Sci. Lett.*, **227**(3-4), 539-556.
- Tommasi A., Vauchez A., Godard M. and Belley F., 2006, Deformation and melt transport in a highly depleted peridotite massif from the Canadian Cordillera: Implications to seismic anisotropy above subduction zones. *Earth Planet. Sci. Lett.*, **252**, 245–259.
- Tommasi, A., Vauchez, A. and Ionov, D. A., 2008, Deformation, static recrystallization, and reactive melt transport in shallow subcontinental mantle xenoliths (Tok Cenozoic volcanic field, SE Siberia). *Earth Planet. Sci. Lett.*, **272**,

65-77.

- Uchimizu, M., 1966, Geology and petrology of alkali rocks from Dogo, Oki Islands. *Journal of the Faculty of Science, University of Tokyo, Series II*, **16**, 85–159.
- Ulich, S. and Mainprice, D., 2005, Does cation ordering in omphacite influence development of lattice-preferred orientation? *J. Struct. Geol.*, **27**, 419-431.
- Uto, K., Takahashi, E., Nakamura, E. and Kaneoka, I., 1994, Geochronology of alkali volcanism in Oki-Dogo Island, Southwest Japan: Geochemical evolution of basalts related to the opening of the Japan Sea. *Geochemical Journal*, **28**, 431–449.
- Uto, K., Hirai, H., Goto, K. and Arai, S., 1987, K–Ar ages of carbonate-and mantle nodule-bearing lamprophyre dikes from Shingu, central Shikoku, Southwest Japan. *Geochem. J.*, **21**, 283–290.
- Uto, K., 1990, Neogene volcanism of Southwest Japan: its time and space on K–Ar dating. PhD thesis, University of Tokyo, Japan.
- Van Achtebergh, E., Griffin, W. L. and Stiefenhofer, J., 2001, Metasomatism in mantle xenoliths from the Letlhakane kimberlites: estimation of element fluxes. *Contrib. Mineral. Petrol.*, **141**, 397–414.
- Vaucher A. Tommasi A. Barruol G. and Maumus J., 2000, Upper mantle deformation and seismic anisotropy in continental rifts. *Phys. Chem. Earth, Part A Solid Earth Geod.*, **25** 111–117.
- Vaucher, A. and Garrido, C. J., 2001, Seismic properties of an asthenospherized lithospheric mantle: constraints from lattice preferred orientation in peridotite from the Ronda massif. *Earth Planet. Sci. Lett.*, **192**, 235–249.
- Vaucher, A. and Tommasi, A., 2003, Wrench faults down to the asthenosphere: Geological and geophysical evidence and thermo–mechanical effects, IN: Storti, F., Holdsworth, R.E., Salvini, F. (eds.), *Intraplate Strike-Slip Deformation Belts*.

- Geological Society of London Special Publications, London, pp. 15–24.
- Vauchez, A., Dineura, F. and Rudnick, R., 2005, Microstructure, texture and seismic anisotropy of the lithospheric mantle above a mantle plume: Insights from the Labait volcano xenoliths (Tanzania). *Earth Planet. Sci. Lett.*, **232**, 295-314.
- Voigt, W., 1928, *Lerrbuch der Kristallphysik*, Teubner-Verlag, Leipzig.
- Vonlanthen, P., Kunze, K., Burlini, L. and Grobety, B., 2006, Seismic properties of the upper mantle beneath Lanzarote (Canary Islands): Model predictions based on texture measurements by EBSD. *Tectonophysics*, **428**, 65–85.
- Wagner, L. S., Beck, S., Zandt, G. and Ducea, M. N., 2006, Depleted lithosphere, cold, trapped asthenosphere, and frozen melt puddles above the flat slab in central Chile and Argentina. *Earth Planet. Sci. Lett.*, **245**, 289–301, doi:10.1016/j.epsl.2006.02.014.
- Watanabe, T., Shirasugi, Y., Yano, H. and Michibayashi, K., 2011, Seismic velocity in antigorite-bearing serpentinite mylonites. *Geological Society, London, Special Publications 2011*, **360**, 97-112.
- West, M., Ni, J., Baldrige, W. S., Wilson, D., Aster, R., Gao, W. and Grand, S., 2004, Crust and upper mantle shear wave structure of the southwest United States: Implications for rifting and support for high elevation. *J. Geophys. Res.*, **109**(B03309), doi:10.1029/2003JB002575.
- Wilkinson, J. F. and Binns, R. A., 1977, Relatively iron-rich lherzolite xenoliths of the Cr-diopside Suite: A guide to the primary nature of anorogenic tholeiitic andesite magmas. *Contrib. Mineral. Petrol.*, **65**, 199–212.
- Williams, W. J. W., 1999, Evolution of Quaternary intra plate mafic lavas from the Potrillo volcanic field, USA, and the San Quintin volcanic field, Mexico. Univ. Texas at El Paso. Unpub PhD dissertation, 186p.

- Wilson, D., Aster, R. and LA RISTRA Team, 2003, Imaging crust and upper mantle seismic structure in the southwestern United States using teleseismic receiver functions. *The Leading Edge*, **22**(3), 232-237.
- Wüstefeld, A., Bokelmann, G., Zarol, C., and Barruol, G., 2008, SplitLab: A shear-wave splitting environment in Matlab. *Computers & Geosciences*, **34**(5), 515-128.
- Wilshire, H. G., Meyer, C. E., Nakata, J. K., Calk, L. C., Shervais, J. W., Nielson, J. E. and Schwartzman, E. C., 1988, Mafic and ultramafic xenoliths from volcanic rocks of the western United States. U.S. *Geological Survey Professional Paper*, **1443**, 179 pp.
- Yamamoto, J., Kagi, H., Kawakami, Y., Hirano, N. and Nakamura, M., 2007, Paleo-Moho depth determined from the pressure of CO₂ fluid inclusions: Raman spectroscopic barometry of mantle- and crust-derived rocks. *Earth Planet. Sci. Lett.*, **253**, 369–377.
- Young, H. P., and Lee, C.-T. A., 2009, Fluid-metasomatized mantle beneath the Ouachita belt of southern Laurentia: Fate of lithospheric mantle in a continental orogenic belt. *Lithosphere*, **1**, 370-383.
- Zhang, S. and Karato, S.-I., 1995, Lattice preferred orientation of olivine aggregates deformed in simple shear. *Nature*, **375**, 774–777.
- Zhao, D., Horiuchi, S. and Hasegawa, A., 1990, 3-D seismic velocity structure of the crust and the uppermost mantle in the northeastern Japan Arc. *Tectonophysics*, **181**, 135–149.